

# Sheffield Hallam University

*Lattice Boltzmann method for Q-tensor nemato-dynamics in liquid crystal display devices.*

SPENCER, Timothy J.

Available from the Sheffield Hallam University Research Archive (SHURA) at:

<http://shura.shu.ac.uk/20393/>

## A Sheffield Hallam University thesis

This thesis is protected by copyright which belongs to the author.

The content must not be changed in any way or sold commercially in any format or medium without the formal permission of the author.

When referring to this work, full bibliographic details including the author, title, awarding institution and date of the thesis must be given.

Please visit <http://shura.shu.ac.uk/20393/> and <http://shura.shu.ac.uk/information.html> for further details about copyright and re-use permissions.

CITY CAMPUS, HOWARD STREET  
SHEFFIELD S1 1WB



**REFERENCE**

ProQuest Number: 10701039

All rights reserved

INFORMATION TO ALL USERS

The quality of this reproduction is dependent upon the quality of the copy submitted.

In the unlikely event that the author did not send a complete manuscript and there are missing pages, these will be noted. Also, if material had to be removed, a note will indicate the deletion.



ProQuest 10701039

Published by ProQuest LLC (2017). Copyright of the Dissertation is held by the Author.

All rights reserved.

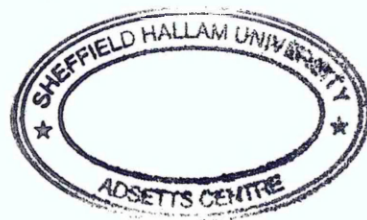
This work is protected against unauthorized copying under Title 17, United States Code  
Microform Edition © ProQuest LLC.

ProQuest LLC.  
789 East Eisenhower Parkway  
P.O. Box 1346  
Ann Arbor, MI 48106 – 1346

# Lattice Boltzmann Method For Q-Tensor Nemato-dynamics In Liquid Crystal Display Devices

Timothy James Spencer

A thesis submitted in partial fulfilment of the requirements of  
Sheffield Hallam University  
for the degree of Doctor of Philosophy



April 2005

## Abstract

Nematic liquid crystals are fluids whose anisometric molecules show long range orientational order but no positional order. The orientational order gives rise to anisotropic properties that have widely been exploited as the basis for liquid crystal display devices. The Ericksen-Leslie director theory has successfully been used to describe many dynamic properties of liquid crystals however there are situations in which a more complete description may be given in terms of the second rank traceless symmetric  $Q$ -tensor.

The development of a liquid crystal device solver is described. The solver calculates the flow, director and order parameter fields in three-dimensions through the  $Q$ -tensor equations of nemato-dynamics. The solver includes elastic, electric, magnetic, thermotropic, flexoelectric, dielectric and surface anchoring effects. Coupled lattice Boltzmann algorithms are used with anisotropic forcing terms included in order to reproduce the governing equations. A Chapman-Enskog analysis demonstrates that the algorithm recovers the target macroscopic equations.

The method is successfully validated against analytical results for the effect of temperature, external electric fields, flow alignment and Miesowicz viscosities. Further validation is given against numerical solutions of a one-dimensional model of a liquid crystal display device proposed by Davidson.

The switching behaviour of a Zenithal Bistable Display is then investigated. It is shown how flexoelectric properties of nematics produce bistability within this device. Defect creation and annihilation processes are shown during device switching for which it is necessary to use a method with variable order parameter. An approach to determine the flexoelectric coefficients is discussed. Results are presented for the preliminary characterisation and operation of this display that may enable optimisation for use in the display industry.

## Acknowledgements

I would like to express my thanks to the people who have supported me during the period of this study. To Prof Chris Care, my director of studies, for his help and guidance. To Dr Doug Cleaver and Dr Ian Halliday for their comments and advice. A thank you also to my colleagues and friends within the Modelling Lab. Thanks to my wonderful Parents, Sister and friends for their love, friendship, encouragement, help and support.

*“I have learned how much of what we think to be necessary is superfluous; I learned how few things are essential, and how essential those things really are.”*

Bernard Ferguson, Chindits, Burma, 1943.

\* \* \* \* \*

## Publications

This thesis contains some work published in the following journal and is attached towards the back:

M. M. Dupin, T. J. Spencer, I. H. Halliday and C. M. Care, *A many component lattice Boltzmann equation simulation for deformable particles*, Phil. Trans. R. Soc. Lond. A, **362**, pages 1885-1914, (2004).

\* \* \* \* \*

## Advanced Studies

The following is a chronological list of related postgraduate work undertaken and meetings attended during the course of study:

- Postgraduate Research Methods Unit, SET Graduate School, Sheffield Hallam University (November 2001).
- BLCS Winter Workshop, University of Hull, (December 2001).
- Undergraduate Unit in Fluid Mechanics, Sheffield Hallam University, (February 2002).
- SIMU - "Novel methods in soft matter simulations", Summer School, Helsinki, Finland, (June 2002).
- IOP Workshop, "Liquid Crystal Colloids", Sheffield Hallam University, (April 2002).
- IOP, Complex Fluids Group Winter School, University of Warwick, (December 2002).
- MRI Research Day "Materials Science and Engineering for the Medical Industry", Sheffield Hallam University, (January 2004). Poster Presentation "Dynamic Modelling for Energy Saving Liquid Crystal Displays".
- BLCS Annual Meeting, Manchester Metropolitan University, (April 2004). Poster presentation, "Mesoscopic Modelling of the Flexoelectric Effect in a Bistable Device".
- UK Grad School, Otterburn, (April 2004).
- MRI Seminar Programme, Sheffield Hallam University (May 2004). Oral Presentation "Simulating liquid crystals and next generation LCD's".
- 20<sup>th</sup> ILCS, Ljubljana, Slovenia, (July 2004). Poster presentation, "Mesoscopic Modelling of the Flexoelectric Effect in a Bistable Device".

- IOP Complex Fluids Group, "Modelling and Simulation of Colloids Conference", Sheffield Hallam University, (September 2004). Poster presentation, "Mesoscopic Modelling of the Flexoelectric Effect in a Bistable Device".
- CCP5 Workshop, "Developments, and applications of, the lattice Boltzmann technique", Sheffield Hallam University, (November 2004).
- "Mini-Symposium on Chirality and Nonlinearity in Liquid Crystals", The Rank Prize Funds, Grasmere (November 2004). Oral presentation, "Micro-textured surfaces within a Landau DeGennes framework".
- BLCS Annual Meeting, Exeter University, (March 2005). Poster presentation, "Dynamic Latching in a Zenithal Bistable Device".

\* \* \* \* \*

# Contents

<b>1</b>	<b>Introduction</b>	<b>1</b>
1.1	The Study . . . . .	1
1.1.1	Aims and Objectives . . . . .	2
1.1.2	Organisation of Thesis . . . . .	2
1.2	Liquid Crystal Primer . . . . .	4
1.2.1	Physical Properties of Liquid Crystals . . . . .	7
1.2.2	Liquid Crystal Display Materials and Fabrication . . . . .	14
1.2.3	Liquid Crystal Display Modes . . . . .	19
1.2.4	Bistable Liquid Crystal Display Modes . . . . .	21
1.3	Phenomenological Methods for Liquid Crystals . . . . .	25
<b>2</b>	<b>Landau deGennes Theory of Liquid Crystals</b>	<b>27</b>
2.1	Introduction . . . . .	27
2.1.1	The Nematic Order Parameter . . . . .	27
2.1.2	Nematic - Isotropic Phase Transition . . . . .	31
2.1.3	Curvature Elasticity . . . . .	33
2.1.4	Flexoelectricity . . . . .	35
2.1.5	Electric and Magnetic Fields . . . . .	36
2.1.6	External Anchoring . . . . .	38
2.2	The Equilibrium States . . . . .	38
2.3	Defects . . . . .	40
2.4	Dynamic Evolution . . . . .	42
2.4.1	Dynamic Equations . . . . .	45
2.4.2	Time and Length Scales . . . . .	47

<b>3</b>	<b>Lattice Boltzmann Methods Background</b>	<b>50</b>
3.1	Introduction to the LBM . . . . .	50
3.2	Background to the LBM . . . . .	59
3.2.1	Lattice Gas Automata . . . . .	59
3.2.2	Developments of LGA to LBM . . . . .	61
3.3	Practical Issues in LBM Implementation . . . . .	63
3.3.1	Stress Calculation . . . . .	63
3.3.2	Body Forcing Flows . . . . .	64
3.3.3	Lattice Gradients . . . . .	65
3.4	Example LBGK Study: Laminar flow over a backward facing step . . . . .	65
3.5	Conclusions . . . . .	71
<b>4</b>	<b>A Lattice Boltzmann Method For Nemato-dynamics</b>	<b>72</b>
4.1	Introduction . . . . .	72
4.1.1	Linearised LB Scheme for EL Dynamics . . . . .	73
4.1.2	Lattice Boltzmann Method for Beris Edwards Dynamics . . . . .	74
4.1.3	Single Lattice Boltzmann Equation for QS Dynamics . . . . .	75
4.2	A Proposed Method for LB Q-tensor Nemato-dynamics . . . . .	76
4.2.1	Reiteration of the Governing Q-Tensor Equations . . . . .	77
4.2.2	Statement of the Algorithm . . . . .	78
4.2.3	Analytical Algorithm Analysis (Chapman-Enskog Procedure) . . . . .	80
4.2.4	Lattice Units and Time Scales . . . . .	86
4.2.5	Boundaries . . . . .	88
4.3	Treatment of Externally Applied Fields . . . . .	89
4.3.1	Electric Field Solver . . . . .	90
4.3.2	Dielectric Cylinder in a Uniform Field . . . . .	91
4.4	Testing the LB LC Solver . . . . .	92
4.4.1	Equilibrium Phase Behaviour . . . . .	92
4.4.2	Shear Flow Alignment . . . . .	93
4.4.3	Miesowicz Viscosity Ratio's . . . . .	95
4.4.4	Kickback and Backflow Example . . . . .	96
4.5	Conclusions . . . . .	99

<b>5</b>	<b>Idealised Model Of A Bistable LC Device</b>	<b>106</b>
5.1	The Model . . . . .	106
5.2	Statics . . . . .	110
5.3	Dynamics . . . . .	119
5.3.1	Pre-tilts . . . . .	120
5.3.2	Switching . . . . .	122
5.4	Summary and Conclusions . . . . .	130
<b>6</b>	<b>Modelling of the Zenithal Bistable Device</b>	<b>133</b>
6.1	Overview of Current ZBD Operation . . . . .	133
6.1.1	Experimental Studies . . . . .	133
6.1.2	Theoretical and Simulation Studies . . . . .	134
6.2	The Equilibrium States . . . . .	135
6.2.1	Geometry and Parameter Set . . . . .	136
6.2.2	Calculated Profiles . . . . .	138
6.2.3	Why Flexoelectricity can cause Bistability . . . . .	143
6.2.4	Effects of Opposite Field Strength . . . . .	145
6.3	Switching Behaviour In The ZBD . . . . .	151
6.3.1	$\mathcal{D}$ to $\mathcal{C}$ State Switching . . . . .	151
6.3.2	$\mathcal{C}$ to $\mathcal{D}$ State Switching . . . . .	156
6.3.3	Comparison of Simulation to Experimental Work . . . . .	162
6.4	The Effect of Flexoelectric and Dielectric Contributions upon Switching. . . . .	163
6.5	Conclusions. . . . .	165
<b>7</b>	<b>Further Modelling of the Zenithal Bistable Device</b>	<b>167</b>
7.1	The Hydrodynamic Effects . . . . .	167
7.1.1	$\mathcal{D}$ to $\mathcal{C}$ State Switching . . . . .	168
7.1.2	$\mathcal{C}$ to $\mathcal{D}$ State Switching . . . . .	173
7.2	The Electrostatic Effects . . . . .	179
7.2.1	$\mathcal{D}$ to $\mathcal{C}$ State Switching . . . . .	181
7.2.2	$\mathcal{C}$ to $\mathcal{D}$ State Switching . . . . .	184
7.3	A First Step to Quantifying Device Operation . . . . .	189

7.4	A Temperature Variation . . . . .	194
7.5	Conclusions . . . . .	198
<b>8</b>	<b>Discussion, Conclusions and Further Work</b>	<b>199</b>
8.1	Discussion . . . . .	199
8.2	Conclusions . . . . .	202
8.3	Further Work . . . . .	203
<b>A</b>	<b>EILBGK Model</b>	<b>I</b>
<b>B</b>	<b>Ericksen-Leslie EL Theory</b>	<b>III</b>
<b>C</b>	<b>Measurement of the Flexoelectric Coefficients.</b>	<b>IV</b>

# Chapter 1

## Introduction

The topic of liquid crystals (LC's) is a multidisciplinary field. It has scope to accommodate physicists, chemists, biologists, mathematicians and engineers. This thesis will be examining LC's mainly from the view point of the physicist and mathematician but it will become evident of the wider scope which the field holds. LC's are an important class of materials, their applications ranging from display devices, optoelectronic devices, sensors, biological and structural materials. By far the most technologically important of these applications has been the display devices and it is towards this which the current study is aimed.

### 1.1 The Study

This study has been established with a three fold purpose. First to report a lattice Boltzmann (LB) simulation method for complex fluids: we will report a method by which we may adapt LB methods to simulate macroscopic continuum equation of non-Newtonian complex fluids. Secondly to use the method to predict LC dynamics of variable director, order and flow fields. In particular we focus on those situations where the use of a variable order parameter scheme is expected to be essential in order to recover the correct behaviour of a LC system. Lastly we apply these methods to situations of experimental relevance, in particularly to situations in which flexoelectric properties of LC become important such that they may control the behaviour of LC displays (LCD's) and towards the development of bistable LCD technologies.

### 1.1.1 Aims and Objectives

The main purpose of this work is to develop and build a generic method by which systems of confined LC's particularly those of LCD's may be modelled. The method is to include hydrodynamic, director and order parameter variations, allowing for arbitrary enclosed geometries and be subjected to external magnetic or electric fields. We then wish to apply our method to situations in which flexoelectric properties of LC's are of importance. The notable exclusion from our method is electrohydrodynamics: the conduction of ions and impurities within LC samples associated with a conductivity anisotropy. However we hope that with improved experimental methods in sample purity and using pseudo ac driven methods these effect are small enough to be ignored.

In solving the system of equations for LC's the LB method will be utilised. We will address within the LB method how to account for the differences in time scales of the fast hydrodynamic variations compared to the slow director evolution. The LB solutions will be verified/validated against analytical and numerical solutions to the governing equations. We will also discuss the advantages of an order variation within simulations.

We will then apply our methods to the study of the complex experimental zenithal bistable devices (ZBD); this employs situations of variable geometry and defect dynamics. We aim to track the correct creation and annihilation of defects, which we believe to be the first time, in the switching process between continuous and defect bistable states. A comparative study of the significance of order parameter variations versus director only descriptions will then follow to highlight the differences in the methods. Finally we will further examine some switching properties in the ZBD.

### 1.1.2 Organisation of Thesis

For the remainder of Chapter 1 an introduction to LC, LCD properties and a discussion of phenomenological simulation techniques is given for those not familiar with LC's. This may be safely omitted by a reader familiar with these subjects and its associated notations.

In Chapter 2 we overview the phenomenological continuum theory for the Lan-

dau deGennes order parameter. The relevant properties, free energies are described with the static and dynamic equations that govern the behaviour.

In Chapter 3 the LB method for isotropic fluids is discussed and the algorithm is described. A short LB investigation into isotropic laminar flow over a backward facing step is reported comparing pressure driven and body forced methods. Results are compared to experimental and numerical work [1] in the same geometry and agreement is obtained to a satisfactory level of accuracy.

In Chapter 4 the LB methods for  $Q$ -tensor nemato-dynamics are discussed. We provide a statement of the algorithm used in the work and a Chapman-Enskog analysis to justify its form. We report a method for treating the electric field within the LB solver. The full solver is tested against simple analytical solutions of the governing equations: phase behaviour, shear flow, Miesowicz viscosities and a kickback cell.

In Chapter 5 the solver is applied to an idealised bistable device model [2]. We recover previous numerical results for this model from a constant order parameter method. The additional information the  $Q$ -tensor method can yield and to what extent a more detailed description than [2] of this device can give is studied.

In Chapter 6 the statics and dynamics of the ZBD are studied. We simplify the theory to show the source of the bistable behaviour. Switching between states is shown and the dielectric anisotropy versus flexoelectric contributions to the switching studied.

In Chapter 7 a more complete description of the ZBD is given examining the influence of hydrodynamics and electrostatics, the temperature range of the device and we study some device properties upon the relaxation dynamics.

In Chapter 8 a summary of the main results of this thesis and the conclusions are given. Directions are suggested for future work. A bibliography is included.

## 1.2 Liquid Crystal Primer

In general, most substances have a single melting point where a solid possessing a positional and orientational order changes upon melting to an isotropic liquid that has neither positional nor orientational order. However some materials when melted from the solid state change into a cloudy liquid [3] with only orientational order at one temperature and upon further heating to an isotropic liquid that has no order. For this reason LC's have been dubbed mesomorphic (meaning intermediate) phases that exist above the melting temperature  $T_m$  of the crystalline phase and below the clearing point  $T_{IN}$  of the liquid (isotropic) phase, see figure 1.1. This type of LC in which the mesophase is defined by the temperature between  $T_m$  and  $T_{IN}$  is called a thermotropic LC. If the mesophase is defined by a solvent concentration it is called a lyotropic LC. As thermotropic LC are predominantly used for display applications we only consider their behaviour for this thesis (lyotropic systems can give rise to different physics from their larger molecular dimensions and properties).

Most LC materials are organic compounds that consist of rod-like or disc-like shaped molecules. For display applications LC materials with rod-like shaped molecules are the most commonly used. The LC mesophase may be broadly classi-

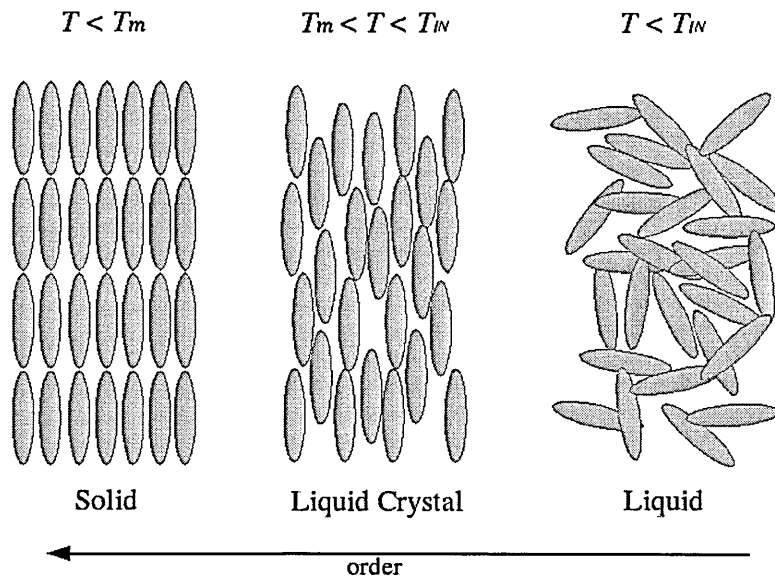


Figure 1.1: Sketch of solid, LC and liquid phases. The solid phase has positional and orientational ordering of molecules. The LC phase has orientational order, no positional order. The liquid phase has no positional or orientational order, it is isotropic.

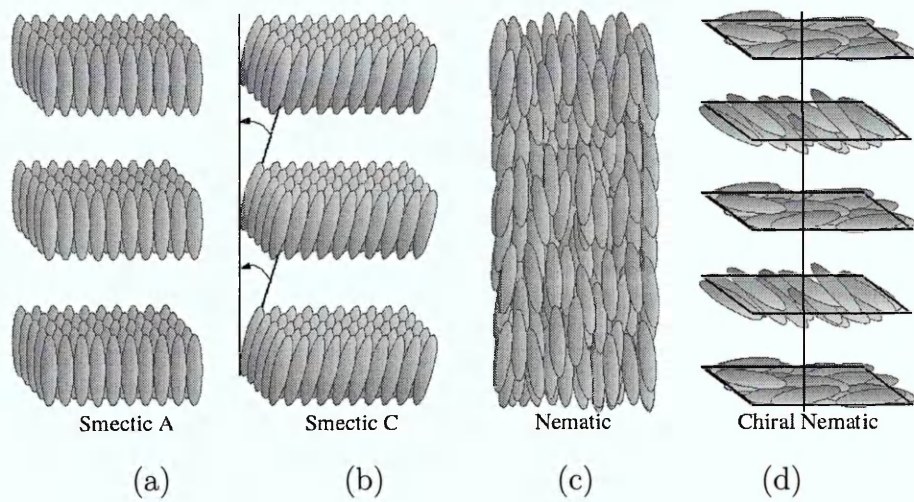


Figure 1.2: Sketch of LC molecular orientations in the LC phases (a) smectic A, (b) smectic C, (c) nematic and (d) chiral nematic (cholesteric).

fied into three further types (phase) namely the smectic, nematic and chiral nematic (cholesteric) according to their molecular order, see figure 1.2. The smectic phases generally have the rod shaped molecules arranged in layers with the molecules approximately parallel to each other (2-dimensional ordering). There are many different smectic phases with smectic A (molecular long axis approximately perpendicular to the layers) and smectic C (molecular long axis tilted from the perpendicular of the layers) being the most common. In the nematic phase the rod shaped molecules long axis are approximately parallel to each other but the individual molecules move relatively easily in the direction of their long axis without a layered structure. In the chiral nematic phase in addition to the nematic phase properties there exists a spatial variation of the long axis of the molecules that leads to a helical structure: consider a series of planes through the material perpendicular to the helical axis, each contains the order of the nematic phase but the local long axis alignment in changing planes is slightly rotated. The same substance may exhibit more than one LC mesophase as the temperature is varied in the  $T_m < T < T_{IN}$  region, for example, with increasing temperature a substance may change from a smectic to a nematic phase, then finally an isotropic liquid above  $T_{IN}$ . The nematic and chiral nematic phases are the most widely used for display applications.

An example of a nematic LC material is 4'-n-pentyl-4-cyanobiphenyl (5CB) [4] with a nematic phase in the range  $24^{\circ}C$  to  $35^{\circ}C$  [5]. In 5CB, see figure 1.3, the

biphenyl rings are nearly coplanar and form approximately a rigid rod about  $20\text{\AA}$  long by  $5\text{\AA}$  wide. The terminal groups (cyano and pentyl) and conjugated bonds in the molecular core are largely responsible for many anisotropic properties of these materials. Many thousands of LC materials have been discovered and engineered each with their own specific parameters. The LC materials used in current LCD's are typically highly developed mixtures of various compounds that are tailored to meet environmental stability of wide operating temperatures, fast response to external field influences and high electrical resistivity for addressing purposes.

The rod-like molecules in a nematic LC are characterised well by an ellipsoid, see figure 1.3, although they may not necessarily be cylindrically symmetric due to their shape or charge distribution. With such shape symmetry the nematic is termed uniaxial and may be characterised microscopically by a unit orientational vector  $\hat{u}$  along the molecular long axis. The states  $\hat{u}$  and  $-\hat{u}$  are physically indistinguishable indicating 'head-tail' symmetry of the molecule. Averaging  $\hat{u}$  over a collection of molecules gives the average orientation of a set of molecules called the director  $\hat{n} \equiv \langle \hat{u} \rangle$  in which  $\langle \rangle$  denotes the average over an ensemble of molecules. The

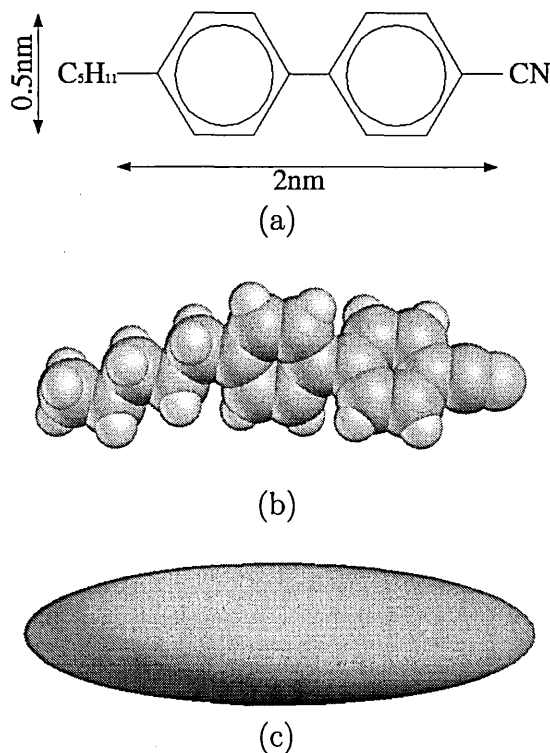


Figure 1.3: Sketch of a common LC called 5CB. (a) chemical composition, (b) atomistic arrangement [6] page 6 figure 1.1, (c) common molecular dynamics simulated LC ellipsoid.

director is a course grained macroscopic observable, it is physically measurable.  $\hat{n}$  is also a unit vector  $\hat{n} \cdot \hat{n} = 1$  with ‘head-tail’ equivalence  $\langle \hat{u} \cdot \hat{n} \rangle = 0$ , however  $\langle (\hat{u} \cdot \hat{n})^2 \rangle \neq 0$  and thus may be used as a measure of ordering i.e. how well aligned the molecules are to  $\hat{n}$ . The degree of order is given by the even set of Legendre polynomials, of which the second is termed the uniaxial scalar order parameter,  $S = \frac{1}{2} \langle 3 \cos^2 \theta - 1 \rangle$  in which  $\theta$  is the angular difference from the director. Typically  $0 < S < 1$  characterises the nematic phase: for perfect alignment of molecules  $S = 1$ , for a random configuration of molecules (isotropic)  $S = 0$ . It should be noted  $S = -\frac{1}{2}$  is a possibility but is physically hard to imagine given that all molecular orientations must be perpendicular to  $\hat{n}$ . In thermotropic LC’s  $S = S(T)$  where  $T$  stands for the temperature of the system. The transition from the nematic to isotropic phase at  $T_{IN}$  is indicated within  $S$  as it changes discontinuously to zero indicating a first order phase transition.

In a well defined LC sample in which the characteristic variation  $l < 1\mu m$  of  $\hat{n}$  is much larger than the molecular dimensions  $a \sim 10\text{\AA}$  we have  $\frac{a}{l} \ll 1$  and  $S \sim S_0$  is constant. A director description of the sample thus surfaces. However situations occur such as the influence of external parameters upon the sample in which  $\hat{n}$  may change abruptly but over this range  $S(\underline{x})$  changes continuously; it has a mesoscopic length scale (one can expect  $S$  to lower according to its definition if molecular alignments vary). Samples of this kind would be better characterised by both  $\hat{n}$  and  $S$ . One such continuous parameter that combines both of these is an alignment tensor  $Q_{\alpha\beta} = Q_{\alpha\beta}(\hat{n}; S)$  with the properties  $Q_{\alpha\alpha} = 0$  and  $\varepsilon_{\gamma\alpha\beta} Q_{\alpha\beta} = 0$ . Here and throughout this thesis Einstein summation convention is implied over repeated Greek indicies and  $\varepsilon_{\alpha\beta\gamma}$  is the Levi-Civita symbol ( $\varepsilon_{123}$  permutations = 1,  $\varepsilon_{321}$  permutations = -1, and 0 for all other cases). The elements of  $Q_{\alpha\beta}$  are real and related to  $\hat{n}$  and  $S$  through its eigenvectors and eigenvalues.

### 1.2.1 Physical Properties of Liquid Crystals

The ordered structure of LC molecules give rise to anisotropic properties. That is, various physical properties such as dielectric constant  $\epsilon$ , refractive index  $n$ , magnetic susceptibility  $\chi$ , conductivity  $\sigma$ , viscosity  $\eta$ , have different values in the directions parallel ( $\parallel$ ) and perpendicular ( $\perp$ ) to the molecular long axis. These anisotropic

physical properties in conjunction with the ease of controlling the initial orientations (boundary conditions) through surface alignments and the ease of re-orientating the molecular axis through applying voltages is the basis for the application of LC's in displays [5].

### Dielectric Anisotropy

Dielectric anisotropy in LC molecules occurs due to their permanent and induced dipoles. The magnitude of the permanent LC molecular dipoles is small and such that with no external applied field there is no net polarisation, see figure 1.4a and figure 1.4b. With the application of an external electric field,  $\underline{E}$ , the molecules re-orientate themselves with respect to the field. The induced dipoles occur when the external field produces a force upon the atomic charges displacing like charges to opposing ends of the molecule creating a dipole which then re-orientates the entire molecule with respect to the field, see figure 1.4c and figure 1.4d.

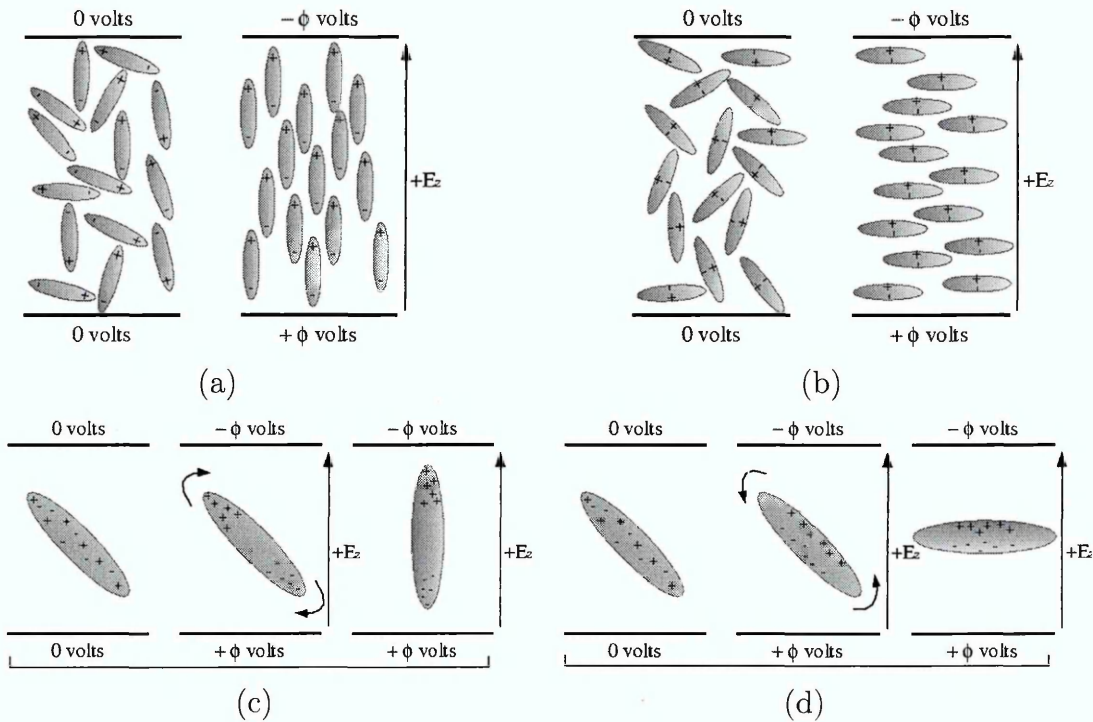


Figure 1.4: For no external electric field molecules are arranged so that no net polarisation is present. For permanent dipoles upon application of an electric field the molecules re-orientate with respect to the field dependent upon (a)  $\Delta\epsilon_a > 0$ , (b)  $\Delta\epsilon_a < 0$ . For induced dipoles the charges separate along (c) the long axis of the molecule ( $\Delta\epsilon_a > 0$ ) or (d) the short axis of the molecule ( $\Delta\epsilon_a < 0$ ).

The dielectric anisotropy is expressed as  $\Delta\epsilon_a = \epsilon_{\parallel} - \epsilon_{\perp}$  where  $\epsilon_{\parallel}$  and  $\epsilon_{\perp}$  are the dielectric constants measured parallel and perpendicular to the LC director. LC materials that exhibit positive  $\Delta\epsilon_a$  (p-type) tend to align themselves, for large fields, with their molecular long axis parallel to the applied electric field. LC materials that exhibit negative  $\Delta\epsilon_a$  (n-type) tend to align themselves, for large enough fields, with their molecular long axis perpendicular to the electric field. Both positive and negative applied fields induce the same molecular re-orientations. The magnetic susceptibility of a LC behaves in an analogous way to the dielectric effect, with the magnetic anisotropy defined  $\Delta\chi_a = \chi_{\parallel} - \chi_{\perp}$ . Both electric and magnetic fields have the effect of stabilising an orientation leading to an increase in the level of ordering among molecules,  $S$  (all be it small). Generally the dielectric constant  $\epsilon_{\parallel}$  decreases with increasing frequency [7] due to the relaxation phenomenon, oppositely  $\epsilon_{\perp}$  varies little over a large frequency range. At a cross over frequency  $f_c$ , typically in the range  $100kHz$  to  $1MHz$ , where  $\epsilon_{\parallel} = \epsilon_{\perp}$  the LC becomes dielectrically isotropic. The dielectric constants also change as a function of temperature and thus  $S$  ( $S = S(T)$ ) becoming equal  $\epsilon_{\parallel} = \epsilon_{\perp} = \epsilon_{iso}$  as the temperature approaches  $T_{IN}$ .

### Refractive Index Anisotropy

Materials displaying birefringence, such as LC's, have anisotropic refractive indices. They have two principle refractive indices  $n_o$  and  $n_e$ , see figure 1.5. For the ordinary refractive index  $n_o$ , the electric field vector of the light beam oscillates perpendicular to the optic axis and for the extraordinary refractive index  $n_e$ , the

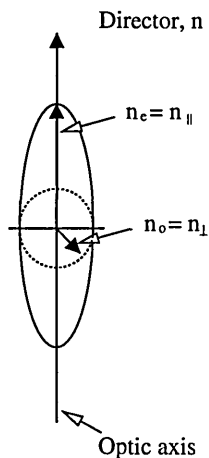


Figure 1.5: Sketch of the anisotropy in the refractive indices for a uniaxial LC.

electric field vector oscillates parallel to the optic axis. In uniaxial nematic LC's the optic axis is given by the director, so  $n_o = n_{\perp}$  and  $n_e = n_{\parallel}$  with the optical anisotropy (birefringence)  $\Delta n_a = n_{\parallel} - n_{\perp} = n_e - n_o$ . Like the dielectric constants the refractive indices vary with  $S(T)$ . Additionally the refractive indices are wavelength  $\lambda$  dependent.

### Elastic Anisotropy

The orientation of an ensemble of LC molecules is given by its director,  $\hat{n}(\underline{x})$ . In a larger pure sample the preferred equilibrium orientation of the director is to seek a constant - undistorted alignment (see figure 1.2c). The director orientation may be imposed by boundary conditions, if the LC sample is then perturbed from equilibrium by application or removal of an electric field, a distortion from equilibrium occurs. The transition of the director from one direction to the other induces curvature strain in the medium of which there are three principle types; Splay ( $K_{11}$ ), Twist ( $K_{22}$ ) and Bend( $K_{33}$ ), see figure 1.6, which all vary in strength. The  $K_{ii}$  are elastic constants proportional to the curvature strain experienced in the sample. A sample experiencing curvature strain has variation in molecular alignment and thus

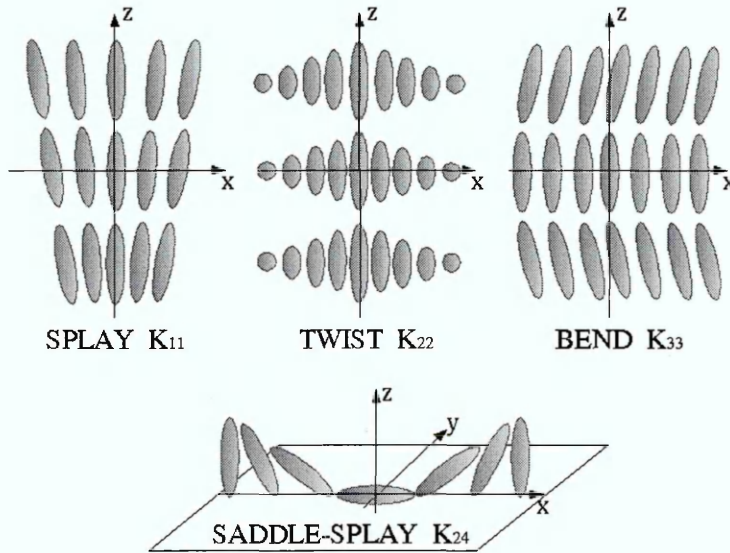


Figure 1.6: Sketch of the different characteristic deformations from equilibrium in the molecular arrangement. Splay, twist and bend characteristic of bulk deformations. The less well known saddle-splay occurring at the surface for complex structures.

a destabilising effect upon the local order parameter. As with most LC parameters the  $K_{ii}$  depend upon temperature,  $S(T)$ , becoming  $\sim$  zero below  $T_{IN}$ .

### Flexoelectric Effect

There are two ways flexoelectricity affects LC's, both weakly affect the molecular orientations through polar induced distortions. Firstly [8] molecules that have an asymmetry in their shape may contain small permanent electric dipoles. The prime examples being 'banana' or 'pear' shaped molecules. For undeformed LC samples the molecular configurations show no net polar symmetry, the molecular dipoles cancel giving a zero bulk dipole, see figure 1.7a or figure 1.7c. If the sample is now distorted in shape or through the application of an external field the molecules re-orientate in order to better fill the shape volume or to align their dipoles to the electric field, see figure 1.7b or figure 1.7d. In doing so it creates a) a distortion splay or bend and b) a net polarisation and hence electric field. The effect of flexoelectricity upon the order parameter is not obvious as it has a distortion property (lowering  $S$ ) together with a polarisation (increasing  $S$ ) property. The splay and bend distortions are represented by flexoelectric coefficients  $e_{11}$  and  $e_{33}$  respectively that are functions of  $S(T)$ . It is important to note that applying a positive or negative electric field will cause different and opposite distortions, unlike the dielectric effect, as discussed earlier.

The second way is for molecules that are symmetric to have quadrupolar symmetry [9]. Again an undeformed sample has no net polarisation but upon distortion

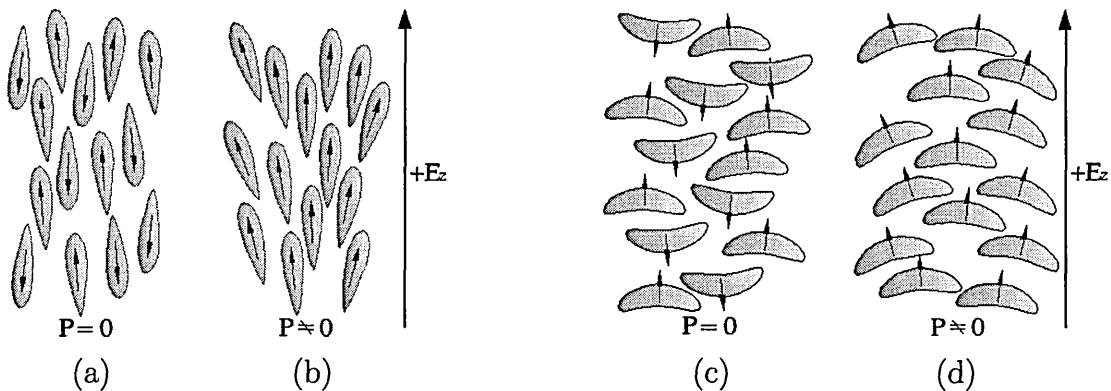


Figure 1.7: Sketch of the dipolar flexoelectric LC effect for molecules in their undistorted (a),(c) and distorted states (b),(d).

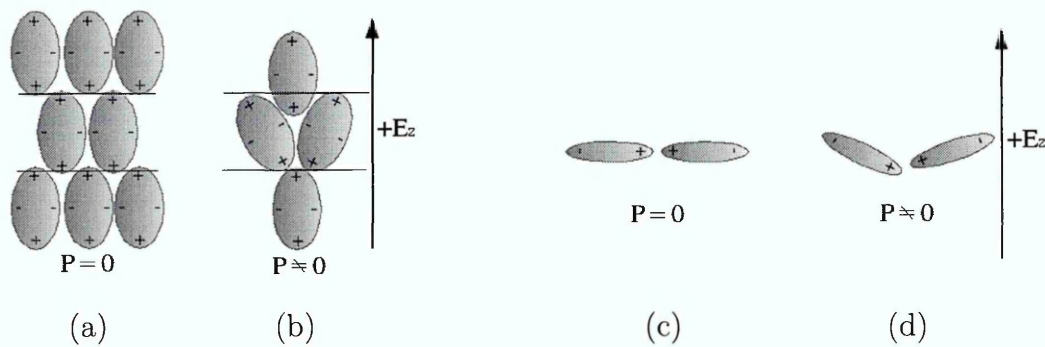


Figure 1.8: Sketch of the quadrupolar flexoelectric LC effect for molecules in their undistorted (a),(c) and distorted states (b),(d).

or application of an electric field the quadrupolar charge orientates the molecules so as to induce a distortion and a net polarisation which is sign dependent, see figure 1.8a and 1.8b. Alternatively [10] symmetric molecules could pair off ‘dimerise’ through quadrupolar interactions see figure 1.8c and 1.8d. Again upon distortion or applied electric field a sign dependent distortion is created with a net polarisation. Quadrupolar effects are typically described by a single temperature dependent flexoelectric coefficient  $e$ .

### Flow Anisotropy

The viscosity of a fluid is a measure of its resistance to flow. The viscosity of a LC sample varies dependent upon the molecular orientations within the sample. This can be seen in a LC material in between two parallel plates and measuring the force necessary to move one plate past the other at a certain velocity, see figure 1.9. The force necessary to move the plate at a certain velocity  $u_x$ , is different for the three fixed molecular alignments. For laminar flows the viscosity is proportional to the force applied and from figure 1.9  $F_x(b) < F_x(a) < F_x(c)$  and we have viscosities  $\eta(c) > \eta(a) > \eta(b)$ . There exist five independent viscosity coefficients in the uniaxial nematic phase that are strongly temperature dependent,  $S(T)$ , in comparison to the singular isotropic weakly temperature dependent viscosity above  $T_{IN}$ .

The magnitude of the viscosities in a nematic LC are all the same order of magnitude as that of water which has a singular isotropic viscosity. LC materials can therefore flow readily and in doing so the different velocity profiles create forces upon the LC molecules tending to re-orientate them, analogous in essence to the concept

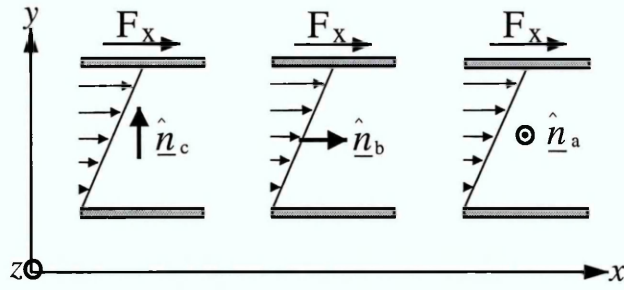


Figure 1.9: Sketch of the three arrangements for the measurement of the Miesowicz viscosities. The force,  $F_x$ , required to move the top plate at a constant velocity,  $u_x$ , is different for each director alignment hence a different viscosity is observed for each case.

of logs flowing in a river. This effect of flow effecting molecular reorientations is usually coined backflow. Oppositely should the LC molecules rotate due for example to an external electric field or imposed boundary conditions, they create flows. This leads to a highly complex coupled relationships between the flow fields, molecular orientations and ordering in a system undergoing change. In dynamically changing LC samples flow increases distortions and one can expect a lowering in order, however for a constant  $\hat{n}(x)$  flow aligned sample in a laminar regime we can expect a stabilising effect upon the order (all be it small).

### Electro-Optic Characteristics

When a constant electric field is applied to a LC with an initial director orientation (boundary condition achieved via surface alignment techniques) it will change to a new director orientation due to the dielectric anisotropy,  $\Delta\epsilon_a$ . This change in director is accompanied by a change in optical transmission and reflection characteristics due to the birefringence  $\Delta n_a$ . This phenomena forms the basis for LCD's and is known as the electro-optic effect. The application of the field produces an electrical free energy, the resultant distortion produces an elastic free energy and flexoelectric free energy. The final equilibrium director configuration in the LC sample is given by a competition of all these individual terms and represents a minimum of the total free energy,  $\mathcal{F}$  of the LC, given by the sum of the electric, flexoelectric and elastic contributions.

The transition from an undeformed state to a distorted state is known as the Fredericksz transition and it occurs at a critical electric field value,  $E_C$ . Below  $E_C$

no distortions occur but above  $E_C$  deformation increases with increasing  $E$ . The value of  $E_C$  depends on the LC material parameters  $K_{ii}$ ,  $\Delta\epsilon_a$  and  $d$  (the sample thickness).

### 1.2.2 Liquid Crystal Display Materials and Fabrication

The important orientational behaviour of LC's makes them useful for display devices. They also contain further attributes including low drive voltages, low power consumption, thin form factor (flat panel displays), light weight, full colour, grayscale with wide dynamic (even in sunlight) range, full motion video, superior image quality and high reliability (life span). These reasons make LC's the preferred approach for battery-powered portable applications ranging from the wrist watch to traditional televisions to laptop computer displays to large screen projections, they have even started to replace cathode ray tubes (CRT).

LCD's are by no means the conclusive display, they are just one technology in the quest to find the holy grail in displays - electronic paper. It was said about electronic paper [11]:

*'Ink on paper is simply the pinnacle of the display industry. Ink on paper is a bistable, bright, high contrast, inexpensive material that consumes no power in retaining an image and can easily be viewed from many different angles even in sunlight.'*

For the purposes of this work we do not consider other technologies competing for the multi-million pound display market but would refer interested parties to electronic ink references [12]. LCD technology is still in the early development stages to achieve electronic paper. At the time of writing the current developments are to improve viewing angles, improve image quality, lower power consumption and larger displays. We outline below some of the typical techniques in the manufacture of LCD's [5, 13].

In figure 1.10 is shown a schematic of a general passive matrix addressed LCD. In figure 1.11 the general construction process is indicated in a flow chart.

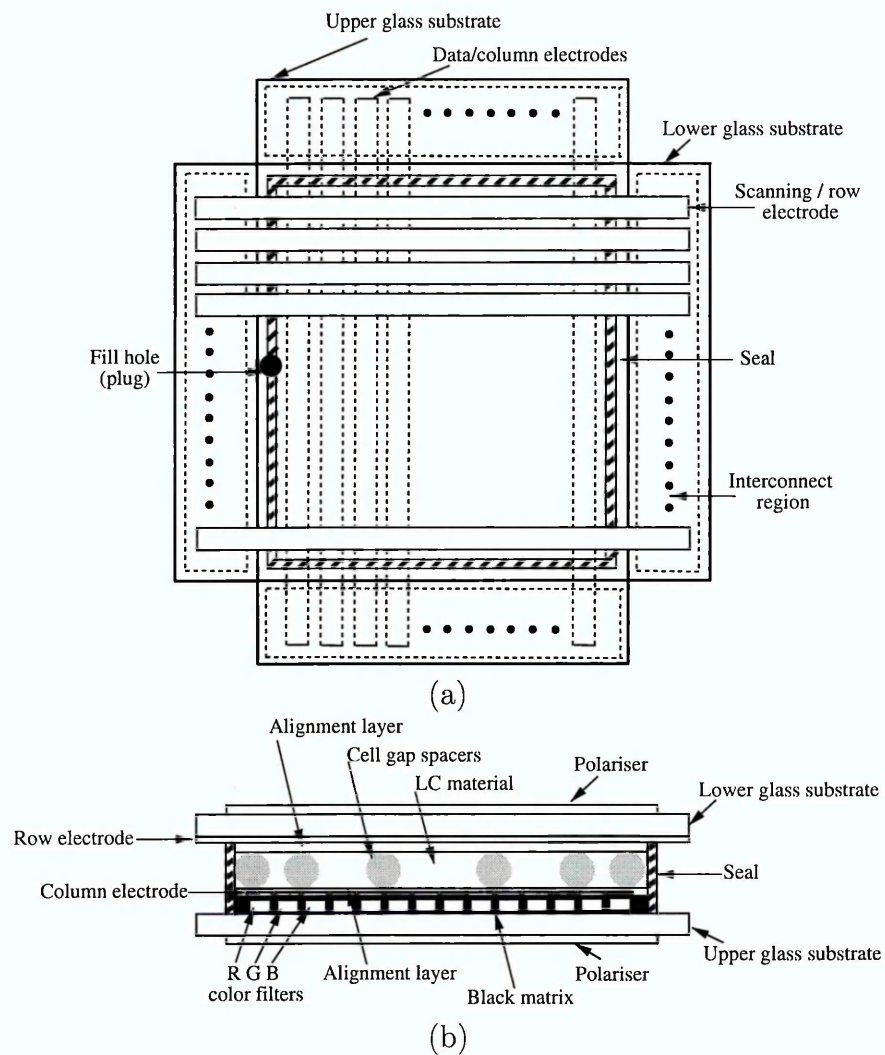


Figure 1.10: Sketch of the typical passive matrix addressed colour LCD adapted from [14]. (a) Plan view and (b) cross-section view.

## Glass Substrate

Glass quality must be chemically compatible with the LC materials, flat defect free, and have dimensional stability under the processing temperatures it will be submitted too. Typically LCD display gaps are of 1 to 10  $\mu\text{m}$  highlight the need for flatness, whereas surface defects and scratches will lead to poor electrode operation and poor uniform cell spacing. Polished glasses such as borosilicate and aluminosilicate are typically used of thickness 0.7 to 1.1 mm.

## Colour Filters

Colours are generated through red, green, blue (RGB) filters at each pixel compatible with the white back light system. Colour filter thickness is usually 2  $\mu\text{m}$

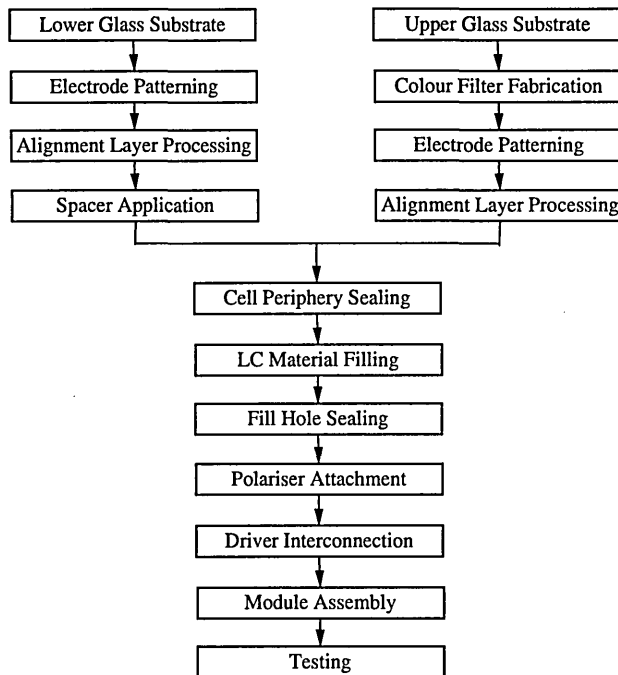


Figure 1.11: A flow chart for the manufacturing and assembly processes involved in a typical LCD.

made from dyes or photo resists that are applied using photo lithography. A Black matrix material is applied between colour filters to block inter pixel light transmission. This can be optically finished with a smooth barrier layer of  $\text{SiO}_2$  to attach electrodes.

### Transparent Electrodes

Typically indium tin oxide (ITO) of 90%  $\text{In}_2\text{O}_3$  and 10%  $\text{SnO}_2$  is used due to its good transmission levels. 50 to 300 nm thick layers are deposited via evaporation or sputtering techniques with a typical resistivity of the order  $10^{-4} \Omega \text{ cm}^{-1}$ .

### Alignment Techniques

Surface alignment is crucial to the LCD operation. It aligns the LC molecules to specific orientations with a specific strength to remain in that orientation. There are four main types of alignment. Planar arrangement orientates the LC direction anywhere within the plane of the surface. Homogeneous alignment is in the plane of the surface but with a preferred direction. Homeotropic alignment is perpendicular to the surface and conical alignment describes a director with a fixed polar angle from the surface but a free azimuthal angle. Further it is sometimes useful to

add pre-tilts to device surfaces, these being typically a finite angle from one of the above types of anchorings. Inorganic films such as obliquely evaporated SiO or organic materials such as rubbed polyimide are commonly used to impose the required alignments.

### **Cell Spacing and Sealing**

After alignment the cell assembly starts. The cell thickness is controlled by spacers, typically plastic fibres or spheres of set size, that are positioned both in active areas and peripherals. A compatible epoxy type adhesive then seals the cell with a small fill opening left to inject the LC material. The upper and lower surfaces are then aligned before curing via heating or UV exposure methods. Seals are typically 1 to 3 mm wide and 2 to 3 mm from the active area of the display. Sealant must prevent moisture and contaminants getting into the cell.

### **LC Material Filling**

Small LC cells are usually filled by evacuating the cell in a vacuum chamber, submersing the cell below the fill hole level into the LC material then increasing the chamber pressure. Raising the pressure causes the cell to fill via capillary action. When full the fill hole is sealed with compatible epoxy adhesive.

### **External Components**

These include polarisers, reflectors, display drivers and backlights. A reflector is applied to the back of a display to reflect the ambient light and does not require back lighting though it can be done so. More commonly the transmissive mode is used with back light. Polarisers are attached to the front and back of the cell with the axis polarisation set dependent on display type operation. Polarisers are typically a three layer composite with polarising polyvinyl alcohol (PVA) then two outer triacetyl cellulose (TAC) films for protection from environmental damage. Polarisers can be 99.9% efficient but only 45% transmissive.

Display row and column integrated circuit (IC) drivers are then attached to the row and column pads of the display via tape-automated bonding (TAB) or chip on glass (COG) approaches. A fluorescent lamp and diffuser generates a uniform back light that can also be used to control image brightness.

## Display Addressing

There are essentially three types of display addressing techniques allowing for the different demands of display types: direct (static) addressing, passive matrix (PM) addressing and active matrix (AM) addressing. For low information content displays segmented electrodes are used with simple direct addressing (voltage drive signals are given for each segment/pixel), for example the numeric seven segment display in a calculator. This method becomes impractical for high information content displays due to the vast number of interconnections required; we now turn to matrix addressing.

PM addressing has a matrix of transparent conducting row and column electrodes as in figure 1.10. They are the simplest and least expensive addressing systems for LCD manufacturers. For example a colour VGA graphics array of pixels  $640 (\times 3 = 1920)$ H by 480 V has 1920 columns and 480 rows with 2400 interconnections used to address a 921600 pixelled display.

In PM addressing a voltage,  $+V_r$ , is applied to each row sequentially, the columns of a given row are then driven in parallel during that row time with a voltage,  $\pm V_c$ , a pixel is either on or off depending upon the sum of the voltages  $V_r \pm V_c$ . During the frame time  $t_f$ , for an  $N$  row display the pixels in any one row will receive its full voltage on for  $t_r = t_f/N$  of the time. Whilst the other rows are addressed there will be a smaller voltage which, from figure 1.13c, will lead to less contrast hence why devices with steeper electro-optic curves were developed (see § 1.2.3). Operation can be enhanced (speed and content) by splitting the display in half where the rows in each half are scanned simultaneously and synchronously.

AM addressing removes multiplexing (number addressable rows) limitations of PM methods by including a non-linear control element into each pixel using a stored charge. The AM address is depicted in figure 1.12, it shows the three main components required at a pixel: thin film transistor (TFT), pixel electrode ( $C_{LC}$ ) and storage capacitor ( $C_s$ : introduced to correct for offsets such as a temperature changes). The manufacturing process is complicated and usually done using more expensive photo lithographic methods. As with the PM addressing and most matrix addressing displays, with line at a time addressing, the rows (gate of the TFT) are scanned sequentially with a select gate pulse  $V_{g,sel}$  during the frame time  $t_f$ , while all

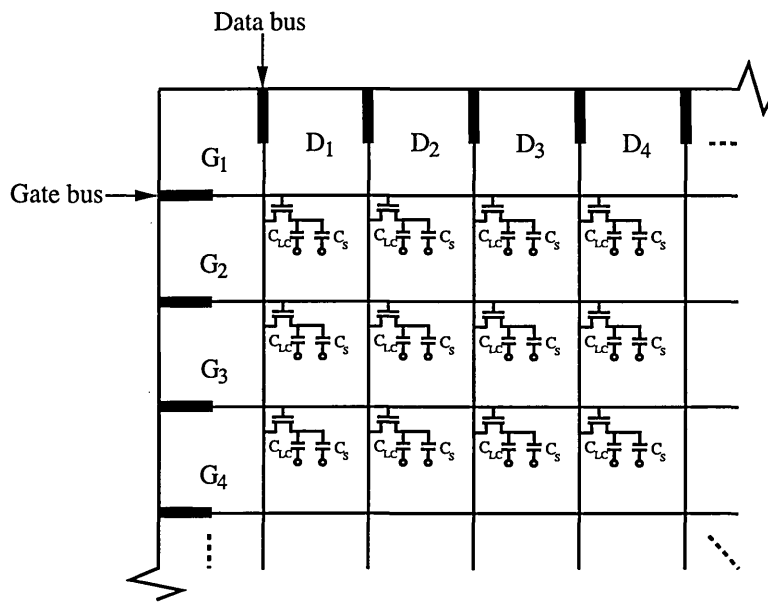


Figure 1.12: Sketch of an active matrix controlled LCD substrate surface. Each pixel contains a TFT and pixel electrode and storage capacitor.

the pixels in a row are addressed simultaneously with a data voltage  $\pm V_d$  during the row time,  $t_r (= t_f/N)$ . During the row time the select gate voltage switches the TFT on to charge the pixel capacitor and storage capacitor to the data voltage. After the row time the TFT is switched off via a non select  $V_{g,non-sel}$  which isolates the charge from the matrix and maintains the pixel voltage for time  $t_f$ . This isolation vastly improves contrast and switching time making it the addressing choice for high speed video applications. It should be noted the pixels should be driven in an ac fashion with  $+V_d$  and  $-V_d$  on alternate frames. This avoids net dc build up of ions in the LC due to anisotropy in the conductivity  $\Delta\sigma_a$  which causes pixel flicker and image sticking effects.

### 1.2.3 Liquid Crystal Display Modes

Schadt and Helfrich [15] then of Sharp Laboratories were the first to construct LC's for displays but the principles by which LCD's can operate vary. Many different operational types of display exist. We highlight here just some of the common operating modes that exist [16].

## Twisted Nematic (TN) Mode

The TN [15] arrangement is shown in figure 1.13a. A nematic LC with  $\Delta\epsilon_a > 0$  lies in a cell with directors homogeneously aligned  $90^\circ$  from each other on opposing surfaces with a small,  $3^\circ$  pre-tilt that will avoid reverse tilt disclinations. The rest state of a normally white mode display has uniform director twist throughout the cell with crossed polarisers attached with their polarisation axis parallel to the director on that substrate. For a pitch of the LC greater than the optical wavelength the linearly polarised incident light rotates  $90^\circ$  with the LC optic axis and exits the second polariser appearing bright. Applying a voltage aligns molecules as figure 1.13b and the optical rotation is lost and the cell appears dark due to the polarisers. Typical operating voltages are 2 to 5 Volts with a response time of 10 ms, the typical response being shown approximately in figure 1.13c from which, by varying the voltage we may achieve gray scale control. TN devices are best addressed on an active matrix system due to the shallow electro optic response limiting multiplexibility.

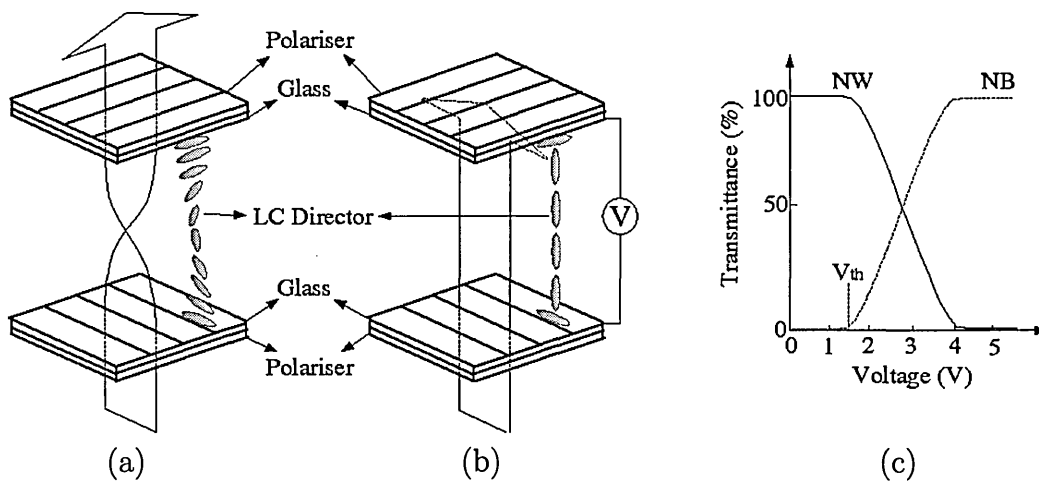


Figure 1.13: Sketch of a normally white TN device in the (a) 'off-state': incoming light is linearly polarised which then follows the optic axis ( $\hat{n}$ ) allowing it to escape the second polariser appearing white. (b) 'on-state': the incoming light is linearly polarised but for this alignment there is no anisotropy, polarisation remains linear and light is extinguished by the second polariser. (c) a typical optical response curve of transmission versus applied voltage.

## Super TN (STN) Mode

STN [17] were developed to achieve a steep electro-optic curve (steeper than figure 1.13c), that will allow for high multiplexability. The STN uses the same setup as the TN with large pre-tilt angles and a larger twist angle  $180^\circ$  to  $270^\circ$  between upper and lower surfaces (achieved via chiral additants to the LC mixture). Typical STN response times are of the order of 150 ms with a lower contrast ratio and narrower viewing angle than the TN.

## Electrically Controlled Birefringence (ECB) Modes

These display modes [18] work by controlling the cell birefringence via electric fields. There are many arrangements. The DAP is a homeotropically aligned sample throughout the cell and has  $\Delta\epsilon_a < 0$  between crossed polarisers. For no field there is no birefringence for incident light. For an increasing field there is increasing birefringence creating elliptically polarised light that makes the cell appear bright. Oppositely a homogeneously aligned cell may be used of  $\Delta\epsilon_a > 0$ . The HAN (hybrid aligned nematic) is another variation in which one surface is homeotropic and the other homogeneous. Here both positive and negative  $\Delta\epsilon_a$  materials can be used and since there is no clear Fredericksz threshold voltage it has a low drive voltage. Another arrangement is called in-plane switching (IPS) that has homogeneous alignment and interdigitated electrodes on one surface and  $\Delta\epsilon_a > 0$ . Upon application of the field the directors rotate in-plane by  $90^\circ$  to align between the electrodes.

### 1.2.4 Bistable Liquid Crystal Display Modes

In the development of LCD's towards the idealist electronic paper, one of the characteristic requirements is bistability. This is the property that under the influence of no externally applied fields the LC has two equally stable configurations. If in addition the two stable states are optically distinct in a reflective display cell this would lead to a static image being displayed for zero power expenditure. Power is then only needed if the image were to be changed (updated), this is in contrast to the modes of §1.2.3 where a constant applied field is needed to retain an image. This ability has potentially a dramatic influence upon the display market, particularly

for portable devices. With power consumption reduction the operational life time of batteries is increased and smaller batteries may be used. The added complication to these displays is that switching is preferred to occur electrically with dc-fields applied between upper and lower substrates.

As bistable displays have pixels that are bistable they retain their states indefinitely and there is less ‘cross-talk’ between pixels (less image flicker) which have threshold voltages between the two states thus the cheaper passive matrix driving technologies may be used with unlimited multiplexing capabilities.

Over the years there has been increased research towards achieving bistable LCD’s aimed to reduce operating voltages and widen applications, the following will describe such technologies. Cholesteric LCD’s [19] with one state having planar twisted reflective state (bright) the other having a focal conic texture absorbing (dark) state, the switching between states is done by switching the electric field off quickly or slowly. Bistable twisted nematic (BTN) [20] have one state with a 360° twist the other homogeneous, the switching between states achieved by different threshold voltages. Bend-Splay nematics [21, 22] that have high surface pre-tilt angles allowing for a bend state and a splay state, the switching being achieved by interdigitated electrodes on one or both surfaces. The post aligned bistable nematic (PABN) [23] uses a three dimensional array of micron high planar aligned posts on one surface and the other surface homeotropically flat, two hybrid states are found in which defects position around the posts and are shifted for each state, switching is achieved by the polarity of the applied voltage. The Bistable electrophoretic nematic (BEN) display has been developed by the Defence Evaluation and Research Agency and involves both surfaces having rounded wells and reflective particles that sit in each well, applying an electric field can pull the particle from one surface to the other with both being positions being stable.

Another bistable candidate is the surface nano-rubbing device [24] in which one surface is rubbed by atomic force microscopy into small checker board segments of opposite alignments the other surface being homeotropic, switching has yet to be achieved by vertical dc fields. Similarly to the nano-rubbed bistable device methods research into chemically nano-patterened surfaces [25, 26] is being studied. We give more detail below of some the more developed and commercially promising bistable

modes that are being developed.

### Ferroelectric SmC\* LCD

Ferroelectric LCD's [27] are of the smectic C\* phase possessing a chirality perpendicular to the layers. Molecules possess permanent polarisations proportional to the amount of tilt and for large enough samples no net polarisation (due to chirality). Placing in a LC cell with planar alignment conditions, the smectic layers form perpendicular to the surface in a 'bookshelf' geometry, see figure 1.14, so that the optic axis is parallel to the surface. For a small enough cell ( $\lesssim 1\mu m$ ) there is no chirality and a net polarisation occurs perpendicular to the surfaces. Coupling the polarisation to an electric field allows the LC to be switched between optically distinct locally stable states. These LCD's give very fast switching times due to the coupling to a polarisation and good viewing angle due to small cell size however they have a lack of achievable gray levels and are very susceptible to shock; slight external pressures destroys the smectic layering and the image is lost.

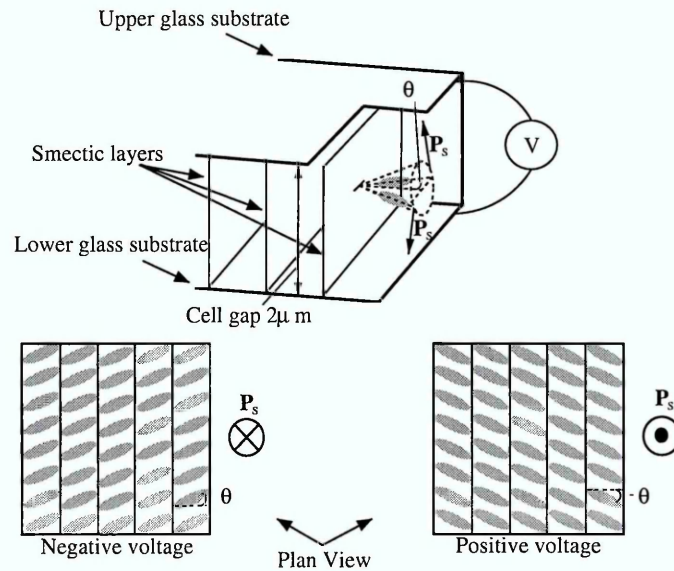


Figure 1.14: Sketch of the ferroelectric smectic C\* display. The upper picture shows the 'bookshelf' geometry within a small micron sized cell. The lower plan view picture shows how the polarisation couples to the direction of the applied field causing the selection of the two states.

## Surface Controlled Bistable Nematic

Early variants of this device were investigated by Berreman [28], the more recent and advanced variants by Dozov et al [29]. This device has a simple construction with a chirally doped nematic of pitch  $P_{ch} = 4d$  ( $\pi/2$  twist within  $d$ ) placed in a cell with homogeneous anchoring on both surfaces with  $\Delta\epsilon_a > 0$ . This creates two stable states of a homogeneously aligned cell, figure 1.15a, or a  $\pi$  twisted cell, figure 1.15c. One surface is weakly anchored so that a large enough voltage breaks the surface director to align with the field, figure 1.15b. Upon removal of the field, dependent upon its waveform, the cell can then relax to either the homogeneous state or  $\pi$  twisted states. A slowly decreasing waveform relaxes to the homogeneous state, an instantaneous removal of the field causes a large hydrodynamic effect transforming the orientation to the  $\pi$  twisted state.

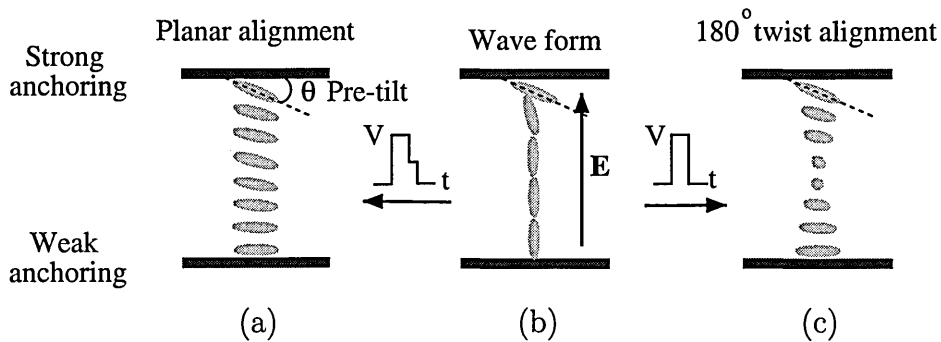


Figure 1.15: Sketch of the 180° surface controlled nematic. The equilibrium states (a) planar untwisted and (c) twisted. Applying an electric field breaks the lower surface anchoring and the waveform decides the switched state.

## Zenithally Bistable Nematic Device (ZBD)

The ZBD uses a surface structure to induce bistability of a nematic  $\Delta\epsilon_a > 0$ . Early variants of this device were investigated by [30] and more recently and advanced variants by [31]. One surface of the cell is flat whilst the other is that of a grating, see figure 1.16. Surface alignment induces homeotropic alignment everywhere (normal to the surface). Due to the grating morphology two optically distinct states called the continuous, figure 1.16a, and defect, figure 1.16b states exist. In the defect state the director changes abruptly at the peak and troughs of the grating where as the director changes continuously in the continuous state with no defects. Switching

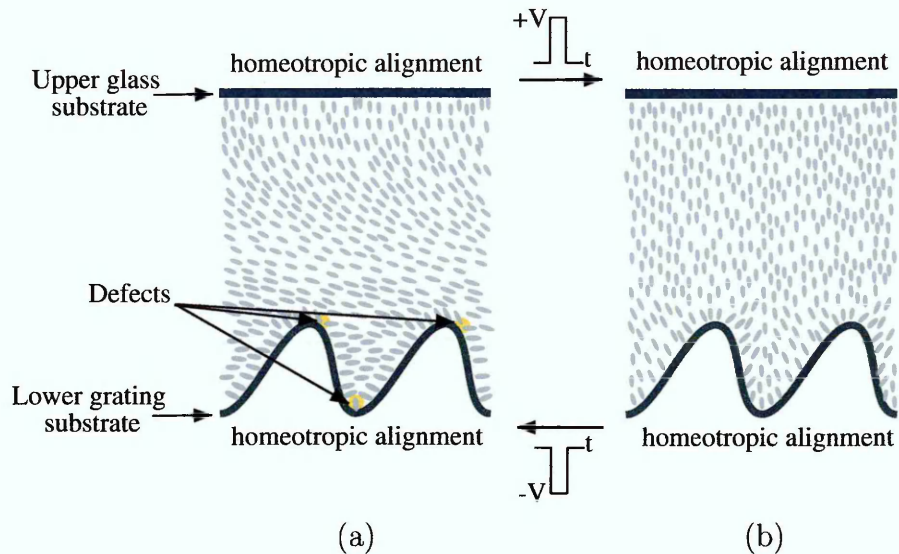


Figure 1.16: Sketch of the equilibrium states of the ZBD. The defect state (a) has hybrid alignment with defects situated around the grating surface. The continuous state (b) has an almost continuous vertical director structure the does not contain defects. Switching between states is chosen by the sign of the electric field.

between states is achieved via polar pulsed fields and it involves complicated creation and annihilation of defects to latch between states.

### 1.3 Phenomenological Methods for Liquid Crystals

In studying the behaviour of liquids and LC's a full statistical mechanics treatment is highly non-trivial when compared to that of rare gases or idealised solids. On one hand computers are often used to aid through molecular simulation of such liquids but on the other hand molecular simulations of macroscopic properties and systems are not within reach yet. For the study of LCD cells a molecular simulation would undoubtedly provide accurate detailed information about switching behaviour but for typical cell heights  $1-10 \mu\text{m}$  these fall within a macroscopic regime. Very often the detailed microscopic description of a system is not even needed to predict its macroscopic properties and behaviour. In such cases a phenomenological description suffices in which an appropriate macroscopic system can then be followed more readily with the aid of the computer simulation and continuum mechanics.

The first accepted phenomenological theories for LC were based on the director description of the nematic phase (at constant order parameter). Frank [32]

constructed an appropriate form for the elastic free energy of a LC which when minimised gave correct equilibrium configurations. However the time evolution of this minimisation failed to agree with experimental observations. The dynamic simulations of both the director description and flow behaviour then followed to better predict this time evolution. Ericksen [33] and Leslie [34] developed the accepted constitutive theories for flows and directors in what is now termed nemato-dynamics. The Ericksen-Leslie (EL) theory couples the flow to the director and the director to the flow. The EL method has been experimentally verified in terms of its predictions and in comparing calculated optical transmission of switched LCD's. DeGennes [35] developed seminal works in phenomenological theory to extend the aforementioned theories to study critical phenomena, LC's near their transition point  $T_{IN}$ . He included the order parameter degree of freedom into the director description via the alignment tensor or  $Q$ -tensor. This latter approach is followed in the development of a solver for LC dynamics in this thesis.

Over the last few decades the static structures of confined LC and LC defects cores (discontinuous in the director and molecular orientations) have been studied thoroughly. Dynamic studies followed next to observe time evolution of such systems switching phenomena in LCD's. Very often the dynamics of LC including those of defects are studied via the director description, neglecting hydrodynamic flow entirely. While the director description is perfectly adequate for problems not involving any defects well into the nematic phase, the neglect of flow is always questionable. Hence in order to give a proper treatment of defect dynamics one must use a tensor method as well as take into account hydrodynamic effects. Using a tensor method does not bring any significant complications - it yields richer structures. Its drawbacks are to introduce wider parameter space and that it introduces a microscopic length scale (the order parameter) which sets an upper limit to the conceivably macroscopic length scales that can be reached via simulation.

# Chapter 2

## Landau deGennes Theory of Liquid Crystals

In this chapter we briefly review phenomenological theory for LC hydrostatics and hydrodynamics within the Landau deGennes framework.

### 2.1 Introduction

A phenomenological theory of phase transitions [36] was established by Landau [36]. In the simplest cases through the definition of an appropriate order parameter,  $Q$ , the macroscopic behaviour of a phase may be followed. Typically  $Q = 0$  in the more symmetric (less ordered) phases and  $Q \neq 0$  in the less symmetric (more ordered) phases. For example in a liquid-gas system the order parameter is the difference in scalar density between the liquid and the gas phase. However order parameters are not just restricted to simple scalar quantities, more complicated formulations may be required and derived from the language of group theory. It was seminal works by deGennes [35, 37] who first used an appropriate order parameter to describe properties of the nematic isotropic phase transition motivated from his studies of pre-transitional phenomena of thermotropic nematics.

#### 2.1.1 The Nematic Order Parameter

Nematic orientation is characterised by a unit vector with ‘head-tail’ symmetry called the director,  $\hat{n}_\alpha$ . With the director aligned along the z-axis of a laboratory frame of reference we may define a second microscopic co-ordinate frame of reference at a particular molecule of unsaid symmetry. This reference frame is given, from the director, by its three Eulerian angles:  $(\theta, \phi, \psi)$ . This microscopic state

of alignment can be described by a continuous orientational distribution function (ODF)  $f(\theta, \phi, \psi)$  describing the probability of finding a collection of molecules orientated within a solid angle,  $d\Omega$ . The fraction of molecules in the sample with this solid angle is then given by  $N(\Omega) = f(\theta, \phi, \psi)d\Omega$  that should be normalised such that  $\int f(\theta, \phi, \psi)d\Omega = 1$  when integrated over a whole solid angle. In the isotropic phase this simply gives  $f(\Omega) = 1/8\pi^2$ .

A nematic may be considered uniaxial due to its rapid molecular tumbling (typical time scale of  $10^{-16}$  s [3]) giving an effective cylindrically symmetric molecular shape. The molecule long axis orientation,  $\hat{u}_\alpha$ , can then be given from its spherical co-ordinates: polar ( $\theta$ ) and azimuthal ( $\phi$ ) angles,  $\cos\theta = \hat{n}_\alpha\hat{u}_\alpha$ . The ODF in this case is  $f(\theta, \phi)$ . Further  $\hat{n}_\alpha$  is independent of  $\phi$  thus  $f(\Omega) = f(\theta)$ .  $f(\theta)$  can be expanded in various ways but for LC it is useful to expand in terms of Legendre polynomials,  $P_m(x)$  where  $m$  is the order. The first few are given as:  $P_0 = 1$ ,  $P_1(x) = x$ ,  $P_2(x) = \frac{1}{2}(3x^2 - 1)$ ,  $P_3(x) = \frac{1}{2}(5x^3 - 3x)$ . These have the useful property that  $P_m(1) = 1$ . Expanding  $f(\theta)$  in these terms:

$$f(\theta) = \frac{1}{4\pi^2} \sum_{m=0}^{\infty} f_m P_m(\cos\theta) \quad (2.1)$$

where the polynomials satisfy the orthogonality relations:

$$\int_0^\pi P_n(\cos\theta)P_m(\cos\theta) \sin\theta d\theta = \frac{2\delta_{nm}}{2m+1} \quad (2.2)$$

and  $f_m$  are the expansion coefficients determined from:

$$f_n = \frac{2n+1}{2} \int_0^\pi f(\theta)P_n(\cos\theta) \sin\theta d\theta \quad (2.3)$$

and  $\delta_{\alpha\beta}$  is the Kronecker delta symbol ( $\delta_{\alpha\beta} = 1$  when  $\alpha = \beta$  and  $\delta_{\alpha\beta} = 0$  for  $\alpha \neq \beta$ ). Defining the average value of a quantity  $X(\theta)$  [3] over all molecules in a macroscopic ensemble as:

$$\langle X(\theta) \rangle \equiv \int_0^\pi X(\theta)f(\theta) \sin\theta d\theta \quad (2.4)$$

we get for the expansion coefficients:

$$f_n = \frac{2n+1}{2} \langle P_n(\cos\theta) \rangle \quad (2.5)$$

where  $\langle P_n(\cos\theta) \rangle$  is the average Legendre polynomial over all molecules.

Examining terms in order of decreasing significance in equation 2.1, the zeroth order coefficient  $f_0 = 1/2$  is insensitive to any type of molecular ordering hence we seek higher order terms. All  $P_{2n-1}(\cos \theta)$  polynomials are odd functions whereas  $P_{2n}(\cos \theta)$  polynomials are even and similarly the ODF is even ( $f(\theta) = f(\theta + \pi)$ ) due to the nematics ‘head-tail’ symmetry. Thus all odd order coefficients  $f_n$  are identically zero. Looking to the next highest order non-zero coefficient,  $n = 2$ , we have:

$$f_2 = \frac{5}{2} \int_0^\pi f(\theta) P_2(\cos \theta) \sin \theta d\theta = \frac{5}{2} \langle P_2(\cos \theta) \rangle = \frac{5S}{2} \quad (2.6)$$

in which the ensemble scalar order parameter  $S = \langle \frac{1}{2}(3 \cos^2 \theta - 1) \rangle$  is defined.  $S$  therefore quantifies the degree of nematic ordering with respect to  $\hat{n}_\alpha$  as described in § 1.2. Up to the second order the ODF can then be written as:

$$\begin{aligned} f(\theta) &= \frac{1}{4\pi^2} \left( \frac{1}{2} + \frac{5S}{2} P_2(\cos \theta) \right) = \frac{1}{4\pi^2} \left( \frac{1}{2} + \frac{5S}{4} (3 \cos^2 \theta - 1) \right) \\ &= \frac{1}{8\pi^2} \left( 1 + \frac{5S}{2} (3(\hat{n}_\alpha \hat{u}_\alpha)^2 - 1) \right) = \frac{1}{8\pi^2} \left( 1 + \frac{5S}{2} (3\hat{n}_\alpha \hat{n}_\beta - \delta_{\alpha\beta}) \hat{u}_\alpha \hat{u}_\beta \right) \\ &= \frac{1}{8\pi^2} (1 + 5Q_{\alpha\beta} \hat{u}_\alpha \hat{u}_\beta) \end{aligned} \quad (2.7)$$

where  $Q_{\alpha\beta}$  is defined by:

$$Q_{\alpha\beta} = \frac{S}{2} (3\hat{n}_\alpha \hat{n}_\beta - \delta_{\alpha\beta}) \quad (2.8)$$

and is called the tensor order parameter or uniaxial alignment tensor, also often referred to as the quadrupolar moment of the ODF. The alignment tensor contains information on both average molecular alignment  $\hat{n}_\alpha$  and on the degree of order  $S$ . It has the properties  $Q_{\alpha\alpha} = 0$  (traceless) and  $\varepsilon_{\alpha\beta\gamma} Q_{\alpha\beta} = 0$  (symmetric) and is dimensionless. Obviously including higher order terms will lead to a more accurate ODF but for most theoretical and experimental works in LC’s, the characteristic second moment parameter equation 2.8 is enough to describe the molecular ordering.

Equivalently [38] nematic ordering can explicitly be described by constructing a symmetric and traceless ordering matrix from the assumed rigid rod-like molecular orientations:

$$Q_{\alpha\beta} = \frac{1}{2} \left( \frac{3 \sum_i \hat{u}_{i\alpha} \hat{u}_{i\beta}}{N} - \delta_{\alpha\beta} \right) \quad (2.9)$$

because this matrix is symmetric it is always possible to find a frame of reference in which it is diagonal where the eigenvalue with the largest absolute value can be identified as  $S$  and the corresponding eigenvector as  $\hat{n}_\alpha$ .

For a biaxial nematic, the cylindrical symmetry of  $f(\theta)$  is broken. In addition to the director, two additional characteristic directions appear,  $\hat{m}_\alpha$  and  $\hat{l}_\alpha$  forming an orthonormal triad with  $\hat{n}_\alpha$ . Although there are thermotropic LC's that are biaxial, many are uniaxial which under external constraints such as electric and magnetic fields, confinement, sheared flows and elastic distortions, the symmetry of  $f(\theta)$  is broken and the LC exhibits biaxial characteristic. As before an ODF can be used to define an alignment tensor though the process is more lengthy. Expansion in terms of spherical harmonics [3] and taking the quadratic terms as before results in:

$$\left. \begin{aligned} Q_{\alpha\beta} &= \frac{S}{2} (3\hat{n}_\alpha\hat{n}_\beta - \delta_{\alpha\beta}) + \frac{P_B}{2} (\hat{l}_\alpha\hat{l}_\beta - \hat{m}_\alpha\hat{m}_\beta) \\ &= \frac{S}{2} (3\hat{n}_\alpha\hat{n}_\beta - \delta_{\alpha\beta}) - \frac{P_B}{2} (\hat{m}_\alpha\hat{m}_\beta - (\hat{n} \times \hat{m})_\alpha (\hat{n} \times \hat{m})_\beta) \end{aligned} \right\} \quad (2.10)$$

which introduces the biaxial order parameter  $P_B = \frac{3}{2} \langle \sin^2 \theta \cos 2\theta \rangle$ . Diagonalising the tensor results in three different eigen values,  $S$ ,  $-\frac{1}{2}(S + P_B)$ ,  $-\frac{1}{2}(S - P_B)$ . As  $Q_{\alpha\beta}$  is symmetric and traceless it has five independent terms reflecting the five quantities to determine the ODF at second order: order parameters  $S$  and  $P_B$ , director angles  $\theta$  and  $\phi$  together with a third to determine the direction of  $\hat{m}_\alpha$ .

The level of microscopic ordering in the alignment tensor is reflected in the macroscopic quantities such as the dielectric and magnetic susceptibility, refractive index and conductivity. This leads to an experimentally macroscopic way to determine  $Q_{\alpha\beta}$ . Consider the diagonalised macroscopic susceptibility tensor, then making it traceless:

$$\begin{aligned} \Delta\chi_{\alpha\beta} &= \chi_{\alpha\beta} - \frac{\chi_{\gamma\gamma}\delta_{\alpha\beta}}{3} \\ &= \begin{pmatrix} -\frac{1}{3}(\chi_{\parallel} - \chi_{\perp}) & & \\ & -\frac{1}{3}(\chi_{\parallel} - \chi_{\perp}) & \\ & & \frac{2}{3}(\chi_{\parallel} - \chi_{\perp}) \end{pmatrix} \end{aligned} \quad (2.11)$$

normalising the tensor through the maximum anisotropy  $\Delta\chi_a^{max} = (\chi_{\parallel} - \chi_{\perp})/S$  we have:

$$Q_{\alpha\beta} = \frac{3}{2\Delta\chi_a^{max}} \left( \chi_{\alpha\beta} - \frac{\chi_{\gamma\gamma}\delta_{\alpha\beta}}{3} \right) \quad (2.12)$$

The use of an order parameter defined in this way is valuable as it makes no assumptions about the constituent molecules or their flexibility. Likewise equation 2.12 shows how changes in macroscopic properties arise from microscopic changes in order.

## 2.1.2 Nematic - Isotropic Phase Transition

In general there are two different types of phase transitions at which matter undergoes a change in its micro-structural symmetry. A phase transition is of first order when the order parameter changes discontinuously at the transition. At a continuous phase transition, or critical point, the order parameter changes continuously but is discontinuous in a higher derivative. The nematic-isotropic phase transition is weakly first order [35]. The Landau-deGennes theory of the nematic-isotropic transition starts by assuming that a spatially invariant dimensionless, order parameter is small in the nematic phase close to the transition point. The difference in free energy density (per unit volume) of the two phases is thus expanded in powers of the order parameter. For the order parameter identified in §2.1.1:

$$F_{LdG}(P, T, Q_{\alpha\beta}) = F_0 + A_{\alpha\beta\gamma\theta} Q_{\alpha\beta} Q_{\gamma\theta} + B_{\alpha\beta\gamma\theta\delta\lambda} Q_{\alpha\beta} Q_{\gamma\theta} Q_{\delta\lambda} + C_{\alpha\beta\gamma\theta\delta\lambda\mu\nu} Q_{\alpha\beta} Q_{\gamma\theta} Q_{\delta\lambda} Q_{\mu\nu} \quad (2.13)$$

where  $F_0$  is the energy density of the isotropic phase,  $A$ ,  $B$  and  $C$  are tensor preserving the symmetry of the phase, constructed in the usual way such that the energy density is invariant under rotations and reflections [39].  $P$ ,  $T$ , are thermodynamic variables of which  $P$  is pressure and  $T$  the temperature. The equilibrium state can be obtained from the minimum of this free energy with respect to  $Q_{\alpha\beta}$  for a fixed  $P$  and  $T$ . The most general form capturing the uniaxial phase [38] is typically truncated at fourth order and is:

$$F_{LdG}(P, T, Q_{\alpha\beta}) = F_0 + \alpha_F Q_{\alpha\beta} Q_{\beta\alpha} + \beta_F Q_{\alpha\beta} Q_{\beta\gamma} Q_{\gamma\alpha} + \gamma_F Q_{\alpha\beta} Q_{\beta\alpha} Q_{\gamma\tau} Q_{\tau\gamma} \quad (2.14)$$

where  $\alpha_F$ ,  $\beta_F$  and  $\gamma_F$  are the Landau deGennes coefficients. For notational convenience we adopt the equivalent form of equation 2.14 to match the notation given in [40] and thus provide a consistency in subsequent chapters of this work:

$$F_{LdG}(P, T, Q_{\alpha\beta}) = F_0 + \frac{\alpha_F}{2} Q_{\alpha\beta} Q_{\beta\alpha} - \beta_F Q_{\alpha\beta} Q_{\beta\gamma} Q_{\gamma\alpha} + \gamma_F Q_{\alpha\beta} Q_{\beta\alpha} Q_{\gamma\tau} Q_{\tau\gamma} \quad (2.15)$$

where  $\alpha_F$ ,  $\beta_F$  and  $\gamma_F$  are again the Landau deGennes coefficients and in  $\gamma_F$  is absorbed the equivalence of terms  $Q_{\alpha\beta} Q_{\beta\alpha} Q_{\gamma\tau} Q_{\tau\gamma} = \frac{1}{2} Q_{\alpha\beta} Q_{\beta\gamma} Q_{\gamma\delta} Q_{\delta\alpha}$ . The analysis of this equation is identical to the usual approaches where it is assumed the first Landau deGennes coefficient taking the form,  $a(T - T^*)$ , changing sign at some temperature  $T^*$ , while the variation of the other coefficients with  $T$  is assumed to

be unimportant and is neglected. Inserting the uniaxial order tensor definition, equation 2.8, in equation 2.15 with the above said assumptions results in:

$$F_{LdG}(P, T, Q_{\alpha\beta}) = F_0 + a(T - T^*)S^2 - BS^3 + CS^4 \quad (2.16)$$

where  $a(T - T^*) = \frac{3\alpha_F}{4}$ ,  $B = \frac{3\beta_F}{4}$ ,  $C = \frac{9\gamma_F}{4}$ . The first order transition is usefully characterised by the following observations:

$$\frac{\partial F}{\partial S} = 0, \quad F(S, T, P) - F(0, T, P) = 0, \quad \frac{\partial^2 F}{\partial S^2} > 0 \quad (2.17)$$

which from it is deduced:

$$\left. \begin{aligned} S_{IN} &= \frac{B}{2C} \\ T_{IN} &= T^* + \frac{B^2}{4aC} \\ T^{**} &= T_{IN} + \frac{B^2}{32aC} \\ \Delta E &= \frac{T_{IN}aB^2}{4C^2} \\ S &= \frac{3B + \sqrt{B^2 - 32aC(T - T_{IN})}}{8C} \end{aligned} \right\} \quad (2.18)$$

Figure 2.1 illustrates equation 2.16 from where it can be seen for  $T \gg T_{IN}$  the minimum in energy correspond to an isotropic ( $S = 0$ ) phase and for  $T \ll T_{IN}$  the minimum in energy corresponds to a nematic phase. In between these temperatures the behaviour is more intricate. At  $T^*$  (lower limit for super cooling of the isotropic

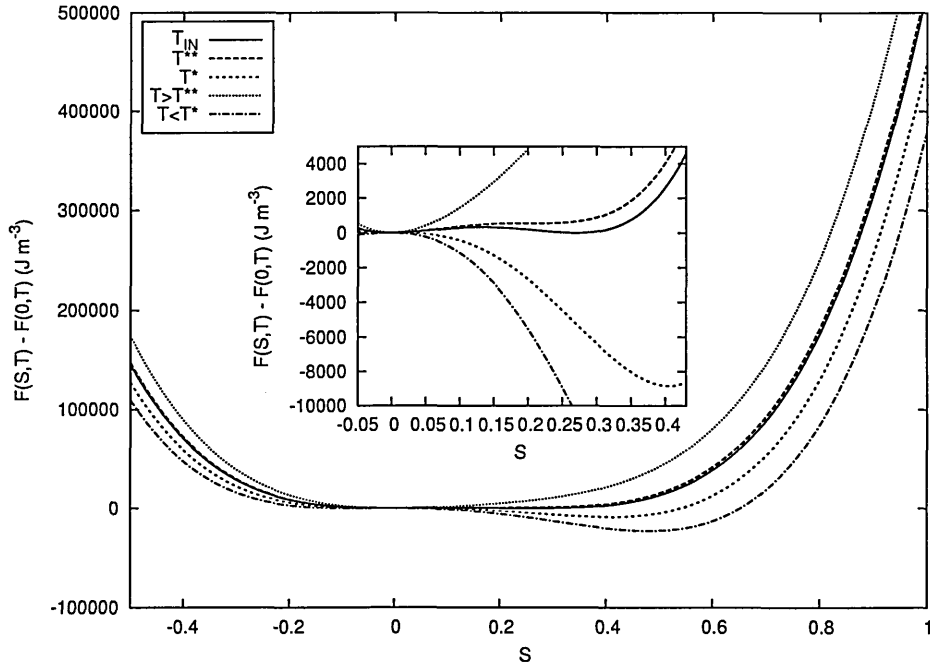


Figure 2.1: Plot of the free energy dependence upon the order parameter at various temperatures over the nematic-isotropic transition range.

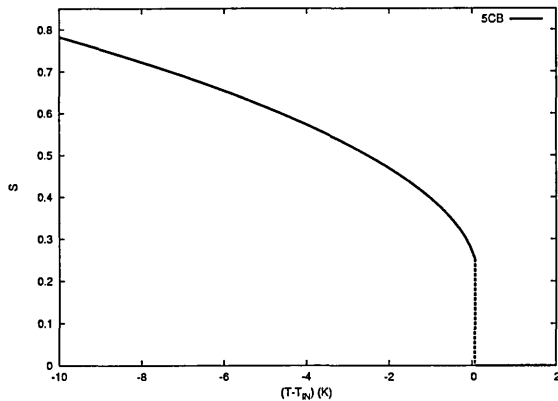


Figure 2.2: The equilibrium order parameter dependence (c.f. equation 2.18) upon temperature for the Landau material parameters appropriate for 5CB as given in [40].

phase) a metastable ordered state occurs in which the isotropic state becomes unstable for decreasing  $T$ , at  $T^{**}$  (upper limit for super heating of the nematic phase) the nematic state becomes unstable for increasing  $T$ .  $\Delta E$  of equation 2.18 is the expected change in entropy indicative of the phase transition.

The temperature behaviour of the order parameter is shown in figure 2.2 as predicted in equation 2.18, it gives the equilibrium order parameter value of an undistorted nematic for a given set of Landau deGennes coefficients, the discontinuity clearly being visible. It should be noted in this approach that  $S$  is unbounded for lower and lower temperatures and from the initial assumptions the expansion should really be applied for small  $S$ . However from figure 2.2 we see the behaviour of the order parameter in the nematic region is not unreasonable. In this thesis we will work mainly well into the nematic phase ( $S \sim 0.6$ ) applying this theory without reservation. We also point out that expansions in term of  $Q_{\alpha\beta}$  are unbounded in that there exist an infinite number of orders of  $Q_{\alpha\beta}$  but to make practical use of the Landau deGennes theory we only keep terms that allow a one to one mapping of the current experimentally used parameters which are based upon an  $\hat{n}_\alpha$  expansion that is bounded due to its unit vector property.

### 2.1.3 Curvature Elasticity

A nematic prefers to lie in an undistorted state. For a nematic in a confined system the effect of walls is to impose an ordering upon the molecules that may vary spatially. Considering  $Q_{\alpha\beta} = Q_{\alpha\beta}(\underline{r})$ , weak distortions represent an increase in

energy and a measure of this increase can be obtained from the gradients in  $Q_{\alpha\beta}$  provided the characteristic length scale associated with changes in  $Q_{\alpha\beta}$  is longer than the molecular dimensions (typically 1nm). A linear expansion yields the free energy density:

$$F_F = F_F(\partial_\gamma Q_{\alpha\beta}) = F_0 + L_{\alpha\beta\gamma} \partial_\gamma Q_{\alpha\beta} + \frac{K_{\alpha\beta\gamma\theta\mu\nu}}{2} \partial_\alpha Q_{\beta\gamma} \partial_\theta Q_{\mu\nu} \quad (2.19)$$

where  $F_0$  is the energy of the undistorted,  $L_{\alpha\beta\gamma}$  allows for a chiral nematic phase with a spontaneous twist as its ground state ( $P_{ch} = \text{helix pitch}$ ) while  $K_{\alpha\beta\gamma\theta\mu\nu}$  represents the nematic elasticity; notice  $\mathbf{K}$  is symmetric in  $\beta\gamma$  and  $\mu\nu$  and that  $K_{\alpha\beta\gamma\theta\mu\nu} = K_{\theta\mu\nu\alpha\beta\gamma}$ . A usual decomposition of the terms to second order in  $Q_{\alpha\beta}$  leaves a degeneracy in the splay and bend elastic constants contrary to many experimental measurements, thus taking a single extra third order term in  $Q_{\alpha\beta}$  [41] we get:

$$F_F = \frac{L_1}{2} \partial_\mu Q_{\nu\gamma} \partial_\mu Q_{\nu\gamma} + \frac{L_2}{2} \partial_\mu Q_{\nu\mu} \partial_\gamma Q_{\nu\gamma} + \frac{L_3}{2} \partial_\mu Q_{\nu\gamma} \partial_\gamma Q_{\nu\mu} + \frac{L_4}{2} Q_{\mu\nu} \partial_\mu Q_{\gamma\tau} \partial_\nu Q_{\gamma\tau} + \frac{4\pi L_1}{P_{ch}} \varepsilon_{\mu\nu\gamma} Q_{\mu\tau} \partial_\nu Q_{\gamma\tau} - \frac{4\pi L_4}{P_{ch}} \varepsilon_{\mu\nu\gamma} Q_{\mu\eta} Q_{\eta\tau} \partial_\nu Q_{\gamma\tau} \quad (2.20)$$

Although there are seven third order terms in  $Q_{\alpha\beta}$  we only include one [42] to ensure non-equal elastic constants and to prevent having undefined constants. (That is undefined constants regarding mapping onto experimentally used  $K_{ii}$  values. We may also view higher order terms as small ( $Q_{\alpha\beta} \ll 1$ ) corrections to the energy.) Upon using the uniaxial, constant order parameter tensor, equation 2.8 it is found:

$$F_F = \frac{9S_0^2}{8} (2L_1 + L_2 + L_3 - S_0 L_4) (\nabla \cdot \hat{n})^2 + \frac{9S_0^2}{8} (2L_1 - S_0 L_4) \left( (\hat{n} \cdot \nabla \times \hat{n})^2 + \frac{4\pi}{P_{ch}} (\hat{n} \cdot \nabla \times \hat{n}) \right) + \frac{9S_0^2}{8} (2L_1 + L_2 + L_3 + 2S_0 L_4) (\hat{n} \times (\nabla \times \hat{n}))^2 - \frac{9S_0^2}{8} (2L_1 + L_3 - S_0 L_4) \nabla \cdot [\hat{n} (\nabla \cdot \hat{n}) + \hat{n} \times (\nabla \times \hat{n})] \quad (2.21)$$

Helpful identities are:

$$\left. \begin{aligned} \partial_\beta \hat{n}_\mu \partial_\mu \hat{n}_\beta &\equiv (\nabla \cdot \hat{n})^2 - \text{div}(\hat{n} \text{div} \hat{n} + \hat{n} \times \text{curl} \hat{n}) \\ \partial_\alpha \hat{n}_\beta \partial_\alpha \hat{n}_\beta &\equiv \nabla \cdot \hat{n} : \nabla \hat{n} + (\hat{n} \cdot \text{curl} \hat{n})^2 + (\hat{n} \times (\text{curl} \hat{n}))^2 \\ \hat{n}_\mu \partial_\gamma \hat{n}_\mu &= 0 \end{aligned} \right\} \quad (2.22)$$

or equivalently a Frank [32] form:

$$F_F = \frac{1}{2} \left[ K_{11} (\nabla \cdot \hat{n})^2 + K_{22} \left( (\hat{n} \cdot \nabla \times \hat{n})^2 + \frac{4\pi}{P_{ch}} (\hat{n} \cdot \nabla \times \hat{n}) \right) + K_{33} (\hat{n} \times (\nabla \times \hat{n}))^2 - (K_{22} + K_{24}) \nabla \cdot [\hat{n} (\nabla \cdot \hat{n}) + \hat{n} \times (\nabla \times \hat{n})] \right] \quad (2.23)$$

Comparing equations.2.21 and 2.23 identifies the elastic constants:  $K_{11} = \frac{9S_0^2}{4} (2L_1 + L_2 + L_3 - S_0L_4)$  ,  $K_{22} = \frac{9S_0^2}{4} (2L_1 - S_0L_4)$  ,  $K_{33} = \frac{9S_0^2}{4} (2L_1 + L_2 + L_3 + 2S_0L_4)$ ,  $K_{24} = \frac{9S_0^2}{4} L_3$ .

Mathematically the saddle-splay ( $K_{24}$ ) contribution is a divergence term and therefore does not influence bulk behaviour, indeed for fixed anchoring (infinite strength) it has no affect even at the surface but if anchoring is weak on the surfaces the saddle-splay term may contribute to surface ordering and thus change the bulk ordering. There exists another divergence term known as splay-bend,  $K_{13}$ . It is obtained by taking the second derivatives of  $Q_{\alpha\beta}$  in a linear expansion, the extra terms being  $N_{\alpha\beta\gamma\theta}\partial_\gamma\partial_\theta Q_{\alpha\beta} + \frac{1}{2}M_{\alpha\beta\gamma\theta\mu\nu\lambda\epsilon}\partial_\alpha\partial_\beta Q_{\gamma\theta}\partial_\mu\partial_\nu Q_{\lambda\epsilon}$ . The term was proposed by Nehring-Saupe [43] and it is known that its inclusion can lead to difficulties in search for stable states in nematics by means of variational calculus [39]. For this reason and the lack of experimental data for its value we only consider terms in the first derivatives for the remainder of this work.

### 2.1.4 Flexoelectricity

For an undistorted equilibrium flexoelectric nematic there is no discernible macroscopic difference from a conventional uniaxial rod-like nematic. However, if the LC is distorted or if an external electric field is applied a polarisation results as originally discovered by Meyer [8]. He shows the electric polarisation and free energy density due to polar molecules are given by:

$$F_{Flexo} = -E_\alpha P_\alpha = -e_{\alpha\beta\gamma}\partial_\gamma\hat{n}_\beta E_\alpha \quad (2.24)$$

where tensor  $e_{\alpha\beta\gamma}$  is temperature dependent and dependent upon molecular shape [44]. (It essentially arises because, a molecular distortion can induce polarisation which in turn effects the local electric field; conversely an electric field may induce distortion and thus polarisation and further electric fields terms.) The tensor  $e_{\alpha\beta\gamma}$  can also be connected to quadrupolar properties of molecules [9]. Following [45] flexoelectricity theories should really allow for order parameter variations and thus:

$$F_{Flexo} = -E_\theta P_\theta = -C_{\alpha\beta\gamma\theta}\partial_\gamma(Q_{\alpha\beta})E_\theta \quad (2.25)$$

the tensor  $C_{\alpha\beta\gamma\theta}$  is symmetric in  $\alpha\beta$  and decomposed in the usual manner ( $Q_{\mu\nu}$ ,  $\delta_{\mu\nu}$  combinations). It may be expressed

$$P_\theta = C_1 \partial_\gamma Q_{\theta\gamma} + C_2 Q_{\theta\gamma} \partial_\mu Q_{\gamma\mu} \quad (2.26)$$

in which  $C_i$  are ‘weakly’ temperature dependent flexoelectric coefficients. There exist three second order terms in  $Q_{\alpha\beta}$ . However as before we include only one (the  $C_2$  term) to enable, as will be seen, independence of polar flexoelectric coefficients and to retain a formulism in which experimental parameters can be matched without introducing unknown coefficients. Using the uniaxial constant order parameter tensor equation 2.8 we find:

$$P_\theta = \left( \frac{3S_0 C_1}{2} + \frac{3S_0^2 C_2}{2} \right) \hat{n}_\theta \partial_\mu \hat{n}_\mu + \left( \frac{3S_0 C_1}{2} - \frac{3S_0^2 C_2}{4} \right) \hat{n}_\gamma \partial_\gamma \hat{n}_\theta \quad (2.27)$$

or equivalently in the convention of Meyer:

$$P_\theta = e_{11} \hat{n}_\theta \partial_\mu \hat{n}_\mu + e_{33} \hat{n}_\gamma \partial_\gamma \hat{n}_\theta \quad (2.28)$$

comparing equation 2.27 and 2.29 we see  $e_{11} = \left( \frac{3S_0 C_1}{2} + \frac{3S_0^2 C_2}{2} \right)$ ,  $e_{33} = \left( \frac{3S_0 C_1}{2} - \frac{3S_0^2 C_2}{4} \right)$ .

At first order in  $Q_{\alpha\beta}$  it is apparent  $e_{11} = e_{33} = \frac{3S_0 C_1}{2}$  and corresponds to the quadrupolar case of [9], going to second order allows an  $e_{11}$ ,  $e_{33}$  independence. There are no flexoelectric terms arising from second derivatives, due to symmetry arguments these are identically zero. If upon substitution of equation 2.8 into equation 2.26, we treat  $S$  as a variable ( $S = S(\underline{r})$ ) and neglect  $\hat{n}$  variations we may deduce the polarisation contribution from  $S$  alone, known as the order electric effect [39] that may be important in situations in which  $S$  changes abruptly and is given by

$$P_\theta = \left( \frac{3C_1}{2} + \frac{3C_2 S}{4} \right) \hat{n}_\theta \hat{n}_\mu \partial_\mu S + \left( -\frac{C_1}{2} + \frac{C_2 S}{4} \right) \partial_\theta S \quad (2.29)$$

### 2.1.5 Electric and Magnetic Fields

External electric and magnetic fields have an ordering effect upon the molecules of the nematic. Constructing the usual linear expansions [39] we have the free energy density:

$$F_{EM} = -P_\alpha E_\alpha - \frac{1}{2} \epsilon_{\alpha\beta} E_\alpha E_\beta - M_\alpha H_\alpha - \frac{1}{2} \chi_{\alpha\beta} H_\alpha H_\beta \quad (2.30)$$

The tensor  $P_\alpha$  was dealt with in §2.1.4 and  $M_\alpha$  has to be zero otherwise the LC is polar. This leaves  $\epsilon_{\alpha\beta}$  and  $\chi_{\alpha\beta}$  which can be expanded in terms of appropriate contractions of  $\delta_{\mu\nu}$ ,  $Q_{\mu\nu}$ . Using the definition of  $Q_{\alpha\beta}$  in equation 2.12 we find:

$$F_{EM} = -\frac{\Delta\epsilon_0\epsilon_a^{max}}{3}E_\alpha Q_{\alpha\beta}E_\beta - \frac{\epsilon_0\epsilon_{\gamma\gamma}E^2}{6} - \frac{\Delta\mu_0\chi_a^{max}}{3}H_\alpha Q_{\alpha\beta}H_\beta - \frac{\mu_0\chi_{\gamma\gamma}H^2}{6} \quad (2.31)$$

Examining equation 2.31 we see for a positive anisotropic material  $\epsilon_{\parallel} - \epsilon_{\perp} > 0$  (or equivalently  $\chi_{\parallel} - \chi_{\perp} > 0$ ), the lowest energy state is that in which  $Q_{\alpha\beta}$  is collinear with  $\underline{E}$  and thus a positive dielectric anisotropy aligns the nematic molecules with the direction of the field. Conversely for a negative anisotropy  $\epsilon_{\parallel} - \epsilon_{\perp} < 0$  the lowest energy state is that in which  $Q_{\alpha\beta}$  is perpendicular with  $\underline{E}$ : the nematic molecules align perpendicular to the applied field. The other terms containing the trace in equation 2.30 are independent of the nematic orientation, they may be important only where nearing the phase transition.

The presence of an electric field is more complicated than that of a magnetic field [46]. Conducting impurities within a LC sample are attracted to the field and will form regions of charge. For this reason many experiments use square wave fields to prevent ion build ups. Additionally as the dielectric anisotropy of a LC is far greater than the diamagnetic anisotropy, a distortion in the ordering of the sample will cause an electric field distribution in the sample to vary according to Maxwell's electrostatic equations [47]:

$$\left. \begin{aligned} \partial_\alpha D_\alpha &= \sigma_f \\ D_\alpha &= \epsilon_0\epsilon_{\alpha\beta}E_\beta + P_\alpha \\ E_\beta &= -\partial_\beta\phi \\ \underline{\nabla} \times \underline{E} &= 0 \end{aligned} \right\} \quad (2.32)$$

where  $\phi$  is the electric potential (voltage) and  $P_\alpha$  the spontaneous polarisation and free charge  $\sigma_f = 0$  for a perfect insulator as we assume in our work. Strictly speaking for accuracy when dealing with magnetic fields Maxwell's equations ( $\partial_\alpha B_\alpha = 0$ ,  $\underline{\nabla} \times \underline{H} = 0$ ) should also be solved. These equations amount to the Euler-Lagrange constraints for minimising the free energy with respect to  $Q_{\alpha\beta}$  (see §2.2).

Despite these added complications electric fields are still the preferred ordering effect in LCD devices due to the lower threshold fields for electro-optic phenomena.

## 2.1.6 External Anchoring

LC's that are in contact with a surface are ordered to some greater or lesser extent to a preferred direction. We associate with this preferred direction an energy imposing a penalty for deviations and characterised by the surface symmetry variables  $Q_{\alpha\beta}$  and  $\hat{k}_\alpha$  - a unit vector indicative of the preferred direction. In general the surface energy will depend on both these quantities and can be expressed as [39]:

$$F_S = F_0 + \gamma_1 \hat{k}_\alpha Q_{\alpha\beta} \hat{k}_\beta + \gamma_2 Q_{\alpha\beta} Q_{\beta\alpha} + \gamma_3 \hat{k}_\alpha Q_{\alpha\beta} Q_{\beta\mu} \hat{k}_\mu + \gamma_4 \left( \hat{k}_\alpha Q_{\alpha\beta} \hat{k}_\beta \right)^2 \quad (2.33)$$

The phenomenological parameters  $\gamma_i$  are 'weakly' temperature dependent anchoring coefficients and can only be determined from microscopic models of the surface interaction forces and the inter molecular forces. The  $\gamma_1$ ,  $\gamma_3$  and  $\gamma_4$  terms impose the alignment and the  $\gamma_2$  term imposes an order. There exists a lack of data on the surface energy coefficients thus an alternative form was proposed [48]

$$F_S = \frac{W}{2} (Q_{\alpha\beta} - Q_{\alpha\beta}^o)^2 \quad (2.34)$$

in which  $W$  is the sole anchoring coefficient and  $Q_{\alpha\beta}^o$  is a preferred alignment tensor given by equation 2.10. Assuming the uniaxial constant order limit (equation 2.8) in equation 2.33 and 2.34 both reduce to the traditional Rapini-Popular [49] form; for equation 2.34 this is:

$$F_S = \frac{9S_0^2 W}{4} (1 - (\hat{n}_\alpha \hat{n}_\alpha^o)^2) = -\frac{A}{2} (\hat{n}_\alpha \hat{n}_\alpha^o)^2 \quad (2.35)$$

where we see  $W = \frac{2A}{9S_0^2}$ ,  $A$ , is the Rapini-Papoular anchoring coefficient. The magnitude of the anchoring coefficient determines how strongly a preferred ordering is imposed. Another way to view this as suggested by deGennes [46] is in terms of an extrapolation length, figure 2.3, Where  $A = \frac{K}{l_e}$ , here  $K$  is a typical elastic constant and  $l_e$  is the extrapolation length. The larger  $A$  the smaller the extrapolation length and thus  $A$  determines how far from the preferred direction the surface order lies. For the case were the anchoring strength  $\rightarrow \infty$  we may assume Dirichlet boundary conditions by just setting the surface ordering to be any desired value.

## 2.2 The Equilibrium States

In the previous sections we have given the free energy density that describes LC behaviour,  $F = F(Q_{\alpha\beta}, \partial_\gamma Q_{\alpha\beta})$ . The total free energy in the LC sample is then

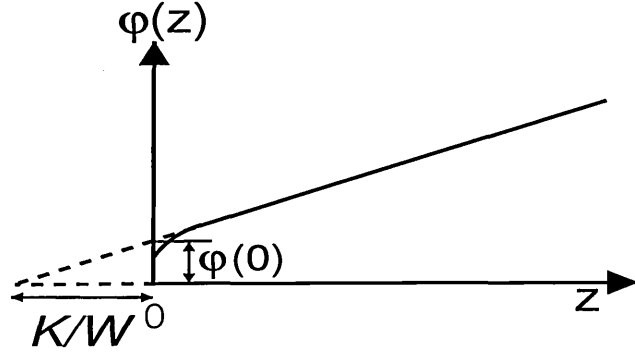


Figure 2.3: Definition of the extrapolation length  $K/W$  as defined by deGennes [46].

the superposition of all the energy densities integrated over the entire LC volume and limiting surfaces:

$$\mathcal{F} = \int_V F(Q_{\alpha\beta}, \partial_\gamma Q_{\alpha\beta}) dV + \int_S F_S(Q_{\alpha\beta}) dS \quad (2.36)$$

the search for stable states of the LC is performed from equation 2.36 and according to continuum theory the thermodynamical stable states are those characterised by a minimum free energy with respect to all variations in  $Q_{\alpha\beta}$ . Constructing a variation in  $\mathcal{F}$ ,  $\delta\mathcal{F}$ , for all virtual variations of the alignment:

$$\begin{aligned} \delta\mathcal{F} &= \delta \int_V F(Q_{\alpha\beta}, \partial_\gamma Q_{\alpha\beta}) dV + \delta \int_S F_S(Q_{\alpha\beta}) dS \\ &= \int_V \left( \frac{\partial F}{\partial Q_{\alpha\beta}} \delta Q_{\alpha\beta} + \frac{\partial F}{\partial \partial_\gamma Q_{\alpha\beta}} \delta(\partial_\gamma Q_{\alpha\beta}) \right) dV + \int_S \frac{\partial F_S}{\partial Q_{\alpha\beta}} \delta Q_{\alpha\beta} dS \end{aligned} \quad (2.37)$$

where  $\delta(\partial_\gamma Q_{\alpha\beta}) = \partial_\gamma(\delta Q_{\alpha\beta})$ , that is the variation operator commutes, thus with the aid of the identity (obtained from a simple product rule and divergence theorem):

$$\int_V \partial_\alpha (f_{\alpha\beta} g_\beta) dV = \int_V g_\beta \partial_\alpha f_{\alpha\beta} dV + \int_V f_{\alpha\beta} \partial_\alpha g_\beta dV = \int_S \hat{\nu}_\alpha f_{\alpha\beta} g_\beta dS \quad (2.38)$$

( $\hat{\nu}_\alpha$  being an outward pointing unit normal vector from the surface.) We may now write equation 2.37 as:

$$\delta\mathcal{F} = \int_V \left( \frac{\partial F}{\partial Q_{\alpha\beta}} - \partial_\gamma \frac{\partial F}{\partial(\partial_\gamma Q_{\alpha\beta})} \right) \delta Q_{\alpha\beta} dV + \int_S \left( \hat{\nu}_\gamma \frac{\partial F}{\partial(\partial_\gamma Q_{\alpha\beta})} + \frac{\partial F_S}{\partial Q_{\alpha\beta}} \right) \delta Q_{\alpha\beta} dS \quad (2.39)$$

This minimisation is constrained to be both symmetric and traceless thus with Lagrange multipliers results in the equilibrium conditions:

$$\frac{\partial F}{\partial Q_{\alpha\beta}} - \partial_\gamma \frac{\partial F}{\partial(\partial_\gamma Q_{\alpha\beta})} + \lambda^B \delta_{\alpha\beta} + \lambda^B \varepsilon_{\alpha\beta\gamma} = 0 \quad (2.40)$$

$$\hat{\nu}_\gamma \frac{\partial F}{\partial(\partial_\gamma Q_{\alpha\beta})} + \frac{\partial F_S}{\partial Q_{\alpha\beta}} + \lambda^S \delta_{\alpha\beta} + \lambda^S \varepsilon_{\alpha\beta\gamma} = 0 \quad (2.41)$$

Equations.2.40 and 2.41 are the standard Euler-Lagrange equations, the solutions to which yield the equilibrium rest state/s of a LC system. In the infinitely strong anchoring limit the boundary condition equation 2.41 can be ignored as the boundaries are constant. Including all free energies listed in previous sections requires equations.2.40 and 2.41 to be solved numerically due to their complexity. They will often show more than one solution corresponding to local minima in the free energy, thus for the real solutions the energy must be calculated for all possible solutions starting from random configurations and slowly quenching or by starting with different initial conditions.

## 2.3 Defects

For real unconstrained macroscopic LC samples a perfect homogeneous (undeformed) director pattern is rare. Typically there exist a number of arbitrarily locally orientated domains, the point at which the domains meet giving rise to defects. These are readily observed through optical microscopy, the nematic phase owes its name to the ‘thread like’ defects (so called Schleiern texture) which are seen under the microscope [46]. The defects can be points, lines, or walls around which the director is not well defined. Although walls are unstable [46] tending to degrade to a number of lines and can be avoided by appropriate treated tilted boundary conditions. The characteristic of a defect is for the local director field to be distorted accompanied by a significant decrease (melting) of the degree of order and by an increase in biaxiality to avoid the high deformation energies. The free energy of any defect state is obviously greater than in an unconstrained sample but may correspond to the ‘ground state’ depending upon boundary constraints.

The point and line (commonly called disclinations) defects can be approximately analysed considering the surrounding two dimensional plane such that  $\hat{n}_\alpha = \hat{n}_\alpha(x, y) = (\cos \theta, \sin \theta)$ . Using a coordinate system with origin at the defect core we imagine a closed loop encircling the defect. Moving along this loop, the local  $\hat{n}_\alpha$  rotates, and in one complete circle the continuity of  $\hat{n}_\alpha$  dictates that  $\theta(\phi + 2\pi) = \theta(\phi) + 2\pi m$  ( $\phi$  is a polar angle position along the circle). Here  $m$  is integer or half integer commonly known as the defect strength [46]. Assuming a constant order parameter and one elastic constant ( $K_{ii} = K$ ) the bulk free elastic

energy associated with a director distortion is then  $F = \frac{K}{2} \int (\partial_\gamma \partial_\gamma \theta)^2 dV$  which in solving the Euler Lagrange equation yields solutions for  $\theta(\phi) = m\phi + \theta_0$  where  $\theta_0$  is the director angle at the start of the enclosing circle. The director fields for typical

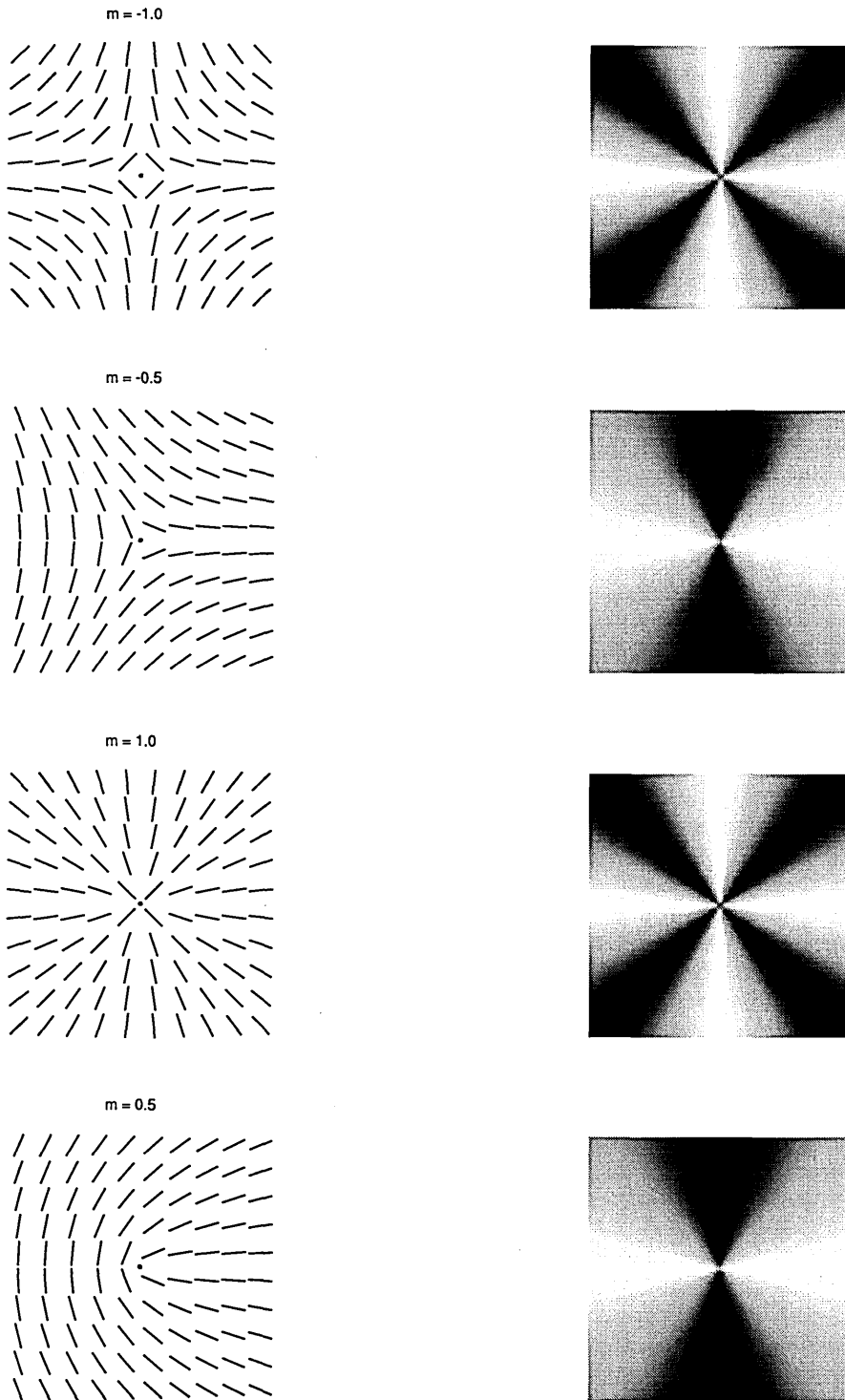


Figure 2.4: Director fields (left) and their associated crossed polar plot,  $\sin^2(2\theta)$ , (right) for common topological defects of different strengths  $m$ .

defects are thus shown in figure 2.4 for this approximate equation. Obviously for a full solution one needs to numerically solve the alignment tensor equations allowing for variations in  $S$  and  $P_B$ .

The defect strength can always be found from the analytical expression [50]:

$$m = \frac{1}{8\pi} \int \varepsilon_{\alpha\beta\gamma} \hat{n} \cdot (\partial_\beta \hat{n} \times \partial_\gamma \hat{n}) dS_\alpha \quad (2.42)$$

Defects generally tend to occur in pairs of opposite strength. The creation or annihilation process of defects typically occurs between opposite strength defects and generally lower  $m$  states are preferred energetically over higher  $m$  states [5] as their energy tends as  $m^2$ .

The half integer defects are not directly recovered with simulation using the vector director theories [50] because vectors have direction that cause a miscalculation of the derivatives where as in a nematic there is a ‘head-tail’ symmetry. Tensor representations  $Q_{\alpha\beta}$  are thus required to recover defect processes. It is also useful to know for the  $\pm 1$  defects that the director at the core tends to escape into the third dimension in order to lower its energy and thus a 3 dimensional tensor is required when studying defects.

## 2.4 Dynamic Evolution

The literature surrounding the governing dynamic evolution equations for the alignment tensor is complex and subjective. There exists no unifying, agreed, methodology and works have often been poorly acknowledged, a state that is likely to remain until further experimental and theoretical enlightenment. Despite the lack of a unifying theory, much work has been done and we endeavour to mention the literature developments offering references. A complete and thorough comparison is not done, but as will be seen is worthy in the near future if only to unify the works in this area.

For the complete dynamic evolution equations of LC’s it is necessary to follow both the alignment and velocity fields. The first phenomenological continuum theory for nematics adopted the director to describe molecular alignment. It was first developed by Ericksen [33] and Leslie [34] (and Parodi [51] to an extent through his Onsager relation on the viscosities) and here on dubbed EL theory. It is based upon

conservation laws for energy, linear momentum and moment of momentum. It fully couples the complex interplay of flow and orientation assuming that the LC is both uniaxial and has constant order parameter  $S(\underline{r}) = S_0$  (or at least where  $\xi_n \gg \xi_s$  in which  $\xi$  are characteristic lengths of a director and order variation respectively).

The governing equations (as laid down by EL theory) have since been derived in many ways. DeGennes [46] put the EL into a nice framework of irreversible thermodynamics (along the lines of deGroot [52]), Sonnet [53] used Lagrange's equations and a Rayleigh dissipation function, and Forster [54] used Poisson brackets to consider the conserved and hydrodynamic Goldstone modes. Although the derivations are all markedly different they may all be cast in the form of the EL theory lending support to the governing equations. The seminal EL theory has been widely accepted as 'the' theory by experimentalists and the five independent viscosity coefficients that it predicts have been calculated and verified, namely the Leslie viscosities  $\alpha_{ii}$ . The EL theory when used in conjunction with Jones  $2 \times 2$  matrix method [55] or the Berreman  $4 \times 4$  matrix method [56] (these are one dimensional; for three dimensional LC optics the finite difference time domain, FDTD, methods are required [57]) to calculate the optical transmission through a LCD cell has proven to be extremely accurate [58, 59].

Despite the success of the EL theory there exist physical situations in which it fails to provide a complete description of nematic orientational order: these are mainly associated with defects. Firstly it can introduce discretisation error when neighbouring directors are nearly anti parallel, secondly it does not take into account possible biaxial characteristics and lastly the effects of order parameters are not considered. One can employ several tricks to bypass parts of these features. We can give the director a tensor symmetry from the dyad  $\hat{n}_\alpha \hat{n}_\beta$  [60, 61, 62] to ensure the equivalence of  $\pm \hat{n}_\alpha$  in calculations, this amounts to using the  $Q_{\alpha\beta}$  with constant eigenvalues. Alternatively we may extend the EL director theory to a vector theory [63] (sometimes also referred to as the scalar director) where the order parameter is built into the size of the vector, though this provides little gain as the director symmetry is still lacking. These shortcomings are realised more so when considering half integer defects [64] which theoretically requires variable order, biaxiality and symmetry considerations, factors that are all taken into account when

using a  $Q_{\alpha\beta}$  tensor theory.

DeGennes [35] and Lubensky [41] pioneered the development and use of  $Q_{\alpha\beta}$  as a macroscopic variable to describe liquid crystals. In [35, 46] is laid the necessary framework of irreversible thermodynamics to derive the EL equations in equivalent  $Q_{\alpha\beta}$  tensor form. DeGennes studied pretransitional phenomena thus only considered homogeneous terms of zeroth order in  $Q_{\alpha\beta}$ . Imura [65] used the methods in [35] to find the temperature dependence of the Leslie viscosities to second order in  $Q_{\alpha\beta}$  and in doing so finds eight ‘weakly’ temperature dependent uniaxial viscosities arise (a fact that repeatedly arises in subsequent works). This highlights the fact that when using  $Q_{\alpha\beta}$  tensor theories the phenomenological linear expansion never converges as it does for a linear expansion in terms of  $\hat{n}_\alpha$  as the variable (unit vector properties), thus the EL theory has a maximum of five viscosities.

Later Hess [66] and Olmsted [67] re-derived these equations explicitly in their studies of shear ordering on phase transitions of homogeneous alignments, also generalised by [68] to include non-homogeneous variations. These however failed to recover the full anisotropy in viscosities predicted in the EL theory (arguably there is no need if only considering the phase transition where  $Q_{\alpha\beta} \rightarrow 0$ ). Further works by Hess [69, 70] recovered the complete anisotropy but failed to give fully independent coefficients. Qian [40] later stated an expansion retaining the full independence and anisotropy of the EL viscosities.

From a different stand using the molecular ODF and the Fokker-Planck equation with some closure and microscopic approximations works [71, 72, 73] have described the homogeneous evolution in terms of  $Q_{\alpha\beta}$  for fixed flows of LC polymers. Tsuji [74] allowed for a spatially varying orientation in this setting.

Other settings have been established by Beris [42] using Hamiltonian formulation and Poisson brackets or Pleiner [75] or Doi [76] developing methods appropriate for Lyotropic low molecular weight LC’s. Sonnet [53] provided a nice framework from a Rayleigh dissipation function from within which it is possible to establish many of the afore-mentioned formulations.

For works in this thesis simulations are carried out well into the nematic phase and we use the  $Q_{\alpha\beta}$  tensor equations as first stated in full by Qian [40] allowing for the simulation of thermotropic LC’s whilst retaining the five independent EL

viscosities. This latter point we believe to be important considering the lack of an experimentally verified microscopic theory to connect the viscosities and the vast array of materials.

### 2.4.1 Dynamic Equations

The governing momentum and order evolution equations for isothermal, incompressible ( $\partial_\gamma u_\gamma = 0$ ) nemato-dynamics in the limit of weak velocities are [40]:

$$\rho \dot{u}_\alpha = \partial_\beta (-P \delta_{\alpha\beta} + \sigma_{\alpha\beta}^v + \sigma_{\alpha\beta}^d + \sigma_{\alpha\beta}^{EM}) \quad (2.43)$$

$$J \ddot{Q}_{\alpha\beta} = h_{\alpha\beta}^B + h_{\alpha\beta}^v - \lambda^B \delta_{\alpha\beta} - \varepsilon_{\alpha\beta\gamma} \lambda_\gamma^B \quad (2.44)$$

Here the local variables are  $\rho$  the liquid crystal density,  $\underline{u}$  the fluid velocity,  $P$  the pressure,  $J$  the moment of inertia,  $\lambda^B$  and  $\lambda_\gamma^B$  are Lagrange multipliers as introduced in § 2.2.  $\sigma_{\alpha\beta}^d$  and  $h_{\alpha\beta}^B$  are called the distortion stress and bulk molecular field respectively defined from a system free energy,  $F$ , via perturbation and variational calculus methods:

$$\sigma_{\alpha\beta}^d = -\frac{\partial F}{\partial(\partial_\alpha Q_{\mu\nu})} \partial_\beta Q_{\mu\nu} \quad (2.45)$$

$$h_{\alpha\beta}^B = -\frac{\partial F}{\partial Q_{\alpha\beta}} + \partial_\gamma \frac{\partial F}{\partial(\partial_\gamma Q_{\alpha\beta})} \quad (2.46)$$

$\sigma_{\alpha\beta}^v$  and  $h_{\alpha\beta}^v$  are the viscous stress tensor and viscous molecular field defined from standard irreversible thermodynamic principles, they are:

$$\begin{aligned} \sigma_{\alpha\beta}^v = & \beta_1 Q_{\alpha\beta} Q_{\mu\nu} A_{\mu\nu} + \beta_4 A_{\alpha\beta} + \beta_5 Q_{\alpha\mu} A_{\mu\beta} + \beta_6 Q_{\beta\mu} A_{\mu\alpha} \\ & + \frac{\mu_2 N_{\alpha\beta}}{2} - \mu_1 Q_{\alpha\mu} N_{\mu\beta} + \mu_1 Q_{\beta\mu} N_{\mu\alpha} \end{aligned} \quad (2.47)$$

$$h_{\alpha\beta}^v = -\frac{\mu_2 A_{\alpha\beta}}{2} - \mu_1 N_{\alpha\beta} \quad (2.48)$$

Here  $\beta_i, \mu_i$  are equivalent to the EL viscosities with ‘weak’ temperature dependence,  $N_{\alpha\beta}$  is the co-rotational derivative:  $N_{\alpha\beta} = \dot{Q}_{\alpha\beta} - \varepsilon_{\alpha\mu\nu} \omega_\mu Q_{\nu\beta} - \varepsilon_{\beta\mu\nu} \omega_\mu Q_{\alpha\nu}$ .  $A_{\alpha\beta} = \frac{1}{2} (\partial_\alpha u_\beta + \partial_\beta u_\alpha)$  and  $W_{\alpha\beta} = \frac{1}{2} (\partial_\alpha u_\beta - \partial_\beta u_\alpha)$  are the symmetric and anti-symmetric velocity gradient tensors with the vorticity being  $\omega_\gamma = \frac{1}{2} \varepsilon_{\gamma\alpha\beta} W_{\alpha\beta}$ . Terms  $\sigma_{\alpha\beta}^v, h_{\alpha\beta}^v$  are the irreversible component forces and terms  $A_{\alpha\beta}, N_{\alpha\beta}$  conjugate reversible component fluxes. This leaves  $\sigma_{\alpha\beta}^{EM}$  to be defined as the imposed electrostatic stress from externally applied electro-magnetic fields [77]:

$$\sigma_{\alpha\beta}^{EM} = \frac{1}{2} (H_\alpha B_\beta + H_\beta B_\alpha) - \frac{H_\gamma B_\gamma}{2} \delta_{\alpha\beta} + \frac{1}{2} (E_\alpha D_\beta + E_\beta D_\alpha) - \frac{E_\gamma D_\gamma}{2} \delta_{\alpha\beta} \quad (2.49)$$

where  $\mathbf{E}$  ( $\mathbf{H}$ ) is the electric (magnetic) field strength,  $\mathbf{D}$  the electric displacement vector and  $\mathbf{B}$  the magnetic flux density.

Equations 2.43-2.49 together with the free energies of § 2.1 describe the dynamic behaviour of nematic LC's. Equation 2.46 can be seen to be similar, minus the Lagrange multipliers, to equation 2.40: it is the minimisation of the system free energy. Indeed if in equation 2.44 it is set that  $J = 0$  and  $u_\alpha = 0$ , (approximations not too unjust in some circumstances) equation 2.40 is recovered with a simple time derivative on the left hand side. In this approximation the orientation dynamics are purely relaxational and form a type of time dependent Euler model [78].

Inserting the uniaxial constant order equation 2.8 into the governing equations as done in §2.1 yields after plenty of algebra the EL equations of motion (see appendix B) from which we identify the Leslie viscosities as:

$$\begin{aligned} \alpha_1 &= \frac{9\beta_1 S_0^2}{4} & \alpha_2 &= \frac{3\mu_2 S_0}{4} - \frac{9\mu_1 S_0^2}{4} & \alpha_3 &= \frac{3\mu_2 S_0}{4} + \frac{9\mu_1 S_0^2}{4} \\ \alpha_4 &= \beta_4 - \frac{\beta_5 S_0}{2} - \frac{\beta_6 S_0}{2} & \alpha_5 &= \frac{3S_0 \beta_5}{2} = \frac{3S_0}{4} (\beta_5 + \beta_6 - \mu_2) & & \\ \alpha_6 &= \frac{3S_0 \beta_6}{2} = \frac{3S_0}{4} (\beta_5 + \beta_6 + \mu_2) & \gamma_1 &= \frac{9S_0^2 \mu_1}{2} & \gamma_2 &= \frac{3S_0 \mu_2}{2} \end{aligned} \quad (2.50)$$

To complete the dynamic equations of any problem boundary conditions are required. As standard in fluid dynamics the velocity conditions imposed is the so called 'non slip' boundary in which the fluid velocity at any stationary boundary is zero. For the LC alignment, realising situations of weak anchoring in which the surface alignment can vary significantly a surface evolution equation was suggested [79] and has been used by several authors [80, 81] in the EL theory. Extending this boundary condition to a  $Q_{\alpha\beta}$  tensor theory is straight forward.

$$\mu_s \partial_t Q_{\alpha\beta} = h_{\alpha\beta}^S - \lambda^S \delta_{\alpha\beta} - \varepsilon_{\alpha\beta\gamma} \lambda_\gamma^S \quad (2.51)$$

here  $h_{\alpha\beta}^S = -\hat{\nu}_\gamma \frac{\partial F}{\partial(\partial_\gamma Q_{\alpha\beta})} - \frac{\partial F_S}{\partial Q_{\alpha\beta}}$  is a surface molecular field and the four  $\lambda^S$ ,  $\lambda_\gamma^S$  are surface Lagrange multipliers ensuring the tensor symmetries.  $\mu_S = \frac{2\gamma_S}{9S_0^2}$  is dubbed the surface viscosity commonly defined as the bulk rotational viscosity times a characteristic surface length ( $l$ ),  $\mu_S = \mu_1 l$ . Measured values for  $\gamma_S$  are few but it is generally believed [82]  $l$  lies in the range  $10^{-8}$  to  $10^{-6}$  m. The surface viscosity of equation 2.51 is seen to alter the time derivative and thus may be thought of as a rate at which the surface will relax to equilibrium.

## 2.4.2 Time and Length Scales

In numerical studies it is of up-most importance to take into consideration the correct time and length scales of the problem at hand in order to calculate correct spatial and temporal variations of the relevant fields. A standard non-dimensionalisation of the governing equations of the previous sections yields three key dimensionless numbers; the Reynolds, Ericksen and Deborah numbers defined:

$$Re = \frac{\rho \bar{U} \bar{L}}{\eta_{eff}} \sim 10^{-7} \quad (2.52)$$

$$Er = \frac{\mu_1 \bar{U} \bar{L}}{L_1} \sim 10^{-2} \quad (2.53)$$

$$De = \frac{\mu_1 \bar{U}}{\alpha_F \bar{L}} \sim 10^{-7} \quad (2.54)$$

where  $\eta_{eff} = \frac{1}{2}(\beta_4 - \frac{\mu_2^2}{4\mu_1})$ ,  $\bar{U}$ ,  $\bar{L}$  are characteristic velocity and lengths of the situation. Using typical values of weakly perturbed LCD materials:  $\bar{L} \sim 10^{-6}$  m,  $\bar{U} \sim 10^{-6}$  m s<sup>-1</sup>,  $\mu_1 \sim \eta_{eff} \sim 10^{-2}$  kg m<sup>-1</sup> s<sup>-1</sup>,  $\alpha_F \sim 10^5$  kg m<sup>-1</sup> s<sup>-2</sup>,  $L_1 \sim 10^{-12}$  kg m s<sup>-2</sup>,  $\rho \sim 10^3$  kg m<sup>-3</sup>, these numbers can be estimated. (Note the length of the flow, director and order are not necessarily the same.) The  $Re$  number gives the ratio of the inertial to viscous forces, the  $Er$  number the ratio of viscous to elastic forces and  $De$  number the ratio of relaxation to observational times - indicative of the materials solidity. From the law of similarity, provided the dimensionless numbers of one system match that of another the results can be compared.

Extracting the characteristic time scales for variation in these quantities gives:

$$\bar{\tau}_P = \frac{\rho \bar{L}^2}{\eta_{eff}} \sim 10^{-7} \text{s} \quad (2.55)$$

$$\bar{\tau}_n = \frac{\mu_1 \bar{L}^2}{L_1} \sim 10^{-2} \text{s} \quad (2.56)$$

$$\bar{\tau}_S = \frac{\mu_1}{\alpha_F} \sim 10^{-7} \text{s} \quad (2.57)$$

Thus we observe that the relaxation rate of the momentum compared to the director is much quicker, as is the relaxation rate of the order compared to the director. Examination of the characteristic time ratio  $\bar{\tau}_P/\bar{\tau}_n \sim 10^{-5}$  shows it to be small and thus the velocity field is adapted quickly to a given director field and its time derivative. This often leads to the non-linear and partial time derivative on the left hand side of equation 2.43 being dropped and solving for its steady state value at any given time in equation 2.44.

Examining the characteristic time ratio  $\bar{\tau}_S/\bar{\tau}_n \sim 10^{-5}$  also shows to be small so that the order parameter field is adapted quickly to a given director field and its time derivative. This means for simulation of quantitative defect dynamics an explicit order and director field time scale separation should be done in which equation 2.44 is split, the order for a given director field being given by its steady state value [40]:

$$\frac{3}{2}\mu_1\dot{S} = -\frac{\partial F}{\partial S} + \partial \left( \frac{\partial F}{\partial_\lambda \partial S} \right) \quad (2.58)$$

However as the ratio  $\bar{\tau}_P/\bar{\tau}_S \sim 1$  both time derivatives of equation 2.58 and equation 2.43 are seen to be required.

For work in this thesis, as a second approximation (the first being EL theory), we omit the time scale involving order variation. The dynamic effects of this approximation to both equation 2.43 and equation 2.44 is hoped to be pursued in future studies. As will be seen in § 4.2.4 the order parameter tends to its equilibrium value in relatively few algorithmic time steps  $O(10)$  and since the viscous forces upon  $S$  are  $10^7$  times smaller than temperature and elastic forces we can expect simulations to be dynamically qualitatively correct. To the authors knowledge no numerical treatments of the time dependence of the order parameters have been covered in the literature. It is though, quite common to study the time dependent Euler model in which  $S$  and  $\hat{n}$  are treated with no separation.

Simulations are generally constrained in size in terms of resolution. This is usually determined from the smallest characteristic length in the simulation. In LC's this smallest length can be determined by considering an approximate free energy consisting of elastic and temperature energies:

$$F = F_0 + \frac{L_1}{2}\partial_\mu Q_{\nu\gamma}\partial_\mu Q_{\nu\gamma} + \frac{\alpha_F}{2}(Q_{\alpha\beta})^2 - \beta_F Q_{\alpha\beta}Q_{\beta\gamma}Q_{\gamma\alpha} + \gamma_F(Q_{\alpha\beta}Q_{\beta\alpha})^2 \quad (2.59)$$

In the uniaxial approximation (equation 2.8) the Euler-Lagrange equation for  $S$ , putting  $\nabla n$  to zero is:

$$\frac{3L_1}{2}\nabla^2 S - \frac{\partial F}{\partial S} = 0 \quad (2.60)$$

Linearising this for small deviations from equilibrium,  $S(\underline{x}) = S_b + \Delta S(\underline{x})$  and retaining only lowest order terms gives:

$$\nabla^2 \Delta S - \frac{2}{3L_1} \frac{\partial^2 F}{\partial S^2} \Big|_{S_b} \Delta S = 0 \quad (2.61)$$

solving the resultant ODE yields the general form  $\Delta S(\underline{x}) = Ae^{-\underline{x}/\xi}$  where  $A$  is a constant set by boundary conditions and  $\xi$  the characteristic length variation of the order given by:

$$\xi = \sqrt{\frac{3L_1}{2 \left. \frac{\partial^2 F}{\partial S^2} \right|_{S_b}}} = \sqrt{\frac{L_1}{\alpha_F - 3\beta_F S_b + 18\gamma_F S_b^2}} = \sqrt{\frac{L_1}{\frac{4}{3}a(T - T^*) - 3\beta_F S_b + 18\gamma_F S_b^2}} \quad (2.62)$$

which provided  $\xi$  is greater than the molecular dimension the continuum theory holds. (Note  $\xi$  grows as  $T$  increases (as does  $\bar{\tau}_S$ ) and for parameters quoted in [40]  $\xi \sim 1\text{nm}$ .)

# Chapter 3

## Lattice Boltzmann Methods Background

This chapter aims to introduce the lattice Boltzmann method (LBM), the technique we will utilise in chapter 4 to solve the equations of motion for liquid crystal dynamics seen in chapter 2, and then subsequently apply to situations of current interest.

### 3.1 Introduction to the LBM

In the last fifteen years or so there has been much progress in developing the LBM ([83, 84, 85, 86]) as an alternative, computational technique for solving complex fluid dynamic systems [87, 88]. It was originally developed from the lattice gas automata (LGA) methods [89] c.f. § 3.2.1. Adopting the macroscopic method for computational fluid dynamics (CFD), the macroscopic variables of interest, namely the velocity  $\underline{u}$  and pressure  $P$ , are usually obtained by solving the Navier-Stokes (NS) equations [90, 91]. In the LBM approach we solve the kinetic equation for the particle distribution function  $f(\underline{x}, \underline{\xi}, t)$  where  $\underline{\xi}$  is the particle velocity and  $\underline{x}$  the spatial position and  $t$  is the time. The macroscopic quantities such as the mass density  $\rho$  and momentum  $\rho\underline{u}$  can then be obtained by evaluating the hydrodynamic moments of the distribution function  $f$ . This approach was first adopted by Frisch [92] with the additional theoretical foundations established in later papers by most notably McNamara [83], Higuera [84], Koelman [87], and Qian [86].

The popular kinetic model adopted in the LBM literature is based on the single relaxation time (SRT) approximation called the Bhatnagar-Gross-Krook [93] (BGK)

model:

$$\partial_t f + \xi_\alpha \partial_\alpha f = -\frac{1}{\lambda} (f - f^{(eq)}) \quad (3.1)$$

where  $f^{(eq)}$  is an equilibrium distribution function, the Maxwell-Boltzmann distribution function, and  $\lambda$  is the relaxation time ( $\lambda \ll 1$ ) with a corresponding viscosity  $\nu = \lambda RT$  in which  $R$  is the gas constant and  $T$  the temperature.

In solving equation 3.1 for  $f$  in the LBM we must first discretise the velocity space using a set of finite velocities  $\underline{\xi}_i$  without affecting the conservation laws [88, 94]:

$$\partial_t f_i + \xi_{i,\alpha} \partial_\alpha f_i = -\frac{1}{\lambda} (f_i - f_i^{(eq)}) \quad (3.2)$$

Here  $f_i(\underline{x}, t) \equiv f(\underline{x}, \underline{\xi}_i, t)$  is the distribution function associated with the  $i^{\text{th}}$  velocity vector  $\underline{\xi}_i$  and  $f_i^{(eq)}$  is its corresponding equilibrium distribution function. In practice the two dimensional nine velocity square lattice model [86] (D2Q9 see figure 3.1) has been successfully used for simulation of 2D flows. In this D2Q9 model  $\underline{e}_i$  is used to denote the discrete velocity set:

$$\left. \begin{aligned} e_{i\alpha} &= (0, 0) , & i &= 0 \\ e_{i\alpha} &= c \left[ \cos \left( \frac{(i-1)\pi}{2} \right) , \sin \left( \frac{(i-1)\pi}{2} \right) \right] , & i &= 1, 2, 3, 4 \\ e_{i\alpha} &= \sqrt{2}c \left[ \cos \left( \frac{(i-1)\pi}{2} + \frac{\pi}{4} \right) , \sin \left( \frac{(i-1)\pi}{2} + \frac{\pi}{4} \right) \right] , & i &= 5, 6, 7, 8 \end{aligned} \right\} \quad (3.3)$$

where  $c = \Delta x / \Delta t$ , and  $\Delta x$  and  $\Delta t$  are the lattice unit constant space and time

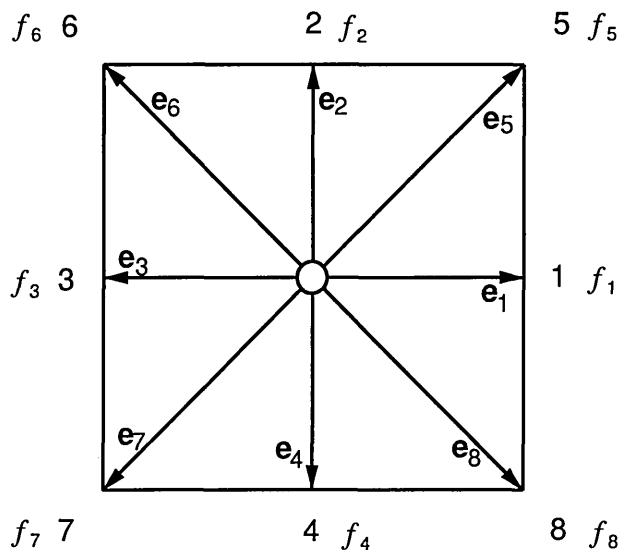


Figure 3.1: The 2-D 9-velocity (D2Q9) model. A regular repeating structure with nine distributions located at each node.

steps respectively. The equilibrium distribution function takes the form:

$$f_i^{(eq)} = \rho t_i \left( 1 + \frac{e_{i\alpha} u_\alpha}{c_s^2} + \frac{(e_{i\alpha} u_\alpha)^2}{2c_s^4} - \frac{u_\alpha u_\alpha}{2c_s^2} \right) \quad (3.4)$$

where for the D2Q9 model  $t_i$  are weighting factors and  $c_s$  is the speed of sound, these given by:

$$\left. \begin{aligned} t_i &= 4/9, & i &= 0 \\ t_i &= 1/9, & i &= 1, 2, 3, 4 \\ t_i &= 1/36, & i &= 5, 6, 7, 8 \\ c_s &= 1/\sqrt{3} \end{aligned} \right\} \quad (3.5)$$

With the discretised velocity space, the density and momentum can be evaluated as:

$$\left. \begin{aligned} \rho(\underline{x}, t) &= \sum_{i=0}^8 f_i(\underline{x}, t) \\ \rho u_\alpha(\underline{x}, t) &= \sum_{i=0}^8 f_i(\underline{x}, t) e_{i\alpha} \end{aligned} \right\} \quad (3.6)$$

and the equation of state is that of the ideal gas:

$$P = \rho(\underline{x}, t) c_s^2 \quad (3.7)$$

Qian [86] and Luo [94] report many other types of lattices used in simulating 1-D, 2-D and 3-D flows all with  $f_i^{(eq)}$  given as in equation 3.4 but with different lattice weights (equation 3.5) which are dependent of the lattice velocity vectors. Some example lattices are given in table 3.1.

Model	Unit cell	$t_0$ 0	$t_1$ 1	$t_2$ $\sqrt{2}$	$t_3$ $\sqrt{3}$	$t_4$ 2	$c_s^2$	Order of Isotropy
D1Q3	line	$\frac{2}{3}$	$\frac{1}{6}$	0	0	0	$\frac{1}{3}$	4
D1Q5	line	$\frac{1}{2}$	$\frac{1}{6}$	0	0	$\frac{1}{12}$	1	6
D2Q7	hexagonal	$\frac{1}{2}$	$\frac{1}{12}$	0	0	0	$\frac{1}{4}$	4
D2Q9	square	$\frac{4}{9}$	$\frac{1}{9}$	$\frac{1}{36}$	0	0	$\frac{1}{3}$	4
D2Q13	hexagonal	$\frac{11}{25}$	$\frac{9}{100}$	0	$\frac{1}{300}$	0	$\frac{3}{10}$	6
D3Q15	cubic	$\frac{2}{9}$	$\frac{1}{9}$	0	$\frac{1}{72}$	0	$\frac{1}{3}$	4
D3Q19	cubic	$\frac{1}{3}$	$\frac{1}{18}$	$\frac{1}{36}$	0	0	$\frac{1}{3}$	4
D3Q27	cubic	$\frac{8}{27}$	$\frac{2}{27}$	$\frac{1}{54}$	$\frac{1}{216}$	0	$\frac{1}{3}$	4

Table 3.1: LBGK lattice parameters for a selection of commonly used models indicating the lattice shape, velocity directions and equilibrium distribution weights.

Equation 3.2 is known as the discrete velocity model (DVM) first being introduced by Broadwell [95, 96]. Developments of and studies with the DVM can be found in [97, 98, 99]. Numerically this model can be solved using a discretised

form. By applying a first order finite difference scheme in time, the first order upwind discretisation for the convective term, equation 3.2 is thus:

$$f_i(\underline{x} + \underline{e}_i \delta t, t + \delta t) - f_i(\underline{x}, t) = -\frac{1}{\tau} \left( f_i(\underline{x}, t) - f_i^{(eq)}(\underline{x}, t) \right) \quad (3.8)$$

with time step  $\Delta t$  and space step  $\underline{e}_i \Delta t$  ( $\underline{e}_i \Delta t / \Delta x = 1$ ),  $\underline{x}$  a point in discretised space and where  $\tau = \lambda / \Delta t$ . This is the discrete LB equation with BGK approximation, and is commonly solved in two stages of ‘collision’ :

$$\tilde{f}_i(\underline{x}, t + \delta t) = f_i(\underline{x}, t) - \frac{1}{\tau} \left( f_i(\underline{x}, t) - f_i^{(eq)}(\underline{x}, t) \right) \quad (3.9)$$

(the  $\tilde{\phantom{f}}$  denotes a post collision state) and ‘streaming’:

$$\tilde{f}_i(\underline{x} + \underline{e}_i \Delta t, t + \Delta t) = \tilde{f}_i(\underline{x}, t + \Delta t) \quad (3.10)$$

Splitting the computation in this manner eliminates the need to store both  $f_i(\underline{x}, t + \delta t)$  and  $f_i(\underline{x}, t)$  during the calculations: information at one time level is sufficient in the computation of non-equilibrium systems.

In order to derive the NS equations from the LBM a Chapman-Enskog expansion [100] is used. This may be viewed as a standard multi-scale expansion [101] in smallness of the parameters time and space. The perturbative expansion parameter being the Knudsen number ( $Kn$ ) which is the ratio between molecular mean free path and the shortest scale at which macroscopic variations can be appreciated:  $\varepsilon \equiv Kn = l_{mfp} / l_m \ll 1$ . The particle distribution function,  $f_i$ , is expanded as:

$$f_i = \sum_{n=0}^{\infty} \varepsilon^n f_i^{(n)} \quad (3.11)$$

where  $n = 0$  denotes local equilibrium and  $n > 0$  represents departures from this equilibrium. The space-time expansion is crucial to the multi-scale method. These are expanded in a hierarchy of slow-fast scales such that each variable is  $O(1)$  at that scale:

$$\left. \begin{array}{ll} t_1 = \varepsilon t & t_2 = \varepsilon^2 t \\ x_1 = \varepsilon x & x_2 = \varepsilon^2 x \end{array} \right\} \quad (3.12)$$

Here  $x_1, t_1$  are linear regimes (sound wave) and  $x_2, t_2$  are the longer dissipative modes. The corresponding differential operators are:

$$\left. \begin{array}{l} \partial_\alpha = \varepsilon \partial_{\alpha_1} + \varepsilon^2 \partial_{\alpha_2} \\ \partial_t = \varepsilon \partial_{t_1} + \varepsilon^2 \partial_{t_2} \end{array} \right\} \quad (3.13)$$

An example in using this expansion is shown in chapter 4.

In the incompressible flow limit in which the Mach number,  $Ma = |\underline{u}|/c_s \ll 1$  the expansion leads to the mass and momentum conservation equations (continuity and NS):

$$\partial_\alpha u_\alpha = 0 \quad (3.14)$$

$$\partial_t u_\alpha + u_\beta \partial_\beta u_\alpha = -\frac{1}{\rho} \partial_\alpha P + \nu \partial_\beta \partial_\beta u_\alpha \quad (3.15)$$

with the corresponding viscosity in the NS equation 3.15 derived as [86]:

$$\nu = \frac{c_s^2}{2} (2\tau - 1) \Delta t \quad (3.16)$$

The modified viscosity from  $\nu = \lambda c_s^2$  in equation 3.1 corrects for the truncation error in the discretisation of equation 3.2 and makes the LBGK scheme formally a second order method for solving incompressible flows at small  $Re$  number [94]. The lattice viscosity is thus changed via  $\tau$  in which stability requires  $0 < 1/\tau \leq 2$  (positive viscosity). The pressure is obtained from the equation of state equation 3.7.

The collision step of the LBM, equation 3.9, should be noted as completely local and the streaming step, equation 3.10, involves no computation just a streaming of particle distributions. The LBM is thus seen to be easy to implement and straight forwardly amenable to efficient parallelisation on many computer processors.

The LBM can be viewed as an alternative computational technique to solve the NS equations but the method differs from traditional CFD NS techniques in many aspects [102]. The NS equations are second order partial differential equations (PDEs) whereas the DVM, from which the LBM is derived, is a set of first order PDEs. This is notable by which the equations are discretised. The CFD NS solvers have to treat the nonlinear ( $u_\beta \partial_\beta u_\alpha$ ) convective term where the LBM avoids this convective term because the convection is done via advection (streaming step). The CFD NS solvers need to solve the Poisson equation for the pressure field at every given time over the entire system whereas in the LBM the pressure is locally obtained by the equation of state. In the LBM the Courant-Friedrichs-Lewy (CFL) number [103] is proportional to  $\Delta t/\Delta x$  for which in LBM is a fixed unity ( $\Delta x = \Delta t = 1$ ) thus the time dependent LBM is inefficient for solving steady state problems. The LBM depends on grid structures but for CFD solvers of NS, which

may take integral of differential forms, are in vector forms that are independent on the coordinates of the grid.

As for all computational problems the boundary condition can be the single most important problem especially in complex geometries and complex fluids. For CFD NS solvers normal and shear stress components are required to be calculated at the normal and tangent of a complex surface which utilise one-sided extrapolations. For the LBM solvers boundary issues arise as there is no non-slip counter part to the continuum level on the scale  $f_i$ . As the LBM is a kinetics based approach, physics associated with the molecular level of interaction can be incorporated into the model, thus LBM is a mesoscale technique. The spatial discretisation of the LB equation is governed by the particle velocity discretisation, this coupling of velocity space to configuration space gives rise to regularly shaped triangular or square grids. This in turn limits the LBM when considering boundary conditions of complex arbitrary smooth shapes that in a near field require small grids dealing with high  $Re$  flows but in the far field may not necessarily require such a small grid.

These features of the LBM have led to its successful use in simulating fluid flows involving complicated boundaries and complex fluids such as flows over structures with complicated geometry [104], Rayleigh Taylor instability between two fluids [105], multicomponent flow through porous media [106], particles suspended in fluids [107, 108], chemically reacting flows [109], combustions [110], magnetohydrodynamics [111], crystallisation [112], and others [87].

Efforts to extend the use of the LBM to all the above said flows and others are actively being studied. Work to extend the LBM to higher  $Re$  numbers flows near the turbulence regime hope to better solve fluid engineering problems. From this several coupled issues to the higher  $Re$  number flows arise. Recurrent issues for all these types of flows arise, namely those of boundaries, grid resolutions and numerical stability. We will proceed to briefly review works in these areas.

## **Boundary Conditions**

There are two classes of boundaries in fluid dynamics, open boundaries and solid boundaries. Open boundaries are lines or planes of symmetry, periodicity, infinity, and inlets/outlets; the closed boundaries are solid walls. For CFD solvers the

macroscopic velocity and pressure are usually enough to fix fluid flows. Conversely in the LBM no boundary condition for the particle distributions  $f_i$  is known. The  $f_i$  must be suitably constructed based upon macroscopic flow variables. For symmetry and periodic boundaries this is not an issue and outlets can usually be given by extrapolation given simple enough geometry.

This issue is highlighted in figure 3.2. After a collision step  $\tilde{f}_i(\underline{x}_f)$  at node  $\underline{x}_f$ , on the fluid side is known for all  $i$  but  $\tilde{f}_i(\underline{x}_b)$ , the post-collision distribution function coming from the solid node  $\underline{x}_b$  to the fluid node  $\underline{x}_f$  is not known (here a  $\tilde{}$  upon an  $i$  represents reversed velocity link  $\underline{e}_{\tilde{i}} = -\underline{e}_i$ ). In order to complete the streaming step  $\tilde{f}_i(\underline{x}_b, t)$  is needed to give exactly  $f_i(\underline{x}_f, t + \delta t)$  post streaming.

Popularly and efficiently the bounce back scheme [113, 114] is used from the LGA methods: that is the momentum of an incoming distribution  $\tilde{f}_i(\underline{x}_f, t)$  is bounced back in the opposite direction after it hits the wall:  $\tilde{f}_{\tilde{i}}(\underline{x}_b, t) = \tilde{f}_i(\underline{x}_f, t)$  and if the wall is moving an additional momentum should be added:

$$\tilde{f}_{\tilde{i}}(\underline{x}_b, t) = \tilde{f}_i(\underline{x}_f, t) + \frac{2t_i \rho^w \underline{e}_i \cdot \underline{u}^w}{c_s^2} \quad (3.17)$$

were the superscript  $w$  indicates value at the wall. Ladd [115] showed second order accuracy for the non-slip boundary condition if the wall is placed in the middle of nodes, in other words  $\Delta \equiv \frac{|\underline{x}_f - \underline{x}_w|}{|\underline{x}_f - \underline{x}_b|} = \frac{1}{2}$  and the wall is a straight line. (BBL scheme.)

For arbitrary geometries and smooth curved boundaries more accurate treatments are needed to achieve second order accuracy. Bouzidi [116] presented a simple and efficient boundary condition based on bounce back of any arbitrary position

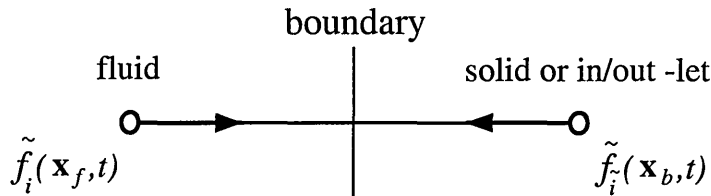


Figure 3.2: Known distributions at node  $x_f$  and unknown distributions at node  $x_b$ . The Bounce Back boundary condition that gives  $\tilde{f}_{\tilde{i}}(\underline{x}_b, t) = \tilde{f}_i(\underline{x}_f, t)$ , where  $\tilde{}$  denotes post-collision value.

(BBC). Using the Lagrange polynomial:

$$y(x) = \sum_{k=1}^n \left[ \prod_{\substack{j=1 \\ k \neq j}}^n \frac{(x - x_j)}{(x_k - x_j)} \right] \cdot y_k \quad (3.18)$$

he interpolates the appropriate  $f_i$ . Using the parameters defined in figure 3.3, to second order:

$$\left. \begin{aligned} \tilde{f}_i(\underline{x}_f, t) &= \Delta(1 + 2\Delta)\tilde{f}_i(\underline{x}_f, t) + \\ & (1 - 4\Delta^2)\tilde{f}_i(\underline{x}_f - \underline{e}_i\delta t, t) + \\ & \Delta(2\Delta - 1)\tilde{f}_i(\underline{x}_f - 2\underline{e}_i\delta t, t) + \frac{t_i\rho^w \underline{e}_i \cdot \underline{u}^w}{c_s^2} \quad , \quad 0 \leq \Delta \leq \frac{1}{2} \\ \tilde{f}_i(\underline{x}_f, t) &= \frac{1}{\Delta(1+2\Delta)}\tilde{f}_i(\underline{x}_f, t) + \\ & \frac{(2\Delta-1)}{\Delta}\tilde{f}_i(\underline{x}_f, t) + \\ & \left( \frac{1-2\Delta}{1+2\Delta} \right) \tilde{f}_i(\underline{x}_f - \underline{e}_i\delta t, t) + \frac{t_i\rho^w \underline{e}_i \cdot \underline{u}^w}{\Delta(2\Delta+1)c_s^2} \quad , \quad \frac{1}{2} \leq \Delta < 1 \end{aligned} \right\} \quad (3.19)$$

This reduces nicely to the original bounce back at the node (BBN) and bounce back at the link (BBL) schemes for  $\Delta = 0$  and  $\Delta = \frac{1}{2}$  respectively. This is often called continuous bounce back (BBC). They applied the method to channel flow over an array of cylinders reporting second order accuracy. It should be noted that the method treats the boundary differently dependent upon whether  $\Delta \leq \frac{1}{2}$  or  $\Delta > \frac{1}{2}$ .

For the work in this thesis on LC's and LCD's we need only consider enclosed systems that have boundaries of periodicity and solid walls, so equation 3.19 is

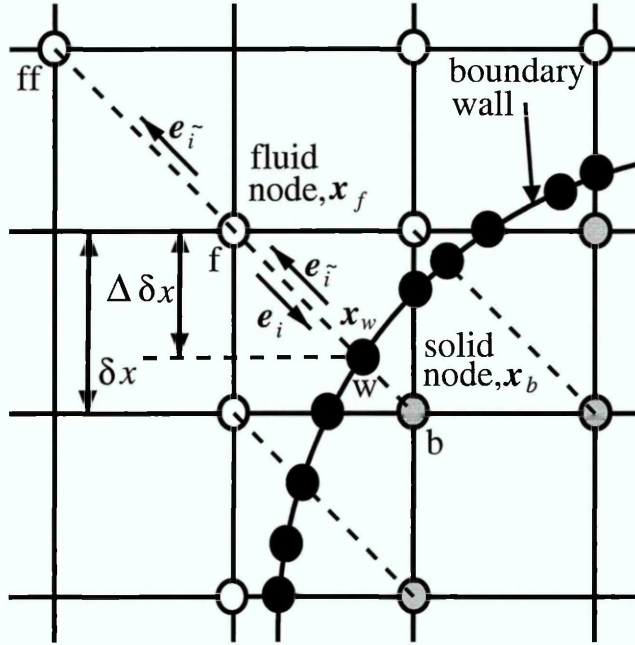


Figure 3.3: Layout of a D2Q9 lattice structure around a curved wall.

sufficient to close a simulation.

## Grid Resolution

The LBM was developed upon a constant grid size in contrast to CFD techniques that can allow grid stretching techniques to be used. In simulations often higher resolution is desirable in high gradient regions such as flow near a wall at moderate to high  $Re$ . In the LBM the grid is thus chosen to obey these regions. For regions of low gradient or far field calculations where such resolution is redundant the calculation becomes inefficient and resources can be wasted. In order to increase both the LBM efficiency and its accuracy it is desirable to introduce non-uniform grids.

Much work towards grid refinement has been done. He [117] solved the LBM on a non-uniform grid in which  $f_i$ 's were streamed to non-grid points and spatial interpolations used for streaming to grid points. Mei [118] solved the DVM in curvilinear coordinates with a finite difference formalism. Tolke [119] also solved the DVM but using adaptive grid refinements, and more recently adaptive grids for the LBGK method. Bouzidi [120] has presented LBM work upon a rectangular lattice in order to achieve arbitrary grid aspect ratio's. Peng [121] used an unstructured lattice with a finite volume scheme.

More notably and usefully in the LBM Filippova [122] worked on a local grid refinement method. For example a coarse grid with patches of fine grids were placed around a solid object (a cylinder in channel flow). Both grids were marched in time with the coarse grid acting as a boundary condition for the fine grids. In essence the method is based on continuity of variables across different gridded domains: viscosity, mass, momentum and stresses.

Yu [123] used the multi-block method in the LBM where each block has an 'interface' connection in which a similar rescaling of  $f_i$ 's is done, as in [122], supplemented by interpolations. This method was then tested in a lid driven cavity simulation showing particular improvement in the calculation of high pressure regions near the driven lid.

## Numerical Stability

For situations of high  $Re$  and sharp geometries, such as corners or obstacles, it is often found spatial oscillations in the pressure and velocity fields will occur in LBGK simulations. These have been termed instabilities and dispersion by Lallemand [124]. These instabilities can in part be attributed to the fact the LBGK method uses a SRT ( $\tau$ ). In contrast various multi-relaxation time (MRT) LB methods have been proposed by d’Humières [125] and Lallemand [124]. MRT methods also share their name with the generalised LB method in which the collision operator takes matrix form. The basic idea is in the SRT method the bulk and shear viscosity have fixed ratio ( $\eta = 3\zeta/2$ ), both determined by the  $\tau$  parameter. Oppositely the MRT method can relax different modes at different relaxation times. Consequently the bulk and shear viscosities may be adjusted independently.

In simulations it is common to generate small pressure waves due to initial conditions or singularities. For an independently increased bulk viscosity, it may help to damp out such waves thus increasing numerical stability of the solution and its convergence to steady state, particularly for simulations containing high gradients.

The MRT has undergone detailed analysis theoretically and numerically by Lallemand [124]. Mei [126] compared the SRT and MRT performances for flows of Stokes and flow over a cascade, they showed in the short time limit the MRT error is much smaller than the SRT but at the long times towards equilibrium there is no discernible differences. Further they found the need for high grid resolutions is lessened when using a MRT method.

## 3.2 Background to the LBM

Although the LBM can be derived in various ways it is instructive follow its development from earlier LGA methods.

### 3.2.1 Lattice Gas Automata

In the model by Broadwell [95, 96] the kinetic equation with discrete single particle speed was used to simulate flow induced from a shock wave. In the model both

time and space are continuous as given by equation 3.2. Hardy [89] proposed a fully discretised kinetic model on a square lattice by coupling the minimalistic boolean cellular automata lattice models introduced by Ulam and vonNeuman [127] with the kinetic equation. However due to a lack of isotropy of the lattice this model did not recover NS type behaviour. Frish, Hasslacher and Pomeau [92] (FHP) developed this 2-D kinetic model upon a hexagonal lattice (FHP model) which enforced the isotropy condition yielding for the first time NS behaviour and recovery of the NS equations.

In this LGA FHP model a two dimensional regular hexagonal unit cell lattice space is used, see figure 3.4. The lattice is then populated at each node and link by identical particles of unit mass, moving with the same speeds and at the same time. A particle presence is represented by a boolean variable 1 and an absent particle is represented by a boolean variable 0 ( $n_i(\underline{x}, t) \in i = 1 \dots b$ , where  $b$  is the number of possible particle velocities). No two particles may have the same identical velocity at a lattice node - an exclusion principle, so at most a lattice node can be simultaneously occupied by six particles. Due to the discrete space, time and velocity all particles momenta is such that particles hop from node to node in each time step. Minimalistic collision rules are then defined for symmetric binary and triple collisions that must conserve momentum and particle number (mass) as indicated in figure 3.4.

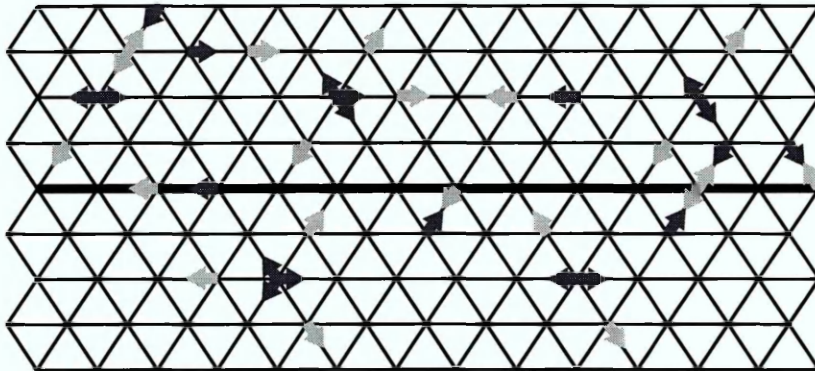


Figure 3.4: Simplified schematic of the FHP LGA model. Dark and light arrows represent particles with the velocities corresponding to time  $t$  and  $t + 1$  respectively. The thicker black line represents a boundary at which particle velocities are reversed.

The evolution equation of this LGA follows as

$$n_i(\underline{x} + \underline{e}_i, t + 1) - n_i(\underline{x}, t) = \Omega_i(n_i(\underline{x}, t)) \quad (3.20)$$

where  $\underline{e}_i$  are the particle velocities and  $\Omega_i$  a collision operator. It has two steps of ‘streaming’ particles to nearest neighbour nodes along its velocity direction  $i$  (left hand side of equation 3.20), then ‘collision’ where particles arriving at nodes collide with each other and change their velocity directions according to collision rules. The construction of the collision rules is crucial to the LGA in recovering NS behaviour.

To incorporate boundaries to the LGA model and impose the macroscopic non-slip condition particles of velocity  $\underline{e}_i$  arriving at a wall simply invert their velocity  $\overline{\underline{e}}_i$ , where the over bar denotes reversed velocity. The process is also depicted in figure 3.4 by the thick line indicating boundary. It keeps the simplistic computational Boolean collision rules of the main body of lattice sites. This process is called bounce back at the node (BBN).

Both advantages and disadvantages of the LGA scheme become plain. The evolution of the system is extremely simple. Only Boolean computations are needed. Interactions are localised and dictated by look up tables with unconditional stability. Dedicated parallelised machines can be designed for such an algorithm. However the smooth macroscopic variables need to be obtained by averaging [128] over vast numbers of nodes and over long times as the process produces statistical noise. This introduces further problems when looking at higher order physical quantities such as stress and vorticity that involve the derivatives of the macroscopic variables.

### 3.2.2 Developments of LGA to LBM

In going from the LGA to the LBM the Boolean variables,  $n_i(\underline{x}, t)$ , in the LGA were replaced by continuous floating point variables,  $f_i = \langle n_i \rangle$ , where  $\langle \rangle$  represents an ensemble average and  $f_i$  the momentum distribution function. In moving to the continuous  $f_i$  the collision rules had to be redefined, the discrete evolution equation now reading as

$$f_i(\underline{x} + \underline{e}_i \delta t, t + \delta t) - f_i(\underline{x}, t) = \Delta t \Omega_i(f_i(\underline{x}, t)) \quad (3.21)$$

where  $\Omega_i(f_i(\underline{x}, t))$  is now the collision operator representing the rate of change of  $f_i$  due to collisions,  $\Delta t$  is the time step and  $\underline{e}_i = \Delta x / \Delta t$ . The coordinates of the next nearest neighbour points of  $\underline{x}$  are given by  $\underline{x} + \underline{e}_i \Delta t$ . In equation 3.21 the collision operator is still localised and is a function of the lattice structure. The macroscopic variables of density and momentum are calculated from the moments of the particle distribution function, as in kinetic theory, as:

$$\rho(\underline{x}, t) = \sum_{i=0} f_i(\underline{x}, t), \quad \rho u_\alpha(\underline{x}, t) = \sum_{i=0} f_i(\underline{x}, t) e_{i\alpha} \quad (3.22)$$

where  $i$  ranges over all discrete velocity vectors. The collision operator must satisfy conservation laws of mass and momentum at each node:

$$\sum_{i=0} \Omega_i(\underline{x}, t) = 0, \quad \sum_{i=0} \Omega_i(\underline{x}, t) e_{i\alpha} = 0 \quad (3.23)$$

$\Delta t$  is physically very small, it is the actual time required for a particle move from one node to the next along  $\underline{e}_i$  and it is much smaller than the time scale characterising the variation of the physical macroscopic variables. A subsequent Taylor series expansion in space and time of equation 3.21 yields a continuous form of the kinetic equation accurate to second order in  $\Delta t$ :

$$\Delta t (\partial_t + c_{i\alpha} \partial_\alpha) f_i(\underline{x}, t) + \frac{\Delta t^2}{2} (\partial_t + c_{i\alpha} \partial_\alpha)^2 f_i(\underline{x}, t) + O(\Delta t^3) = \Delta t \Omega_i(f_i(\underline{x}, t)) \quad (3.24)$$

Interestingly keeping only first order in  $\Delta t$  terms is the kinetic Boltzmann equation. Assuming the particle distribution function is close to its equilibrium value state the  $f_i$  can be expanded as equation 3.11

$$f_i = \sum_{n=0}^{\infty} \varepsilon^n f_i^{(n)} = f_i^{(0)} + \varepsilon f_i^{(1)} + \varepsilon^2 f_i^{(2)} + O(\varepsilon^3) \quad (3.25)$$

where the equilibrium distribution function,  $f_i^{(eq)} = f_i^{(0)}$ , and the non-equilibrium distribution function  $f_i^{(neq)} = \sum_{n=1}^{\infty} f_i^{(n)}$  of which  $f_i^{(1)}$  is the leading order perturbation. Substitution of equation 3.25 at  $O(\varepsilon)$  into the collision operator  $\Omega_i(f_i)$  in equation 3.24 and then using a Taylor series expansion at linear order one gets:

$$\Omega_i(f_i) = \Omega_i(f_i^{(eq)}) + \sum_j \varepsilon \frac{\partial \Omega_i(f_i^{(eq)})}{\partial f_j} f_j^{(1)} + O(\varepsilon^2) \quad (3.26)$$

By definition a fluid in equilibrium is unaffected by collisions and thus  $\Omega_i(f_i^{(eq)}) = 0$ , this is equivalently stated through substituting equations 3.25 and 3.26 in equation 3.24. This then leads to:

$$\left. \begin{aligned} \Omega_i(f_i) &= \varepsilon \sum_j \frac{\partial \Omega_i}{\partial f_j} f_j^{(1)} &= \varepsilon \sum_j \frac{\partial \Omega_i}{\partial f_j} f_j^{(neq)} \\ &= \varepsilon \sum_j \frac{\partial \Omega_i}{\partial f_j} \left( f_j - f_j^{(eq)} \right) \\ &= \varepsilon \sum_j \Delta_{ij} \left( f_j - f_j^{(eq)} \right) \end{aligned} \right\} \quad (3.27)$$

where  $\Delta_{ij} \equiv \left. \frac{\partial \Omega_i}{\partial f_j} \right|_{f_i=f_i^{(eq)}}$  is the linearised collision matrix of coefficients [84].  $\Delta_{ij}$  may be defined [128] as cyclic and symmetric; the elements only dependent upon the angle between the directions  $e_{i\alpha}$  and  $e_{i\beta}$ ; the collision must conserve mass and momentum so that

$$\sum_{i=0} \Delta_{ij}(\underline{x}, t) = 0, \quad \sum_{i=0} \Delta_{ij}(\underline{x}, t) e_{i\alpha} = 0 \quad (3.28)$$

The linear collision matrix elements although obviously constrained are still not all fixed and may be changed to place the scheme in a stable regime that reduces, dampens, spurious quantities commonly referred to as ghost modes [129].

If we further assume that the local particle distributions relax to an equilibrium state with the same relaxation time  $\lambda$  it can be seen:

$$\Delta_{ij} = -\frac{1}{\lambda} \delta_{ij} \quad (3.29)$$

and subsequently the LBGK [93] collision is obtained:

$$f_i(\underline{x} + \underline{e}_i \Delta t, t + \Delta t) = f_i(\underline{x}, t) - \frac{1}{\tau} \left( f_i(\underline{x}, t) - f_i^{(eq)}(\underline{x}, t) \right) \quad (3.30)$$

This historical development of the LBM helps to paint a picture of how it operates with ‘particles’ moving around a lattice and can aid the understanding towards algorithm implementation.

## 3.3 Practical Issues in LBM Implementation

### 3.3.1 Stress Calculation

Fluid mechanics often requires the evaluation of stresses in a system. The NS stress tensor has pressure and velocity gradient terms:

$$\sigma_{\alpha\beta} = -P\delta_{\alpha\beta} + \rho\nu(\partial_\alpha u_\beta + \partial_\beta u_\alpha) \quad (3.31)$$

For CFD solvers this requires the use of one sided numerical gradient calculations at boundaries. Conversely in the LBM the local pressure simply has equation of state  $P = \rho c_s^2$  and the deviatoric stress  $\tau_{\alpha\beta} = \rho\nu(\partial_\alpha u_\beta + \partial_\beta u_\alpha)$  can be evaluated from the non-equilibrium part of the distribution function:

$$\tau_{\alpha\beta} = \left(1 - \frac{1}{2\tau}\right) \sum_i \left(f_i(\underline{x}, t) - f_i^{(eq)}(\underline{x}, t)\right) \left(e_{i\alpha}e_{i\beta} - \frac{1}{2}e_{i\gamma}e_{i\gamma}\delta_{\alpha\beta}\right) \quad (3.32)$$

Clearly equation 3.32 is local and thus better than any explicit gradient methods. For evaluating the force upon an object embedded in a fluid this is highly desirable however equation 3.32 is only valid at the lattice node, thus for complex curved objects one sided numerical techniques are still needed.

### 3.3.2 Body Forcing Flows

As an alternative to the open boundary pressure and velocity conditions, described in section. 3.1. It is very common in isothermal LBM simulations to combat the compressibility restrictions by emulating a pressure gradient through a body force. A uniform body force or acceleration  $\rho a_\alpha$  may be used to approximate the principle part of a pressure gradient. Such an acceleration arises in the LBM momentum evolution equation (equation 3.8) through an additional term  $F_i$  to the right hand side. The form of  $F_i$  can be obtained by considering the time derivative of the first moment of the equilibrium distribution function in the incompressible limit:  $\partial_t \sum_i e_{i\gamma} f_i^{(eq)} = \rho a_\gamma$ . This yields the moments:

$$\left. \begin{aligned} \sum_i F_i &= 0 \\ \sum_i F_i e_{i\gamma} &= \rho a_\gamma \\ \sum_i F_i e_{i\gamma} e_{i\delta} &= \rho (u_\gamma a_\delta + u_\delta a_\gamma) \end{aligned} \right\} \quad (3.33)$$

Though usually the second moment is assumed  $\sum_i F_i e_{i\gamma} e_{i\delta} = 0$ , leaving the forcing term  $F_i$  as:

$$F_i = \frac{\rho t_i e_{i\alpha} a_\alpha \Delta t}{c_s^2} \quad (3.34)$$

For any system without unidirectional flow, the pressure gradient cannot be uniform. In fact it must solve a Poisson type equation obtained by taking the divergence of the incompressible NS equation:

$$\partial_\beta \partial_\beta \left(\frac{P}{\rho}\right) = -\partial_\alpha u_\beta \partial_\beta u_\alpha + \partial_\alpha a_\alpha \quad (3.35)$$

The solution to which yields an instantaneous pressure for the given velocity distribution.

### 3.3.3 Lattice Gradients

The nice feature of the isotropic LB method is that no explicit gradient calculations are required, computation is local. Often in simulations it is required to know a local gradient or in the case of more complex fluids with structure, gradients in order are required. Explicit gradient calculations are now unavoidable and it is common to resort to standard numerical techniques and thus lose the purely local lattice calculations. Considering a Taylor expansion of a parameter,  $P(\underline{x})$ :

$$P(\underline{x} + \underline{e}_i \Delta t) = P(\underline{x}) + e_{i\alpha} \Delta t \partial_\alpha P(\underline{x}) + \frac{\Delta t^2}{2} e_{i\alpha} e_{i\beta} \partial_\alpha \partial_\beta P(\underline{x}) + \dots \quad (3.36)$$

Taking the zeroth and first moment of equation 3.36 whilst multiplying throughout by  $t_i$  and rearranging will yield second order expressions for the gradient:

$$\partial_\alpha P(\underline{x}) = \frac{\sum_i [t_i e_{i\alpha} P(\underline{x} + \underline{e}_i \Delta t)]}{c_s^2 \Delta t} \quad (3.37)$$

$$\partial_\alpha \partial_\alpha P(\underline{x}) = \frac{2(\sum_i [t_i P(\underline{x} + \underline{e}_i \Delta t)] - P(\underline{x}))}{c_s^2 \Delta t^2} \quad (3.38)$$

## 3.4 Example LBGK Study: Laminar flow over a backward facing step

LB methods have been validated against analytical, experimental and alternative numerical predictions of laminar flows. We here provide further validation for pressure-driven flows of an isotropic fluid over a backward facing step using two different LB methods. The backward facing step is one of the most fundamental geometries causing flow separation and has been extensively investigated in both laboratory [1, 130, 131] and as a standard bench mark test for numerical simulations [132]. This investigation considers the geometry originally proposed by Denham [1], see figure 3.5, which produces flow separation at the step and subsequent reattachment for a ratio of step height to downstream channel width of  $\frac{1}{3}$ . At this step ratio there exist two independent experimental investigations approximating two-dimensional flow [1, 131]. Other LB simulations originate with Qian [133] who investigated the relationship of the length of the recirculation zone and the step ratio with  $Re$ . Chen [134] gave a thorough quantitative comparison of LBGK simulation results with experimental data from Kueny [131]. Here we concentrate on a quantitative comparison with data from Denham [1].

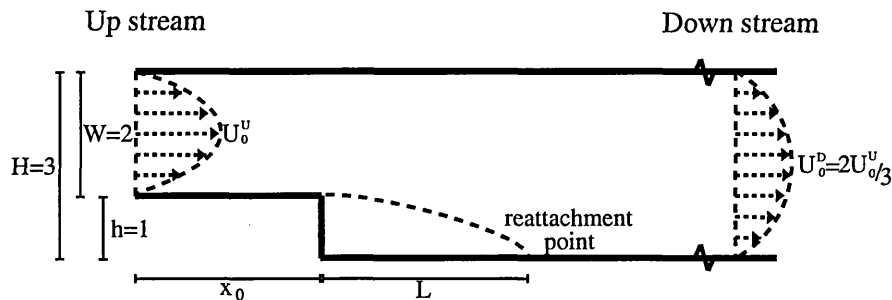


Figure 3.5: Two-dimensional geometry for a backward facing step in channel flow with a step ratio of  $1/3$ . Upstream and downstream of the step behave as Poiseuille flow. The step region introduces a recirculation zone of length  $L$ , the point of reattachment being when the  $x$ -component of the velocity changes sign.

Denham [1] took detailed velocity measurements in the channel, depicted in figure 3.5. All measurements were of the stream wise ( $x$ -direction) velocity component and were in the central plane of the duct to attempt as near as two-dimensional results. Velocity profiles were measured using laser Döppler anemometer and also dye tracer at several transverse sections both upstream and downstream of the step. They observe for all their range of  $Re$  a single primary recirculation but state, for  $Re > 229$  the flow was found to exhibit temporal variations around the reattachment point.

Our results were obtained for a range of  $Re$  numbers using two methods, both assuming two-dimensional flow. Our first method used standard LBGK in D2Q9 with mid-link bounce back (BBL) at solid boundaries, periodic boundaries in the direction along the pipe and forcing with a conservative body force to approximate the principle part of the pressure field. No pressure gradient is set explicitly. The overall pressure field is extracted as described below. Using this method the ‘pressure term’ ( $-c_s^2 \partial_\alpha \rho$ ) in the lattice NS equation is regarded as a correction to a principle pressure field which we may approximate as a potential function for the appropriate body force. The body force in the narrow part of the channel is  $\frac{27}{8}$  times that of the wide part of the channel, based upon matching parabolic flow rates. The potential function for this conservative body-force field is:

$$\Phi(x) = \begin{cases} P_{in} - \frac{27}{8}Gx, & x < x_0 \\ P_{in} - G(x + \frac{27}{8}x_0), & x_0 < x < L \end{cases} \quad (3.39)$$

in which  $G$  is the adjustable force constant and  $x_0$  the step length. The pressure field of the body-force LBGK is now determined by the expression  $c_s^2 \rho + \Phi$ . Mass is

strictly conserved and the pressure across the width of the inlet and outlet throats was held constant. The length of the lattice was chosen to minimise compressibility errors (which may be measured from the velocity divergence in the steady state continuity equation

$$\partial_\alpha u_\alpha = -\frac{u_\alpha}{\rho} \partial_\alpha \rho \quad (3.40)$$

but are otherwise ignored here.)

Our second method uses the exactly incompressible EILBGK model which allows pressure and velocity boundary conditions to be applied more accurately at the inlet and outlets. The EILBGK is very similar to the LBGK and is detailed in appendix A. Again non-slip boundaries are invoked using BBL at solid walls. Flow is now induced by setting discharge-matched parabolic velocity profiles at the inlet and outlet and by fixing the inlet pressure while allowing the outlet pressure to develop to accord with the necessary pressure gradient (itself an observable). Because of the direct link between density and pressure, the total mass of this simulation increases asymptotically to a steady-state value.

Using the law of similarity we compare body-forced LBGK and EILBGK simulations with experimental results from [1] based on their definition of  $Re$ :

$$Re = \frac{\bar{U}h}{\nu} \quad (3.41)$$

in which  $\bar{U}$  is the average flow velocity upstream of the step,  $h$  step height and  $\nu$  the kinematic viscosity. Comparison of simulated and experimental data was made by normalising velocities to the appropriate  $\bar{U}$ , distances to the step height  $h$ . For all our velocity data we note the body-forced LBGK and EILBGK results give very similar results for a given  $Re$ , so velocity figures are representative of both models used. For all velocity data, flow profiles in the inlet and outlet were in good agreement compared with parabolic flow, supporting the assumption of fully developed flow. All results are analysed in their steady state solutions, found by measuring the residual:

$$R(t) = \sum_{\underline{x}} |\underline{u}(\underline{x}, t)| \quad (3.42)$$

For the EILBGK system there is an additional condition on the total mass, which must be constant at steady state.

From stream-function data, the recirculation zone was seen to increase with increasing  $Re$ . The position of the vortex centre is given by the co-ordinates ( $x_c = 0.3L_R$ ,  $y_c = 0.6h$ ); this is in agreement with the co-ordinates given by Denham.

We define the recirculation length to be the distance  $x$  from the step at  $y = 0$  in which a change in the sign of the x-velocity direction occurs. Figure 3.6 displays normalised recirculation length against  $Re$  for the step ratio of  $\frac{1}{3}$ . Note that the LBGK data provided in figure 3.6 are more accurate and cover a greater range of  $Re$  than in previous studies [133].

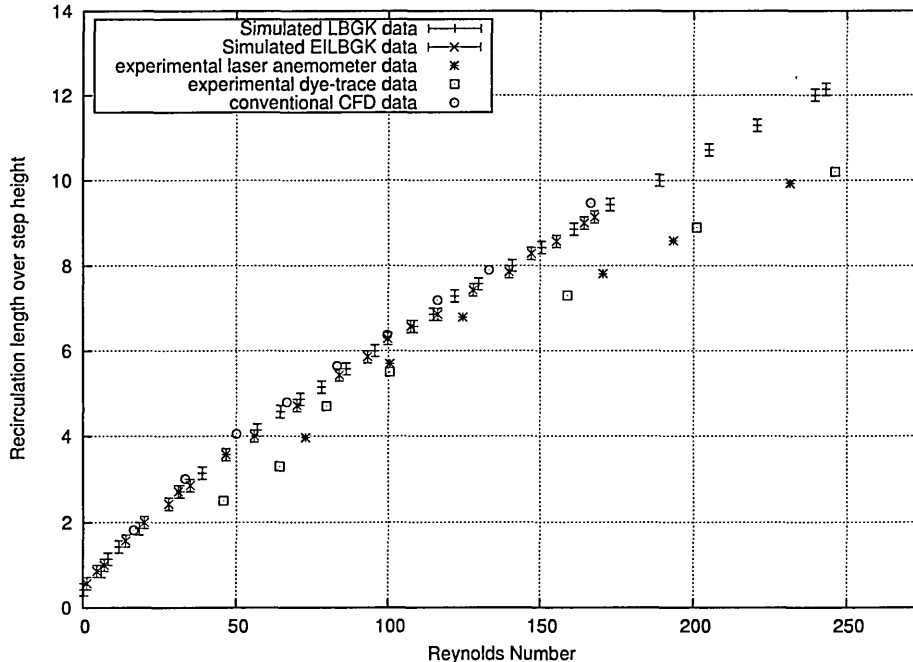


Figure 3.6: The recirculation length as a function of  $Re$  for the expansion ratio  $1/3$ . Data are compared to experimental values obtained via dye trace, laser anemometer measurements and also CFD data [1]

Both LBGK and EILBGK data are in good agreement. For the given lattice resolution it was observed that the range of accessible  $Re$  for the EILBGK is less than those for body-forced LBGK, owing to a more stringent incompressibility constraint. The experimental data points, taken from Denham contain a  $\pm 2\%$  tolerance for measurements of velocity. Including the tolerance limits, experimental results lie just below the simulated points, the discrepancy increases as  $Re$  increases. But CFD simulations [132] agree with our LBM models.

Velocity profiles obtained at different locations along the simulation are compared with experimental velocity profiles in figure 3.7. Recall that the agreement

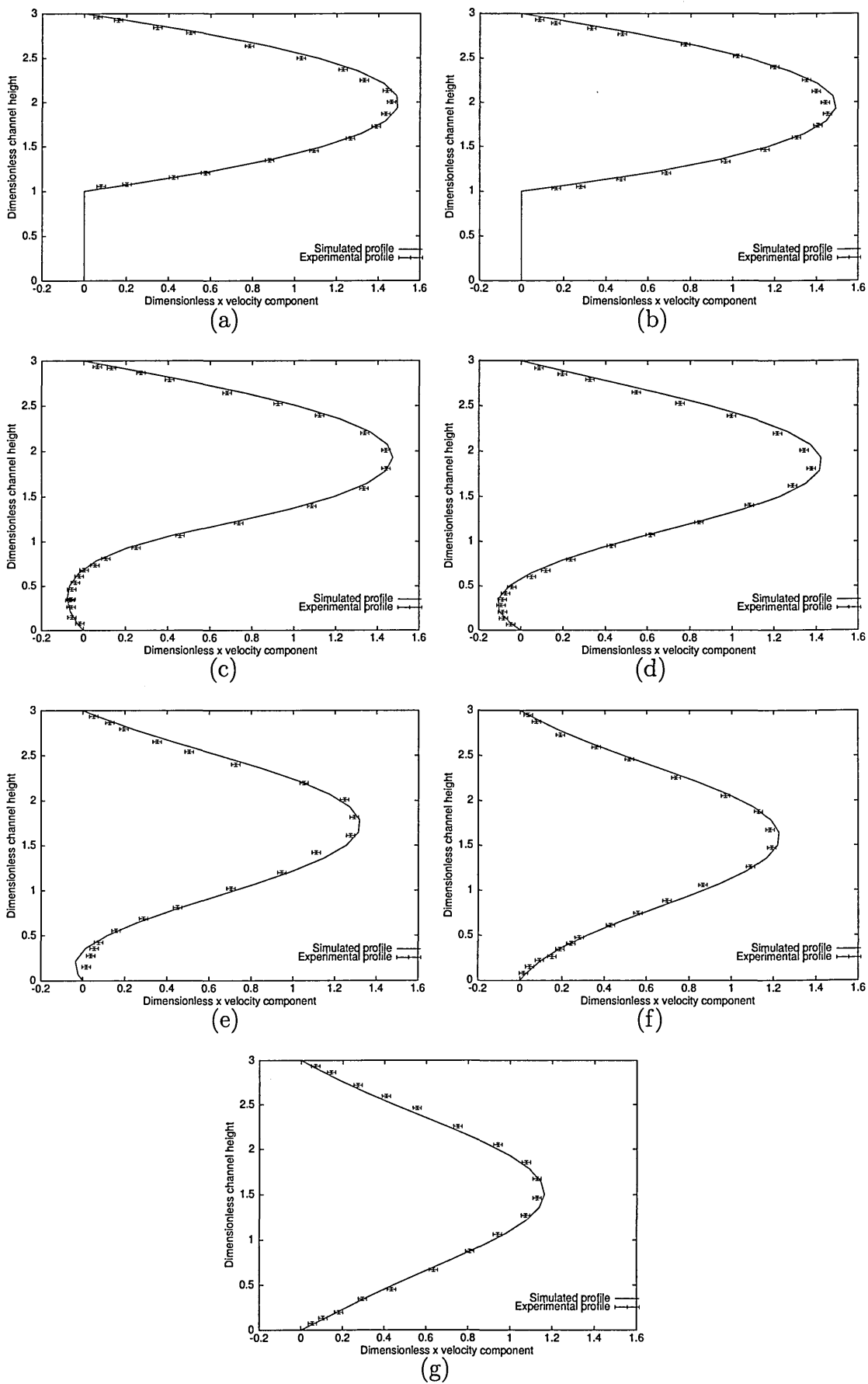


Figure 3.7: Comparison of simulated velocity profiles to experimental profiles obtained in [1] in the step region at  $Re = 73$  for various dimensionless distances from the step position: (a) -1.3, (b) 0.0, (c) 0.8, (d) 2.0, (e) 4.0, (f) 6.0, (g) 8.0.

between EILBGK and body-forced LBGK data is good and figure 3.7 shows only one set of simulation data, which agrees satisfactorily with experimental results at  $Re = 73$ . Upstream of the step, discrepancies are probably due to an inadequate development length in the experimental inlet [1]. At higher  $Re$ , there emerge further discrepancies throughout the length of the system probably due to three dimensional effects. Later experiments on a backward facing step with a step ratio of  $\frac{1}{2}$  [130] support this conclusion.

Figure 3.8 shows steady state pressure contours at different  $Re$ , for body-forced LBGK and pressure-driven EILBGK. Recall that it is EILBGK which accommodates pressure boundary conditions with outlet pressure developing freely in comparison to the body-forced LBGK in which an approximate pressure potential is used as a supplement to the real pressure. Qualitative agreement is good, with the

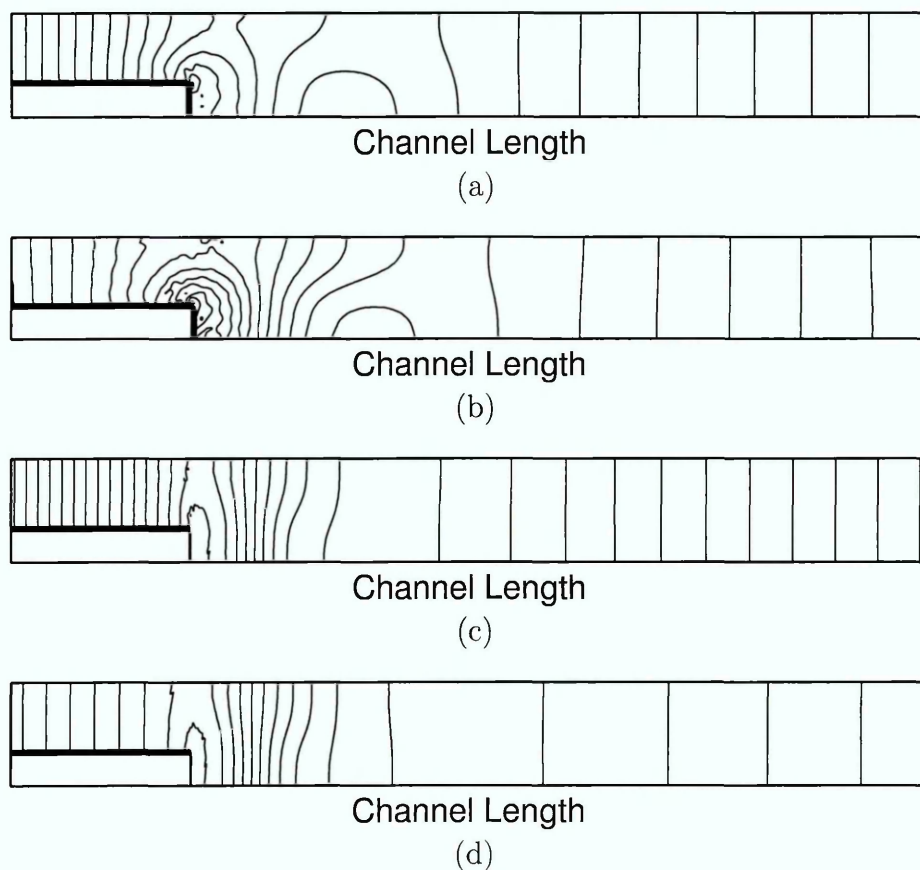


Figure 3.8: Pressure contours for (a), (b)  $Re = 31$  and (c), (d)  $Re = 174$  for (a), (c) pressure driven EILBGK and (b), (d) body-forced LBGK. Both simulations use identical velocity boundary conditions (refer to text) but only in the EILBGK simulation does the pressure develop freely. There is qualitative agreement between pressure fields (e.g. minimum pressure occurring in the recirculation zone.)

minimum pressure occurring in the recirculation zone for both simulations. Notwithstanding this, there are small quantitative differences between these pressure fields of the same order as those which routinely appear between CFD solutions obtained by different methods. Unfortunately no experimental information on the pressure exists. The ‘wiggles’ in the pressure contours of figure 3.8 are in the main due to the grid resolution. Further work may be done as mentioned in §3.1 to eliminate these through variable LB grids.

As can be seen from figure 3.8, our two methods produce slightly different pressure contours. However, given their very different representations of a pressure field, the correspondence between the results is highly reassuring. Body-forced LBGK implementation essentially assumes a uniform gradient of pressure which is perturbed. While intuitively valid at most points in the simulation domain, this assumption is weak in the step region, where forced LBGK and EILBGK show differences.

### 3.5 Conclusions

The LB method for simple fluids has been introduced. Some advantages and disadvantages of the technique have been looked. An example in using the LB method is given for the case of pressure driven flow over a backward facing step in comparison to experimental measurements. For many engineering computations in the LB literature, flow is induced by a uniform body forced method for easy algorithmic implementation. The results suggest that, if only velocity information is required, then this method may be used with confidence and, with appropriate adjustment, can produce a good representation of the pressure field.

# Chapter 4

## A Lattice Boltzmann Method For Nemato-dynamics

The aim of this chapter is to present and derive a LBM solver for LC nemato-dynamics in a  $Q$  tensor form. In contrast to others LB solvers for nemato-dynamics the current LBM solves for the full dynamic equations of Qian [40] with separation of time scales of the fast (hydrodynamic) and slow (director) variables. In addition, details are given on boundary closure and the treatment of externally applied fields. Furthermore results are reported of numerical tests of the solver against analytical expressions and standard numerical solutions. The LB method provides an effective method of solving the equations of nemato-dynamics. As the governing equations are complicated, numerical techniques are required if we want to usefully aid LC research.

### 4.1 Introduction

The development of the LB methods for LC's has been pioneered by two main research groups/collaborations. Several works have been produced aimed at recovering different macroscopic equations. Care [135, 136] has developed schemes aimed to recover constant order (EL) and variable order (QS) methods. Whilst Denniston [137, 138] has developed methods to recover the Beris Edwards governing equations in 2D and 3D geometries. Below we look at these methods in more detail.

### 4.1.1 Linearised LB Scheme for EL Dynamics

Care et al [135] proposed a coupled LB scheme aimed at recovering the EL equations (appendix B) of motion for nematic LC's in which the scheme is strictly two-dimensional (director and flow can not occur out of plane). A linearised LB method is followed in which the collision matrix induces anisotropic scattering to the momentum evolution equation and a supplementary forcing term (similar to the body force form of § 3.3.2) is used to recover part of the EL viscous stress and the distortion stress tensor. A second angular distribution function is then defined,  $\theta_i$ , representing the director ( $\hat{n} = [\sin \theta, \cos \theta]$ ), that advects on the same lattice as the momentum distribution function. The angular distribution function is then inserted into a LBGK type relaxation scheme resulting in a macroscopic convection diffusion type equation for the director angle which is then supplemented by a forcing term to introduce the anisotropic effects.

With the addition of magnetic field terms to the molecular field the numerical accuracy of the method was shown by measuring the Miesowicz viscosity ratio. They also test for the viscosity dependent director angle achieved in a shear flow. Both tests have analytical solutions and accuracy was achieved below 0.2% error.

The MRT type anisotropic collision serves to place the scheme in a stable regime and recover four of the five independent Leslie viscosity coefficients. However the non local gradient calculations will hinder parallelisation. This is required because the collision matrix is unable to reproduce all the terms in the viscous stress tensor, hence the need for the additional forcing terms. The viscous term associated with the  $\alpha_1$  viscosity was omitted in this work, mainly because to be reproduced from the scattering matrix it requires the lattice basis set to be isotropic upto 8<sup>th</sup> order (a complex, intensive lattice structure and even more so in three dimensions). Instead a 6<sup>th</sup> order D2Q13 (3 speed hexagonal) lattice was used. We however point out that the  $\alpha_1$  term could have been added to their force term explicitly.

Their director evolution scheme is memory unintensive (evolves single  $\theta$  instead of a vector or tensor) and simply contains the equal elastic constant representation. Additional LC properties (for example unequal elastic constants) would have to be explicitly added to the forcing term as was done for the magnetic field. The SRT parameter is found to directly relate to the LC elastic constant. We note the

momentum equilibrium distribution function is unchanged from standard isotropic LB schemes. Similarly for the angular scheme the isotropic equilibrium distribution function is simply premultiplied by the director angle:  $\theta_i^{(eq)} = \frac{\theta f_i^{(eq)}}{\rho}$ .

Though easily resolved (as two separate schemes are used) the time step chosen for the angular scheme was identical to the momentum scheme and thus all time dynamic information is invalid, only the steady state value can be used. With further advances this method provides a useful EL solver limited in application to situations in which biaxial behaviour, order variation, and three dimensional motion are unimportant. Further work is required to provide a weak anchoring boundary condition, to extend the use to three dimensions and to convert the lattice units in to useful SI units.

#### 4.1.2 Lattice Boltzmann Method for Beris Edwards Dynamics

Denniston et al [137, 138] have developed coupled LB algorithms for the nematodynamic equations as laid down by Beris and Edwards [42]. These equations are based on an alignment tensor  $\mathbf{Q}$  (where this  $\mathbf{Q}$  is  $\frac{2}{3}\mathbf{Q}$  of the previous chapters) and thus allows for variable order parameters and simulation of both isotropic and nematic phases. The momentum evolution equation takes the form of an LBGK type relaxation scheme with an additional force term (body force like) to reproduce the full anisotropy, as in [135]. However the equilibrium distribution function is changed from standard isotropic LB to include a term of the form  $e_{i\alpha}e_{i\beta}E_{i\alpha\beta}$  in which the tensor  $\mathbf{E}_i$  depends on  $\mathbf{Q}$  and its gradients to form part of the viscous stress tensor.

The second (alignment) algorithm governing the evolution of  $\mathbf{Q}$  uses a LBGK form with standard equilibrium distribution function modified as:  $g_{i\alpha\beta}^{(eq)} = Q_{\alpha\beta}f_i^{(eq)}$ , again with an additional force term providing the required anisotropy. Note the lattice distribution functions are now enhanced to tensor quantities and are therefore memory intensive.

The LBGK evolution equation used in both algorithms is of predictor-corrector form introduced in order to improve stability of the scheme and eliminate lattice viscosity terms.

This LB model of nemato-dynamics has been applied to numerous studies suit-

able for Lyotropic LC's [137, 138, 139, 140, 141, 142, 143, 144, 145, 146, 147, 148]. They have reported the shear alignment,  $\pm\frac{1}{2}$  defect annihilation, pouseuille flow, shear thickening/thinning, backflow in Freedericksz cells with an electric field, bistable LCD devices, phase ordering, domain motion in two and three dimensions, and poiseuille flow in chiral nematics.

We point out however no mention is made of the separation of fast momentum and slow director time scales and it is implied both algorithms run at the same time step  $\Delta t$ . Conversion of lattice units to SI units requires some what arbitrary choices for a length scale, time scale and pressure scale that are then used to calculate the SI units of LC coefficients. Further their treatment of the electric field as a constant is not strictly correct (see §2.1.5). No surface viscosity expressions are quoted even though weak anchoring conditions are used.

The Beris Edwards formalism is based on a microscopic relation of transport coefficients to molecular properties such as size and aspect ratio. In the limit of constant order and uniaxial rods, it can be reduced to the exact EL formalism. Within this limit it is found that only three viscosity coefficients are independent due to the truncation in the  $\mathbf{Q}$  expansion [42]: in contrast the EL theory finds macroscopically there are five independent viscosity coefficients in the nematic phase. This is a common feature of all microscopic dynamic theories for nematics and warrants further experimental clarification.

### 4.1.3 Single Lattice Boltzmann Equation for QS Dynamics

Care et al [136] extended their work to include the alignment tensor allowing for variable order parameters. Further they managed to compress the momentum and order evolution equations into a single two dimensional LB algorithm in contrast to the coupled LB schemes of §4.1.1 and §4.1.2. This was deemed to more efficiently solve the LC equations of motion. The equations that are recovered are those of Qian [40] suitable for themotropic LC's and retain the five independent EL viscosity coefficients.

As with the method in §4.1.2 a tensorial distribution function is used but contained within the tensor the equivalent scalar densities,  $f_i$ , are held along the trace. In order to do this the alignment tensor,  $\mathbf{Q}$ , is converted to an ordering matrix of

unit trace. The LB evolution equation follows a ‘LBGK - type’ relaxation with a direction dependent relaxation parameter supplemented by terms to conserve mass, momentum and the two force terms to complete the set of anisotropic properties. The  $\beta_1$  viscosity is omitted as an  $8^{th}$  order isotropic lattice basis is required; again we point out this could have been inserted to the momentum forcing term. The standard isotropic equilibrium distribution function is used:  $g_{i\alpha\beta}^{(eq)} = S_{\alpha\beta} f_i^{(eq)}$  where  $S_{\alpha\beta}$  is the unit trace ordering matrix.

The algorithm was numerically tested in lattice units against analytical results for both the director and order at steady state and in a shear and magnetic field. The scalar alignment and Miesowicz viscosity ratio were tested, results accurate to less than 0.3% error. The algorithm was further extended for a nematic-isotropic interface [149]. Using the advantages of the LB technique for multi-component fluids they used the segregation technique of Gunstensen [150] and Lishchuk [151].

The drawbacks of this method is that the time step of both momentum and order evolution equations are fixed identically. The time evolution properties predicted can not be used. So the algorithm may only be used for equilibrated systems. In this way the method becomes inefficient compared to standard numerical techniques. The method also draws on the  $6^{th}$  order lattice basis of a hexagonal D2Q13. Extensions to a three dimensional lattice of the same order are non-trivial.

## 4.2 A Proposed Method for LB Q-tensor Nematodynamics

In the previous section we saw some LB methods for nemato-dynamics. It is seen that the work of Care [136] to recover the dynamic evolution equations of Qian [40] has some drawbacks, being largely limited to two dimensions at steady state and some degree of freedom around choice of parameters. Here we will modify, and possibly simplify, the method in an attempt to be able to extract correct time dynamics and relation to SI units. To tackle the issue of time dynamics in which a momentum time step is vastly shorter than that of the LC director we must separate the combined scheme in [136] into two coupled schemes as in [135] or [137]. Further we will insert all anisotropy into the force terms whilst keeping the isotropic equilibrium distribution function.

## 4.2.1 Reiteration of the Governing Q-Tensor Equations

The LC evolution equations stated by Qian [40] are given in § 2.4.1. We will first rearrange these to present it in a form more suitable for a lattice evolution equation consisting of streaming and collision. As is commonly done we assume the angular velocity relaxes quickly [40] so the moment of inertia is set to zero ( $J = 0$ ). We then substitute equation 2.48 into equation 2.44 to yield:

$$0 = h_{\alpha\beta}^B - \frac{\mu_2 A_{\alpha\beta}}{2} - \mu_1 N_{\alpha\beta} - \lambda^B \delta_{\alpha\beta} - \varepsilon_{\alpha\beta\gamma} \lambda_\gamma^B \quad (4.1)$$

Rearranging equation 4.1 for the co-rotational derivative, we may substitute into the viscous stress tensor, equation 2.47, to eliminate the time derivatives:

$$\begin{aligned} \sigma_{\alpha\beta}^v = & \beta_1 Q_{\alpha\beta} Q_{\mu\nu} A_{\mu\nu} + \beta_4 A_{\alpha\beta} + \beta_5 Q_{\alpha\mu} A_{\mu\beta} + \beta_6 Q_{\beta\mu} A_{\mu\alpha} \\ & + \frac{\mu_2 h_{\alpha\beta}^B}{2\mu_1} - \frac{\mu_2 \lambda^B \delta_{\alpha\beta}}{2\mu_1} - \frac{\mu_2 \varepsilon_{\alpha\beta\gamma} \lambda_\gamma^B}{2\mu_1} - \frac{\mu_2^2 A_{\alpha\beta}}{4\mu_1} - Q_{\alpha\mu} h_{\mu\beta}^B \\ & + Q_{\alpha\mu} \varepsilon_{\mu\beta\gamma} \lambda_\gamma^B + \frac{\mu_2 Q_{\alpha\mu} A_{\mu\beta}}{2} + Q_{\beta\mu} h_{\mu\alpha}^B - Q_{\beta\mu} \varepsilon_{\mu\alpha\gamma} \lambda_\gamma^B - \frac{\mu_2 Q_{\beta\mu} A_{\mu\alpha}}{2} \end{aligned} \quad (4.2)$$

Upon substitution of the explicit form of  $N_{\alpha\beta} = \dot{Q}_{\alpha\beta} - \varepsilon_{\alpha\mu\nu} \omega_\mu Q_{\nu\beta} - \varepsilon_{\beta\mu\nu} \omega_\mu Q_{\alpha\nu}$  into equation 4.1, we may re-order terms to express the order evolution equation in the convenient form:

$$\dot{Q}_{\alpha\beta} = \frac{h_{\alpha\beta}^B}{\mu_1} - \frac{\lambda^B \delta_{\alpha\beta}}{\mu_1} - \frac{\varepsilon_{\alpha\beta\gamma} \lambda_\gamma^B}{\mu_1} - \frac{\mu_2 A_{\alpha\beta}}{2\mu_1} + \varepsilon_{\alpha\epsilon\lambda} \omega_\epsilon Q_{\lambda\beta} + \varepsilon_{\beta\epsilon\lambda} \omega_\epsilon Q_{\alpha\lambda} \quad (4.3)$$

the left hand of which is appropriate for the streaming step of the LB algorithm.

To identify the form of the Lagrange multipliers  $\lambda^B$  and  $\lambda_\gamma^B$  we analyse equation 4.1 for  $h_{\alpha\beta}$  and taking its trace shows:

$$h_{\alpha\alpha}^B = -h_{\alpha\alpha}^v + 3\lambda^B \quad (4.4)$$

explicit substitution of the viscous molecular field (equation 2.48) into the above and due to the fact that  $Q_{\alpha\beta}$  is symmetric and traceless, shows that:

$$\lambda^B = \frac{1}{3} \left( h_{\alpha\alpha}^B - \frac{\mu_2}{2} A_{\alpha\alpha} \right) \quad (4.5)$$

The term in  $A_{\alpha\alpha}$ , zero for incompressible fluids, is kept because the LB fluid is weakly compressible and this should correct any errors at higher velocities. (Remember the condition  $M = \frac{|u|}{c_s^*} \ll 1$  for incompressible fluids.)

Considering the off diagonal elements in equation 4.1 separately we find, for example:

$$\left. \begin{aligned} h_{12}^B &= -h_{12}^v + \lambda_3^B \\ h_{21}^B &= -h_{21}^v - \lambda_3^B \end{aligned} \right\} \quad (4.6)$$

as  $h_{\alpha\beta}^v$  is symmetric and traceless equation 4.6 is rearranged to find  $\lambda_3^B = \frac{1}{2}(h_{12}^B - h_{21}^B)$ . Analysing the other elements shows that:

$$\lambda_\gamma^B = \frac{1}{2}\varepsilon_{\alpha\beta\gamma}h_{\alpha\beta}^B \quad (4.7)$$

For the molecular field as defined in equation 2.46 and phenomenological free energies given in §2.1 we get:

$$\begin{aligned} h_{\alpha\beta}^B = & -\alpha_F Q_{\alpha\beta} + 3\beta_F Q_{\alpha\gamma} Q_{\gamma\beta} - 4\gamma_F Q_{\alpha\beta} Q_{\gamma\tau} Q_{\tau\gamma} \\ & + L_1 \partial_\gamma \partial_\gamma Q_{\alpha\beta} + L_2 \partial_\alpha \partial_\gamma Q_{\gamma\beta} + L_3 \partial_\gamma \partial_\beta Q_{\alpha\gamma} \\ & + \frac{L_4}{2} (2Q_{\mu\nu} \partial_\mu \partial_\nu Q_{\alpha\beta} + \partial_\nu Q_{\alpha\beta} \partial_\mu Q_{\mu\nu} + \partial_\mu Q_{\alpha\beta} \partial_\nu Q_{\mu\nu} - \partial_\alpha Q_{\gamma\tau} \partial_\beta Q_{\gamma\tau}) \\ & + \frac{4\pi L_1}{P_{ch}} (\varepsilon_{\mu\lambda\alpha} \partial_\lambda Q_{\mu\beta} - \varepsilon_{\alpha\nu\gamma} \partial_\nu Q_{\gamma\beta}) \\ & + \frac{4\pi L_4}{P_{ch}} (Q_{\mu\alpha} \varepsilon_{\mu\nu\gamma} \partial_\nu Q_{\gamma\beta} + Q_{\beta\tau} \varepsilon_{\alpha\nu\gamma} \partial_\nu Q_{\gamma\tau} - \varepsilon_{\mu\lambda\alpha} Q_{\mu\epsilon} \partial_\lambda Q_{\epsilon\beta} - \varepsilon_{\mu\lambda\alpha} Q_{\epsilon\beta} \partial_\lambda Q_{\mu\epsilon}) \\ & + \frac{1}{3} \epsilon_0 \Delta \epsilon_a^{max} E_\alpha E_\beta + \frac{1}{3} \mu_0 \Delta \chi_a^{max} H_\alpha H_\beta \\ & - C_1 \partial_\beta E_\alpha + C_2 (E_\alpha \partial_\nu Q_{\beta\nu} - E_\mu \partial_\beta Q_{\mu\alpha} - Q_{\mu\alpha} \partial_\beta E_\mu) \end{aligned} \quad (4.8)$$

and for the distortion stress tensor defined in equation 2.45 we obtain:

$$\begin{aligned} \sigma_{\alpha\beta}^d = & -L_1 \partial_\alpha Q_{\epsilon\lambda} \partial_\beta Q_{\epsilon\lambda} - L_2 \partial_\nu Q_{\epsilon\nu} \partial_\beta Q_{\epsilon\alpha} - L_3 \partial_\beta Q_{\mu\gamma} \partial_\gamma Q_{\mu\alpha} - L_4 Q_{\alpha\mu} \partial_\mu Q_{\epsilon\lambda} \partial_\beta Q_{\epsilon\lambda} \\ & - \frac{4\pi L_1}{P_{ch}} \varepsilon_{\mu\alpha\rho} Q_{\mu\lambda} \partial_\beta Q_{\rho\lambda} + \frac{4\pi L_4}{P_{ch}} \varepsilon_{\mu\alpha\rho} Q_{\mu\epsilon} Q_{\epsilon\lambda} \partial_\beta Q_{\rho\lambda} \\ & + C_1 E_\mu \partial_\beta Q_{\mu\alpha} + C_2 E_\mu Q_{\mu\gamma} \partial_\beta Q_{\gamma\alpha} \end{aligned} \quad (4.9)$$

We have thus identified our target equations for the free energy given in §2.1. The target order evolution equation being equation 4.3 and the target momentum evolution equation still being equation 2.43 but with equivalent (J=0) viscous stress tensor given in equation 4.2.

## 4.2.2 Statement of the Algorithm

The simplest LB routines are the SRT LBGK methods, well proven in solving the NS equation (see chapter 3). It is this method we choose to adopt here, adding the LC anisotropy into an appropriate ‘forcing term’. The equations given are for three dimensional systems, lower dimensional systems are easily studied as a subset of this case by setting periodic boundaries. Here we list the core resultant algorithm needed for implementation. An analysis follows to justify the choices made (§4.2.3).

### The Momentum Evolution Algorithm

The momentum distribution function is evolved as:

$$f_i(\underline{x} + \underline{e}_i \Delta t, t + \Delta t) = f_i(\underline{x}, t) - \frac{1}{\tau_p} \left( f_i(\underline{x}, t) - f_i^{(eq)}(\underline{x}, t) \right) + \phi_i(\underline{x}, t) \quad (4.10)$$

where symbols take there usual meanings, the subscript on the  $\tau_P$  emphasising the SRT for the momentum scheme and the  $\phi_i$  the additive forcing term. The macroscopic observables are extracted from:

$$\left. \begin{aligned} \sum_i f_i &= \rho(\underline{x}, t) \\ \sum_i f_i e_{i\alpha} &= \rho u_\alpha(\underline{x}, t) \end{aligned} \right\} \quad (4.11)$$

the isotropic equilibrium distribution function being the usual:

$$f_i^{(eq)} = t_i \rho \left[ 1 + \frac{e_{i\alpha} u_\alpha}{c_s^2} + u_\alpha u_\beta \left( \frac{e_{i\alpha} e_{i\beta} - c_s^2 \delta_{\alpha\beta}}{2c_s^4} \right) \right] \quad (4.12)$$

in which  $t_i$  and  $c_s^2$  take the same values as in standard LBGK for a set of chosen  $\underline{e}_i$ .

The anisotropic forcing term is:

$$\left. \begin{aligned} \phi_i &= t_i c_{i\lambda} \partial_\beta F_{\lambda\beta} \\ F_{\alpha\beta} &= \frac{\Delta t}{c_s^2} \left[ \sigma_{\alpha\beta}^d + \sigma_{\alpha\beta}^{EM} + \beta_1 Q_{\alpha\beta} Q_{\mu\nu} A_{\mu\nu} + \beta_5 Q_{\alpha\mu} A_{\mu\beta} + \beta_6 Q_{\beta\mu} A_{\mu\alpha} \right. \\ &\quad \left. + \frac{\mu_2 h_{\alpha\beta}}{2\mu_1} - \frac{\mu_2 \varepsilon_{\alpha\beta\gamma} \lambda_\gamma^B}{2\mu_1} - Q_{\alpha\mu} h_{\mu\beta} + Q_{\alpha\mu} \varepsilon_{\mu\beta\gamma} \lambda_\gamma^B \right. \\ &\quad \left. + \frac{\mu_2 Q_{\alpha\mu} A_{\mu\beta}}{2} + Q_{\beta\mu} h_{\mu\alpha} - Q_{\beta\mu} \varepsilon_{\mu\alpha\gamma} \lambda_\gamma^B - \frac{\mu_2 Q_{\beta\mu} A_{\mu\alpha}}{2} \right] \end{aligned} \right\} \quad (4.13)$$

(Note the similarity to equation 3.34 if  $\partial_\beta F_{\lambda\beta}$  where a constant  $a_\lambda$ .) We also identify pressure and isotropic viscosity as:

$$P = \rho c_s^2 + \frac{\mu_2 \lambda^B}{2\mu_1}, \quad \rho c_s^2 (2\tau_P - 1) \Delta t = \beta_4 - \frac{\mu_2^2}{4\mu_1} \quad (4.14)$$

## The Order Evolution Algorithm

The order distribution function is written as a symmetric tensor quantity evolved as:

$$g_{i\alpha\beta}(\underline{x} + \underline{e}_i \Delta t, t + \Delta t) = g_{i\alpha\beta}(\underline{x}, t) - \frac{1}{\tau_Q} \left( g_{i\alpha\beta}(\underline{x}, t) - g_{i\alpha\beta}^{(eq)}(\underline{x}, t) \right) + \chi_{i\alpha\beta}(\underline{x}, t) \quad (4.15)$$

the subscript on the  $\tau_Q$  emphasising the SRT parameter for the order scheme and  $\chi_{i\alpha\beta}$  the additive force term. The macroscopic observables are extracted from:

$$\sum_i g_{i\alpha\beta} = \zeta S_{\alpha\beta} \quad (4.16)$$

where  $S_{\alpha\beta}$  is the alignment tensor of unit trace being simply related to  $Q_{\alpha\beta}$  in three dimensions via:

$$Q_{\alpha\beta} = \frac{3S_{\alpha\beta} - \delta_{\alpha\beta}}{2} \quad (4.17)$$

The parameter  $\zeta \equiv \sum_i g_{i\gamma\gamma}$  has constant value of unity thus may be ignored, however it was included in the analysis to provide a consistency with the work in [136]. Its origin may be considered analogous to that of  $\rho$  in the momentum algorithm and it may be used to investigate if the order algorithm is subject to weak compressibility effects. The appropriate isotropic order equilibrium distribution function is defined:

$$g_{i\alpha\beta}^{(eq)} = t_i \zeta S_{\alpha\beta} \left[ 1 + \frac{e_{i\alpha} u_\alpha}{c_s^2} + u_\alpha u_\beta \left( \frac{e_{i\alpha} e_{i\beta} - c_s^2 \delta_{\alpha\beta}}{2c_s^4} \right) \right] \quad (4.18)$$

in which again  $t_i$  and  $c_s^2$  take the same values as in the momentum schemes. The anisotropic force term is:

$$\chi_{i\alpha\beta} = \frac{\Delta t 2 \zeta t_i}{3} \left[ \frac{h_{\alpha\beta}}{\mu_1} - \frac{L_1 \partial_\lambda \partial_\lambda Q_{\alpha\beta}}{\mu_1} - \frac{\lambda^B \delta_{\alpha\beta}}{\mu_1} - \frac{\varepsilon_{\alpha\beta\gamma} \lambda_\gamma^B}{\mu_1} - \frac{\mu_2 A_{\alpha\beta}}{2\mu_1} + \varepsilon_{\alpha\epsilon\lambda} \omega_\epsilon Q_{\lambda\beta} + \varepsilon_{\beta\epsilon\lambda} \omega_\epsilon Q_{\alpha\lambda} \right] \quad (4.19)$$

We identify the relaxation parameter  $\tau_Q$  with the principal elastic constant:

$$\frac{c_s^2}{2} (2\tau_Q - 1) \Delta t = \frac{L_1}{\mu_1} \quad (4.20)$$

These are two essentially separate algorithms but are highly coupled. Both may be run independently, for example if flow effects are to be ignored or only static equilibrium configurations are desired running the  $g_{i\alpha\beta}$  scheme alone would suffice.

### 4.2.3 Analytical Algorithm Analysis (Chapman-Enskog Procedure)

Although the processes of the Chapman-Enskog analysis are essentially identical we treat the analysis in two stages, one for the momentum scheme and one for the order scheme. The analysis serves two purposes: to ensure the governing equations are recovered and to identify the relation of the LB SRT parameter to transport coefficients and forcing terms.

## Momentum Analysis

We first define the usual lattice moments and constraints as [152]:

$$\left. \begin{aligned} \sum_i f_i^{(0)} \begin{bmatrix} 1 \\ e_{i\alpha} \\ e_{i\alpha}e_{i\beta} \end{bmatrix} &= \begin{bmatrix} \rho \\ \rho u_\alpha \\ \Pi_{\alpha\beta}^{(0)} = \rho c_s^2 \delta_{\alpha\beta} + \rho u_\alpha u_\beta \end{bmatrix} \\ \sum_i f_i^{(n)} \begin{bmatrix} 1 \\ e_{i\alpha} \\ e_{i\alpha}e_{i\beta} \end{bmatrix} &= \begin{bmatrix} 0 \\ 0 \\ \Pi_{\alpha\beta}^{(n)} \end{bmatrix}, \quad n > 0 \end{aligned} \right\} \quad (4.21)$$

Other useful relations that will be used are the velocity summations calculated from an isotropic lattice basis (see [152]) at fourth order:

$$\left. \begin{aligned} \sum_i t_i &= 1 \\ \sum_i t_i e_{i\alpha} &= 0 \\ \sum_i t_i e_{i\alpha} e_{i\beta} &= c_s^2 \delta_{\alpha\beta} \\ \sum_i t_i e_{i\alpha} e_{i\beta} e_{i\gamma} &= 0 \\ \sum_i t_i e_{i\alpha} e_{i\beta} e_{i\gamma} e_{i\theta} &= c_s^4 \Delta_{\alpha\beta\gamma\theta} = c_s^4 (\delta_{\alpha\beta} \delta_{\gamma\theta} + \delta_{\alpha\gamma} \delta_{\beta\theta} + \delta_{\alpha\theta} \delta_{\beta\gamma}) \end{aligned} \right\} \quad (4.22)$$

Using a Taylor expansion on the left hand side of equation 4.10 we obtain:

$$\begin{aligned} \Delta t \partial_t f_i + \frac{\Delta t^2}{2} \partial_t \partial_t f_i + \Delta t e_{i\alpha} \partial_\alpha f_i + \Delta t^2 e_{i\alpha} \partial_t \partial_\alpha f_i + \frac{\Delta t^2}{2} e_{i\alpha} e_{i\beta} \partial_\alpha \partial_\beta f_i \\ = -\frac{1}{\tau_P} \left( f_i - f_i^{(eq)} \right) + \phi_i \end{aligned} \quad (4.23)$$

We suppose the force term  $\phi_i$  takes the form  $\phi_i = t_i c_{i\lambda} \partial_\beta F_{\lambda\beta}$ . We now use the multi-scale expansion, to second order, that is:

$$\left. \begin{aligned} t_1 = \varepsilon t, \quad t_2 = \varepsilon^2 t, \quad \partial_t = \varepsilon \partial_{t_1} + \varepsilon^2 \partial_{t_2} \\ x_1 = \varepsilon x, \quad x_2 = \varepsilon^2 x, \quad \partial_x = \varepsilon \partial_{x_1} + \varepsilon^2 \partial_{x_2} \\ f_i = f_i^{(0)} + \varepsilon f_i^{(1)} + \varepsilon^2 f_i^{(2)} \end{aligned} \right\} \quad (4.24)$$

the above expansion yields:

$$\begin{aligned} \varepsilon \left( \Delta t \partial_{t_1} f_i^{(0)} + \Delta t e_{i\alpha} \partial_{\alpha_1} f_i^{(0)} \right) + \varepsilon^2 \left( \Delta t \partial_{t_1} f_i^{(1)} + \Delta t \partial_{t_2} f_i^{(0)} + \Delta t e_{i\alpha} \partial_{\alpha_1} f_i^{(1)} \right. \\ \left. + \Delta t e_{i\alpha} \partial_{\alpha_2} f_i^{(0)} + \frac{\Delta t^2}{2} \partial_{t_1} \partial_{t_1} f_i^{(0)} + \Delta t^2 e_{i\alpha} \partial_{\alpha_1} \partial_{t_1} f_i^{(0)} + \frac{\Delta t^2}{2} e_{i\alpha} e_{i\beta} \partial_{\alpha_1} \partial_{\beta_1} f_i^{(0)} \right) \\ = -\frac{1}{\tau_P} \left( f_i^{(0)} + \varepsilon f_i^{(1)} + \varepsilon^2 f_i^{(2)} - f_i^{(eq)} \right) + \varepsilon t_i e_{i\lambda} \partial_{\beta_1} F_{\lambda\beta} + \varepsilon^2 t_i e_{i\lambda} \partial_{\beta_2} F_{\lambda\beta} \end{aligned} \quad (4.25)$$

Arranging terms in ascending order of  $\varepsilon$ , we obtain:

$$O(\varepsilon^0) \quad f_i^{(0)} = f_i^{(eq)} \quad (4.26)$$

$$O(\varepsilon^1) \quad -\tau_P \Delta t (\partial_{t_1} + e_{i\alpha_1} \partial_{\alpha_1}) f_i^{(0)} + \tau_P t_i e_{i\lambda} \partial_{\beta_1} F_{\lambda\beta} = f_i^{(1)} \quad (4.27)$$

$$\begin{aligned} O(\varepsilon^2) \quad \left( \frac{1}{2} - \tau_P \right) \Delta t (\partial_{t_1} + e_{i\alpha} \partial_{\alpha_1}) f_i^{(1)} - \tau_P \Delta t (\partial_{t_2} + e_{i\alpha} \partial_{\alpha_2}) f_i^{(0)} \\ - \frac{\tau_P \Delta t}{2} (\partial_{t_1} + e_{i\alpha} \partial_{\alpha_1}) t_i e_{i\lambda} \partial_{\beta_1} F_{\lambda\beta} + \tau_P t_i e_{i\lambda} \partial_{\beta_2} F_{\lambda\beta} = f_i^{(2)} \end{aligned} \quad (4.28)$$

in which we have used the  $O(\varepsilon^1)$  result of equation 4.27 to replace a term of the form  $(\partial_{t_1} + e_{i\alpha}\partial_{\alpha_1})f_i^{(0)}$  in the  $O(\varepsilon^2)$  result.

Taking the zeroth moment ( $\sum_i$ ) of the first and second order equations 4.27, 4.28 whilst respecting equations 4.21 yields:

$$\begin{aligned} O(\varepsilon^1) \quad \partial_{t_1}\rho + \partial_{\alpha_1}(\rho u_\alpha) &= 0 \\ O(\varepsilon^2) \quad \partial_{t_2}\rho + \partial_{\alpha_2}(\rho u_\alpha) &= \frac{c_s^2}{2}\partial_{\gamma_1}\partial_{\beta_1}F_{\gamma\beta} \end{aligned} \quad (4.29)$$

which can be recombined (c.f. equation 4.24) to give the continuity equation:

$$\partial_t\rho + \partial_\alpha(\rho u_\alpha) = 0 \quad (4.30)$$

We note the term of the form  $\frac{c_s^2}{2}\partial_\lambda\partial_\beta F_{\lambda\beta}$  has been omitted from equation 4.30, an assumption not unreasonable as  $F_{\lambda\beta}$  depends on gradients in  $\underline{u}$  and gradients in  $\underline{Q}$  thus making it a negligibly small high order term<sup>1</sup>.

Taking the first moment ( $\sum_i e_{i\beta}$ ) of the first and second order equation 4.27 and equation 4.28 whilst respecting equations 4.21 yields:

$$\begin{aligned} O(\varepsilon^1) \quad \partial_{t_1}(\rho u_\beta) + \partial_{\alpha_1}\Pi_{\beta\alpha}^{(0)} &= \frac{c_s^2}{\Delta t}\partial_{\gamma_1}F_{\beta\gamma} \\ O(\varepsilon^2) \quad \left(1 - \frac{1}{2\tau_P}\right)\partial_{\alpha_1}\Pi_{\beta\alpha}^{(1)} + \partial_{t_2}(\rho u_\beta) + \partial_{\alpha_2}\Pi_{\beta\alpha}^{(0)} &= \frac{c_s^2}{\Delta t}\partial_{\gamma_2}F_{\beta\gamma} - \frac{c_s^2}{2}\partial_{t_1}\partial_{\gamma_1}F_{\beta\gamma} \end{aligned} \quad (4.31)$$

To progress, the  $\Pi_{\beta\alpha}^{(1)}$  term needs evaluating or more specifically  $f_i^{(1)}$  (in equation 4.27). Using equation 4.12 to  $O(\underline{u})$  in equation 4.27, taking its zeroth moment and back substituting the result ( $\partial_{t_1}\rho = -\partial_{\beta_1}(\rho u_\beta)$ ), followed by taking the first moment and another back substitution ( $\partial_{t_1}(\rho u_\beta) = -c_s^2\partial_{\beta_1}\rho - \tau_P c_s^2\partial_{\gamma_1}F_{\beta\gamma}$ ) yields the form:

$$f_i^{(1)} = -\frac{\tau_P\Delta t\partial_{\beta_1}(\rho u_\alpha)H_{i\alpha\beta}}{c_s^2} + \tau_P t_i e_{i\lambda}(\tau_P\Delta t + 1)\partial_{\gamma_1}F_{\lambda\gamma} \quad (4.32)$$

in which  $H_{i\alpha\beta}$  is symmetric and defined:

$$H_{i\alpha\beta} = t_i c_s^2 \left( \frac{e_{i\alpha}e_{i\beta}}{c_s^2} - \delta_{\alpha\beta} \right) \quad (4.33)$$

The symmetry of equation 4.33 allowing us to write  $\partial_\lambda(\rho u_\beta) = \rho A_{\lambda\beta}$  in the incompressible limit.

We now use equation 4.32 to evaluate equation 4.31 more explicitly (substitute equation 4.32 into  $\Pi_{\beta\alpha}^{(1)}$  term and use of equation 4.22); we get in the incompressible

---

<sup>1</sup>In a future work the consequences of the Landau expansion terms present in  $F_{\lambda\gamma}$  will be studied more critically.

limit:

$$O(\varepsilon^0) \quad \partial_{t_1}(\rho u_\beta) + \partial_{\beta_1}(\rho c_s^2) + \partial_{\alpha_1}(\rho u_\alpha u_\beta) = \frac{c_s^2}{\Delta t} \partial_{\gamma_1} F_{\beta\gamma} \quad (4.34)$$

$$O(\varepsilon^1) \quad \partial_{t_2}(\rho u_\beta) + \partial_{\beta_2}(\rho c_s^2) + \partial_{\alpha_2}(\rho u_\alpha u_\beta) \quad (4.35)$$

$$-c_s^2(2\tau_P - 1)\Delta t \partial_{\alpha_1}(\rho A_{\beta\alpha_1}) = \frac{c_s^2}{\Delta t} \partial_{\gamma_2} F_{\beta\gamma} - \frac{c_s^2}{2} \partial_{t_1} \partial_{\gamma_1} F_{\beta\gamma}$$

Recombining equation 4.34 and equation 4.35 gives:

$$\partial_t(\rho u_\beta) + u_\alpha \partial_\alpha(\rho u_\beta) = -\partial_\beta(\rho c_s^2) + c_s^2(2\tau_P - 1)\Delta t \partial_\alpha(\rho A_{\beta\alpha}) + \frac{c_s^2}{\Delta t} \partial_\alpha F_{\beta\alpha} \quad (4.36)$$

Here the term of the form  $-\frac{c_s^2}{2} \partial_t \partial_\gamma F_{\beta\gamma}$  is, as before, neglected assuming high order gradients are negligibly small<sup>1</sup>.

A detailed comparison of the terms in this equation to the target momentum equation (equation 4.2 and equation 2.43) gives the identifications made in equation 4.14. (Note the isotropic terms do not contribute to entropy sources and may be incorporated into the scalar pressure [46].) Comparison of the remaining stress tensor terms reveals the extra stress needed in the LB simulation, that is to say we define equation 4.13. This completes the momentum analysis.

## Order Analysis

We first define the lattice moments and constraints:

$$\left. \begin{aligned} \sum_i g_{i\alpha\beta}^{(0)} \begin{bmatrix} 1 \\ e_{i\alpha} \end{bmatrix} &= \begin{bmatrix} \zeta S_{\alpha\beta} \\ \zeta u_\gamma S_{\alpha\beta} \end{bmatrix} \\ \sum_i g_{i\alpha\beta}^{(n)} \begin{bmatrix} 1 \\ e_{i\alpha} \end{bmatrix} &= \begin{bmatrix} 0 \\ \Omega_{\alpha\beta\gamma}^{(n)} \end{bmatrix}, \quad n > 0 \end{aligned} \right\} \quad (4.37)$$

Velocity summations (equation 4.22) still apply here. It is worth pointing out that unnecessarily we stick to moment definitions of the unit trace order tensor as this work seeks to advance [136]. But as the momentum and order are now in separate algorithms we may equivalently define zero trace moment definitions as in [137] in which  $\zeta$  is then zero.

Using a Taylor expansion on the left hand side of lattice evolution equation (equation 4.15) we obtain:

$$\begin{aligned} \Delta t \partial_t g_{i\mu\nu} + \frac{\Delta t^2}{2} \partial_t \partial_t g_{i\mu\nu} + \Delta t e_{i\alpha} \partial_\alpha g_{i\mu\nu} + \Delta t^2 e_{i\alpha} \partial_t \partial_\alpha g_{i\mu\nu} + \frac{\Delta t^2}{2} e_{i\alpha} e_{i\beta} \partial_\alpha \partial_\beta g_{i\mu\nu} \\ = -\frac{1}{\tau_Q} \left( g_{i\mu\nu} - g_{i\mu\nu}^{(eq)} \right) + \chi_{i\mu\nu} \end{aligned} \quad (4.38)$$

---

<sup>1</sup>In a future work the consequences of the Landau expansion terms present in  $F_{\lambda\gamma}$  will be studied more critically.

We suppose the as yet unknown forcing term  $\chi_{i\mu\nu}$  will be gradient dependent and can be expanded in a general form  $\chi_{i\mu\nu} = \varepsilon\chi_{i\mu\nu}^{(1)} + \varepsilon^2\chi_{i\mu\nu}^{(2)}$  in addition to the usual:

$$\left. \begin{aligned} t_1 = \varepsilon t \quad , \quad t_2 = \varepsilon^2 t \quad , \quad \partial_t = \varepsilon\partial_{t_1} + \varepsilon^2\partial_{t_2} \\ x_1 = \varepsilon x \quad , \quad x_2 = \varepsilon^2 x \quad , \quad \partial_x = \varepsilon\partial_{x_1} + \varepsilon^2\partial_{x_2} \\ g_i = g_{i\mu\nu}^{(0)} + \varepsilon g_{i\mu\nu}^{(1)} + \varepsilon^2 g_{i\mu\nu}^{(2)} \end{aligned} \right\} \quad (4.39)$$

The above expansion will yield:

$$\begin{aligned} & \varepsilon \left( \Delta t \partial_{t_1} g_{i\mu\nu}^{(0)} + \Delta t e_{i\alpha} \partial_{\alpha_1} g_{i\mu\nu}^{(0)} \right) + \varepsilon^2 \left( \Delta t \partial_{t_1} g_{i\mu\nu}^{(1)} + \Delta t \partial_{t_2} g_{i\mu\nu}^{(0)} + \Delta t e_{i\alpha} \partial_{\alpha_1} g_{i\mu\nu}^{(1)} \right. \\ & \left. + \Delta t e_{i\alpha} \partial_{\alpha_2} g_{i\mu\nu}^{(0)} + \frac{\Delta t^2}{2} \partial_{t_1} \partial_{t_1} g_{i\mu\nu}^{(0)} + \Delta t^2 e_{i\alpha} \partial_{\alpha_1} \partial_{t_1} g_{i\mu\nu}^{(0)} + \frac{\Delta t^2}{2} e_{i\alpha} e_{i\beta} \partial_{\alpha_1} \partial_{\beta_1} g_{i\mu\nu}^{(0)} \right) \\ & = -\frac{1}{\tau_Q} \left( g_{i\mu\nu}^{(0)} + \varepsilon g_{i\mu\nu}^{(1)} + \varepsilon^2 g_{i\mu\nu}^{(2)} - g_{i\mu\nu}^{(eq)} \right) + \varepsilon \chi_{i\mu\nu}^{(1)} + \varepsilon^2 \chi_{i\mu\nu} \end{aligned} \quad (4.40)$$

Arranging terms in ascending order of  $\varepsilon$ , we obtain

$$O(\varepsilon^0) \quad \quad \quad g_{i\mu\nu}^{(0)} = g_{i\mu\nu}^{(eq)} \quad (4.41)$$

$$O(\varepsilon^1) \quad \quad -\tau_Q \Delta t (\partial_{t_1} + e_{i\alpha_1} \partial_{\alpha_1}) g_{i\mu\nu}^{(0)} + \tau_Q \chi_{i\mu\nu}^{(1)} = g_{i\mu\nu}^{(1)} \quad (4.42)$$

$$\begin{aligned} O(\varepsilon^2) \quad & \left( \frac{1}{2} - \tau_Q \right) \Delta t (\partial_{t_1} + e_{i\alpha} \partial_{\alpha_1}) g_{i\mu\nu}^{(1)} - \tau_Q \Delta t (\partial_{t_2} + e_{i\alpha} \partial_{\alpha_2}) g_{i\mu\nu}^{(0)} \\ & - \frac{\tau_Q \Delta t}{2} \chi_{i\mu\nu}^{(1)} + \tau_Q \chi_{i\mu\nu}^{(2)} = g_{i\mu\nu}^{(2)} \end{aligned} \quad (4.43)$$

in which we have used the  $O(\varepsilon^1)$  result of equation 4.42 to replace a term of the form  $(\partial_{t_1} + e_{i\alpha} \partial_{\alpha_1}) g_{i\mu\nu}^{(0)}$  in the  $O(\varepsilon^2)$  result.

Taking the zeroth moment ( $\sum_i$ ) of the first order (equation 4.42) expansion whilst respecting equation 4.37 yields:

$$\partial_{t_1} (\zeta S_{\mu\nu}) + \partial_{\alpha_1} (\zeta u_\alpha S_{\mu\nu}) = \sum_i \frac{\chi_{i\mu\nu}^{(1)}}{\Delta t} \quad (4.44)$$

remembering our definition of the unit trace alignment tensor (equation 4.17) we have  $S_{\alpha\beta} = \frac{2Q_{\alpha\beta} - \delta_{\alpha\beta}}{3}$  and thus the above becomes (remember  $\zeta \rightarrow$  constant):

$$\zeta \partial_{t_1} (Q_{\mu\nu}) + \zeta \partial_{\alpha_1} (u_\alpha Q_{\mu\nu}) = \frac{3}{2\Delta t} \sum_i \chi_{i\mu\nu}^{(1)} \quad (4.45)$$

Taking the zeroth moment ( $\sum_i$ ) of the second order (equation 4.43) expansion whilst respecting equation 4.37 and again changing  $\underline{S}$  to  $\underline{Q}$  yields:

$$\left( 1 - \frac{1}{2\tau_Q} \right) \partial_{\alpha_1} \Omega_{\alpha\mu\nu}^{(1)} + \frac{2\zeta}{3} \partial_{t_2} Q_{\mu\nu} + \frac{2\zeta}{3} \partial_{\alpha_2} (u_\alpha Q_{\mu\nu}) = +\frac{1}{\Delta t} \sum_i \chi_{i\mu\nu}^{(2)} - \frac{1}{2} \sum_i \chi_{i\mu\nu}^{(1)} \quad (4.46)$$

To progress further the  $\Omega_{\alpha\mu\nu}^{(1)}$  term needs evaluating or more specifically  $g_{i\mu\nu}^{(1)}$  (in equation 4.42). This is a similar process to obtaining  $f_i^{(1)}$  in the momentum scheme. We use equation 4.18 to  $O(\underline{u})$  in equation 4.42. Taking the first moment of this gives rise to (using the product rule):

$$\Omega_{\gamma\mu\nu}^{(1)} = -\tau_Q \Delta t (\zeta S_{\mu\nu} \partial_{t_1}(u_\gamma) + u_\gamma \partial_{t_1}(\zeta S_{\mu\nu}) + \partial_{\gamma_1}(\zeta S_{\mu\nu} c_s^2)) + \tau_Q \sum_i e_{i\gamma} \chi_{i\mu\nu}^{(1)} \quad (4.47)$$

Remembering the zeroth moment result, equation 4.44, we may replace the term in  $\partial_{t_1}(\zeta S_{\mu\nu})$  and find:

$$\begin{aligned} \Omega_{\gamma\mu\nu}^{(1)} = & -\tau_Q \Delta t \left( \zeta S_{\mu\nu} \partial_{t_1}(u_\gamma) - u_\gamma \partial_{\alpha_1}(\zeta u_\alpha S_{\mu\nu}) + \frac{u_\gamma}{\Delta t} \sum_i \chi_{i\mu\nu}^{(1)} + \partial_{\gamma_1}(\zeta S_{\mu\nu} c_s^2) \right) \\ & + \tau_Q \sum_i e_{i\gamma} \chi_{i\mu\nu}^{(1)} \end{aligned} \quad (4.48)$$

We can further recall an earlier result obtained in text above equation 4.32 to find:

$$\partial_{t_1} u_\beta = -\frac{c_s^2 \partial_{\beta_1} \rho - \tau_P \partial_{\gamma_1} F_{\beta\gamma} c_s^2 + u_\beta \partial_{\gamma_1}(\rho u_\gamma)}{\rho} \quad (4.49)$$

inserting equation 4.49 into equation 4.48 and applying the incompressibility condition gives:

$$\begin{aligned} \Omega_{\gamma\mu\nu}^{(1)} = & -\tau_Q \Delta t \left( -\frac{\zeta S_{\mu\nu} \partial_{\beta_1} (F_{\gamma\beta}) c_s^2 \tau_P}{\rho} - u_\gamma u_\alpha \partial_{\alpha_1}(\zeta S_{\mu\nu}) + \frac{u_\gamma}{\Delta t} \sum_i \chi_{i\mu\nu}^{(1)} + c_s^2 \partial_{\gamma_1}(\zeta S_{\mu\nu}) \right) \\ & + \tau_Q \sum_i e_{i\gamma} \chi_{i\mu\nu}^{(1)} \end{aligned} \quad (4.50)$$

Upon converting  $\underline{S}$  to  $\underline{Q}$  equation 4.50 is inserted in the earlier second order zeroth moment equation 4.46 giving:

$$\begin{aligned} & \zeta \partial_{t_2} Q_{\mu\nu} + \zeta \partial_{\alpha_2}(u_\alpha Q_{\mu\nu}) + \frac{3}{2} \left( 1 - \frac{1}{2\tau_Q} \right) \left[ \frac{2\zeta \tau_P \tau_Q c_s^2 \Delta t \partial_{\alpha_1}(Q_{\mu\nu} \partial_{\beta_1}(F_{\alpha\beta}))}{3\rho} \right. \\ & + \frac{\zeta \tau_P \tau_Q \Delta t \delta_{\mu\nu} c_s^2}{3\rho} \partial_{\alpha_1}(\partial_{\beta_1} F_{\alpha\beta}) + \frac{\zeta^2 \tau_Q \Delta t}{3} \partial_{\alpha_1}(u_\alpha u_\gamma \partial_{\gamma_1} Q_{\mu\nu}) - \tau_Q \partial_{\alpha_1}(u_\alpha \sum_i \chi_{i\mu\nu}^{(1)}) \\ & \left. - \frac{2\tau_Q \Delta t c_s^2 \zeta}{3} \partial_{\alpha_1}(\partial_{\alpha_1} Q_{\mu\nu}) + \tau_Q \partial_{\alpha_1}(\sum_i e_{i\alpha} \chi_{i\mu\nu}^{(1)}) \right] = -\frac{3}{4} \sum_i \chi_{i\mu\nu}^{(1)} + \frac{3}{2\Delta t} \sum_i \chi_{i\mu\nu}^{(2)} \end{aligned} \quad (4.51)$$

Both  $F_{\alpha\beta}$  and  $\chi_{i\alpha\beta}$  depend upon gradients of  $\underline{u}$  and  $\underline{Q}$  thus we omit higher order gradient terms<sup>1</sup> from our analysis in equation 4.51. Further in the limit  $M = \frac{|\underline{u}|}{c_s} \ll 1$ , which holds for low  $Re$  LC's we need only to keep terms of  $O(\underline{u})$ .

Recombining the  $O(\varepsilon^1)$  equation 4.45 and  $O(\varepsilon^2)$  equation 4.51 expansion we obtain:

$$\partial_t Q_{\mu\nu} + u_\alpha \partial_\alpha Q_{\mu\nu} = \frac{c_s^2}{2} (2\tau_Q - 1) \Delta t \partial_\alpha (\partial_\alpha Q_{\mu\nu}) - \frac{3\zeta}{4} \sum_i \chi_{i\mu\nu}^{(1)} + \frac{3}{2\Delta t \zeta} \sum_i \chi_{i\mu\nu}^{(2)} \quad (4.52)$$

<sup>1</sup>In a future work the consequences of the Landau expansion terms present in  $F_{\lambda\gamma}$  will be studied more critically.

A detailed comparison of the terms in this equation and the target order equation (equation 4.3 and equation 4.8) gives the identification made in equation 4.20. We now compare remaining terms with the force terms in equation 4.52. We make an assumption that as the forcing term is gradient dependent we can add it at  $O(\varepsilon^2)$ , so we choose  $\sum_i \chi_{i\mu\nu}^{(1)} = 0$  and that of equation 4.19. This completes the order analysis.

#### 4.2.4 Lattice Units and Time Scales

LBM simulations have units of the lattice, length  $\Delta x$  and time  $\Delta t$  and the transport coefficients are also in lattice units. In order to extract useful information from the lattice simulation we must relate lattice units to the real world (SI) through use of the key dimensionless numbers established in §2.4.2. If we denote lattice units by a prime (for example  $L' =$  number of lattice sites in a given direction) we may carry out a straight forward non-dimensionalisation of the macroscopic lattice evolution equations equation 4.36 and equation 4.52. This results in dimensionless numbers:

$$Re' = \frac{2\bar{U}'\bar{L}'}{c_s^2(2\tau_P-1)} \quad (4.53)$$

$$Er' = \frac{2\bar{U}'\bar{L}'}{c_s^2(2\tau_Q-1)} \quad (4.54)$$

$$De' = \frac{\mu'_1\bar{U}'}{\alpha'_F\bar{L}'} \quad (4.55)$$

Extracting the characteristic timescales for variation in these quantities gives (for now we approximate  $\tau_P = \tau_Q = 1$ ,  $L' = 200$  lattice units):

$$\bar{\tau}'_P = \frac{2\bar{L}'^2}{c_s^2(2\tau_P-1)} \sim 10^5 \Delta t \quad (4.56)$$

$$\bar{\tau}'_n = \frac{2\bar{L}'^2}{c_s^2(2\tau_Q-1)} \sim 10^5 \Delta t \quad (4.57)$$

$$\bar{\tau}'_S = \frac{\mu'_1}{\alpha'_F} \sim 10^1 \Delta t \quad (4.58)$$

Taking the ratio of characteristic SI to LB times gives the time value of the LB discrete time step (one iteration). Using typical values shows that:  $\Delta t_p \sim 10^{-13}s$ ,  $\Delta t_n \sim 10^{-8}s$ ,  $\Delta t_s \sim 10^{-8}s$ . Thus we see the momentum evolution equation needs to be iterated many times to catch up with a single iteration of the order scheme. Alternatively noticing for small laminar creeping flows in which the order changes slowly ( $Re \ll 1$ ) the equilibrium flow field will be reached in a smaller number of  $\Delta t_p$  and we may jump forward in time to the next  $\Delta t_n \sim \Delta t_s$  which reduces the

overall processing time. We also point out that strong forces constrain the order parameter ( $Er/De$ ), thus the order parameter takes only a few time steps to reach equilibrium and thus as a first approximation no explicit separation of the order and director evolution is necessary.

(It should be noted for quantitative dynamics of defects an explicit order and director time scale separation should be undertaken i.e. finding the correct order for a given director structure, see equation 2.58. The quantitative effects of this are ignored in this work but warrants further investigation in future studies.)

To compare the numerical simulation data to experimental data we need to obey the law of similarity. In other words our lattice  $Re'$ ,  $Er'$ ,  $De'$  numbers need to equal the real  $Re$ ,  $Er$ ,  $De$  numbers. Observation of equation 4.53 and 4.54 shows that  $Er' = Re'$  which is in marked contrast to  $Er \neq Re$  of equation 2.52 and equation 2.53. Assuming  $[c_s^2, \tau_P, \tau_Q]^1$  and  $[L']^2$  to be fixed we are only left with  $\bar{U}'$  to be changed to achieve similarity. Also apparent is that  $\bar{U}'$  for the momentum scheme and  $\bar{U}'$  for the order scheme must also be different by an amount  $Er/Re = \bar{\tau}_n/\bar{\tau}_P$ . So in changing the velocity from one scheme to the other the viscous forces are changed, it thus being necessary to scale all other forces by this same amount accordingly in order to re-balance the equations of motion. Once the forces are balanced a simulation may be completed.

To further explain we list the appropriate lattice values denoting a superscript  $P$  for the momentum scheme and superscript  $Q$  for the order scheme, see table 4.1. Note  $S_0$  stands for the equilibrium order parameter not simulation evolved order parameter. The relations in table 4.1 are obtained from the Chapman-Enskog relations equations 4.14 and equation 4.20 and comparisons of the EL and  $Q$  tensor equations. Additional to table 4.1 are other material and situation specific constants such as geometry, in total we typically have a 25 dimensional parameter space making for a formidable numerical task.

In table 4.1 for more complex systems the characteristic elastic constant should be enhanced to the system studied, analogous to the Fredericksz calculations [46].

---

<sup>1</sup>These parameters are fixed by the lattice stencil and it is shown [153] LB schemes are most accurate and stable and  $\tau = 1$

<sup>2</sup>The characteristic lattice length  $\bar{L}'$  is constrained to  $\gtrsim d/\xi$  where  $d$  is the SI simulation length and  $\xi \sim 10 - 100\text{\AA}$  is the coherence length of the order parameter given by equation 2.62. In other words we work at a resolution that is able to resolve variations of the order parameter.

$\mu_1^{IP} = \frac{\mu_1 \rho' c_s^2 (2\tau_P - 1) \Delta t}{2\eta_{eff}}$	$\mu_1^{IQ} = \mu_1^{IP} \left( \frac{Er}{Re} \right)$
$\mu_2^{IP} = \frac{\mu_2 \mu_1^{IP}}{\mu_1}$	$\mu_2^{IQ} = \mu_2^{IP} \left( \frac{Er}{Re} \right)$
$\beta_1^{IP} = \frac{\beta_1 \mu_1^{IP}}{\mu_1}$	$\beta_1^{IQ} = \beta_1^{IP} \left( \frac{Er}{Re} \right)$
$\beta_4^{IP} = \frac{\beta_4 \mu_1^{IP}}{\mu_1}$	$\beta_4^{IQ} = \beta_4^{IP} \left( \frac{Er}{Re} \right)$
$\beta_5^{IP} = \frac{\beta_5 \mu_1^{IP}}{\mu_1}$	$\beta_5^{IQ} = \beta_5^{IP} \left( \frac{Er}{Re} \right)$
$\beta_6^{IP} = \frac{\beta_6 \mu_1^{IP}}{\mu_1}$	$\beta_6^{IQ} = \beta_6^{IP} \left( \frac{Er}{Re} \right)$
$L_1^{IP} = L_1^{IQ} \left( \frac{Er}{Re} \right)^{-2}$	$L_1^{IQ} = \mu_1^{IQ} \frac{c_s^2}{2} (2\tau_Q - 1) \Delta t$
$L_2^{IP} = L_2^{IQ} \left( \frac{Er}{Re} \right)^{-2}$	$L_2^{IQ} = L_2 \frac{L_1^{IQ}}{L_1}$
$L_3^{IP} = L_3^{IQ} \left( \frac{Er}{Re} \right)^{-2}$	$L_3^{IQ} = L_3 \frac{L_1^{IQ}}{L_1}$
$L_4^{IP} = L_4^{IQ} \left( \frac{Er}{Re} \right)^{-2}$	$L_3^{IQ} = L_4 \frac{L_1^{IQ}}{L_1}$
$\alpha_F^{IP} = \alpha_F^{IQ} \left( \frac{Er}{Re} \right)^{-2}$	$\alpha_F^{IQ} = \alpha_F \frac{\bar{L}^2 L_1^{IQ}}{L_1^2 L_1}$
$\beta_F^{IP} = \beta_F^{IQ} \left( \frac{Er}{Re} \right)^{-2}$	$\beta_F^{IQ} = \beta_F \frac{\alpha_F}{\alpha_F^{IQ}}$
$\gamma_F^{IP} = \gamma_F^{IQ} \left( \frac{Er}{Re} \right)^{-2}$	$\gamma_F^{IQ} = \gamma_F \frac{\alpha_F}{\alpha_F^{IQ}}$
$\Delta t_P = \Delta t_Q \left( \frac{Er}{Re} \right)^{-1}$	$\Delta t_Q (= \Delta t_n = \Delta t_s) = \frac{c_s^2}{2} (2\tau_Q - 1) \frac{\Delta t^2 \gamma_1 \bar{L}^2}{K_{22} \bar{L}^2}$
$E^{IP} = E^{IQ} \left( \frac{Er}{Re} \right)^{-3}$	$E^{IQ} = \sqrt{\frac{\epsilon_0 \Delta \epsilon_a E^2 9S_0^2 \mu_1^{IQ} \Delta t_Q}{2\gamma_1 \Delta t \epsilon_0^{IQ} \Delta \epsilon_a^{IQ}}}$
$\mu_s^{IP} = \mu_s^{IQ} \left( \frac{Er}{Re} \right)^{-1}$	$\mu_s^{IQ} = \frac{L_1^{IQ} \gamma_s \Delta \bar{L}}{K_{22} \Delta t_Q \bar{L}}$
$W^{IP} = W^{IQ} \left( \frac{Er}{Re} \right)^{-2}$	$W^{IQ} = \frac{2W \mu_s^{IQ} \Delta t_Q}{\gamma_s \Delta t}$ as per equation 2.34
$e_{11}^{IP} = e_{11}^{IQ} \left( \frac{Er}{Re} \right)^{-1}$	$e_{11}^{IQ} = \frac{e_{11} 9S_0^2 \mu_s^{IQ} \Delta t_Q E}{2\gamma_s \Delta t E^{IQ}}$
$e_{33}^{IP} = e_{33}^{IQ} \left( \frac{Er}{Re} \right)^{-1}$	$e_{33}^{IQ} = \frac{e_{33} 9S_0^2 \mu_s^{IQ} \Delta t_Q E}{2\gamma_s \Delta t E^{IQ}}$

Table 4.1: LB simulation parameters. All parameters above can be calculated for a given set of EL coefficients. For more complex systems elastic constants should be enhanced to characteristic constants of the system. We also choose  $\Delta \epsilon'_a = \Delta \epsilon_a$ ,  $\epsilon_0^{IQ} = 1$ .

As an example a cell involving twist distortion involves just the  $\bar{K} = K_{22}$  elastic constant; for a director confined to just in-plane splay and bend distortions the appropriate constant would be  $\bar{K} = (K_{11} + K_{33})/2$ .

## 4.2.5 Boundaries

Whilst it is important to develop accurate methods for the governing equations, it is probably even more important to establish accurate boundary conditions. This is highlighted when considering an LCD cell whose characteristic width is only a few microns and whose entire bulk behaviour is dominated by molecular surface interactions.

For simulations in this thesis we will only consider boundaries that are either periodic or solid. For the velocity field in a LC it is usual to take the non-slip boundary condition of isotropic fluids. We find the straight forward application of the BBC [116] to be a robust and simple method (equations given in §3.1).

For the alignment fields the boundary condition must obey equation 2.51 for which an equivalent BBC scheme applied to the  $g_{i\mu\nu}$  distribution functions does not apply. As a first approximation we assume all boundaries will lie at a lattice node. We then combine standard numerical methods with the LB method. The collision step on the boundary is then taken as<sup>1</sup>:

$$g_{i\alpha\beta}(\underline{x}_B, t + \Delta t) = \tilde{g}_{i\alpha\beta}(\underline{x}_B, t) = \frac{g_{i\gamma\gamma}(\underline{x}_B, t) (2Q_{\alpha\beta}(\underline{x}_B, t + \Delta t) + \delta_{\alpha\beta})}{3} \quad (4.59)$$

where the  $\tilde{\phantom{x}}$  denotes value post-collision (pre-streaming) and  $Q_{\alpha\beta}(\underline{x}_B, t + \Delta t)$  is a linear evolution of equation 2.51, being:

$$\begin{aligned} Q_{\alpha\beta}(\underline{x}_B, t + \Delta t) &= Q_{\alpha\beta}(\underline{x}_B, t) + \Delta Q_{\alpha\beta} \\ &= Q_{\alpha\beta}(\underline{x}_B, t) + \frac{\Delta t}{\mu_S} (h_{\alpha\beta}^S - \lambda^S \delta_{\alpha\beta} - \lambda_\gamma^S \varepsilon_{\alpha\beta\gamma}) \end{aligned} \quad (4.60)$$

Implemented in this way we presume, for flat surfaces we have second order accuracy but for smooth curved surfaces only first order in both momentum and alignment. We extract surface gradients from second order extrapolations from the bulk. From §2.4.1 we get  $h_{\alpha\beta}^S$ ,  $\lambda^S$ ,  $\lambda_\gamma^S$  to be:

$$\left. \begin{aligned} \lambda^S &= \frac{1}{3} h_{\mu\mu}^S, & \lambda_\gamma^S &= \frac{1}{2} \varepsilon_{\gamma\alpha\beta} h_{\alpha\beta}^S, \\ h_{\alpha\beta}^S &= -L_1 \hat{\nu}_\lambda \partial_\lambda Q_{\alpha\beta} - L_2 \hat{\nu}_\beta \partial_\lambda Q_{\alpha\lambda} - L_3 \hat{\nu}_\lambda \partial_\beta Q_{\alpha\lambda} - L_4 \hat{\nu}_\lambda Q_{\mu\lambda} \partial_\mu Q_{\alpha\beta} \\ &\quad - \frac{4\pi L_1}{P_{ch}} \hat{\nu}_\lambda \varepsilon_{\mu\lambda\alpha} Q_{\mu\beta} + \frac{4\pi L_4}{P_{ch}} \hat{\nu}_\lambda \varepsilon_{\mu\lambda\alpha} Q_{\mu\eta} Q_{\eta\beta} \\ &\quad + C_1 E_\alpha \hat{\nu}_\beta + C_2 Q_{\gamma\alpha} E_\gamma \hat{\nu}_\beta - W(Q_{\alpha\beta} - Q_{\alpha\beta}^\circ) \end{aligned} \right\} \quad (4.61)$$

### 4.3 Treatment of Externally Applied Fields

In § 2.1.5 we noted that for an externally applied field the electric and magnetic fields experienced depends on the local molecular alignment. This implies that we must solve yet another Euler equation or equivalently apply Maxwell's equations of electromagnetism. In LC's the diamagnetism is small and it is usual to use a constant magnetic field strength in calculations. The dielectric parameters are however larger and we must treat this appropriately for accurate results.

---

<sup>1</sup>In a future work the consequences of this boundary update scheme and how it interacts in time with the bulk will be studied more critically.

### 4.3.1 Electric Field Solver

Maxwell's equations (equation 2.32) state (ignoring electro-hydrodynamic ion convection):

$$\partial_\alpha D_\alpha = \sigma_f \quad (4.62)$$

$$D_\alpha = \epsilon_0 \epsilon_{\alpha\beta} E_\beta + P_\alpha \quad (4.63)$$

$$E_\beta = -\partial_\beta \phi \quad (4.64)$$

Setting the free charge to zero we then insert equation 4.64 into equation 4.63 and then subsequently into equation 4.62 giving:

$$-\partial_\alpha (\epsilon_0 \epsilon_{\alpha\beta} \partial_\beta \phi) + \partial_\alpha P_\alpha = 0 \quad (4.65)$$

Making use of equation 2.12 for the dielectric tensor, the product rule and subsequent rearrangement for the  $\partial_\gamma \partial_\gamma \phi$  term:

$$\partial_\gamma \partial_\gamma \phi = \frac{-2\epsilon_0 \Delta \epsilon_a^{max} Q_{\alpha\beta} \partial_\alpha (\partial_\beta \phi) - 2\epsilon_0 \Delta \epsilon_a^{max} \partial_\alpha (Q_{\alpha\beta}) \partial_\beta (\phi) - \epsilon_0 \partial_\beta (\phi) \partial_\beta (\epsilon_{\gamma\gamma}) + 3\partial_\alpha P_\alpha}{\epsilon_0 \epsilon_{\gamma\gamma}} \quad (4.66)$$

which is a Poisson equation and in the isotropic fluid limit is Laplace's equation. (We have presumed a pure LC and that  $\partial_t \epsilon_\perp = \partial_t \epsilon_\parallel = \partial_\alpha \epsilon_\perp = \partial_\alpha \epsilon_\parallel = 0$ ). To solve this equation for  $\phi$  in our simulation lattice we consider a spatial expansion of the potential on our lattice at time  $t$ :

$$\phi(\underline{x} + \underline{e}_i \Delta t, t) = \phi(\underline{x}, t) + \Delta t e_{i\gamma} \partial_\gamma \phi(\underline{x}, t) + \frac{\Delta t^2 e_{i\alpha} e_{i\beta}}{2} \partial_\alpha \partial_\beta \phi(\underline{x}, t) \quad (4.67)$$

summing upon  $i$  throughout and multiplying by the lattice link weight ( $t_i$ ) whilst respecting velocity summation equations 4.22 we get:

$$\sum_i t_i \phi(\underline{x} + \underline{e}_i \Delta t, t) = \phi(\underline{x}, t) + \frac{c_s^2 \Delta t^2}{2} \partial_\gamma \partial_\gamma \phi(\underline{x}, t) \quad (4.68)$$

hence:

$$\phi(\underline{x}, t) = \sum_i t_i \phi(\underline{x} + \underline{e}_i \Delta t, t) - \frac{c_s^2 \Delta t^2}{2} \partial_\gamma \partial_\gamma \phi(\underline{x}, t) \quad (4.69)$$

Equation 4.69 together with equation 4.66 provides an expression for the lattice potential:

$$\phi(\underline{x}, t) = \left. \begin{aligned} & \sum_i t_i \phi(\underline{x} + \underline{e}_i \Delta t, t) - \frac{c_s^2 \Delta t^2}{2\epsilon_0 \epsilon_{\gamma\gamma}} [-2\epsilon_0 \Delta \epsilon_a^{max} Q_{\alpha\beta} \partial_\alpha (\partial_\beta \phi) \\ & - 2\epsilon_0 \Delta \epsilon_a^{max} \partial_\alpha (Q_{\alpha\beta}) \partial_\beta (\phi) - \epsilon_0 \partial_\beta (\phi) \partial_\beta (\epsilon_{\gamma\gamma}) + 3\partial_\alpha P_\alpha] \end{aligned} \right\} \quad (4.70)$$

Keeping the relaxation theme of the LB technique we use a standard successive over relaxation (SOR) scheme:

$$\phi^{g+1} = \phi^g - \omega (\phi^g - \phi^{(eq)}) \quad (4.71)$$

in which  $\phi^{g+1}$  is a better approximation to the potential  $\phi^g$ , and  $\phi^{(eq)}$  is that of equation 4.70. This potential must be solved for each time step of the  $Q$ -tensor scheme.

### 4.3.2 Dielectric Cylinder in a Uniform Field

It is difficult to test equation 4.70 and equation 4.71 of the electrostatic solver against analytical solutions in the anisotropic case. In lieu, we look at the case of an isotropic dielectric cylinder (2D (x,z)) in an isotropic uniform field. Bleaney [47] derives analytical expressions for the case of an infinite medium and sphere. For a cylinder of radius  $R$  in an infinitely uniform electric field,  $E_0$  acting in the x-direction the potential is given by a solution of Laplace's equation:

$$\left. \begin{aligned} \phi_1(\underline{x}) &= \frac{-2E_0\epsilon_2x}{(\epsilon_1+\epsilon_2)}, & \text{for } r < R \\ \phi_2(\underline{x}) &= \frac{-E_0x(R^2(\epsilon_2-\epsilon_1)+(x^2+z^2)(\epsilon_1+\epsilon_2))}{(x^2+z^2)(\epsilon_1+\epsilon_2)}, & \text{for } r > R \end{aligned} \right\} \quad (4.72)$$

in which the region inside the cylinder has dielectric constant  $\epsilon_1$ , and the region outside the cylinder has dielectric constant  $\epsilon_2$ .

Applying the 'LB-type Poisson solver' with  $Q_{\alpha\beta} = 0$  should recover equation 4.72. However we are restricted to finite size. We thus proceed by setting two electrodes at  $x \pm \frac{X}{2}$  with boundary conditions  $\frac{E_0X}{2}$  in which  $X$ , ( $Y$ ), ( $Z$ ) are the number of simulation nodes in the  $x$ , ( $y$ ), ( $z$ ) directions. Periodic boundaries are applied in the  $y$  and  $z$  directions. The cylinder centre is at  $x = y = z = 0$  pointing into the  $y$  direction.

We consider two cases on a lattice of  $X = 100$ ,  $Y = 1$ ,  $Z = 120$  with cylinder  $R = 10$ . Case A has  $\epsilon_1 < \epsilon_2$ , case B has  $\epsilon_1 > \epsilon_2$ . The lines of isopotential of both numerical and analytical solutions are shown in figure 4.1.

Agreement between numerical and analytical solution is good. The small differences arise due to a) finite difference gradient calculations at a boundary and b) the finite size of the numerical calculation (which reduces as system size increases) at the far field boundaries in comparison with the analytical solution that uses infinite

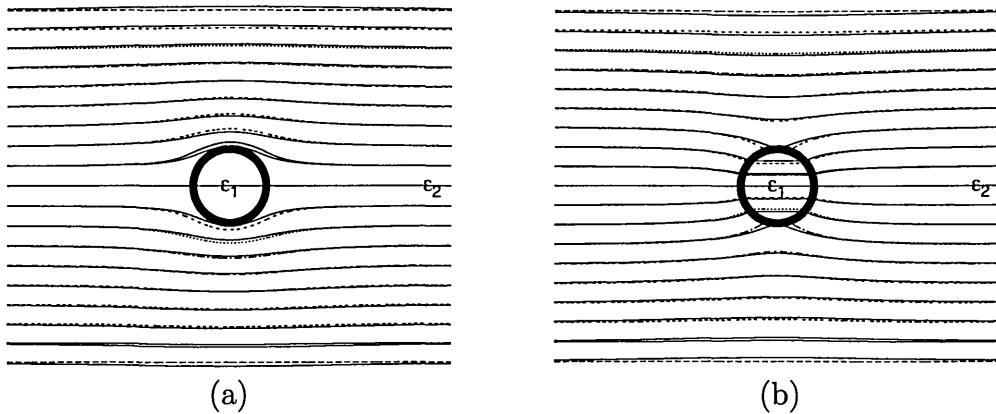


Figure 4.1: Lines of constant isopotential for a cylinder in a uniform electric field. Solid lines represent the analytical solution, as equation 4.72, and dashed lines represent the numerical solution. (a)  $\epsilon_1 = 7$ ,  $\epsilon_2 = 2$  (b)  $\epsilon_1 = 2$ ,  $\epsilon_2 = 7$ .

far field distance. We may now apply with confidence the ‘LB-type Poisson solver’ when treating LC external fields.

## 4.4 Testing the LB LC Solver

In this section we will test the derived LB solver against some analytical and numerical solutions to ensure it is both accurate and applicable. Examination of the Miesowicz viscosities will serve to validate the momentum algorithm. Shear flow alignment will validate the alignment algorithm. Studying a simple backflow cell will emphasise the need for separation of timescales. In all cases we use the  $D3Q27$  lattice whose details are given in table 3.1.

### 4.4.1 Equilibrium Phase Behaviour

In §2.1.2 we introduced the Landau deGennes theory for the nematic-isotropic phase transition. The equilibrium order parameter for unperturbed systems (no flows, no external fields, far from boundaries) with constant director was given by equation 2.18. By varying  $T$  in a periodic system we get values for the equilibrium order parameter. The simulation is initialised with uniform director. We take material parameters suitable for 5CB [40] in which  $a = 65000 \text{ J m}^{-3} \text{ K}^{-1}$ ,  $B = 530000 \text{ J m}^{-3}$ ,  $C = 980000 \text{ J m}^{-3}$ . Figure 4.2 shows numerical results for the order parameter against reduced temperature. The upper and lower limits of super cooling are clearly seen. The line corresponding to ‘V=0, T increasing’ corresponds identically

to the analytical curve in figure 2.2. Accuracy is achieved over the entire range to  $< 0.001\%$ . Also in Figure 4.2 is the equilibrium order parameter with an applied 10 volts and an applied 20 volts with  $\Delta\epsilon_a = 10.3$ . We see this serves to modify the transition temperature and in the 20 volt case the transition is continuous.

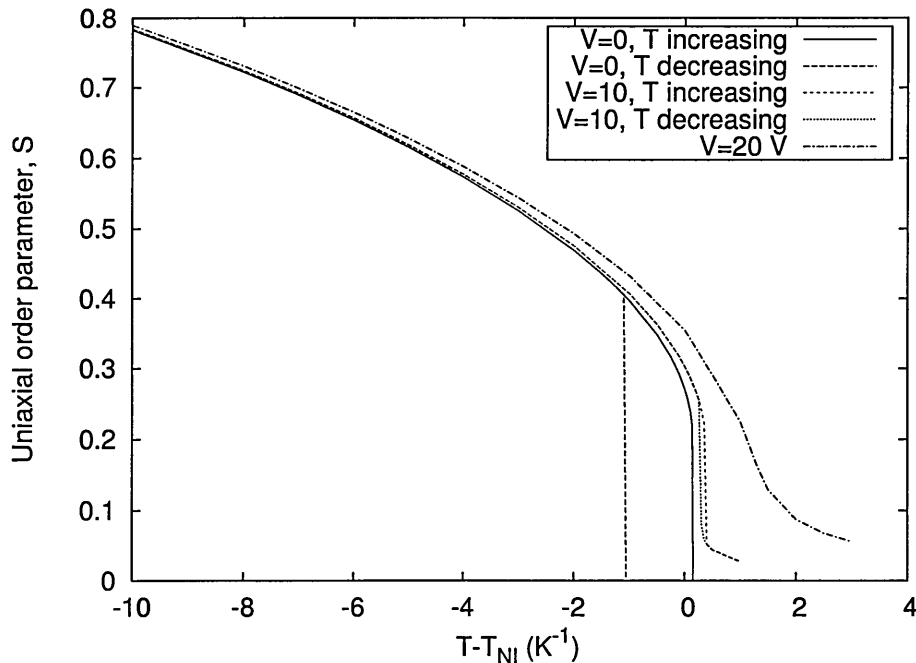


Figure 4.2: Graph showing the calculated equilibrium order parameters over a temperature range and at various applied voltages in an unconstrained nematic.

#### 4.4.2 Shear Flow Alignment

A simple shear is typically introduced to fluids between two rotating concentric cylinders (Couette flows). In nematics this is known to have an aligning effect in which the director minimises its torque. For a large enough channel width and strong enough shear, away from the walls the elastic properties may be ignored, alignment solely being determined by the viscous torque. From equation 4.3 we can solve for the director angle, in the uniaxial limit the result is dependent upon the viscosity ratio:

$$\cos(2\theta) = -\frac{3\mu_1 S}{\mu_2} = -\frac{\gamma_1 S}{\gamma_2 S_0} \quad (4.73)$$

$\theta$  being the angle relative to the velocity direction and  $S$  is the order parameter imposed by the shear and  $S_0$  the equilibrium order parameter. The factor 3 occurs in equation 4.73 as we use a three dimensional system (in [136] an explicit 2D system

gives a factor 4). In the limit  $S \rightarrow S_0$  this reduces to the result obtain from the EL theory [46] ( $\cos(2\theta) = -\gamma_1/\gamma_2$ ). The evolved order parameter in equation 4.73 can similarly be solved in terms of the shear rate,  $\dot{\gamma} = \partial_z u_x$ , we find the order typically being the largest solution to the sixth order polynomial:

$$1296\gamma_F^2 S^6 - 648\beta_F\gamma_F S^5 + (432\alpha_F\gamma_F + 81\beta_F^2)S^4 - 108\alpha_F\beta_F S^3 + 36(\alpha_F^2 + \mu_1^2\dot{\gamma}^2)S^2 - 12\mu_2^2\dot{\gamma}^2 = 0 \quad (4.74)$$

in all cases tested for aligning materials (parameters given below) the order increased, all be it small ( $\Delta S \sim 0.002$ ).

However, Olmsted [67] noted that shear flow is biaxial, thus upon use of equation 2.10 to solve equation 4.3 a more accurate result can be found:

$$\cos(2\theta) = -\frac{3\mu_1}{\mu_2}(3S + P_B) \quad (4.75)$$

We test equation 4.75 in the LB solver as a test of the alignment algorithm. Figure 4.3 shows both analytical and numerical results. Agreement between calculations is to at least 7 significant figures ( $< 0.00001\%$  error). The magnitude of biaxiality is typically  $P_B = 0.002$ . Agreement to equation 4.73 is to  $< 0.01\%$ . Simulations where done in a channel width of  $1.2\mu\text{m}$  with  $\dot{\gamma} \sim 10^4 \text{s}^{-1}$  for a viscosity set

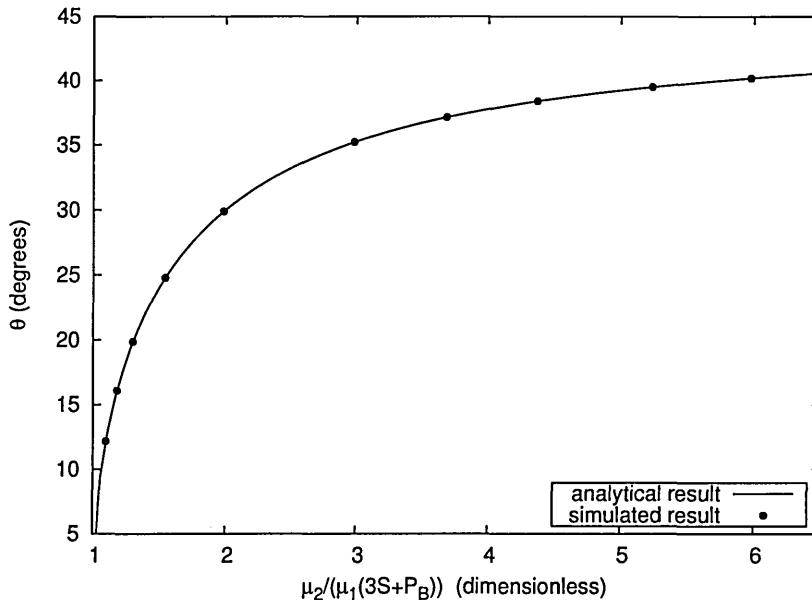


Figure 4.3: Bulk director re-orientation angle,  $\theta$ , as a function of viscosity ratio and order parameters. The continuous curve representing the exact solution to equation 4.75 and points from the LB solver.

( $\alpha_1 = -0.011$ ,  $\alpha_2 = -0.102$ ,  $\alpha_3 = -0.005$ ,  $\alpha_4 = 0.074$ ,  $\alpha_5 = 0.084$ ,  $\alpha_6 = -0.023$ )  $\text{kg m}^{-1} \text{s}^{-1}$  in which  $\alpha_2$  was varied whilst adjusting  $\alpha_6$  to obey the Parodi relation ( $\alpha_3 + \alpha_2 = \alpha_6 - \alpha_5$ ) at a temperature of  $T = T_{IN} - 4(T_{IN} - T^*)$ , well into the nematic phase ( $a, B, C$  are as §4.4.1) and  $\tau_P = \tau_Q = 1$ . At the  $z = 0$  and  $z = L$  boundaries we have infinite homeotropic anchoring and flow is entrained via equation 3.19 at  $+(-)u_x$  at the top (bottom) boundary, periodic boundaries are used in the  $x$  and  $y$  directions.

### 4.4.3 Miesowicz Viscosity Ratio's

An extension of the simple shear alignment of the previous section is with the addition of strong electric or magnetic field to impose a fixed director angle whilst shearing, see figure 1.9. With the field aligned in one of the three Cartesian directions (with positive anisotropy) pinning the director, the effective viscosity with flow in the  $x$  direction is known to be [46]:

$$\left. \begin{aligned} \eta_a &= \frac{1}{2}\alpha_4, & \text{for } \hat{n}_\alpha &= (0, 1, 0) \\ \eta_b &= \frac{1}{2}(\alpha_3 + \alpha_4 + \alpha_6), & \text{for } \hat{n}_\alpha &= (1, 0, 0) \\ \eta_c &= \frac{1}{2}(-\alpha_2 + \alpha_4 + \alpha_5), & \text{for } \hat{n}_\alpha &= (0, 0, 1) \end{aligned} \right\} \quad (4.76)$$

These are called the Miesowicz viscosities. Experimental measurement of these (together with  $\gamma_1$  and  $\eta_{12}$ ) provide a way to determine the Leslie coefficients,  $\alpha_{ii}$ . Solving the  $Q$  tensor momentum evolution equation (equation 2.43) in the uniaxial limit for an arbitrary fixed director angle we may obtain an expression for an effective viscosity,  $\eta^*$ :

$$\eta^* = \frac{\sigma_{\alpha\beta}^v}{2A_{\alpha\beta}} \quad (4.77)$$

$$\begin{aligned} \eta^* &= \frac{\beta_4}{2} + \frac{\mu_2}{8}S(3n_1^2 - 1) - \frac{\mu_2}{8}S(3n_3^2 - 1) + \frac{\beta_5}{4}S(3n_3^2 - 1) + \frac{9\beta_1}{4}S^2n_1^2n_3^2 \\ &+ \frac{\beta_6}{4}S(3n_1^2 - 1) + \frac{9\mu_1}{2}S^2n_1^2n_3^2 + \frac{9\mu_1}{2}S^2n_2^2n_3^2 - \frac{9\mu_1}{8}S^2n_1^2n_2^2 \\ &- \frac{\mu_1}{4}S^2(3n_1^2 - 1)(3n_3^2 - 1) + \frac{\mu_1}{8}S^2(3n_3^2 - 1)^2 + \frac{\mu_1}{8}S^2(3n_1^2 - 1)^2 \end{aligned} \quad (4.78)$$

with the corresponding Miesowicz values of:

$$\left. \begin{aligned} \eta_a &= \frac{\beta_4}{2} - \frac{\beta_5S}{4} - \frac{\beta_6S}{4} & \text{for } \hat{n}_\alpha &= (0, 1, 0) \\ \eta_b &= \frac{\beta_4}{2} + \frac{3\mu_2S}{8} - \frac{\beta_5S}{4} + \frac{\beta_6S}{2} + \frac{9S^2\mu_1}{8} & \text{for } \hat{n}_\alpha &= (1, 0, 0) \\ \eta_c &= \frac{\beta_4}{2} - \frac{3\mu_2S}{8} + \frac{\beta_5S}{4} - \frac{\beta_6S}{2} + \frac{9S^2\mu_1}{8} & \text{for } \hat{n}_\alpha &= (0, 0, 1) \end{aligned} \right\} \quad (4.79)$$

Biaxial contributions to these equations are straight forward but unnecessary because the applied field serves to cancel the biaxial contributions from the shear flow.

Using simulation parameters of the previous section in addition to an electric field ( $\Delta\epsilon = 10.3$ ,  $V = 75$  Volts), we apply non-slip stationary boundary conditions at the  $z = 0$  and  $z = L$  boundaries. Flow is induced by applying a body force at  $z = L/2$ . For a constant body force (hence stress) we have that:  $\eta_a\dot{\gamma}_a = \eta_b\dot{\gamma}_b = \eta_c\dot{\gamma}_c$  and hence:

$$\frac{\eta_a}{\eta_b} = \frac{\dot{\gamma}_a^{-1}}{\dot{\gamma}_b^{-1}}, \quad \frac{\eta_a}{\eta_c} = \frac{\dot{\gamma}_a^{-1}}{\dot{\gamma}_c^{-1}}, \quad \frac{\eta_b}{\eta_c} = \frac{\dot{\gamma}_b^{-1}}{\dot{\gamma}_c^{-1}} \quad (4.80)$$

By measuring the simulation  $\dot{\gamma}$  at  $z = L/4$  in comparison to the theoretical calculations from equation 4.79 gives the values seen in table 4.2 and it can be seen that the accuracy achieved is good.

Theory	Simulation	% error
$\eta_a/\eta_b = 1.446$	$\dot{\gamma}_a^{-1}/\dot{\gamma}_b^{-1} = 1.446$	$1.6 \times 10^{-4}$
$\eta_a/\eta_c = 0.227$	$\dot{\gamma}_a^{-1}/\dot{\gamma}_c^{-1} = 0.227$	$1.4 \times 10^{-4}$
$\eta_b/\eta_c = 0.157$	$\dot{\gamma}_b^{-1}/\dot{\gamma}_c^{-1} = 0.157$	$2.8 \times 10^{-5}$

Table 4.2: Table of theoretical (equation 4.79) and simulated ratio's of the Miesowicz viscosities.

We further test the momentum algorithm by noticing the lattice viscosities are all a linear function of  $\tau_p$ . Plotting  $\dot{\gamma}^{-1}$  as a function of  $\tau_p$  for the three director orientations should yield straight lines with a gradient to intercept ratio of  $-2$ . Figure 4.4 shows these results and table 4.3 shows the straight line fit. Accuracy is again to  $< 0.00001\%$ . These calculations serve to confirm accurate and correct behaviour of the momentum algorithm.

orientation	gradient	intercept	gradient/intercept
$a$	$6.096 \times 10^{-5}$	$-3.048 \times 10^{-5}$	$-2$
$b$	$4.215 \times 10^{-5}$	$-2.107 \times 10^{-5}$	$-2$
$c$	$2.688 \times 10^{-4}$	$-1.344 \times 10^{-4}$	$-2$

Table 4.3: Table of theoretical (equation 4.79) and simulated ratio's of the Miesowicz viscosities. Figures are quoted to 3 s.f. the calculated errors in gradient and intercept values are not shown as all are  $< \pm 10^{-10}$ .

#### 4.4.4 Kickback and Backflow Example

Consider a LC cell with homogeneous boundaries at the  $z = 0$  and  $z = L$  and periodic boundaries in the  $x$  and  $y$  directions, see figure 4.5c. For a nematic of

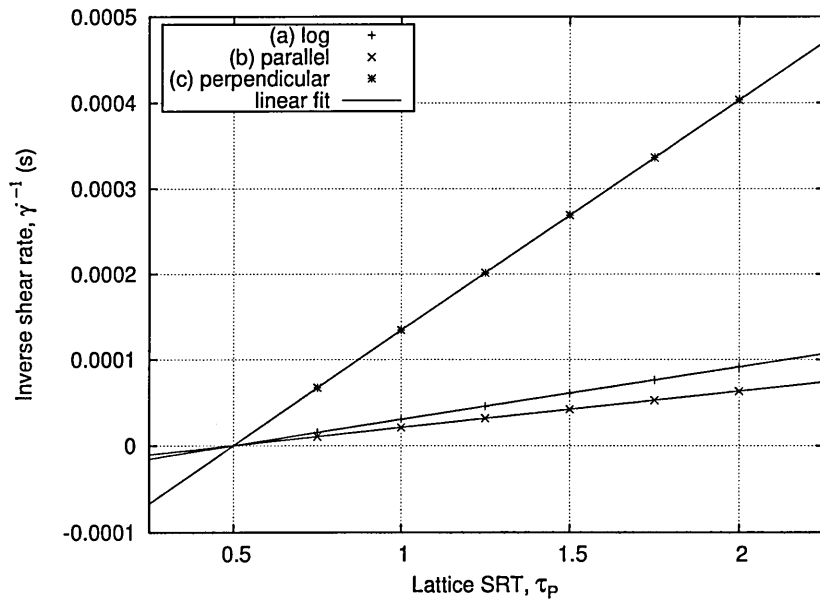


Figure 4.4: Effective viscosity in shear flow as a function of algorithmic parameter  $\tau_P$  showing linear dependence for the three Miesowicz director configurations.

positive dielectric anisotropy, away from the walls, an applied field between the top and bottom boundaries serves to align the director normal to the boundaries, see figure 4.5a. Switching off the field causes the director to over rotate due to flows, see figure 4.5b, ( $\theta > \pi/2$  where  $\theta$  is with respect to the  $x$  direction) and then gradually relax to  $\theta = 0$ , figure 4.5c. These are the well known [154] effects of backflow and kickback respectively.

Considering this set-up we follow the time evolution of the director, fluid velocity and order parameter when the electric field is switched off from 5 volts at a time  $t = 0$ . Material parameters are as the previous sections with the addition of now

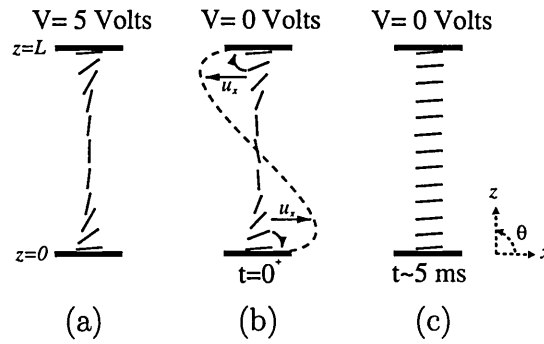


Figure 4.5: Homogeneous aligned nematic cell of positive dielectric anisotropy under (a) the influence of an electric field, (b) at switch off of the electric field, and (c) cell at rest.

infinite strength homogeneous alignment (assumed: uniaxial, pre-tilt  $1^\circ$  and surface order equal to the bulk equilibrium value) and ( $K_{11} = 10$ ,  $K_2 = 7$ ,  $K_{33} = 14$ ,  $K_{24} = 5$ )  $\times 10^{-12}$  m kg s $^{-2}$  and  $L = 1\mu\text{m}$ . Note there is a symmetry of the computation around  $z = L/2$ .

Figure 4.6 shows the director angle evolution at various positions across the cell. Figure 4.6a is a simulation including the time scale separation of the momentum and director dynamics as discussed in §4.2.4. Figure 4.6b does not include this separation and treats both momentum and order algorithms with the same time increment. Figure 4.6c is the case running the alignment algorithm by itself (no flow). When flows are included the kickback is observed ( $\theta > \pi/2$ ) in comparison to the case with no flow. When flows are included the backflow is observed to speed up the director relaxation towards  $\theta = 0$  (cf. figure 4.6c). For the case of the time scale separation a larger kickback is observed at smaller times whereas a smaller kickback at slightly larger times is observed for no time scale separation. The maximum director angle always occurs in the centre of the cell for the time scale separated method and the no flow method, this is not true for the method of no time scale separation.

Similarly we have figures 4.7a, 4.7b, 4.7c showing the order parameter relaxation for a time scale separation, no separation and no flow respectively. For all cases at  $t = 0$  the order falls from the value associated with the electric field instantaneously. We see associated with the kickback is an increase in order parameter in figure 4.7a (all be it small). The minimum in order corresponds to positions nearer the wall. For the case of no time scale separation the order parameter fluctuates rapidly. For the case of no flow the order never rises above the bulk equilibrium value.

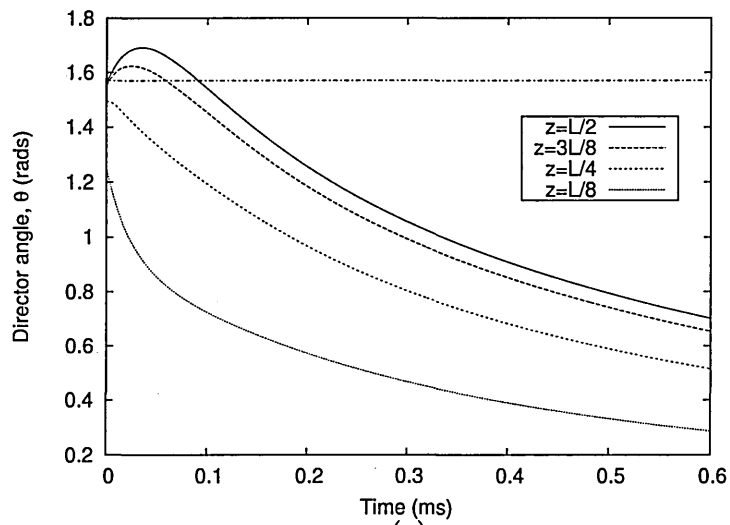
In figure 4.8a and 4.8b we follow the velocity of the time separation method and the no time scale separation method respectively. As the symmetry of the calculation dictates all flows occur in the  $x$  direction. A significantly larger and quicker flow is observed in the positive  $x$  direction for the case of time scale separation and the evolution of velocity is more uniform. Note the maximum velocity occurs at  $z = L/4$ . In contrast when no time scale separation is included the flow velocities associated with the kickback are an order of magnitude smaller. They are also not as uniform with the maximum velocity occurring at the  $z = 3L/8$  position.

The correct profiles both theoretically and physically are those of figures 4.6a, 4.7a and 4.8a which compare qualitatively with [154] (not quantitatively as [154] assumes an infinite field). The spatial evolution of the director, velocity and order may be seen more clearly from figures 4.9, 4.10 and 4.11 respectively.

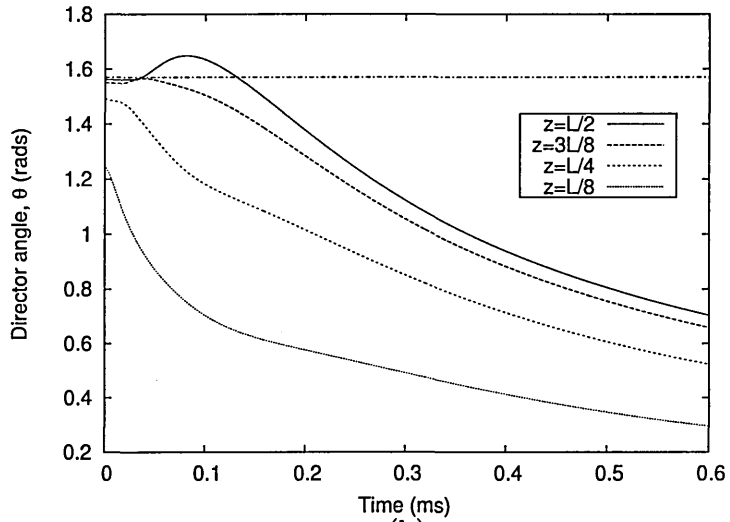
We point out that contained in figures 4.10 are velocity profiles for the time  $t = 0$ . Although physically they should not be present it is an artifact of the numerical gradient calculations and lattice resolution chosen. They arise because numerically both  $\partial_\alpha Q_{\gamma\gamma} = \partial_\alpha Q_{11} + \partial_\alpha Q_{22} + \partial_\alpha Q_{33} \neq 0$  and  $n_\alpha \partial_\gamma n_\alpha = n_x \partial_\gamma n_x + n_y \partial_\gamma n_y + n_z \partial_\gamma n_z \neq 0$ . Thus for a non-uniform system in which gradients in  $\mathbf{Q}$  are present, there exists a residual velocity and is an artifact of all numerical nemato-dynamics calculations which can be reduced with increased resolution.

## 4.5 Conclusions

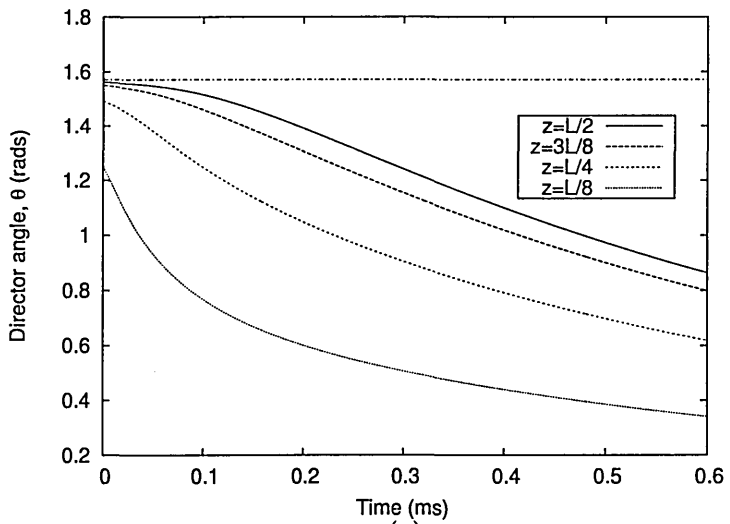
A LB nemato-dynamics scheme is presented together with a Chapman-Enskog analysis to justify its origin. It has been validated against a number of test cases and shown to be in good agreement with predicted values.



(a)



(b)



(c)

Figure 4.6: Director relaxation after the turn off of an applied 5 V field at various positions across a cell. Calculations with (a) correct time scale separation of momentum and director, (b) no time scale separation between momentum and director, and (c) no flow included.

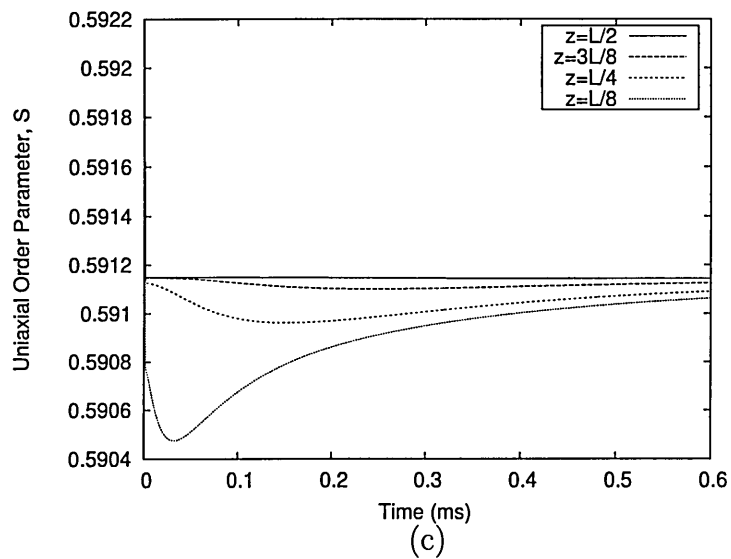
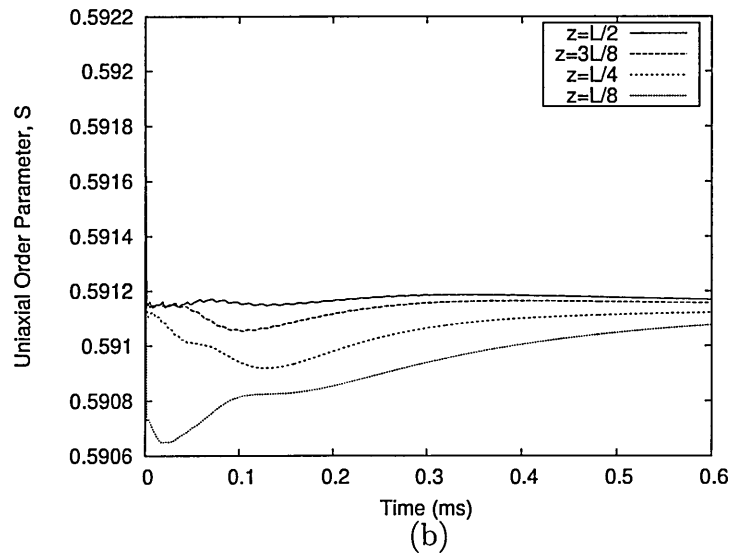
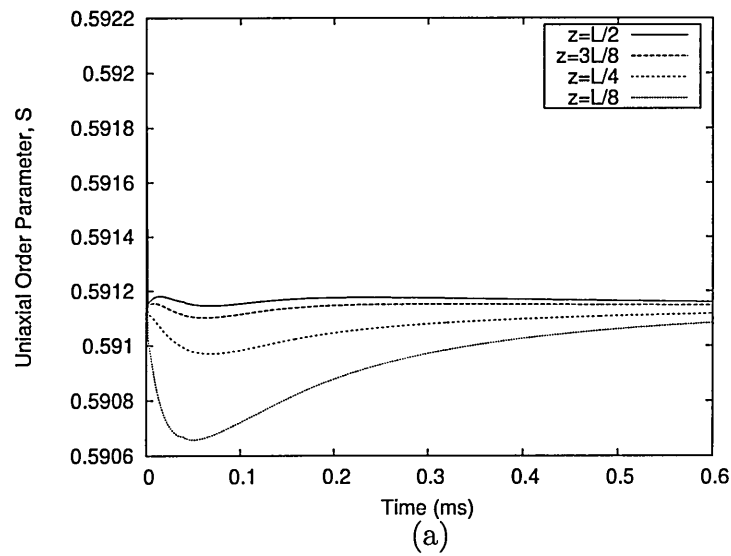


Figure 4.7: Uniaxial order parameter relaxation after the turn off of an applied 5 V field at various positions across a cell. Calculations with (a) correct time scale separation of momentum and director, (b) no time scale separation between momentum and director, and (c) no flow included.

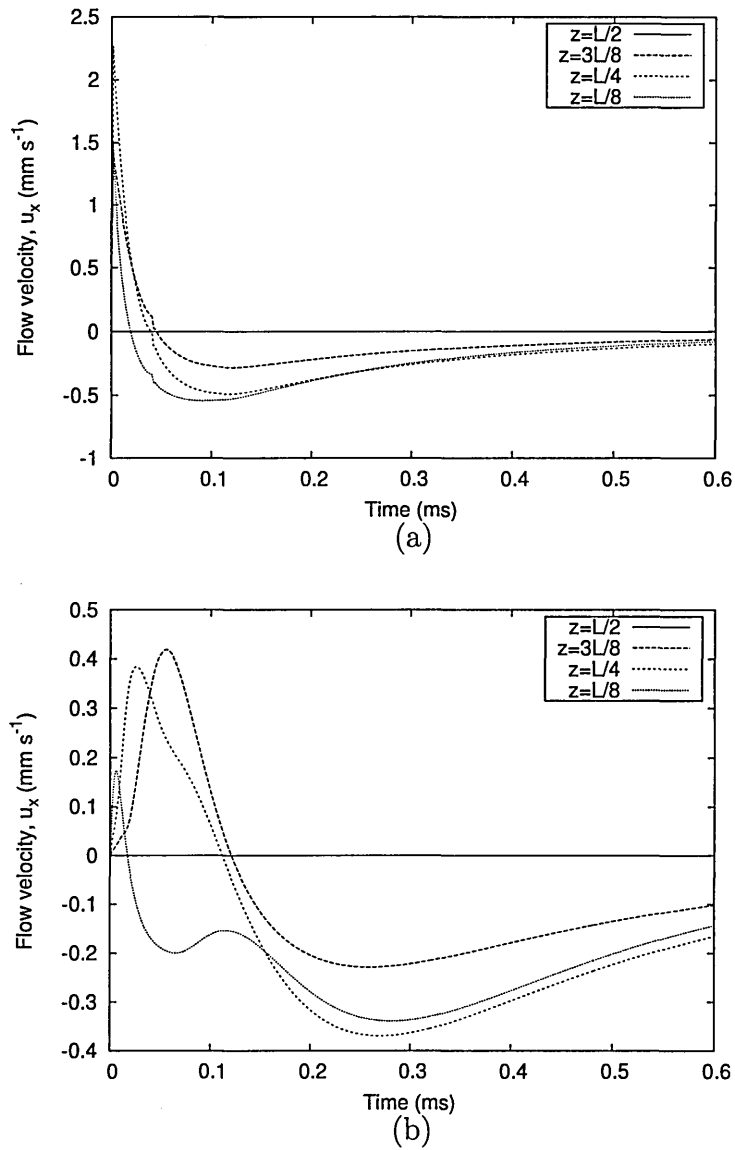
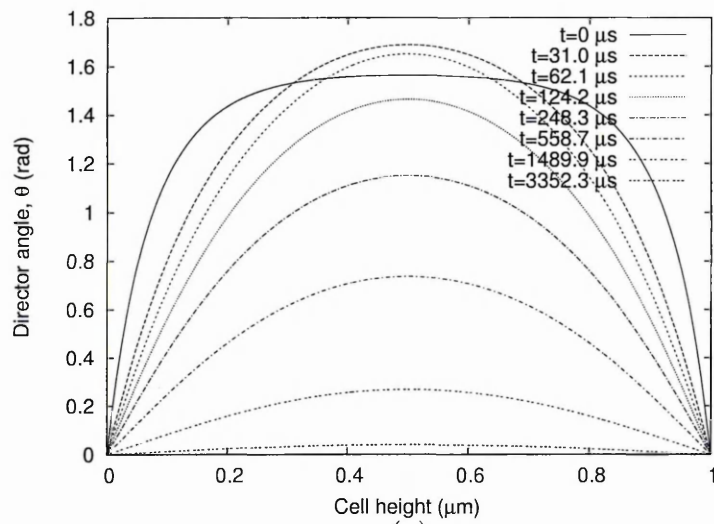
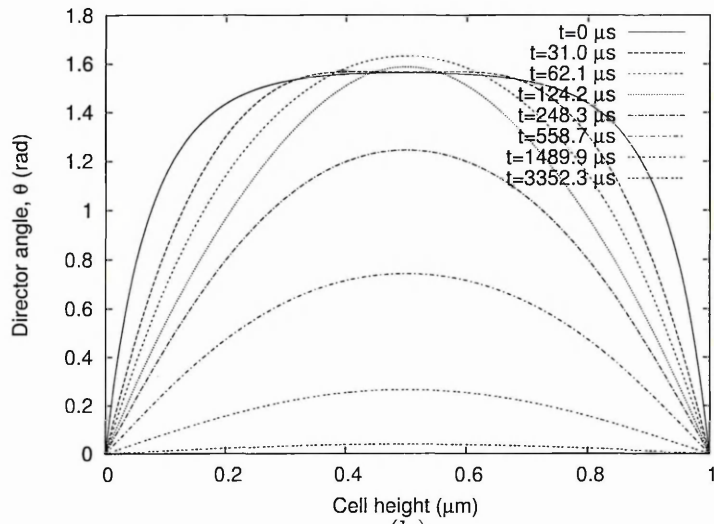


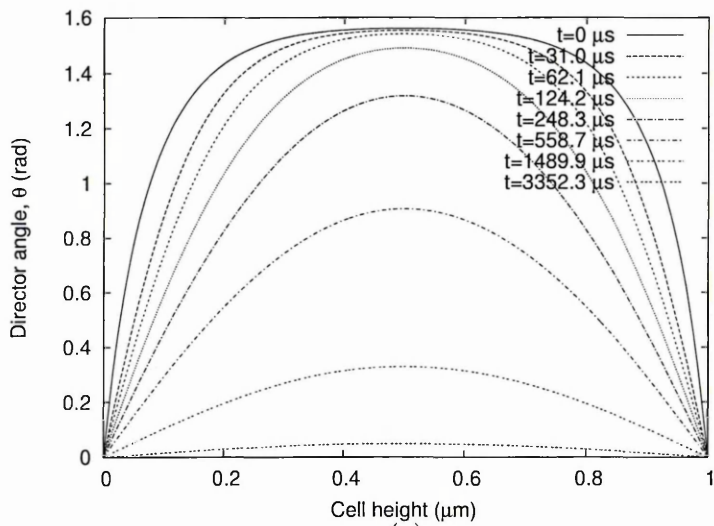
Figure 4.8: Fluid velocity relaxation after the turn off of an applied 5 V field at various positions across a cell. Calculations with (a) correct time scale separation of momentum and director, and (b) no time scale separation between momentum and director. Note the difference in velocity scales on the graphs.



(a)



(b)



(c)

Figure 4.9: Director angle profiles after the turn off of an applied 5 V field. Calculations with (a) correct time scale separation of momentum and director, (b) no time scale separation between momentum and director, and (c) no flow included.

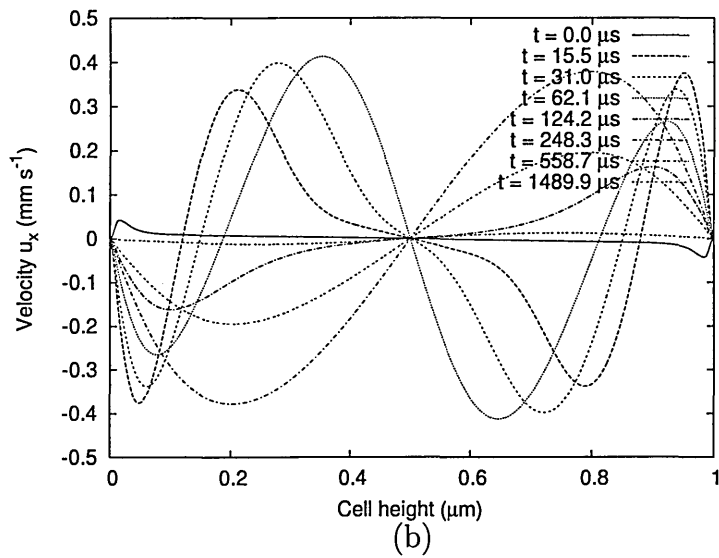
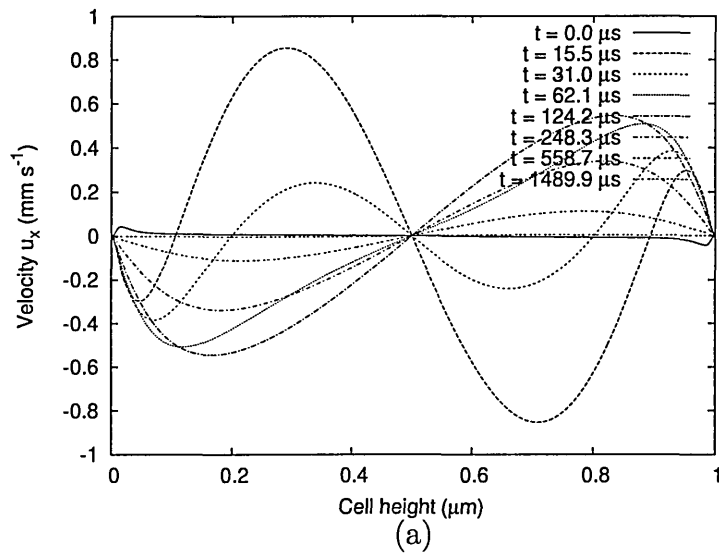


Figure 4.10: Velocity profiles after the turn off of an applied 5 V field. Calculations with (a) correct time scale separation of momentum and director, (b) no time scale separation between momentum and director.

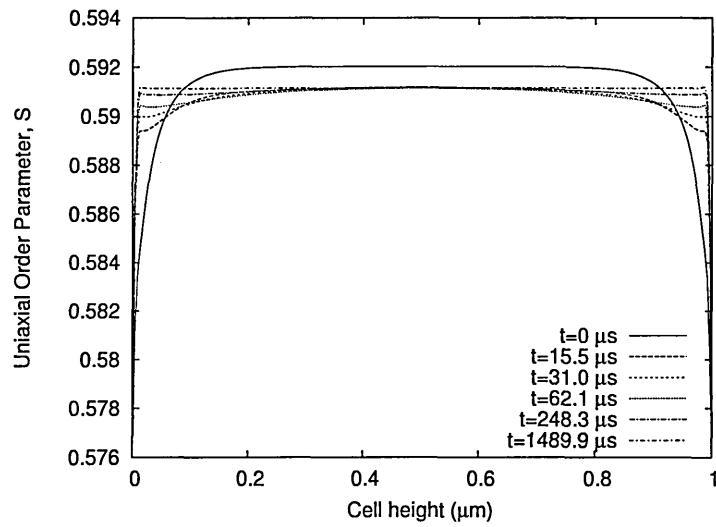


Figure 4.11: Uniaxial order parameter profiles after the turn off of an applied 5 V field. Calculation with with correct time scale separation of momentum and director. Others not shown due to the small changes involving S.

# Chapter 5

## Idealised Model Of A Bistable LC Device

In this chapter we apply the developed model of chapter 4 towards a simple model of a bistable LC device developed by Davidson [2]. It is pertinent in examining the effects of flexoelectricity in devices and how it can induce device bistability. We will compare calculations made from our developed  $\mathcal{Q}$  method with calculations from Davidson [2], who uses the EL theory, as way of both numerical validation and to identify what additional information may be drawn from our method that is not accessible in the EL limit.

### 5.1 The Model

The work by Davidson [2] is aimed at constructing a simple one-dimensional model of the ZBD device introduced in §1.2.4. The ZBD has two stable director configurations that are the result of introducing a surface relief grating. One configuration has continuous vertical director alignment the other has a hybrid alignment and contains defects. In [2] the lower grating surface is cut off and replaced by a flat surface, see figure 5.1 and the upper surface is aligned homeotropically with infinite strength. The replaced flat surface is then given a suitable potential so as to mimic the complicated grating structure and it is hoped this does not significantly alter the bulk behaviour of the cell. The models advantages are that the problem reduces to one-dimension (all parameters  $P = P(z)$  only), the governing equations are simplified, computation is speeded up and defects can be ignored.

The two stable director configurations are now simply a vertically aligned nematic (VAN) and a hybrid aligned nematic (HAN) as indicated in figure 5.2 and  $\theta$

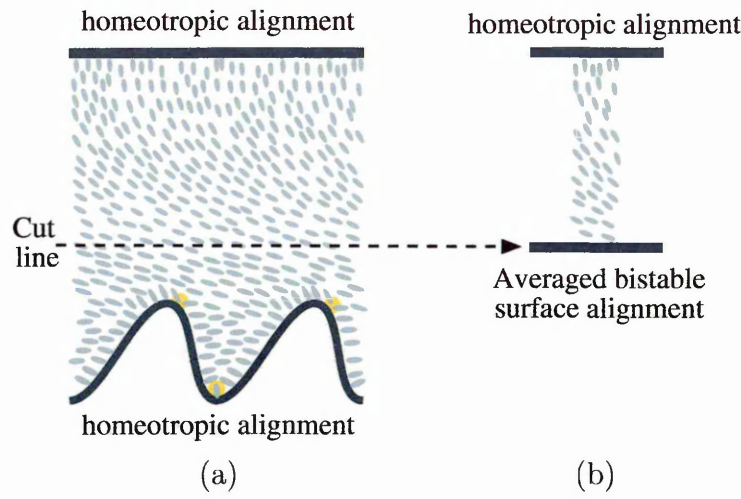


Figure 5.1: Sketch of the ZBD device (a) showing that the effect of the complex grating and defects may be replaced by a flat surface (b) that is given a suitable potential to mimic the bistability and now contains variation only in the vertical direction.

is to be defined from the x-axis. A surface anchoring energy was chosen as:

$$F_S = W \sin^2(2\theta_S) \quad (5.1)$$

where  $W$  is the anchoring strength and  $\theta_S$  the director angle at the bistable surface. This follows the convenient form presented by Kedney [155] for creating a simple theoretical bistable surface but instead this form has minima when  $\theta_S = 0$  and  $\theta_S = \pi/2$ .

For electrodes positioned at  $z = 0$  and  $z = d$  the model may be switched using a dual frequency in which the nematics dielectric anisotropy changes sign at some frequency,  $f_c$ . Alternatively as in the ZBD the device can be switched using dc electric fields of opposite sign in the vertical direction. Davidson [2] shows in this

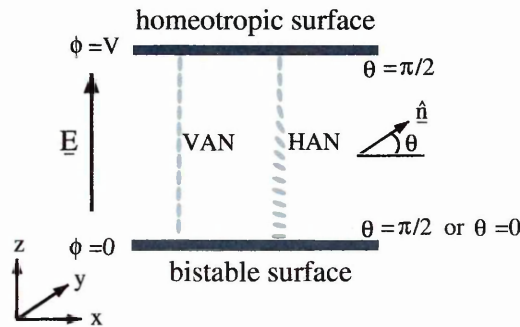


Figure 5.2: Representation of the model co-ordinate frame and bistable states. The lower surface has stable director states for  $\theta(z) = \pi/2$  and  $\theta(z) = 0$ , the upper monostable surface has a single stable state at  $\theta(z) = \pi/2$ .

case switching is then driven by the combination of the flexoelectric effect and the surface viscosity.

In the EL limit, one elastic constant and constant electric field, Davidson [2] shows the free energy contributions are as:

$$\begin{aligned}\mathcal{F} &= \int_0^d \frac{1}{2} \left[ K \left( \frac{\partial \theta}{\partial z} \right)^2 - \epsilon_0 \Delta \epsilon_a E^2 \sin^2 \theta - (e_{11} + e_{33}) E \frac{\partial \theta}{\partial z} \sin(2\theta) \right] dz + W \sin^2(2\theta_S) \\ &= \int_0^d \frac{1}{2} \left[ K \left( \frac{\partial \theta}{\partial z} \right)^2 - \epsilon_0 \Delta \epsilon_a E^2 \sin^2 \theta \right] dz - \frac{(e_{11} + e_{33})}{4} E \cos(2\theta_S) + W \sin^2(2\theta_S)\end{aligned}\quad (5.2)$$

Equation 5.2 shows in the limit that the electric field is considered to be constant the flexoelectric free energy can be integrated to yield a surface contribution. In figure 5.3 we plot these surface energy terms. It shows, for a positive flexoelectric coefficient, that when the applied electric field is positive the flexoelectric contribution destabilises alignment at  $\theta = \pi/2$  (homeotropic) and stabilises alignment at  $\theta = 0$  (homogeneous) and oppositely if the applied electric field is negative the flexoelectric contribution destabilises alignment at  $\theta = 0$  and stabilises alignment at  $\theta = \pi/2$ . This shows that flexoelectricity can lead to a driving mechanism to select the lower surface alignment and a bistable model. In addition to flexoelectricity, key to reproducing dynamic bistability is to include the surface viscosity term as will be seen.

Reducing the EL director equations (see appendix B) Davidson gets for the bulk and surface director evolutions:

$$\begin{aligned}\gamma_1 \frac{\partial \theta}{\partial t} &= K \frac{\partial^2 \theta}{\partial z^2} + \frac{\epsilon_0 \Delta \epsilon_a}{2} E^2 \sin(2\theta) \\ \gamma_S \frac{\partial \theta_S}{\partial t} &= K \frac{\partial \theta_S}{\partial z} - 2W \sin(4\theta_S) - E_{13} E \sin(2\theta_S)\end{aligned}\quad (5.3)$$

in which  $E_{13} = [(e_{11} + e_{33})/2]$  and the upper surface is fixed (infinite anchoring) at  $\theta(d) = \pi/2$ . Equation 5.3 proves difficult to solve analytically but for the steady state zero field case in which the simple solution is:

$$\theta(z) = \left( \theta_S - \frac{\pi}{2} \right) \left( 1 - \frac{z}{d} \right) + \frac{\pi}{2}\quad (5.4)$$

where  $\theta_S$  is given from:

$$\frac{4 \sin(4\theta_S)}{\pi - 2\theta_S} = \frac{K}{Wd}\quad (5.5)$$

We plot equation 5.5 in figure 5.4. This shows indeed the two stable solutions of VAN ( $\theta(z) = \pi/2$ ) and the HAN for which there is a minimum anchoring strength at which the device is bistable.

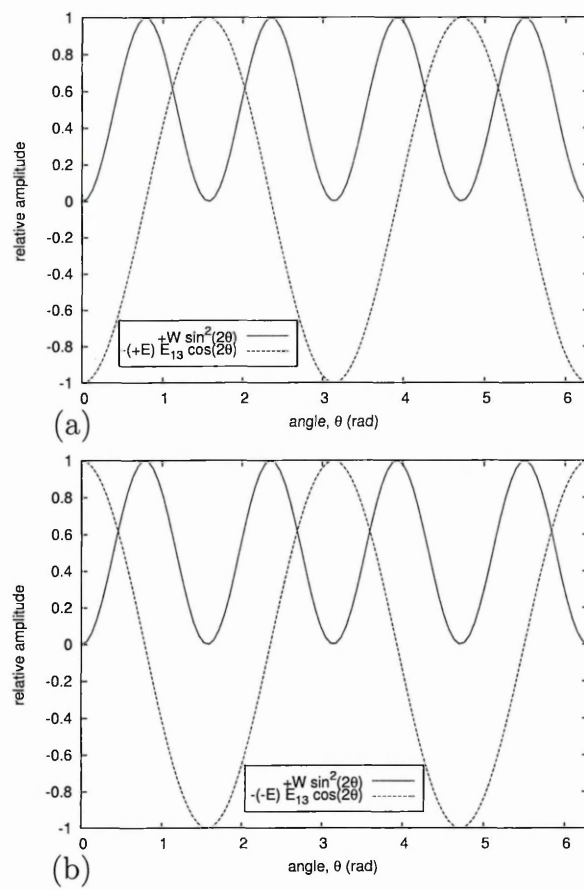


Figure 5.3: Plots of the relative free energy contributions to the bistable surface from the anchoring and flexoelectric components. The surface imposes alignment at both  $\theta_S = 0$  and  $\theta_S = \pi/2$ . The flexoelectric effect imposes for (a) a positive electric field alignment at  $\theta_S = 0$  and (b) a negative electric field alignment at  $\theta_S = \pi/2$ .

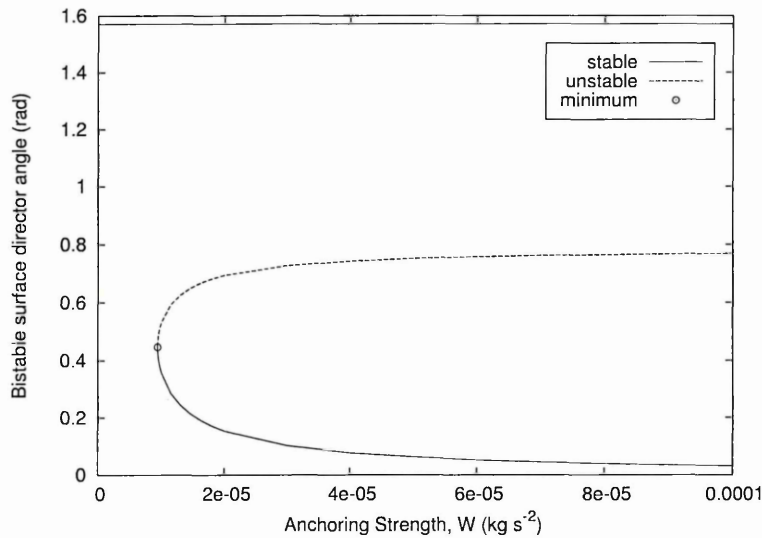


Figure 5.4: Plot of the solutions to equation 5.5 showing the surface director angles for  $K = 1.63 \times 10^{-11} \text{ kg m s}^{-2}$  and  $d = 1 \times 10^{-6} \text{ m}$ . The unstable solutions are degenerate to either of the two stable solutions.

Davidson [2] also notes that in the governing equation 5.3 there is a symmetry regarding the sign of the flexoelectric coefficient,  $E_{13}$ . For parameters chosen such that  $E_{13} > 0$  and  $E < 0$ , they give the same response as parameters  $E_{13} < 0$  and  $E > 0$ . Thus for purposes of calculations it is sufficient to consider the case  $E_{13} > 0$  as from symmetry the  $E_{13} < 0$  case may be deduced. This fact is important to note especially as current literature disagrees over the sign of the flexoelectric coefficients. Even though it produces opposite distortions it is found to be experimentally difficult to measure.

Davidson [2] then goes on to solve numerically equation 5.3 for the equilibrium and dynamic profiles. Davidson's calculations do not include the hydrodynamic coupling in the EL equations. In the next section we compare the numerical solutions of Davidson with those produced from the general solver developed in chapter 4.

## 5.2 Statics

To compare our numerical results to those of Davidson [2] we first need to construct a tensor version of equation 5.1 to provide the bistable surface energy. The most simplest form of which is:

$$F_S = \frac{A}{4} (Q_{\alpha\beta} - Q_{\alpha\beta}^\perp)^2 (Q_{\gamma\tau} - Q_{\gamma\tau}^\parallel)^2 \quad (5.6)$$

where  $A$  is the temperature independent anchoring coefficient and  $Q_{\alpha\beta}^\parallel$ ,  $Q_{\alpha\beta}^\perp$  represent alignment tensors set as equation 2.8 with  $S_0 = S_{Bulk}$  and  $\hat{n}_\alpha^\perp = (0, 0, 1)$  and  $\hat{n}_\alpha^\parallel = (1, 0, 0)$ . This produces two minima for a director aligned either parallel or perpendicular to the surface. We may recover the governing equation 5.3 of Davidson [2] from the tensor version equation 4.3 using equation 2.8 and table 4.1 provided  $A = 64W/(81S_0^4)$ .

Figure 5.5 shows the director profiles across the cell for the case of a positive and negative dielectric anisotropy as calculated by Davidson [2] at various field strengths. It shows that opposing signed electric fields select opposing orientations at the bistable boundary. The actual parameter set used in [2] is misprinted and should read as  $\{\Delta\epsilon_a = \pm 5.7, K = 1.63 \times 10^{-11} \text{ kg m s}^{-2}, W = 1.63 \times 10^{-5} \text{ kg s}^{-2}, E_{13} = 4 \times 10^{-11} \text{ A s m}^{-1}\}$ . Using this set of parameters (with the additional Landau coefficients as used in §4.4.2 and a top surface anchoring coefficient set strong:

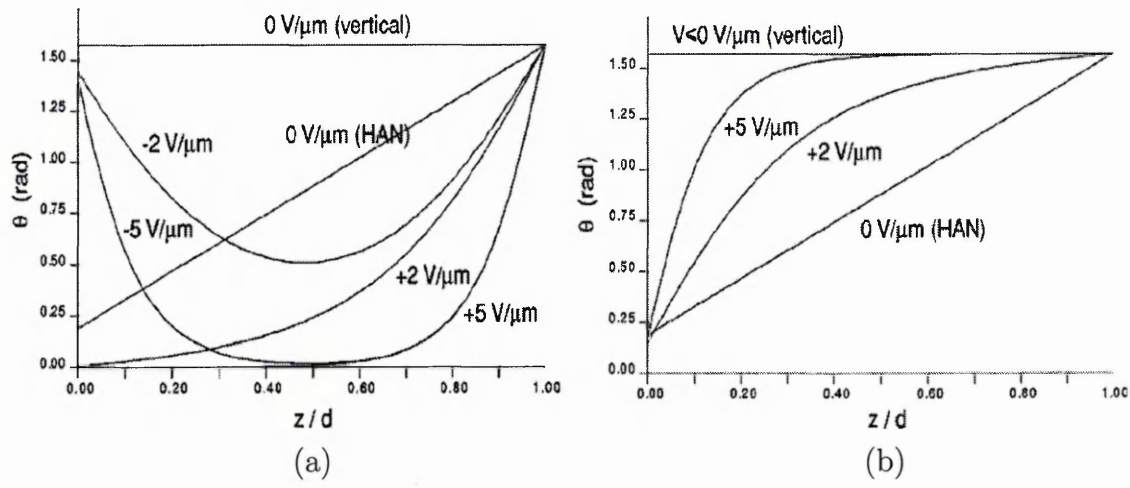


Figure 5.5: Equilibrium director profiles obtained by Davidson [2] for (a)  $\Delta\epsilon_a < 0$  (b)  $\Delta\epsilon_a > 0$  using EL theory at various applied voltages.

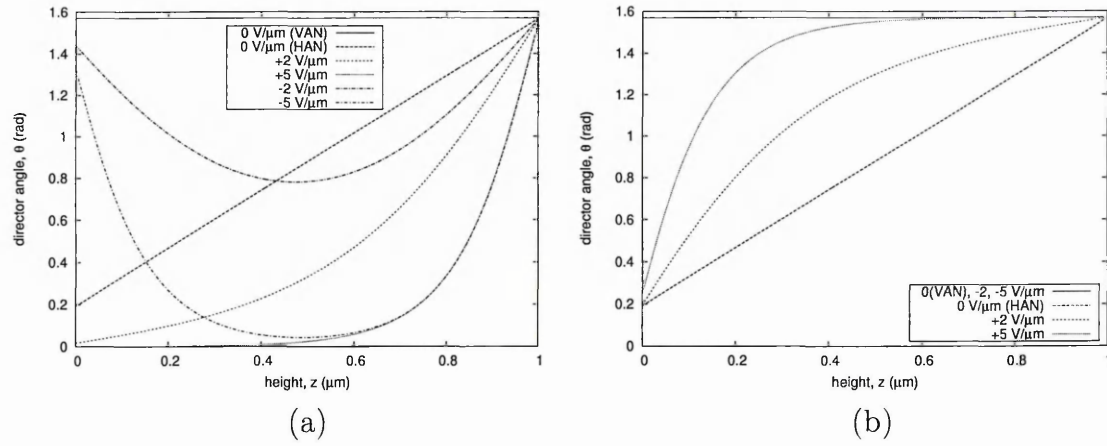


Figure 5.6: Equilibrium director profiles obtained from our solver for (a)  $\Delta\epsilon_a < 0$  (b)  $\Delta\epsilon_a > 0$  using Q-tensor theory at various applied voltages.

$W^{top} = 4 \times 10^{-3} \text{ kg s}^{-2}$ ) we plot the director profiles obtained from our method in figure 5.6. 250 lattice sites were used to reproduce the  $1\mu\text{m}$  cell height on a  $D3Q27$  lattice and periodic boundary conditions in the x and y directions. Calculations performed with double the number of lattice points make no visible differences to the profiles. Agreement between Davidson's calculations and our calculations is very good.

The good agreement serves to highlight that for situations in which the length scale over which director variations take place is much larger than the length scale over which order parameter variations occur there is no need to use the more consuming  $Q$  calculations. However in its use there is extra data available to view in

the form of  $S(z)$  and  $P_B(z)$  which we show in figures 5.7 and figure 5.8 respectively.

For no applied field there is no variation in  $S$  or  $P_B$  for the VAN state, and in the HAN state  $S$  ( $P_B$ ) only decreases (increases) at the weak anchored bistable boundary over a length  $\sim 10nm$ . For applied fields there is increased variations in both  $S$  and  $P_B$ . Generally we see for both bulk and surface values the material of  $\Delta\epsilon_a > 0$  have higher values of  $S$  than the  $\Delta\epsilon_a < 0$  materials and the  $P_B$  value has lower values for the  $\Delta\epsilon_a > 0$  material. The increased variation in order is due to two effects. First for the larger fields (for example  $-5V \mu m^{-1}$  in figure 5.7a) there are higher director gradients towards the cell boundaries that causes  $S$  to

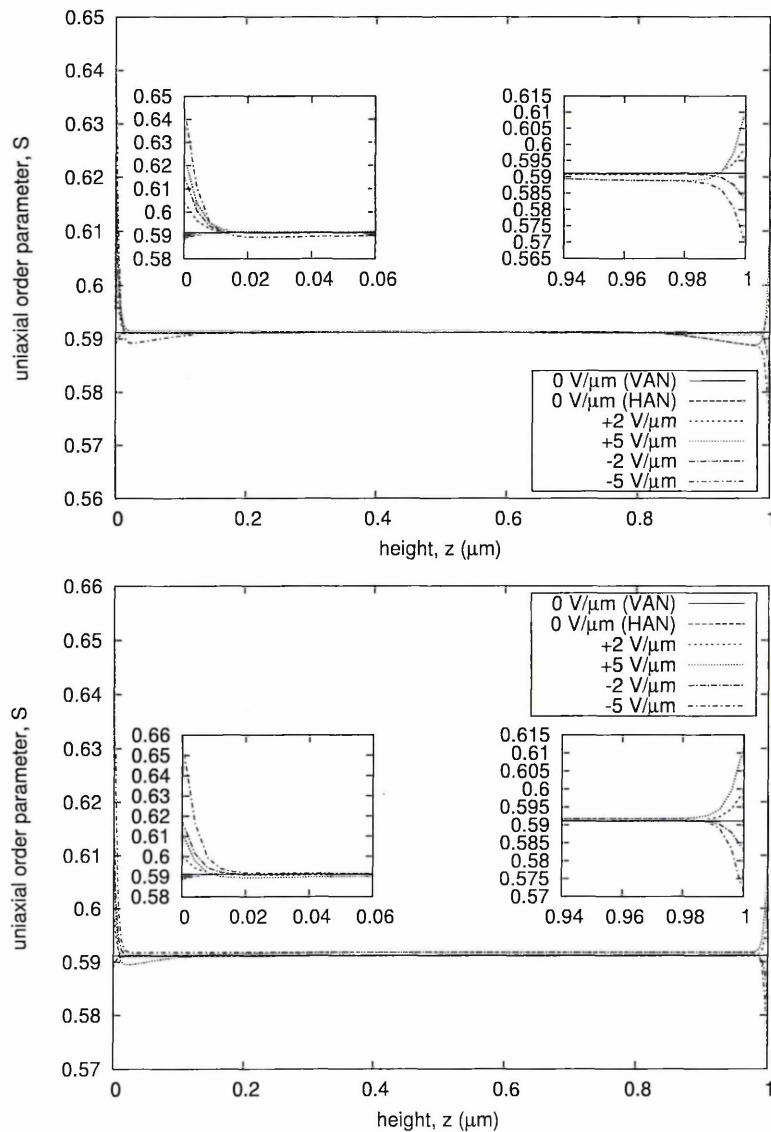


Figure 5.7: Equilibrium uniaxial order parameter profiles for (a)  $\Delta\epsilon_a < 0$  (b)  $\Delta\epsilon_a > 0$  at various applied voltages. Inset are magnified regions of the upper and lower surfaces.

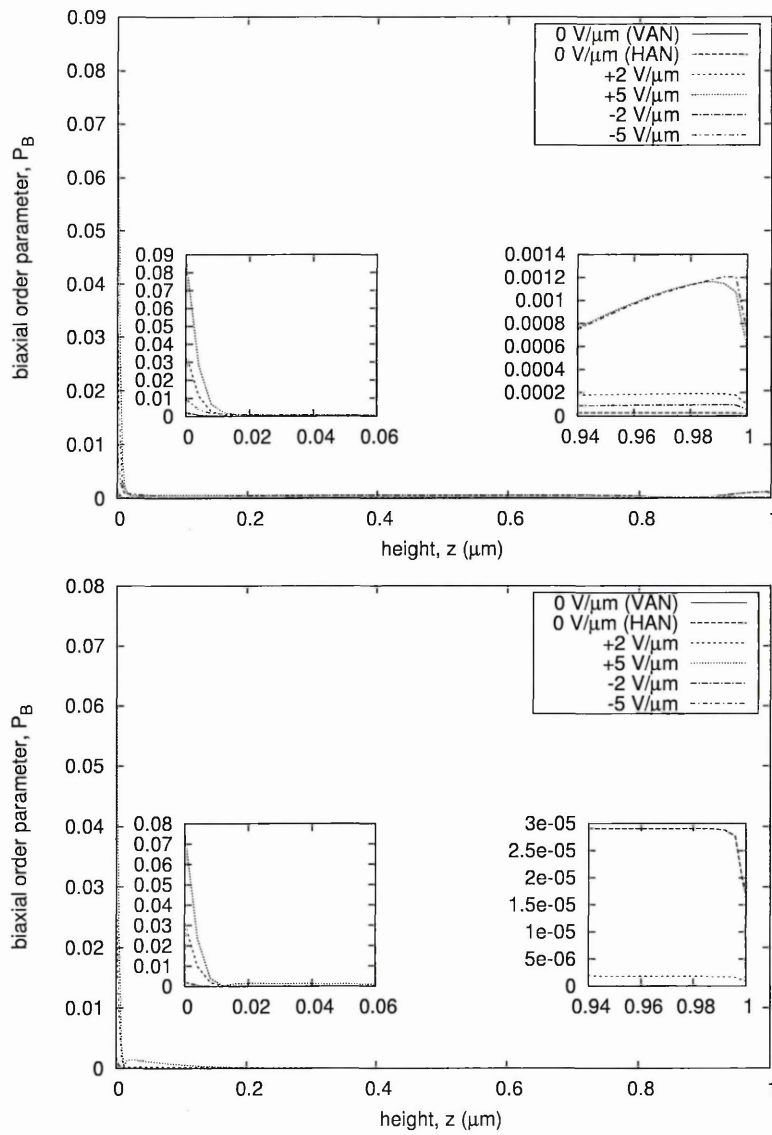


Figure 5.8: Equilibrium biaxial order parameter profiles for (a)  $\Delta\epsilon_a < 0$  (b)  $\Delta\epsilon_a > 0$  at various applied voltages. Inset are magnified regions of the upper and lower surfaces.

decrease due to elastic deformation. Secondly at the surfaces we see flexoelectric and order electric polarisation in a boundary layer of length  $\sim 10 - 15\text{nm}$  which increases for the larger field strengths. It is interesting to see at the lower bistable boundary  $S$  increases for both  $\pm$  fields whereas on the upper monostable boundary  $S$  increases for positive fields and decreases for negative fields. This can be explained with use of equation 5.2 and figure 5.3. The bistable surface anchoring energy is proportional to  $\sin^2(2\theta_S)$  having equilibrium points at both  $\theta_S = 0$  and  $\theta_S = \pi/2$  whereas the monostable surface energy is proportional to  $\sin^2(\theta_S - \frac{\pi}{2})$  that has an equilibrium value at  $\theta_S = \frac{\pi}{2}$  only. Adding the flexoelectric contribution to

this, which is proportional to  $-E \cos(2\theta_S)$ , we see for both positive and negative fields the flexoelectric minimum coincides with a bistable minimum and thus has a stabilising effect (increased order) however for the monostable surface the anchoring is destabilised (decreased order) for a negative field and stabilised (increased order) for a positive field.

In the HAN state equation 5.4 predicts a straight line with the bistable surface director given from equation 5.5. For the parameter set chosen the theoretical  $\theta_S = 0.19043(rad)$ . The simulation  $\theta_S = 0.19242(rad)$ . This shows the surface algorithm is behaving correctly. The 1% difference between analytical and simulation result is expected because the analytic calculation assumes a constant  $S$  value but in the simulation  $S$  decreases slightly at the boundary (see figure 5.7) and in our  $Q$  model the anchoring strength  $W \propto S^4$  and thus small decreases in  $S$  leads to a decrease in effective anchoring strength that leads to the larger  $\theta_S$ .

In figure 5.9 we plot the director profiles obtained from two dimensional calculations with a real grating surface, the calculation of which is described in chapter 6. The director profiles are plotted at several positions along the grating direction and show that provided the lower half of the cell is ignored the director variation is approximately one dimensional.

We now extend the Davidson model [2] to calculate a more accurate representation of the cell equilibrium profiles. We will also restrict our interest to the material of  $\Delta\epsilon_a < 0$  to narrow the parameter space and because it has more varied structures in the negative applied field cases. In figure 5.10 we have added unequal elastic constants  $\{(K_{11} = 14.2, K_{22} = 6.55, K_{33} = 18.4, K_{24} = 2.0) \times 10^{-12} \text{ kg m s}^{-2}\}$  and plotted the new and old (one elastic constant) director profiles. Note the  $K_{24}$  parameter is expected to make little if any contribution to calculations as in the limit of constant order and one-dimensional variation this term is identically zero. In general a reduced splay elastic constant increases splayed deformation regions and a larger bend elastic constant decreases bend deformation regions thus we see in figure 5.10 larger splay regions except for the  $E = -2 \text{ V } \mu\text{m}^{-1}$  case in which the field is such that mainly bend distortion is present.

We next let the electric field term vary to take into account the dielectric anisotropy, the solutions being given as detailed in § 4.3.1. In this case equations 5.2

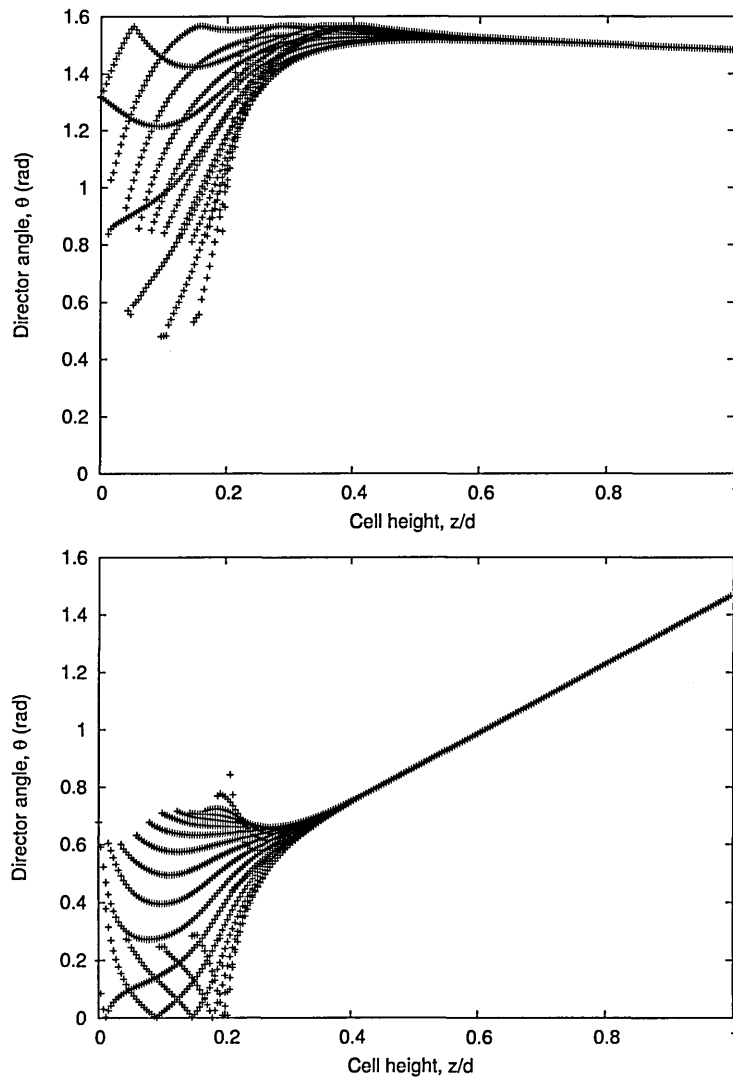


Figure 5.9: Director profiles plotted every 15 lattice sites along the grating for a real ZBD device calculated as described in chapter 6. They serve to show the upper half of the cell may be described well by a one dimensional profile.

are no longer correct and there are bulk contributions from flexoelectricity. The new director profiles are shown in figure 5.11 together with the old (unequal elastic constant) director profiles. There is a marked differences between the calculations suggesting this contribution cannot be neglected when modelling quantitative or qualitative properties in liquid crystal cells. The corresponding uniaxial and biaxial profiles for the variable electric field case are shown in figures 5.12 and 5.13 respectively, here changes are only quantitative.

The voltage and electric field profiles corresponding to figures 5.11 - 5.13 are shown in figure 5.14. The electric field varying by as much as  $\Delta\epsilon_a/d$  in the fully aligned (larger field) cases. For the HAN state in which no external field is applied

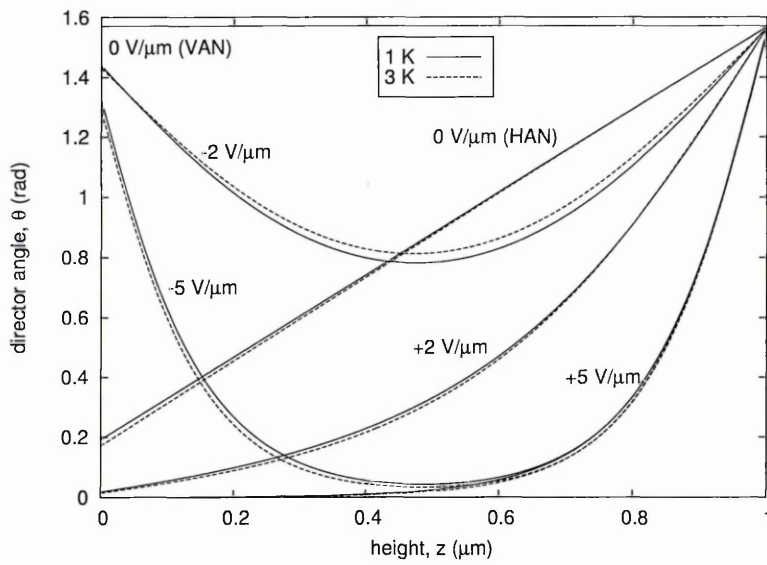


Figure 5.10: Comparison of equilibrium director profiles in the one elastic constant approximation with unequal elastic constants at various applied voltages.

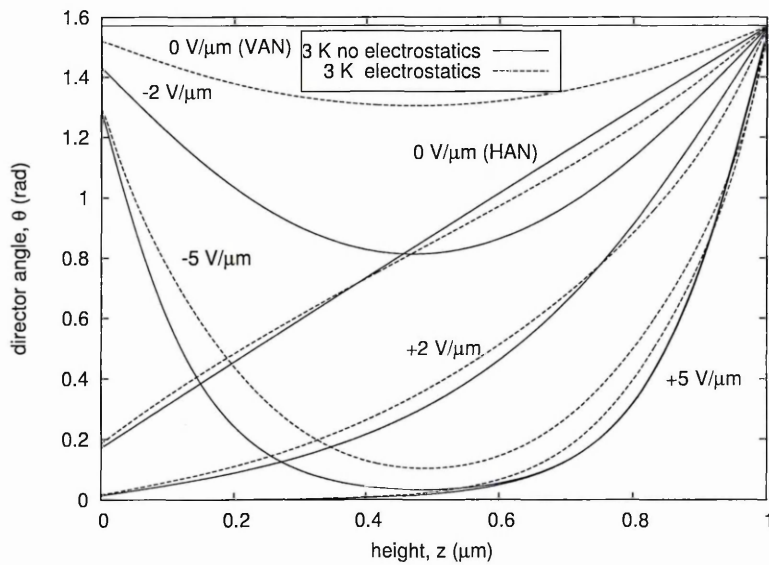


Figure 5.11: Comparison of equilibrium director profiles with unequal elastic constants with those calculated using the electrostatic solver to take into account the dielectric and flexoelectric polarisation terms at various applied voltages.

the flexoelectric effect generates an internal field (see figure 5.14a) giving rise to the characteristic ‘S-shape’ profile of the director in figure 5.11. In the VAN state there are no gradients in director or order and thus no internal field. In the applied field case the gradient of the electric field at the surfaces has opposite directions for opposing applied voltages.

The polarisation due to flexoelectricity is shown in figure 5.15. The polarisation

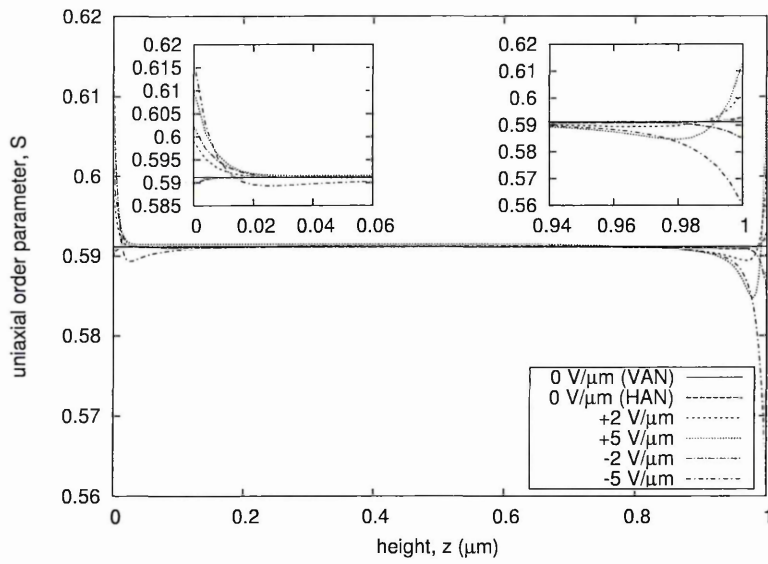


Figure 5.12: Equilibrium uniaxial order parameter profiles for unequal elastic constants and dielectric effect at various applied voltages. Inset are magnified regions of the upper and lower surfaces.

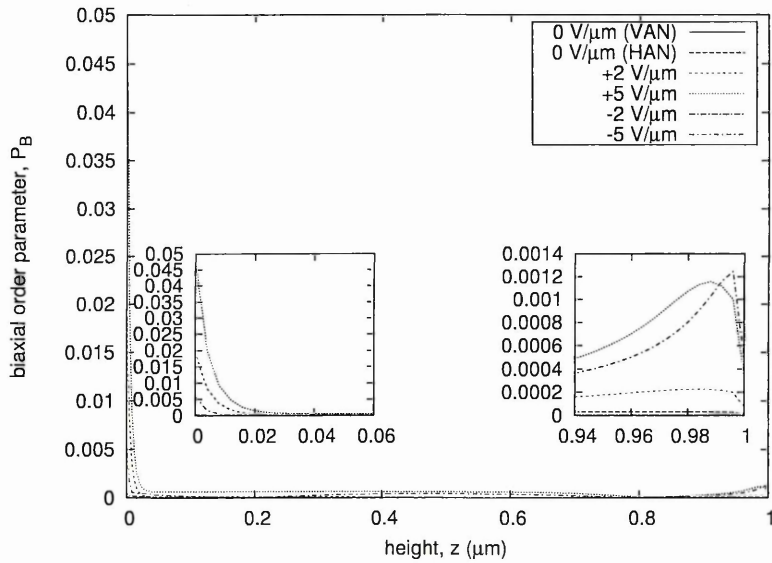


Figure 5.13: Equilibrium biaxial order parameter profiles for unequal elastic constants and dielectric effect at various applied voltages. Inset are magnified regions of the upper and lower surfaces.

is evenly distributed in the HAN state but for the applied field cases the larger polarisation regions are moved to the region of most distortion. The highest polarisations occur at the surfaces coinciding with the variation of the order parameters at the surfaces. The surface polarisation vectors point upwards (downwards) for the positive (negative) applied field cases even though the bulk polarisation may be pointing in the opposite direction. The surface polarisation as defined by Bli-

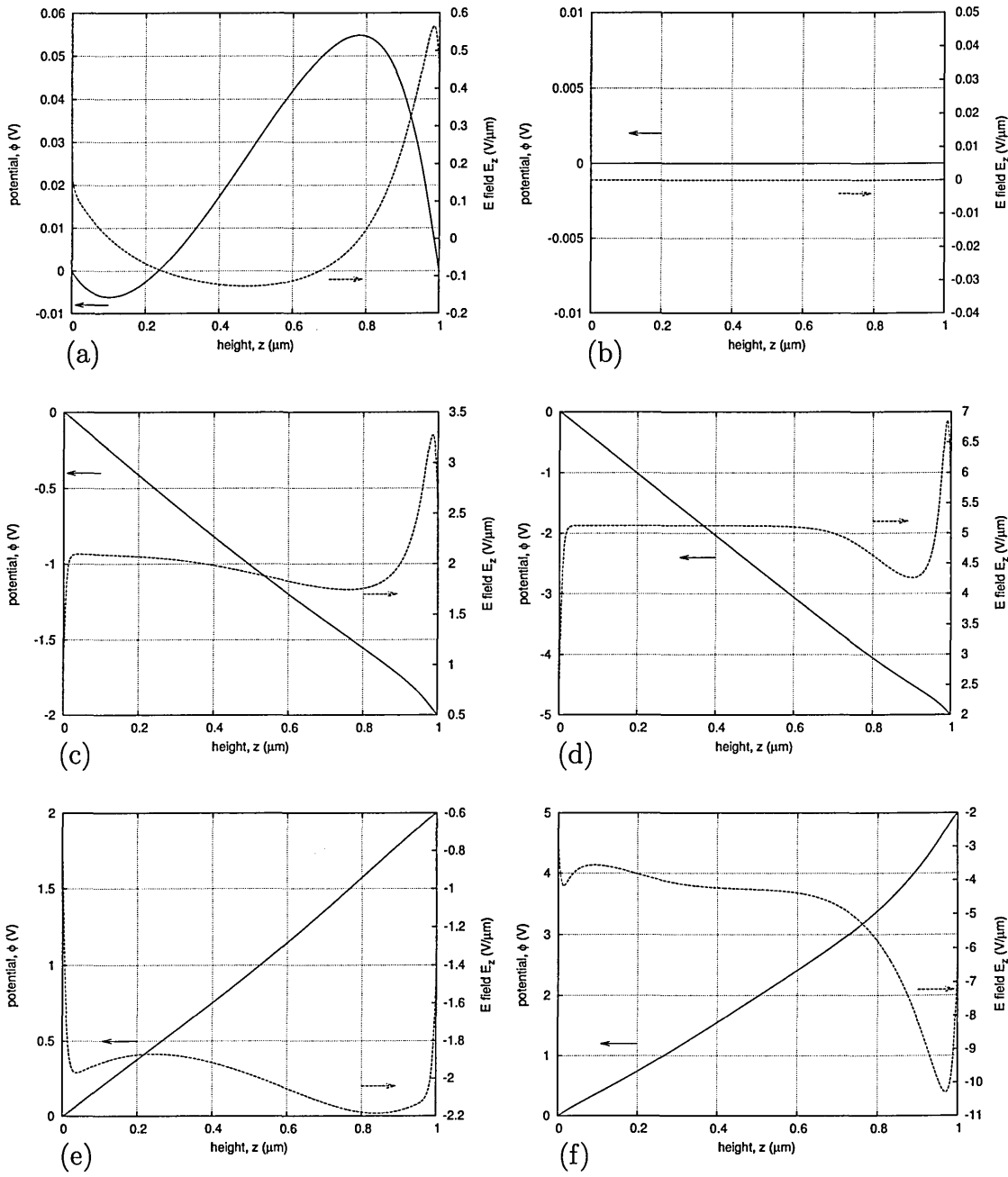


Figure 5.14: Plots showing the equilibrium voltage and electric field profiles across the cell at various applied voltages: (a) 0V (HAN), (b) 0V (VAN), (c) -2V, (d) -5V, (e) +2V, (f) +5V.

nov [156] is  $P_{surf} = P_{bulk}l$  where  $l$  is the surface length over which such a polarisation occurs. Taking  $l = 15$  nm (from figure 5.12) we get  $P_{surf} = 7.5 \times 10^{-13}$  C m $^{-1}$  for the field off case and typically  $P_{surf} = 3.8 \times 10^{-12}$  C m $^{-1}$  for the field on cases. These figures are in good agreement with the values reported in [156] that measure the polarisation via a pyroelectric technique getting values, in a hybrid cell, of  $P_{surf} = 2 \times 10^{-12}$  C m $^{-1}$ . The main contribution to the surface polarisation is from

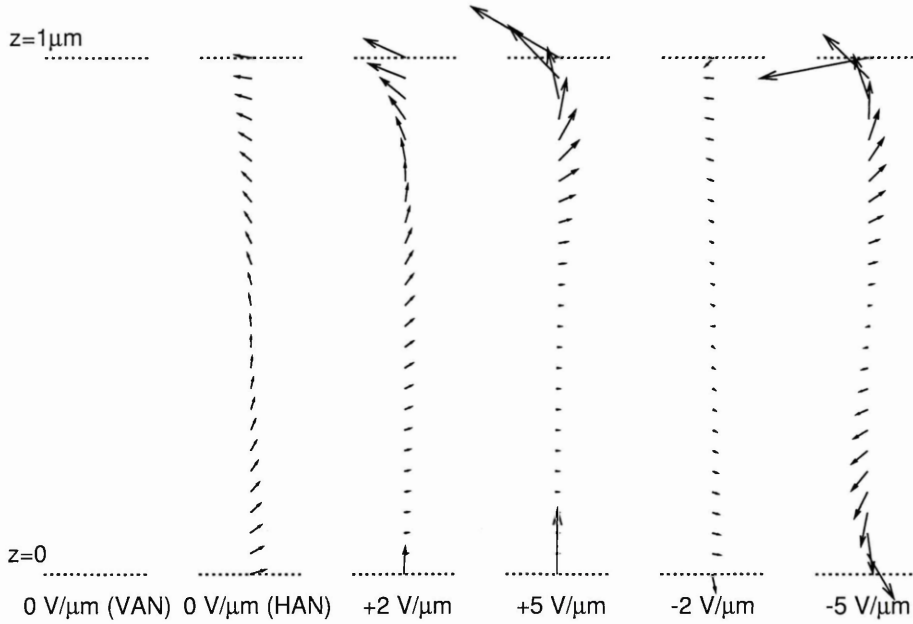


Figure 5.15: Flexoelectric polarisation vectors at various applied voltages at equilibrium. Data plotted every 10 lattice points, the distance between which corresponds to a polarisation of  $8 \times 10^{-5} \text{ C m}^{-2}$ .

the order parameter. This is highlighted if we consider the applied field  $+5 \text{ V } \mu\text{m}^{-1}$  case. Here the director alignment over the lower half of the cell is uniformly planar (obtained from figure 5.11) and thus no gradients in the  $\hat{n}$  appear. Using an EL type model would result in zero surface polarisation yet at the lower surface we see a larger polarisation vector as indicated in figure 5.15.

### 5.3 Dynamics

In this section we will investigate the dynamic behaviour of this one dimensional model with the full LB solver. It is instructive to first consider figure 5.6a. Application of the positive electric field selects the homogeneous surface alignment at the bistable surface due to the flexoelectric effect. The dielectric effect further aligns the bulk orientation towards homogeneous so upon release of the electric field the device is likely to relax to the HAN state. On application of the negative electric field the bistable surface prefers the homeotropic alignment due to the flexoelectric effect. The dielectric effect, as before, aligns the bulk orientation towards homogeneous alignment. Now when the electric field is turned off there are

two possible outcomes: a) The bistable surface remains homeotropically aligned causing the bulk to become homeotropic and reach the VAN state. b) The homogeneous bulk alignment has high elastic deformation that may cause the homeotropic surface alignment to become homogeneous and reach the HAN state. Which final state that is selected depends upon the rate of relaxation of the bulk and surface directors that are governed by  $\gamma_1$  and  $\gamma_S$  respectively.

The simulation parameters for this section are as the previous section (with unequal elastic constants) with the addition of the viscosity parameters  $\{\alpha_1 = -0.011, \alpha_2 = -0.102, \alpha_3 = -0.005, \alpha_4 = 0.074, \alpha_5 = 0.084, \alpha_6 = -0.023\} \text{kg m}^{-1} \text{s}^{-1}$ . This viscosity set fixes the bulk  $\gamma_1 (= \alpha_3 - \alpha_2)$ , the surface viscosity ( $\gamma_s = \gamma_1 l$ ) will be quoted in each section through the surface length  $l$ . The surface viscosity is the unknown value in this model because the lower bistable surface of the real ZBD device was cut off and approximated with a surface free energy instead. Also existing experimental data on surface viscosity values ranges from  $l = 10^{-8} - 10^{-6} \text{ m}$  [82].

Further for all dynamic simulations in this chapter we have set explicitly  $u_z(z) = 0$ . This is because with the weak anchoring and non-standard bistable anchoring free energy used it created non-negligible velocity spikes of the order  $u_z \sim 10^{-3} \text{ m s}^{-1}$  at the bistable surface between 0 and 4 lattice sites in that have the effect of disrupting the bistable properties. Through considering the incompressible continuity equation and the symmetry of the model we can infer  $u_z(z) = 0$  to combat this error.

### 5.3.1 Pre-tilts

Before the dynamics of this model are shown we discuss the importance of introducing a pre-tilt into the surface alignments. Pre-tilts are typically introduced to LCD's in order to either stabilise an alignment, avoid switching frustration, avoid reverse director rotations or to speed up switching times. The pre-tilt is defined by the angle the anchoring imposes on the director away from the homeotropic or homogeneous orientation. To illustrate why a pre-tilt is required in this model we show simulations of the bistable model starting in the VAN state and applying an external positive electric field at time  $t = 0$ . The results are shown in figure 5.16 for various pre-tilt values.

In figure 5.16a the pre-tilt =  $0^\circ$ . Due to the initial vertical director alignment

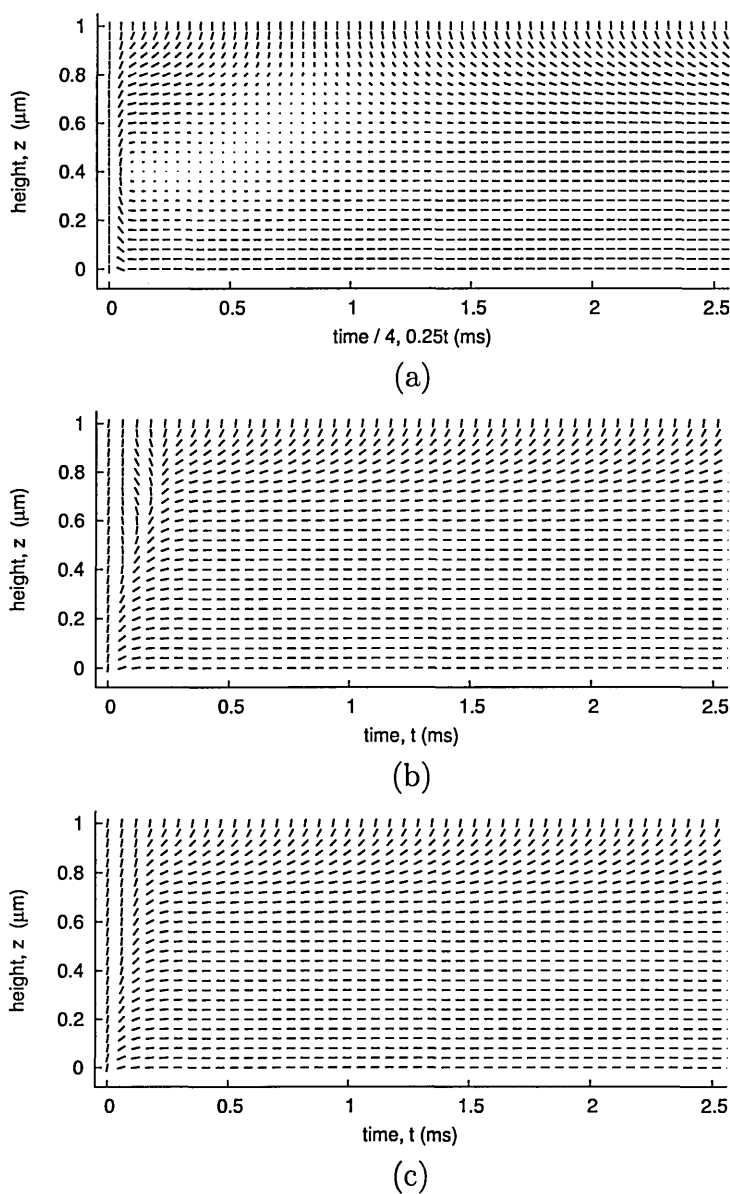


Figure 5.16: Plots of the director field in time across the cell when switching on  $-5V$  from the initial VAN state. (a) zero pre-tilt causes director to rotate out of plane and a reverse tilt final state. (b)  $5^\circ$  pre-tilt has no out of plane rotation but flow induces a frustrated region. (c)  $9^\circ$  pre-tilt has no frustration and a fast response time. Note the time scale plot in (a) is four times longer than in plots (b) and (c).

the director feels no torque from the applied electric field. After a period of time (0.5ms) a build up in numerical noise occurs giving the directors a finite angle. This then interacts with the applied field to cause the system to realign. In doing so it creates a flow field that rotates the directors in opposing directions in the upper and lower halves of the cell. A frustrated region arises in which the free energy is minimised by rotating the director out of plane and then back into plane to reach equilibrium. This out of plane rotation takes a long time.

In figure 5.16b the pre-tilt =  $5^\circ$ . This value is enough to prevent the director from rotating out of plane and reduces the amount of frustration caused by the flow and speeds up the overall time to reach equilibrium. In figure 5.16c the pre-tilt =  $9^\circ$ . This value is such that no rotating out of plane occurs, no frustration is caused from the flow field and the response time to equilibrium is further decreased up.

### 5.3.2 Switching

All of the following switching dynamics have been calculated using a pre-tilt of  $6^\circ$  at top and bottom surfaces to avoid director rotating out of plane. We examine switching for a range of surface viscosity values. The order parameters evolution are not shown, they respond instantaneously to the applied field on and off times to the profiles shown in the static figures of the previous section.

## VAN to HAN: $l = 2 \times 10^{-8}$

Starting in the VAN state  $-2V$  are applied to the cell. When equilibrium is reached the voltage is turned off. The switch on dynamics of the director and flow fields are shown in figures 5.17a and 5.17b and the switch off dynamics in figures 5.17c and 5.17d. The backflow effects upon the director are clearly visible in the switch on dynamics where the initial positive flow direction causes the director to initially rotate against the preferred direction imposed by the electric field. The flow field then reverses direction and dampens out quickly. In the switch off dynamics the flow is unidirectional and relaxes quickly compared to the director which relaxes to the HAN state as expected.

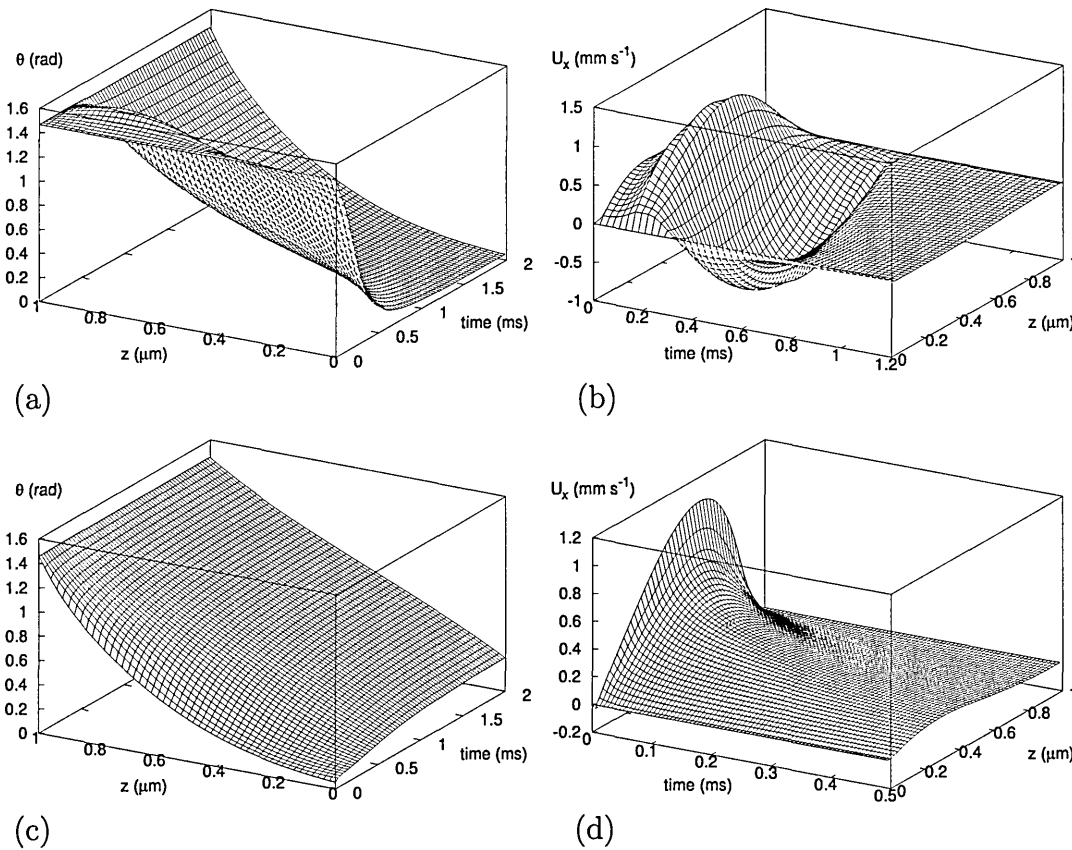


Figure 5.17: VAN to HAN switching.  $-2V$  applied to equilibrium and then turned off.  $l = 2 \times 10^{-8}$  m. (a) director on, (b) flow on, (c) director off, (d) flow off.

## HAN to VAN: $l = 2 \times 10^{-8}$

Starting in the HAN state  $+2V$  are applied to the cell. The switch on dynamics of the director and flow fields are shown in figures 5.18a and 5.18b and the switch off

dynamics in figures 5.18c and 5.18d. The bistable surface director responds quickly to the field causing the initial positive velocity at the lower surface. As the director reaches equilibrium the flow field is damped out. In the switch off dynamics the bulk elastic distortion imposed by the field initially reduces the bistable surface director angle but then the director relaxes to the VAN state with only a small initial flow field.

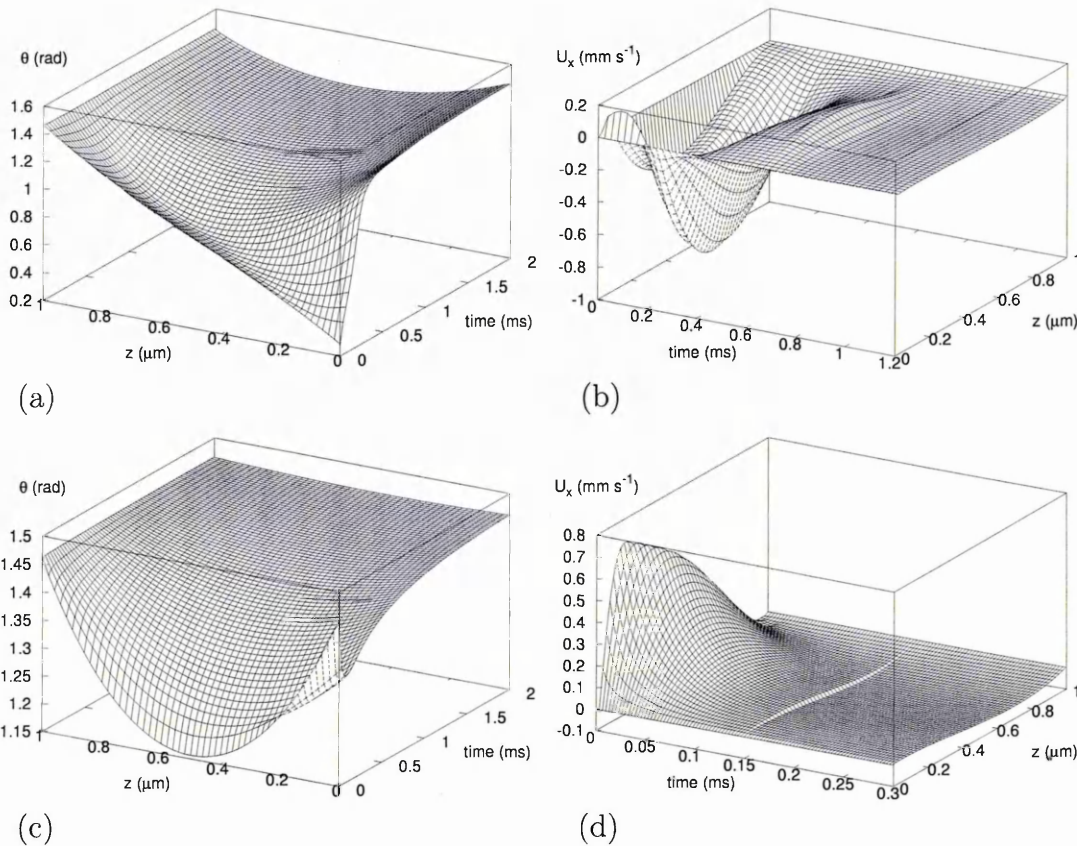


Figure 5.18: HAN to VAN switching. +2V applied to equilibrium and then turned off.  $l = 2 \times 10^{-8}$  m. (a) director on, (b) flow on, (c) director off, (d) flow off.

### VAN to HAN: $l = 2 \times 10^{-8}$

Starting in the VAN state the larger  $-5\text{V}$  are applied to the cell. The switch on dynamics of the director and flow fields are shown in figures 5.19a and 5.19b and the switch off dynamics in figures 5.19c and 5.19d. A much larger back flow effect is felt due to the larger applied voltage. The hollow in figure 5.19a is because of the  $\pm \hat{n}$  equivalence. The flow field is much larger for the larger voltage and the time to reach equilibrium is reduced. The switch off also produces a larger flow field,

is unidirectional relaxing quickly as the director tends to the HAN state. There is no significant alteration in the overall relaxation time between the +2V and +5V cases.

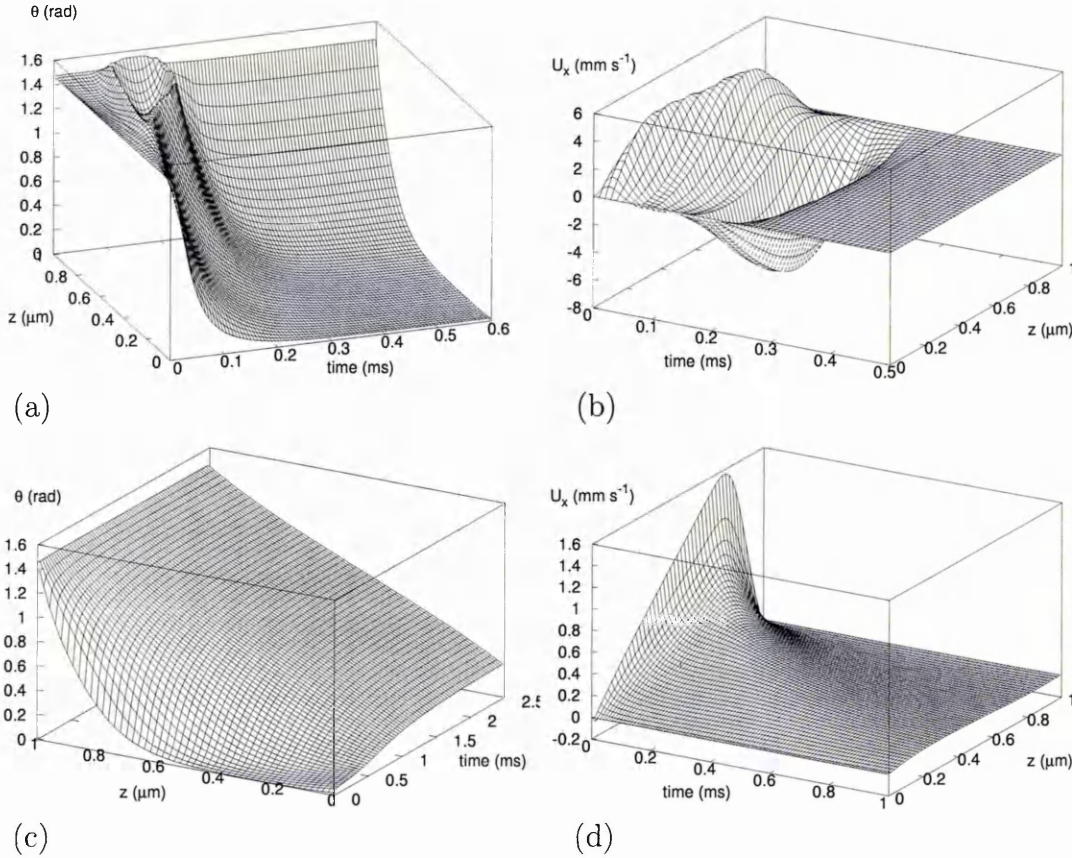


Figure 5.19: VAN to HAN switching.  $-5V$  applied to equilibrium and then turned off.  $l = 2 \times 10^{-8}$  m. (a) director on, (b) flow on, (c) director off, (d) flow off.

### HAN to HAN: $l = 2 \times 10^{-8}$

Starting in the HAN state the larger +5V are applied to the cell. The switch on dynamics of the director and flow fields are shown in figures 5.20a and 5.20b and the switch off dynamics in figures 5.20c and 5.20d. The bistable surface director aligns quickly to the field selecting the homeotropic alignment. The flow field created is larger than the  $-2V$  case. In the switch off dynamics the large bulk elastic distortion now causes the bistable surface director to align with the bulk and the cell relaxes back to the HAN state. This shows we may achieve bistable switching with just a monopolar pulse: +2V giving HAN to VAN and +5V giving VAN to HAN. For the larger dipolar applied voltages ( $\pm 5V$ ) the model is not bistable but this may

be recovered with an increased surface viscosity value.

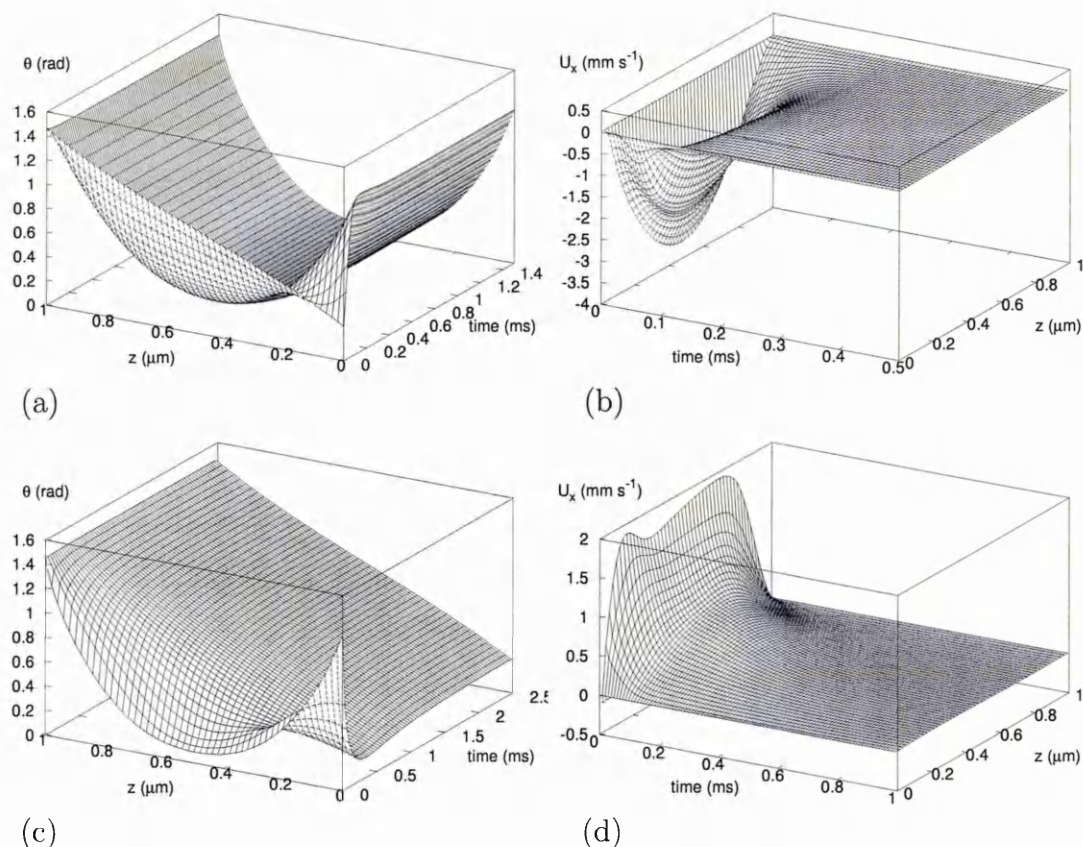


Figure 5.20: HAN to HAN switching. +5V applied to equilibrium and then turned off.  $l = 2 \times 10^{-8}$  m. (a) director on, (b) flow on, (c) director off, (d) flow off.

### HAN to VAN: $l = 4 \times 10^{-7}$

Starting in the HAN state +5V are applied to the cell. The switch on dynamics of the director and flow fields are shown in figures 5.21a and 5.21b and the switch off dynamics in figures 5.21c and 5.21d. With the higher surface viscosity we see the bistable surface director takes longer to reach the homeotropic surface. With this a small positive velocity is seen near the bistable surface. The equilibrium position is the same as the previous simulation at the lower surface viscosity. In the switch off dynamics the large bulk elastic distortion causes the bistable surface director angle to reduce but due to the slower surface relaxation time the bulk elastic energy has time to reduce and the VAN state is reached. So with the larger surface viscosity bistability is recovered with  $\pm 5V$  signals but the bistability with monopolar voltage pulses is lost.

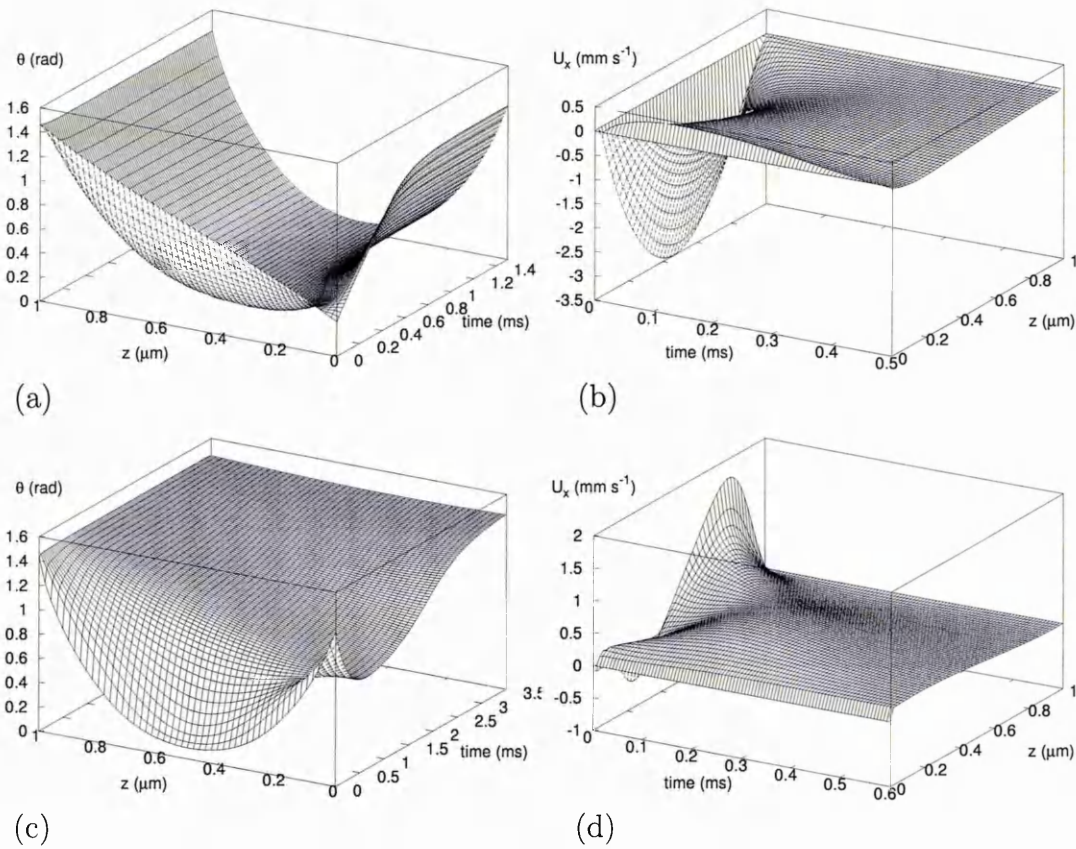


Figure 5.21: HAN to VAN switching. +5V applied to equilibrium and then turned off.  $l = 4 \times 10^{-7}$  m. (a) director on, (b) flow on, (c) director off, (d) flow off.

### Flow effected bistability: $l = 3 \times 10^{-7}$

Simulations over the range of surface viscosity values,  $l = 10^{-8} - 10^{-6}$  m, have been carried out comparing simulations with and without flow effects in order to establish if the hydrodynamics effects the bistability. Apart from the small region of  $2.5 \times 10^{-7} \lesssim l \lesssim 3.0 \times 10^{-7}$  m simulations with and without flow effects show little differences. However in this region it is possible to see that flow can cause a different bistable state to be selected when it is not considered in calculations. Figure 5.22 shows the relaxation from turning off an equilibrated applied +5V to the cell. In figure 5.22a the calculation is without hydrodynamics ( $\underline{u} = 0$ ) and in figure 5.22b the calculation is with hydrodynamics, the associated flow being shown in figure 5.22c. The positive velocity gradient generated near the bistable surface serves to speed up director rotation switching into the HAN state whereas without the flow the switched state is the VAN state. More detailed evolution of the director and flow fields is plotted in figures 5.23.

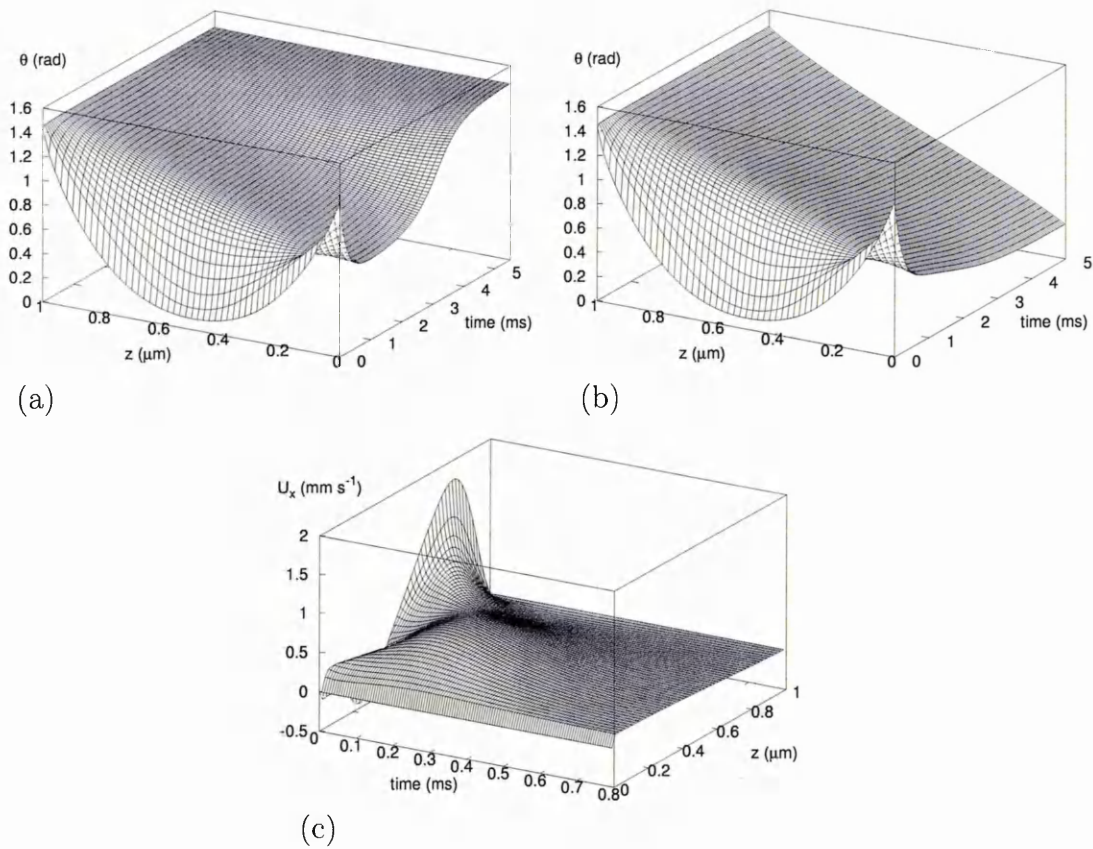


Figure 5.22: Flow effected VAN to HAN switching. +5V applied to equilibrium and then turned off.  $l = 3 \times 10^{-8}$  m. (a) director off without hydrodynamics reaches the VAN state, (b) director off with hydrodynamics reaches the HAN state, (c) flow field off associated with (b).

### More accurate surface representation

A more accurate surface condition for this one-dimensional model was recently proposed by Parry-Jones et al [157]. They noted that the bistable states differ in free energy. This can be observed from equation 5.2, the HAN state free energy being:

$$F = \frac{K}{2d} \left( \frac{\pi}{2} - \theta_S \right)^2 + W \sin^2(2\theta_S) \quad (5.7)$$

and the VAN state free energy being:

$$F = 0 \quad (5.8)$$

For an ideal bistable device one can expect both states to have equal free energy so Parry-Jones et al add an extra term to equation 5.1 in order to impose a free energy in the VAN state:

$$F_S = W_0 \sin^2(2\theta_S) + W_1 \sin^2(\theta_S) \quad (5.9)$$

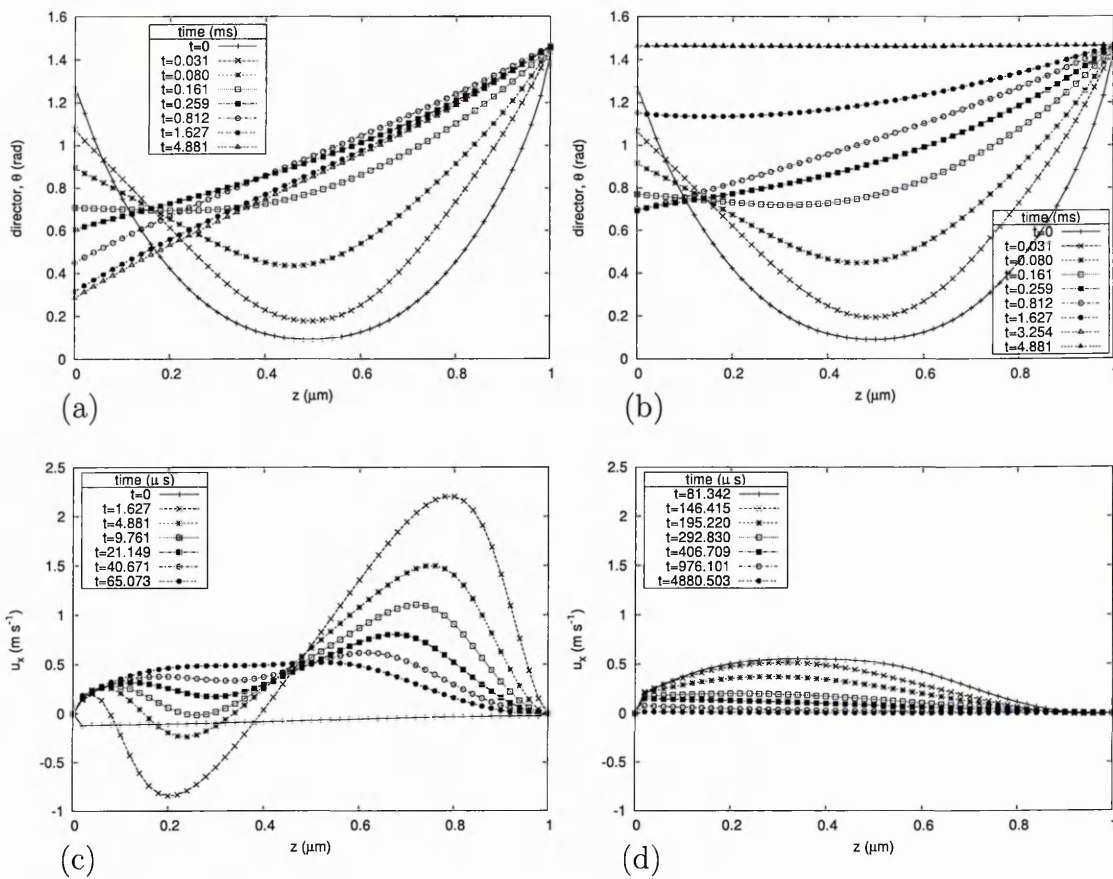


Figure 5.23: More detailed plot of the flow effected VAN to HAN switching. +5V applied to equilibrium and then turned off.  $l = 3 \times 10^{-8}$  m. (a) director off with hydrodynamics reaches the HAN state, (b) director off without hydrodynamics reaches the VAN state, (c) initial flow field off, (d) flow field off continued.

The stable, no applied field, states are still given from equation 5.4 but with  $\theta_S$  now obtained from:

$$\frac{K}{W_0 d} \left( \frac{\pi}{2} - \theta_S \right) = 2 \sin(4\theta_S) + \frac{W_1}{W_0} \sin(2\theta_S) \quad (5.10)$$

The free energy of the VAN state is now

$$F = \frac{K}{2d} \left( \frac{\pi}{2} - \theta_S \right)^2 + W_0 \sin^2(2\theta_S) + W_1 \sin^2(\theta_S) \quad (5.11)$$

and the free energy of the VAN state:

$$F = W_1 \quad (5.12)$$

Through equating the free energy of the bistable states and simultaneously solving with equation 5.10 Parry-Jones et al obtain expression for  $W_1/W_0$  and  $K/W_0 d$  in terms of  $\theta_S$ . Choosing a  $\theta_S$  value with an constants  $K$  and  $d$  then allows us to

determine  $W_0$  and  $W_1$ :

$$\left. \begin{aligned} \frac{W_1}{W_0} &= -\frac{2(\sin^2(2\theta_S) + \sin(4\theta_S)(\frac{\pi}{2} - \theta_S))}{2(\sin^2(\theta_S) - 1) + \sin(2\theta_S)(\frac{\pi}{2} - \theta_S)} \\ \frac{K}{W_0 d} &= \frac{W_1 \sin(2\theta_S) + 2\sin(4\theta_S)}{(\frac{\pi}{2} - \theta_S)} \end{aligned} \right\} \quad (5.13)$$

Following Parry-Jones et al we select  $\theta_S = 0.604$  which corresponds to  $W_0 = 2.070 \times 10^{-6} \text{ kg s}^{-2}$  and  $W_1 = 1.392 \times 10^{-5} \text{ kg s}^{-2}$ . The equivalent Q-tensor surface free energy is given as:

$$F_S = \frac{A_0}{4} (Q_{\alpha\beta} - Q_{\alpha\beta}^\perp)^2 (Q_{\gamma\tau} - Q_{\gamma\tau}^\parallel)^2 + \frac{A_1}{2} (Q_{\alpha\beta} - Q_{\alpha\beta}^\parallel)^2 \quad (5.14)$$

The effect of such a change to the surface potential, as pointed out by Parry-Jones et al, is to firstly give the bistable states equal free energy and secondly with increasing  $\theta_S$  the energy barrier between states is reduced.

Carrying out simulations with this new surface potential does not alter the overall behaviour of the models switching properties. The switching still depends upon the value of the surface viscosity. In figures 5.24 we show the switching from VAN to HAN and HAN back to VAN states with the modified surface potential. The parameter set used is as before but with the modified  $W_0$  and  $W_1$  values calculated above and  $l = 10^{-6} \text{ m}$ . The switching off times are much longer due to the large surface viscosity and the smaller energy between bistable states.

## 5.4 Summary and Conclusions

In this chapter we have examined the Q-tensor equivalent to Davidson's [2] one dimensional model on the ZBD. It is seen how the flexoelectric effect produces a large surface effect which in the presence of weak anchoring may alter the surface alignment.

A comparison of Davidson's static director profiles and our director profiles is good. We further add unequal elastic constants and the dielectric effect through the electrostatic solver. It is found that the electrostatic solver makes large differences to the director profiles.

The bulk order parameter variations are small (1%) but surface order parameter variation is up to 7% and it is shown this variation contributes largely to the surface polarisation.

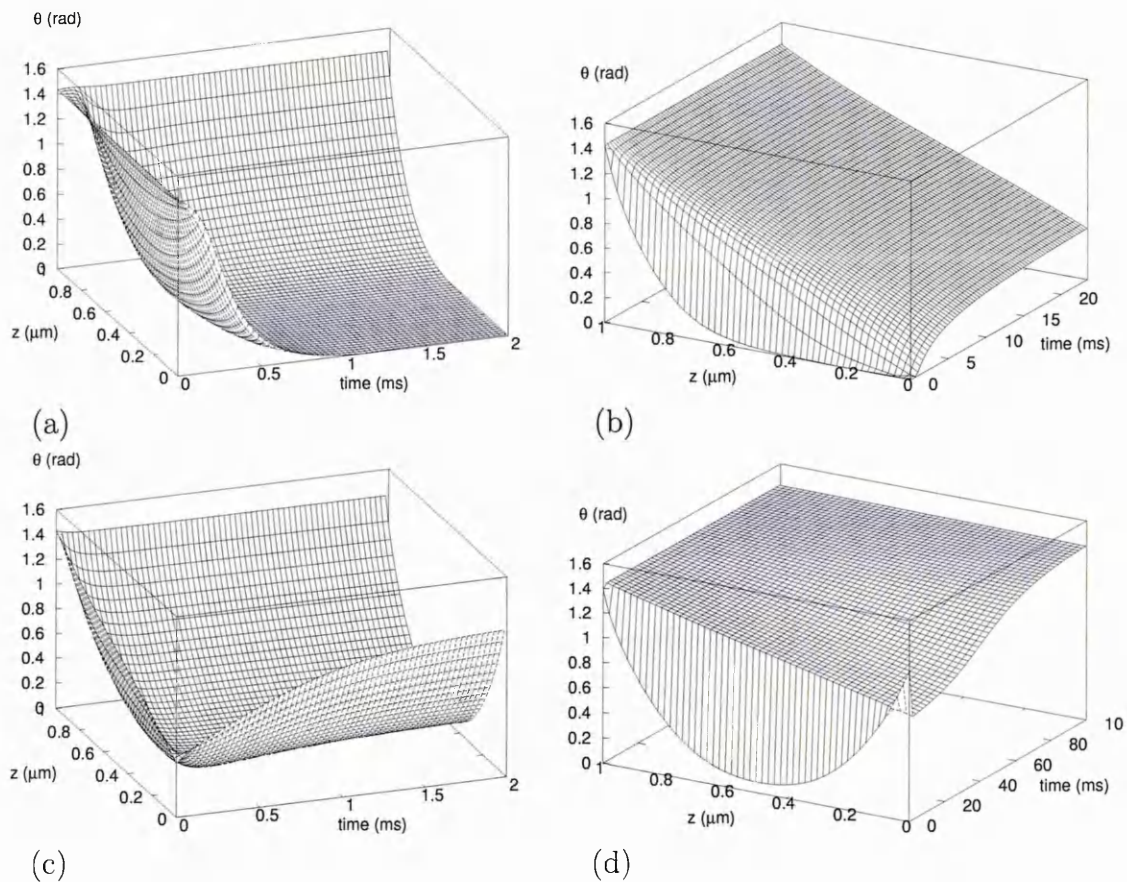


Figure 5.24: VAN to HAN ( $-5V$ ) and HAN to VAN switching ( $+5V$ ). Voltage applied to equilibrium and then turned off.  $l = 1 \times 10^{-6}$  m. (a) director on VAN to HAN, (b) director off VAN to HAN, (c) director on HAN to VAN, (d) director off HAN to VAN.

We add hydrodynamic effects to the calculations and find a pre-tilt is required in order to prevent the director rotating out of plane and reverse director tilts. Flow effects are seen to make little difference to the switching dynamics.

The value of the surface viscosity is critical to the device operation: At small surface viscosity the model may be switched with a single polarity voltage pulse. At large surface viscosity the model may be switched with bipolar voltage pulses to select opposite states. In a small but critical range of surface viscosity values the switched states differ when calculating with momentum dynamics and when not.

The modified surface potential proposed by Parry-Jones et al [157] leads to higher surface tilt angles and slower dynamics as the free energy difference between bistable states is much smaller than in [2]. However similar operational characteristics are seen.

The model's advantage is in its speed but it does little to aid the understanding

of the real underlying bistable surface of the grating. The practical use of such a model for modelling the real ZBD becomes cumbersome. For a particular material and grating shape the models surface potential and anchoring energies together with the surface viscosity are required to be tuned. Subsequent changes to a material or a surface shape then require these parameters to be re-tuned.

# Chapter 6

## Modelling of the Zenithal Bistable Device

In chapter 5 we saw how flexoelectricity produces a large surface effect to switch between VAN and HAN states (and vice-versa) on a flat surface. In practice a flat wall can only have monostable anchoring conditions. One method to recover bistable behaviour is to vary the shape of the wall as done in the ZBD. This chapter sets out to study in more detail the ZBD device introduced in §1.2.4. We will show through simplifying the numerical complexity of the problem how surface flexoelectricity properties of LC's can be responsible for device bistability and how simple comparison to experimental behaviour allows the sign of the flexoelectric coefficients to be determined. We also examine the necessity of using the  $Q$  tensor methods this work has adopted in comparison to a constant order EL type method.

### 6.1 Overview of Current ZBD Operation

Here we will consider the developments of the ZBD through *a*) experimental, and *b*) simulation, investigations.

#### 6.1.1 Experimental Studies

The ZBD as introduced by Bryan-Brown et al [158] consists of a LC cell with one surface flat and the opposite surface shaped like a grating. Treating all surfaces for homeotropic alignment gives two stable director configurations, see figure 1.16. One director configuration has continuous vertical alignment of the director from top to bottom surfaces, the other has a hybrid type alignment from top to bottom in which one defect sits at the grating peaks ( $m = -1/2$ ) and one at the troughs

( $m = +1/2$ ). The two director configurations (hereafter  $\mathcal{C}$  for continuous and  $\mathcal{D}$  for defect) represent minima in the LC free energy and are separated by a free energy barrier. The free energy of the two states and their existence depends, among other factors, upon grating groove depth to pitch ratio. The shallower grating tending to prefer only the  $\mathcal{C}$  state.

The switching between bistable states is achieved via the application of an electric field, the sign of which determines the final state. Due to this polar behaviour it is believed the flexoelectric properties of nematics are responsible for switching between states but how this is so is still unresolved. Placed between crossed polarisers the  $\mathcal{C}$  state appears dark whereas the  $\mathcal{D}$  state appears white thus the device is optically bistable.

Experimentally it is found there exists a voltage threshold in which switching between states occurs (not necessarily the same threshold for  $\mathcal{D}$  to  $\mathcal{C}$  and  $\mathcal{C}$  to  $\mathcal{D}$ ), the threshold being dependent upon time, temperature and cell/surface shape. It is also found that  $\mathcal{D}$  to  $\mathcal{C}$  switching is fast (e.g  $\sim 0.2ms$ ) and that  $\mathcal{C}$  to  $\mathcal{D}$  switching is slow (e.g  $\sim 40ms$ ). Grey scales are achievable via each pixel domain having varying grating uniformities and thus different switching thresholds. Colour is achieved through standard RGB filters. The device is found to have extremely high mechanical shock resistance: it retains its image for large screen deformations.

More recent work [159] has moved towards a device with the flat surface homogeneously aligned imposing a  $90^\circ$  twist when in the  $\mathcal{D}$  state. This leads to wider viewing angles in a display with out effecting operation. They also report the use of bipolar pulses to switch between states. This extends the life time of a display by preventing ionic build up on the surfaces that lead to changes in switching thresholds. The sign dependence of the switched state is retained from the trailing edge of the bipolar pulse.

### 6.1.2 Theoretical and Simulation Studies

Previous efforts to calculate the switching between states have all ignored essential parts of the problem or only investigated static configurations. Works by Bryan-Brown [158] and Jones [159] report calculations for the static director fields using constant order parameter theory for both voltage on and off states. They also cal-

culate the relative energy of the  $\mathcal{C}$  and  $\mathcal{D}$  states as a function of grating groove depth to pitch ratio. Brown et al [160] calculates the effects of anchoring strength on static director states in a bi-grating cell (both top and bottom surfaces have a grating of the same type). Good [161] studies a similar bi-grating and examines director and flow dynamics when switching without flexoelectricity (driven by orthogonal magnetic fields). Newton [162] has used a lattice Monte-Carlo technique to calculate equilibrium states of the director.

There are also some studies that allow for variable order parameters and therefore a more accurate description of the defects in the system. Mottram [163] uses a commercial finite difference package allowing for multi-grids to calculate the equilibrium states on a triangular shaped grating. Denniston [146] used flat surfaces with one surface set so the directors preferred orientation varies spatially, they further show switching behaviour (creation/annihilation of defects) between states by using a quadrupolar flexoelectric surface term, constant  $\underline{E}$  value and setting  $\Delta\epsilon_a^{max} = 0$ . Parry-Jones [164] carries out calculations on a symmetric sinusoidal grating with infinite anchoring strength. As with [146] they set  $\Delta\epsilon_a^{max} = 0$  and aim to show the effect of nematic distortion on the electrical potential lines and their effect upon the creation/annihilation of defects. The switching behaviour in [164] is questionable because they use Landau coefficients an order of magnitude smaller than real values, this leads to a large unnatural length scale of defects and to order parameters  $S > 1$ . Ignoring the  $\Delta\epsilon_a^{max}$  contributions is also unrealistic for the large fields applied since the dielectric contribution varies as  $\underline{E}^2$  in contrast to flexoelectric that varies as  $\underline{E}$ . With the exception of [161] and [146] all the aforementioned studies ignored flow effects in their calculations.

## 6.2 The Equilibrium States

In this section we will use the method developed in chapter 4 to investigate the static equilibrium configurations of this device both with and without an externally applied field.

## 6.2.1 Geometry and Parameter Set

Before we calculate the stable states and the dynamics of this device we need to establish both the geometry and parameter set. The starting point for our geometry is based on the work in [158] and [160]. Brown [160] proposes an analytical function for the profile of the grating:

$$g(x) = \frac{h}{2} \sin \left[ \frac{2\pi x}{w} + A \sin \left( \frac{2\pi x}{w} \right) \right] \quad (6.1)$$

where symbols are defined in figure 6.1. The  $h$  and  $w$  parameters controlling the height and pitch of the grating and the parameter  $A$  the amount of blaze (asymmetry). The advantage of including a blaze is similar to the reason for including the pre-tilt in §5.3.1, it will make sure the directors rotate the same way when switching. The blaze of equation 6.1 is limited to  $A < 0.5$ , above this value and an unnatural inflection occurs in the  $g(x)$ . The advantage of the analytical expression means we may specify exact boundary conditions. From figure 6.2 we see work done by [158] for this grating profile to measure the relative free energy of the two  $\mathcal{C}$  and  $\mathcal{D}$  states using a Frank free energy only method (constant uniaxial order elasticity). They found for a grating depth to pitch ratio of 0.6 the energy of the two states are approximately even. The curves in figure 6.2 are not smooth, possibly due to the lack of order parameter, flexoelectric and surface contributions to the free energy. We further assume the electrodes apply their potential at the top surface and at

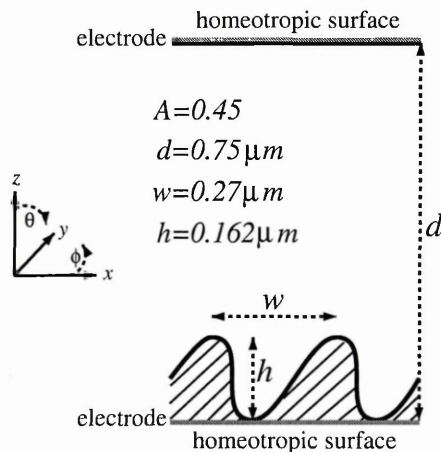


Figure 6.1: Schematic of the two dimensional ZBD geometry over two grating pitches,  $w$ . Homeotropic boundary conditions serve to cause bistability. Electrodes positioned at  $z = 0$  (earth  $\phi = 0$ ) and  $z = d$ .

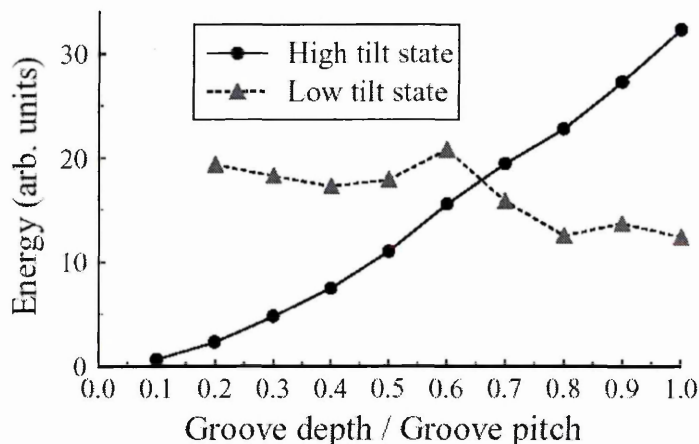


Figure 6.2: Graph taken from [158] showing the relative Frank elastic energy of the two  $\mathcal{C}$  and  $\mathcal{D}$  states for varying the grating features. True bistability and infinite life time occurs when states have equal.

the lowest point of the grating as indicated in figure 6.1. Electrodes following the grating surface would induce transverse electric field components favouring the  $\mathcal{D}$  state.

For the material parameters we choose, in addition to those specified in §4.4,  $W = 7 \times 10^{-4} \text{ kg s}^{-2}$ ,  $\gamma_S = 9.7 \times 10^{-9} \text{ kg s}^{-1}$ ,  $\Delta\epsilon_a = 10.3$ ,  $\epsilon_{\gamma\gamma}^{nem} = 30$ ,  $\epsilon_{\gamma\gamma}^{grat} = 19$ ,  $E_{13} = (e_{11} + e_{33})/2 = 2.35 \times 10^{-11} \text{ A s m}^{-1}$ ,  $\gamma_1 = 0.097 \text{ kg m}^{-1} \text{ s}^{-1}$ . Unfortunately there does not exist a complete set of measurements made for one material, we have thus constructed a best approximation from various materials such as *5CB* and *MBBA*. This is in fact not too unrealistic as in practise commercial displays often consist of a hybrid mixture. Points to note from the parameter set are the positive dielectric anisotropy, uniaxial phase Landau coefficients at temperature of  $T = T_{IN} - 4(T_{IN} - T^*)$  giving an equilibrium order parameter  $S_0 = 0.591$ , a medium to strong anchoring coefficient and quadrupolar flexoelectric coefficient ( $C_2 = 0$  and  $e_{11} = e_{33}$ ) the magnitude of which matches values from [4] (note there exists some ambiguity over the sign of this coefficient and to some extent its magnitude). Points to note from figure 6.1 are that the problem is two dimensional; thus we use periodic boundaries in the  $y$  direction and periodic boundaries in the  $x$  direction to include one grating pitch. We also use device dimension two times smaller than in currently manufactured cells, this is to ease the computational burden of the problem. Results can be expected to linearly scale up in terms of the switching voltages and times.

As we advance the application of the model to a two dimensional geometry with

complex surface grating structure it will serve to, at first, reduce the scope of the problem, it will also aid to identify the influential parts of the theory in the device operation. We thus proceed by first ignoring flow contributions and secondly to assume that it is the electric field (not the displacement field) that is constant.

## 6.2.2 Calculated Profiles

The search for equilibrium states with no external field is done by initialising the system with standard configurations such as homeotropic, planar, twisted and hybrid alignments with opposite director rotation and completely random isotropic states that are slowly cooled to the nematic phase from the isotropic phase. Three equilibrium states are found and depicted in figures 6.3 to 6.5. In these figures the grating substrate is modelled as isotropic and we choose to plot its colour as that of the equilibrium order parameter as a reference to changes.

The first state, figure 6.3, represents the  $\mathcal{C}$  state, it has mainly vertical director alignment apart from the grating region in which the director bends/splays to meet the boundary conditions. The order parameter is constant in the bulk and falls slightly towards the boundaries (8%) due to increased distortion. Similarly the biaxial order parameter is zero in the bulk but increases slightly at the boundaries.

The second state, figure 6.4, is the  $\mathcal{D}$  state, it has a vertical director at the top and continuous anticlockwise rotation as you go down through the cell. It is further characterised by two defects, a  $m = -1/2$  at the grating peak and  $m = +1/2$  at the grating trough. The defect core is a few nanometres wide at which the order parameters melts and the biaxiality rises strongly. It may appear the  $m = +1/2$  defect is stronger because it has a lower order parameter but this is not so, the  $m = -1/2$  defect is more tightly pressed against the surface due to interactions from the bulk of the device.

The third state, figure 6.5, is the  $\mathcal{D}1$  state, it has a vertical director at the top and continuous clockwise rotation of the director as you go down through the cell. Again a pair of  $m = -1/2$  and  $m = +1/2$  defects reside at the peaks and troughs of the grating respectively. The effective alignment just above the grating alignment is more tilted than in the  $\mathcal{D}$  state and the  $m = -1/2$  defect is slightly shifted to the left.

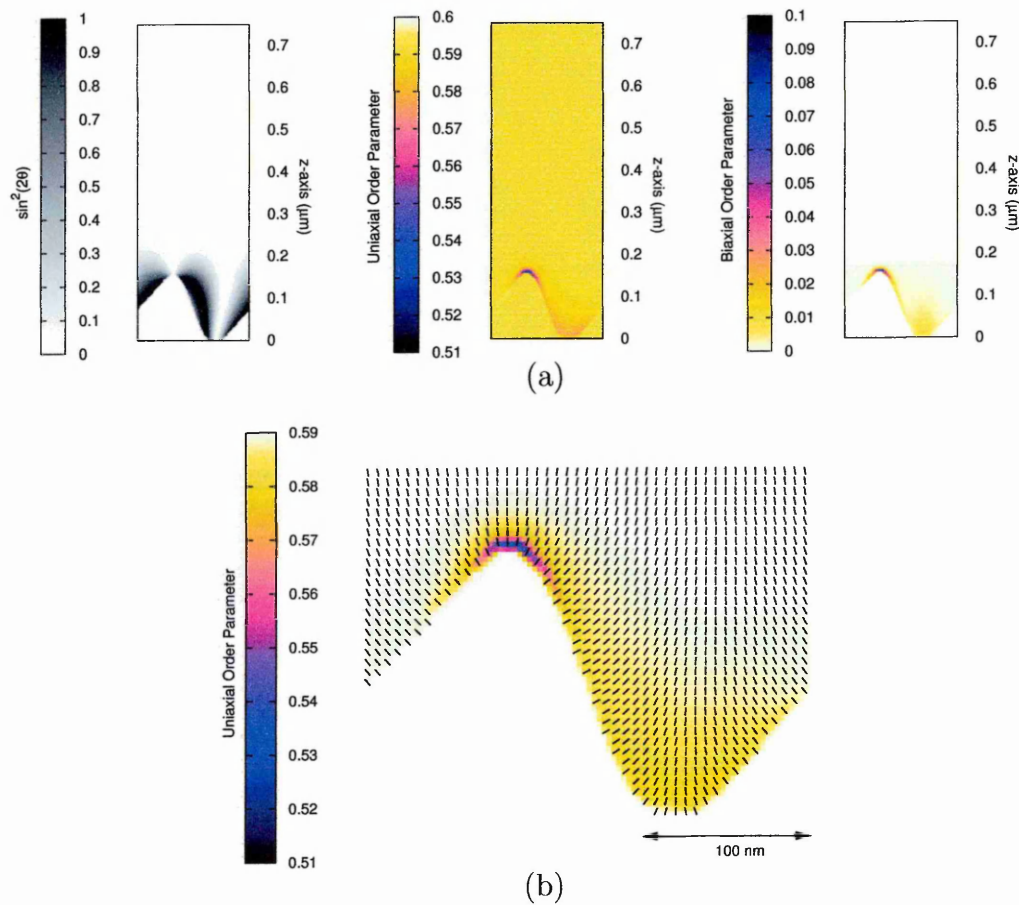


Figure 6.3: Plots of the equilibrium  $\mathcal{C}$  state in the ZBD for (a) the entire simulation cell and (b) a close up of the order and director at the grating surface (data plotted every other lattice point).

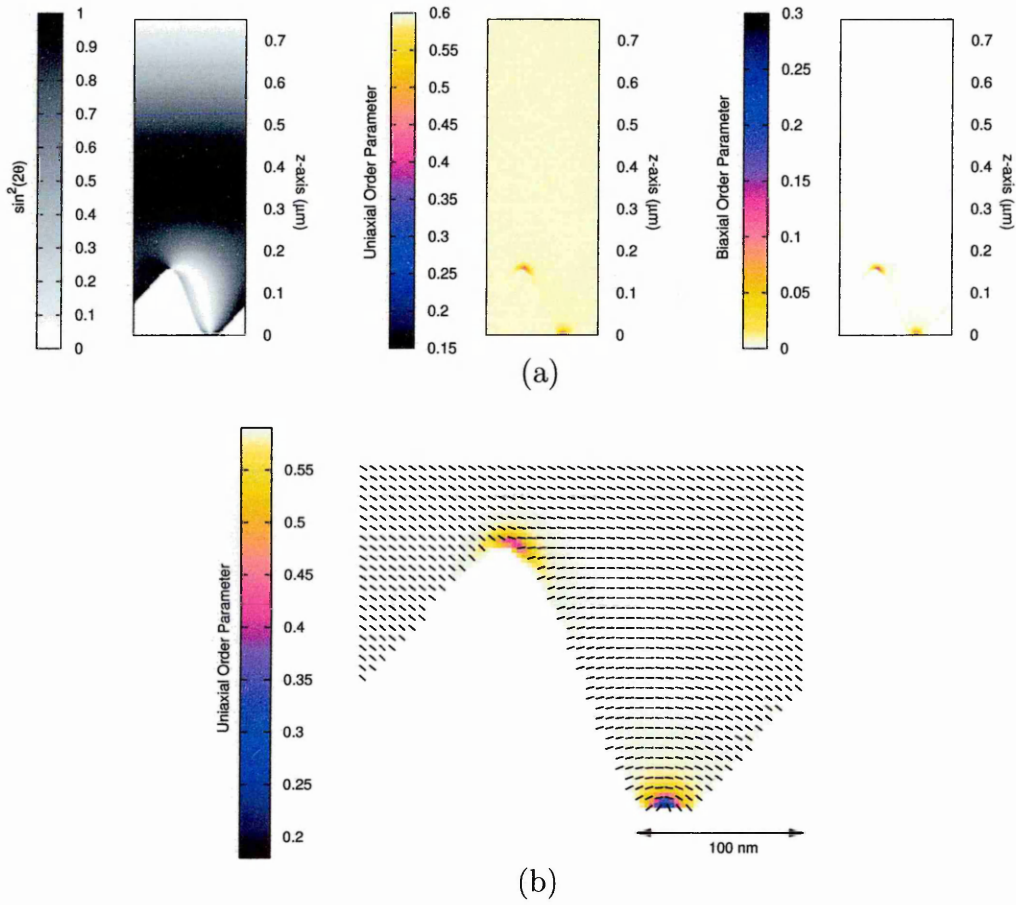


Figure 6.4: Plots of the equilibrium  $\mathcal{D}$  state in the ZBD for (a) the entire simulation cell and (b) a close up of the order and director at the grating surface (data plotted every other lattice point).

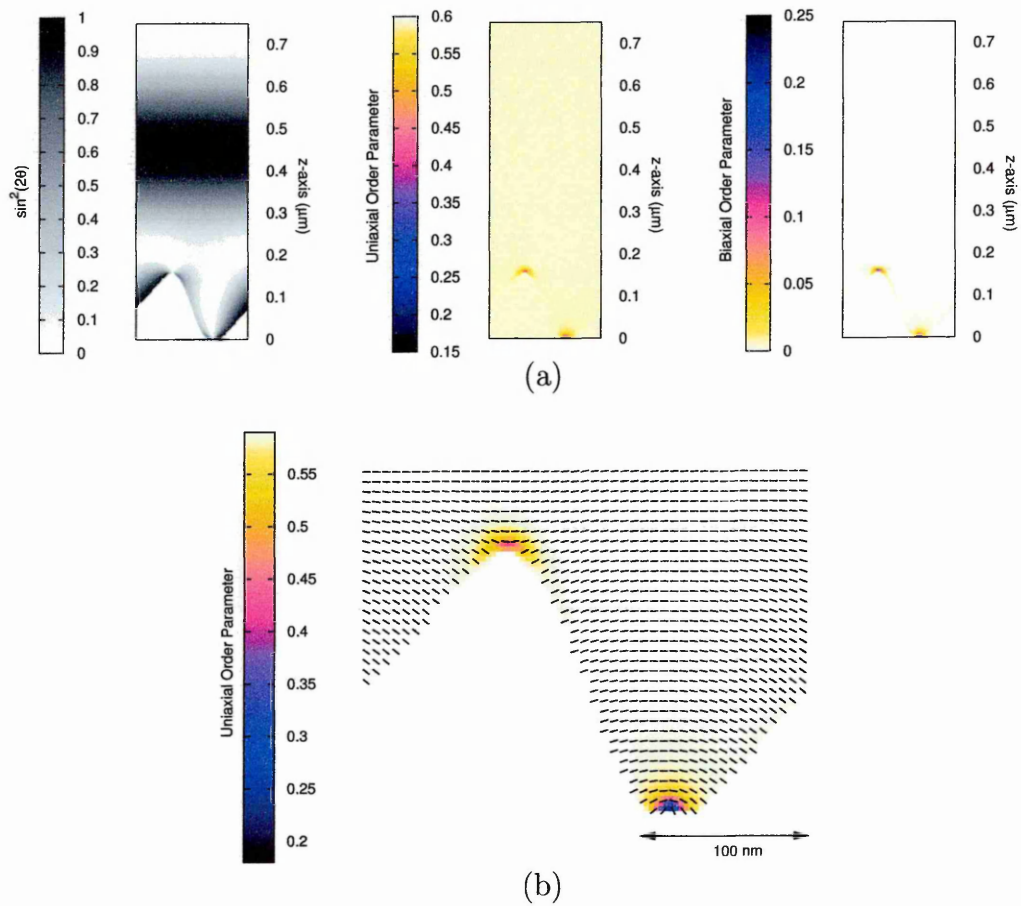


Figure 6.5: Plots of the equilibrium  $\mathcal{D}1$  state in the ZBD for (a) the entire simulation cell and (b) a close up of the order and director at the grating surface (data plotted every other lattice point).

Although we find more than two local minima in the free energy of this device we note the  $\mathcal{D}1$  state is a higher energy and weaker minima in contrast to the  $\mathcal{C}$  and  $\mathcal{D}$  states. Further as we will see in §6.3 as a consequence of the way in which the device switches the  $\mathcal{D}1$  state will never practically be seen which is consistent with light transmission data [158]. We also note that for the cases where the system is initialised in the isotropic phase and then slowly cooled to the nematic phase the  $\mathcal{D}$  state is always found. The surfaces also induce nematic wetting and drive the transition to a nematic phase from the isotropic phase.

Figure 6.6 shows what happens to the ZBD cell if we apply a potential difference between the electrodes ( $\phi(z = 0) = 0V$ ,  $\phi(z = d) = +$  or  $-15V$ ) with  $E_{13} = 0$ . In other words when no flexoelectricity effects are considered both positive and negative applied fields have the same effect (dielectric effect  $\propto E^2$ ). In figure 6.6

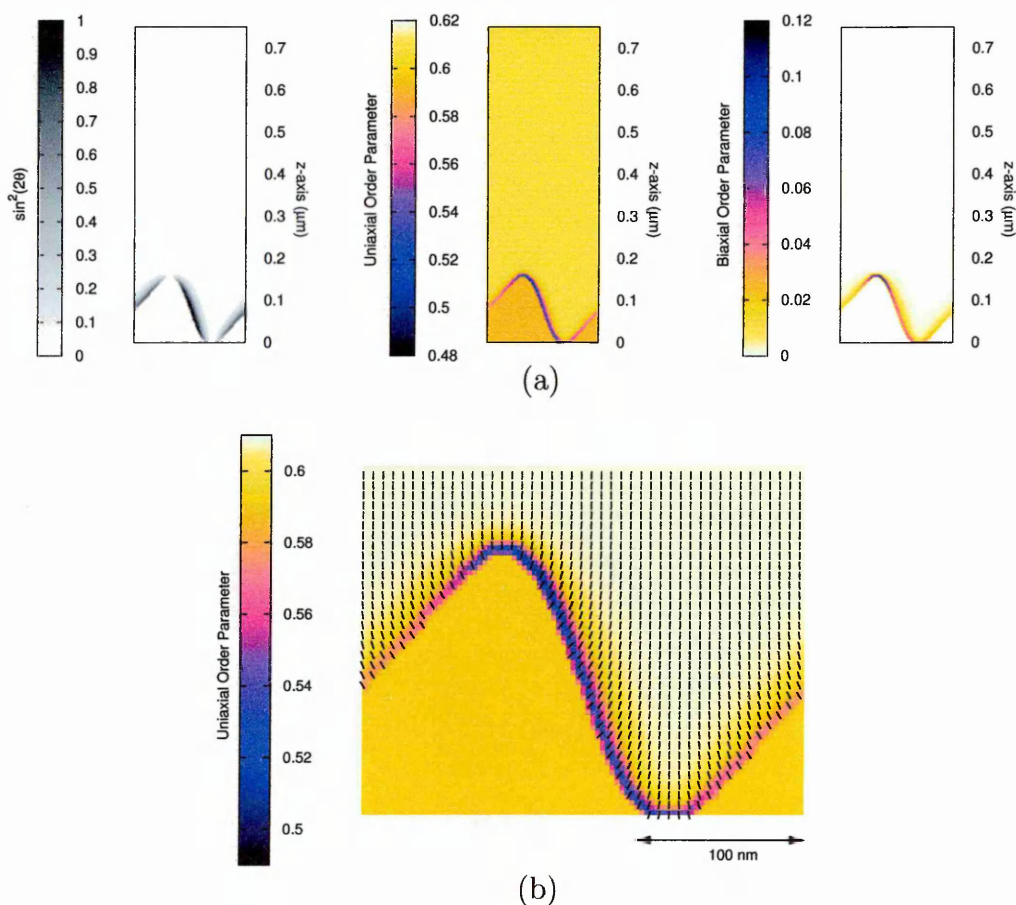


Figure 6.6: Plots of the equilibrium states with either an applied  $+$  or  $-15V$  in the ZBD for  $E_{13} = 0$  (no flexoelectric properties) in (a) the entire simulation cell and (b) a close up of the order and director at the grating surface (data plotted every other lattice point).

the director is even more vertical throughout the cell than the  $\mathcal{C}$  state, the slight distortion is limited to a boundary region of length  $\sim \frac{1}{|\underline{E}|} \sqrt{\frac{K}{\epsilon_0 \Delta \epsilon_a}}$ . Upon turn off of this potential difference it is easiest for the system to relax to the  $\mathcal{C}$  state and this is indeed what happens. So when there is no flexoelectricity modelled the device is monostable (for vertical electric fields). This emphasises that extra polar molecular characteristics need to be included in the calculations in order to recover the observed behaviour of the device.

### 6.2.3 Why Flexoelectricity can cause Bistability

To examine why flexoelectric properties can cause bistability we examine the significantly simplified situation depicted in figure 6.7. Here is shown a one dimensional liquid crystal cell with infinite aspect into the  $x$  and  $y$  directions. We further assume the lower surface can take any arbitrary orientation. Ignoring variation from this surface angle in the  $x$  and  $y$  direction we examine the flexoelectric free energy density as defined in equation 2.25 and equation 2.26:

$$F_{Flexo} = -E_\theta P_\theta = -C_1 E_\theta \partial_\gamma Q_{\theta\gamma} - C_2 E_\theta Q_{\theta\gamma} \partial_\mu Q_{\gamma\mu} \quad (6.2)$$

Examining the flexoelectric free energy at the lower surface in the limit of quadrupolar flexoelectricity ( $C_2 = 0$ ) and uniaxial behaviour (equation 2.8) gives:

$$F_{Flexo} \Big|_{z=0} = \frac{-3S_0 C_1 E_z}{4} (\sin(2\theta) \hat{v}_x + \cos(2\theta) \hat{v}_z) \quad (6.3)$$

in which  $\theta$  is the polar director angle defined from the  $z$  axis. A minimisation of equation 6.3 with respect to  $\theta$  shows how the director prefers to lie at the surface

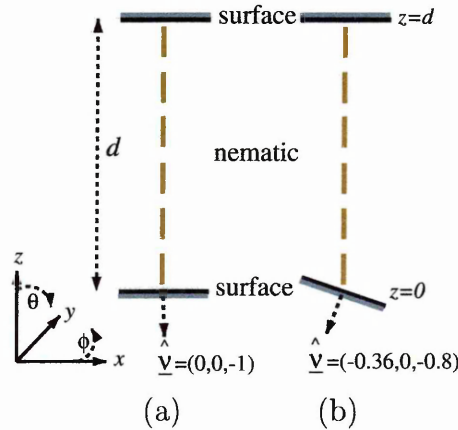


Figure 6.7: Schematic of a simple one-dimensional liquid crystal cell. (a) for the usual horizontal boundaries, (b) allowing the lower boundary to take some orientation.

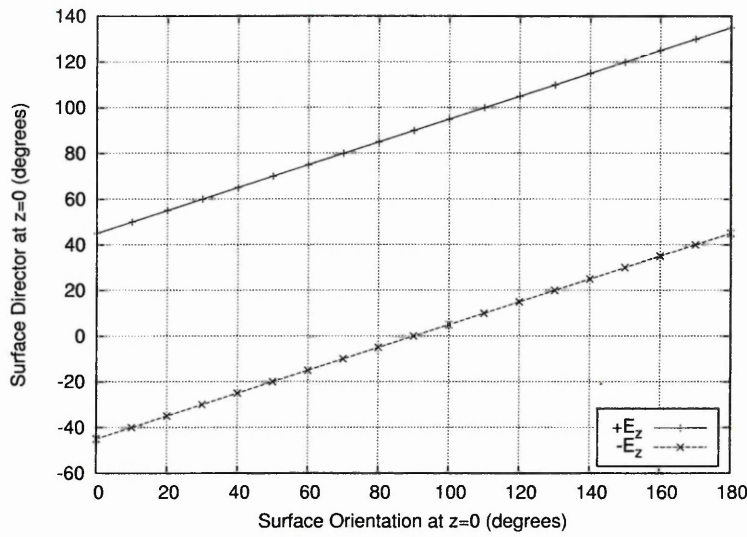


Figure 6.8: Graph showing the  $z=0$  (lower) preferred surface director angles due to both flexoelectric polarisation and surface orientation. For different directions of the applied field the preferred directors are different. Both surface and director angle have been defined with respect to the positive  $z$  axis.  $C_1 > 0$

due to contributions from flexoelectricity. For now, we assume the flexoelectric coefficient  $C_1 = [(e_{11} + e_{33})/3S_0]$  is positive and plot these preferred director angles for various surface orientations in figures 6.8 and 6.9 for both positive and negative field strengths. This shows opposite field strengths cause opposite distortions. The director points up-wards from the surface for negative fields and the director points down-wards from the surface for positive fields.

We can further usefully approximate the device behaviour by assuming *a*) the surface is completely dominated by flexoelectric contributions and *b*) the bulk is dominated by dielectric contributions and aligns with the field direction ( $z$  axis). This behaviour is sketched in figure 6.10 where the equilibrium directors of figure 6.9 have been rearranged into an approximate region of the grating. The negative

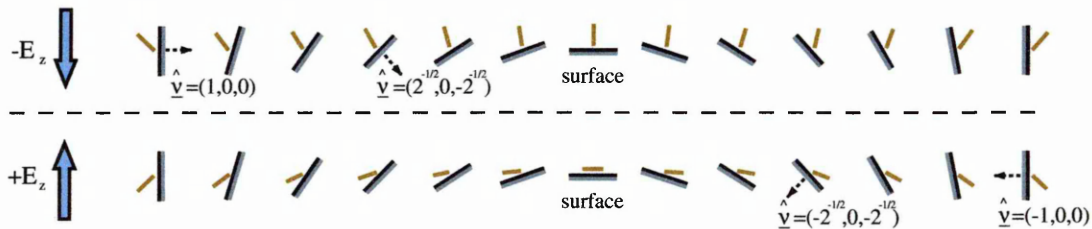


Figure 6.9: Pictorial representation of the preferred director orientation due to flexoelectric polarisation and surface orientation at opposite electric field directions.  $C_1 > 0$

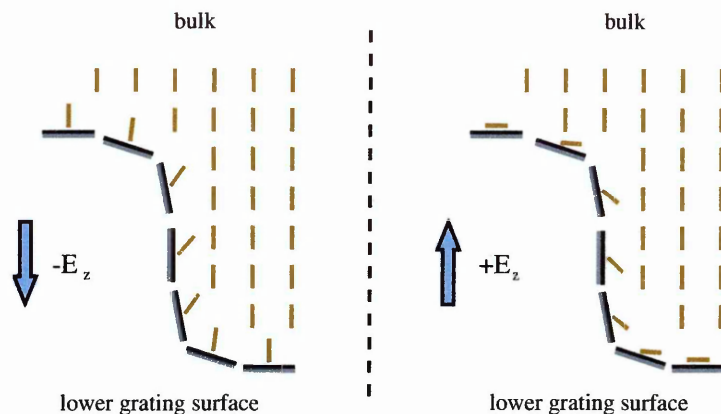


Figure 6.10: Pictorial representation of grating region assuming surfaces are dominated by flexoelectric polarisation and the bulk is dominated by dielectric contributions. For a positive field direction the director field is continuous in the vertical direction. For a negative field direction the director field is discontinuous: defect like regions occur at the grating surface.  $C_1 > 0$

applied field case gives rise to a continuous director structure from the surface to the bulk. Conversely the positive applied field gives a discontinuity of directors in going from surface to bulk. Further, the top corner of the grating, for the positive field case, has similar symmetry equivalent to a  $m = -1/2$  defect defined in figure 2.4 and the bottom grating corner has similar symmetry equivalent to a  $m = +1/2$  defect also defined in figure 2.4. Still further, upon release of the electric field in figure 6.10b there will be a essentially two driving forces: that of elasticity rotating the directors clockwise to-wards the  $\mathcal{C}$  state and that of homeotropic anchoring which will rotate the director anti-clockwise serving to stabilise the formation of two defects.

In the next section we put this simplified mathematical picture to the test by solving the complete system states for applied fields.

#### 6.2.4 Effects of Opposite Field Strength

It is well reported [158] that the ZBD has switching thresholds in switching between states  $\mathcal{C}$  and  $\mathcal{D}$ . Jones et al [165] in their investigation of grey scales, investigate switching thresholds for different sized cells and find the voltage decreases approximately linearly with  $d$ , the device height. For the dimensions quoted in figure 6.1 we may expect a switching threshold from  $\phi \gtrsim \pm 9V$ . Investigation of the effect of applying a voltage above this threshold is shown in figures 6.11 and 6.12. The

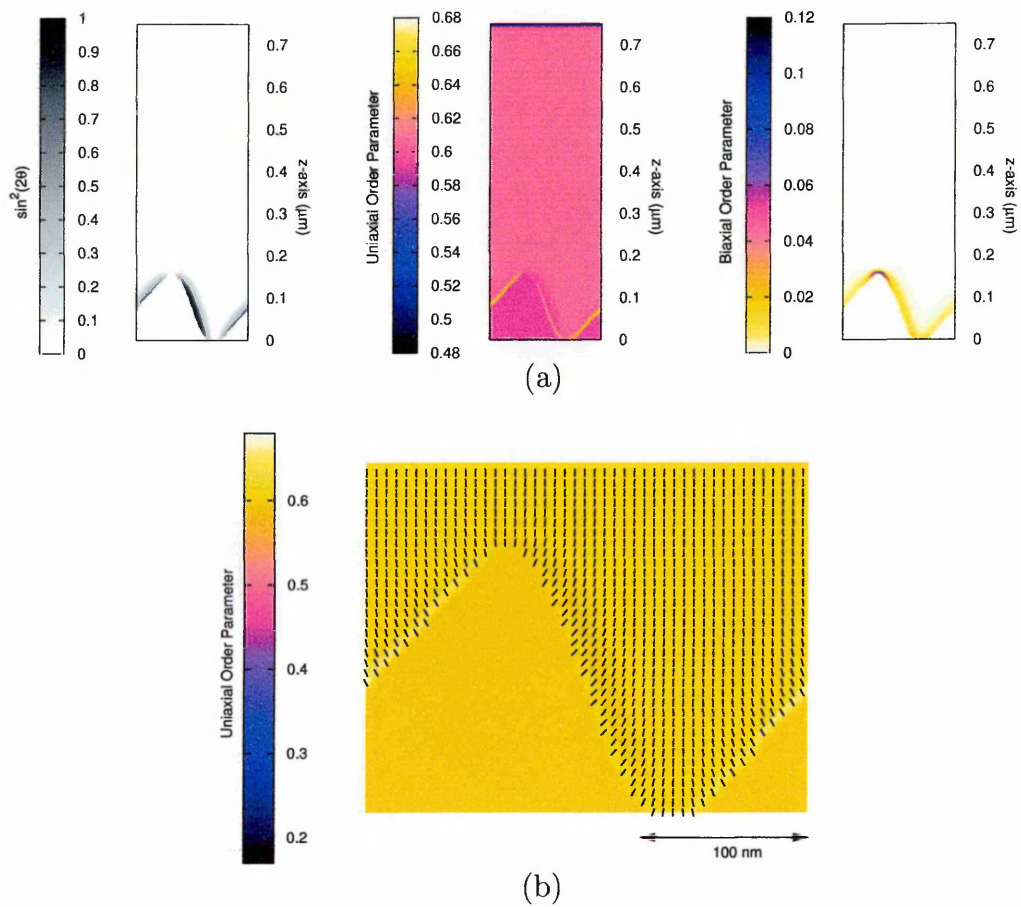


Figure 6.11: Plots of the equilibrium states with an applied +15 V in the ZBD for  $E_{13} = 2.35 \times 10^{11} \text{ A s m}^{-1}$  for (a) the entire simulation cell and (b) a close up of the order and director at the grating surface (data plotted every other lattice point).

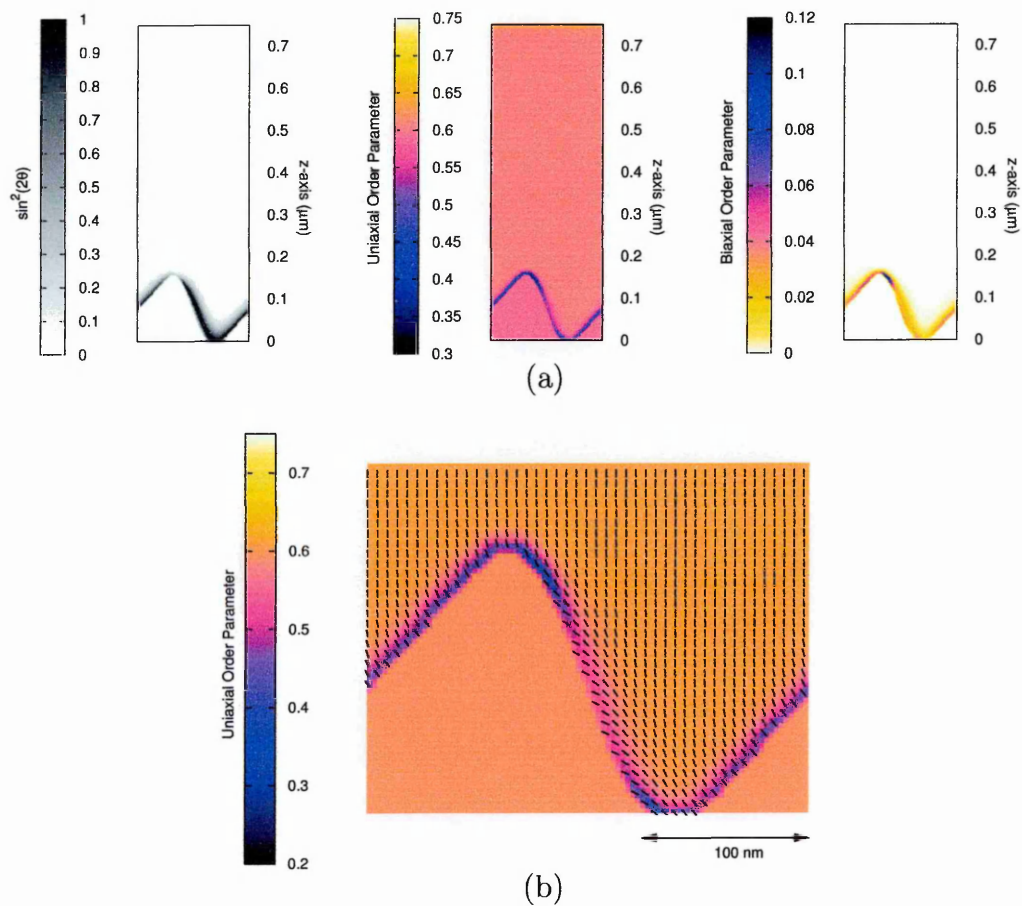


Figure 6.12: Plots of the equilibrium states with an applied  $-15\text{ V}$  in the ZBD for  $E_{13} = 2.35 \times 10^{11}\text{ A s m}^{-1}$  for (a) the entire simulation cell and (b) a close up of the order and director at the grating surface (data plotted every other lattice point).

electrode conditions are such  $\phi(d) = V$  and  $\phi(0) = 0$ .

For the negative electric field the director for the most part is vertical, the distortion around the grating surface is as predicted in §6.2.3 due to flexoelectric polarisation together with an increase in the order parameter (decrease at the upper surface) due to order electric polarisation. For the positive electric field again the director is vertical for most of the cell but the distortion around the grating surface is opposite to the negative field case. As predicted in §6.2.3 a ‘frustrated’ region on the grating forms due to the opposite polarisations where the beginnings of  $m = +1/2$  and  $m = -1/2$  defect regions occur. Note the surface order parameter decreases (increases at the upper surface).

Upon release of the electric field it is the positive electric field case that is likely to form defects for strong enough anchoring conditions. For the negative electric field it will always relax to the  $\mathcal{C}$  state.

In the simplified mathematical conjecture applied in §6.2.3 for the flexoelectric free energy at the surface, equation 6.3 assumed a uniaxial constant order parameter form (EL limit). This poses the question: can we achieve the frustrated surface states and switching in the much simpler EL framework? In doing this comparison it will help to identify the differences in using an EL form from the  $Q$  tensor approach for the study of defects and their dynamics.

Figures 6.13 show the  $\mathcal{C}$  and  $\mathcal{D}$  states as calculated in the EL limit. Comparison of directors with figure 6.3 show little difference for the  $\mathcal{C}$  state. Comparison of directors with figure 6.4 shows differences only at the defect sites as expected with the larger length scales imposed by the EL limit.

To impose the EL limit through our LB method, at every time step we calculate  $\hat{n}_\alpha$  and then reconstruct  $Q_{\alpha\beta}$  so it obeys equation 2.8 with the order parameter set to its equilibrium value. Further the parameters  $\alpha_F = \beta_B = \gamma_F = 0$ , whilst everything else remains unchanged. A simpler normalisation method,  $Q_{\alpha\beta} = Q_{\alpha\beta}/S$  [61] will not work as the tensor can still take biaxial forms. Imposing the EL limit this way ensures  $\pm\hat{n}_\alpha$  equivalence allowing for the  $m = \pm 1/2$  defects to have correct symmetry.

Figures 6.14 show the equilibrium states calculated in the EL limit for applied voltages. In figure 6.14a, +15V has been applied and reproduces the states of

figure 6.11 well. In figure 6.14b  $-35\text{V}$ , has been applied in order to reproduce the surface ‘frustrated’ state of figure 6.12. The fact that for opposite voltages in the EL limit we still form continuous and defect structures suggest switching between states may be achieved via the simpler theory. However the route to formation and annihilation of the defects may be different.

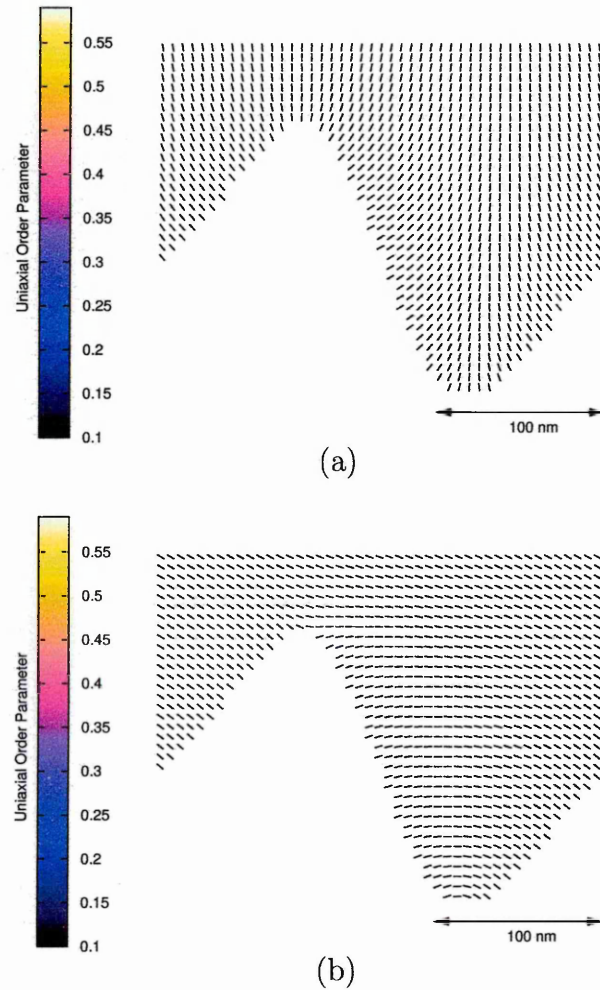
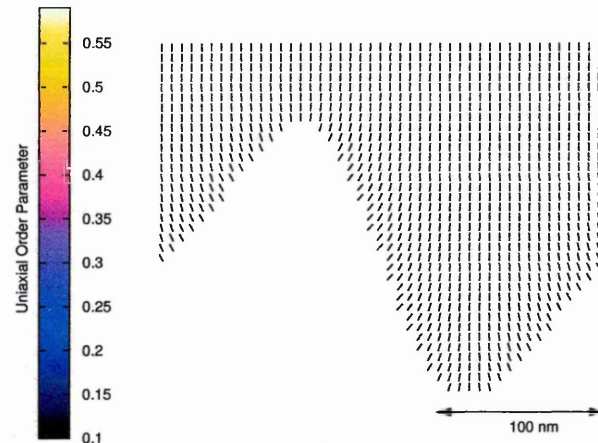
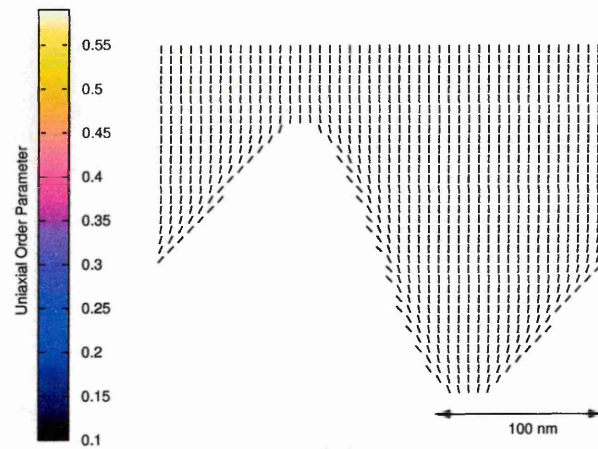


Figure 6.13: Plots of the equilibrium director in the EL limit of (a)  $\mathcal{C}$ , (b)  $\mathcal{D}$  states in the ZBD at the grating surface (data plotted every other lattice point).



(a)



(b)

Figure 6.14: Plots of the equilibrium director in the EL limit for an applied (a) +15 V, (b) -35 V at the grating surface (data plotted every other lattice point).

## 6.3 Switching Behaviour In The ZBD

In the previous section we saw that when a flexoelectric nematic is used it produces opposite surface distortions for opposing field directions. The negative field favouring a more continuous alignment and for the positive field regions in which defects appear. This section will study the dynamics of the device switching. We will also contrast the dynamic differences of the  $Q$  tensor and EL methods during the switching.

### 6.3.1 $\mathcal{D}$ to $\mathcal{C}$ State Switching

Starting from the calculated  $\mathcal{D}$  states we apply a  $\phi = +15$  volts (negative  $\underline{E}$ ) until the system reaches steady state and then turn it off  $\phi = 0$  volts. The resulting process for the  $Q$  tensor and EL calculations are shown in figures 6.15 to 6.18. (Only the grating region is shown for clarity, above this region behaves simply.)

For the  $Q$  tensor method we see the bulk directors rotate quickly to align to the applied field. Next there is an increase in the order parameter at the surface due to flexoelectric and order electric polarisation. As defects generally follow downward gradients in  $S$ , the defects are projected off the surfaces due to the polarisation, figure 6.15d. A band of slightly decreased  $S$  forms in which a larger bend-splay distortion occurs through which the defects travel to annihilate. After which the system reaches the steady state that was predicted. After the field is removed the surface polarisation reduces and the system relaxes to the  $\mathcal{C}$  state. Relaxation into the  $\mathcal{C}$  state happens relatively quickly.

For the EL limit method again bulk directors align quickly to the applied field. The defects are not projected off the surface but remain there. This causes a large bend-splay region distortion in which to lower the free energy the director structure breaks leaving behind a pair of opposite strength defects at the grating peaks and troughs. Even though the defects have opposite strength it is found they do not annihilate even at stronger applied electric fields. This seems to be an artifact of the constant order parameter method in which it distinguishes between surface defects and bulk defects: only surface-surface defects and bulk-bulk-defects may annihilate/create. Upon release of the field the surface defects remain in place and the the  $m = -1/2$  defect rises out of the trough to annihilate with the bulk

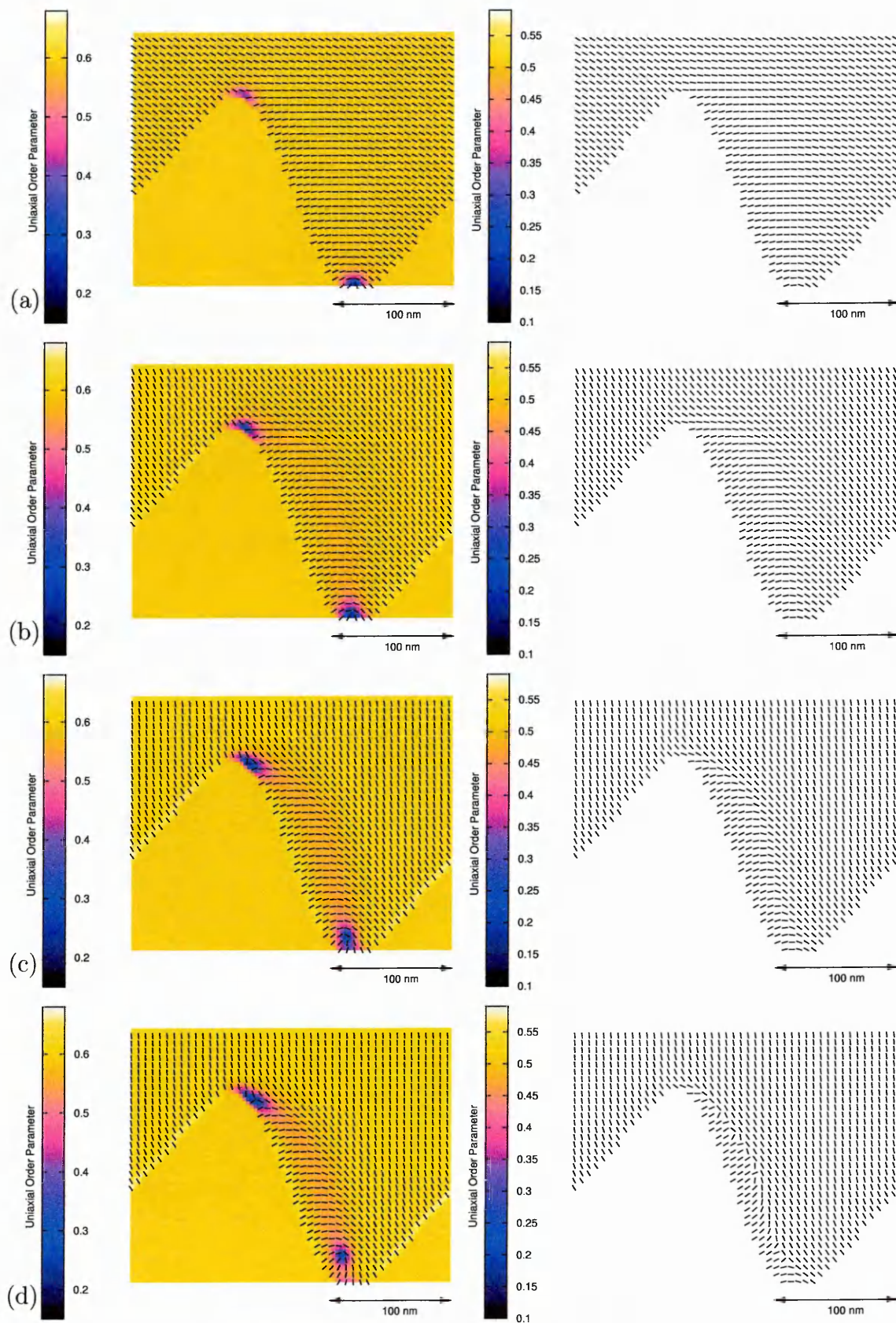


Figure 6.15: Switching from the  $\mathcal{D}$  to  $\mathcal{C}$  state through application of +15 V at  $t = 0$  to  $t = 34.92\mu\text{s}$ . Left (right) indicate calculations from the Q tensor (EL limit). (a)  $t = 0\text{s}$ , (b)  $t = 3.492\mu\text{s}$ , (c)  $t = 6.984\mu\text{s}$ , (d)  $t = 8.73\mu\text{s}$ . (Data plotted every other lattice point.)

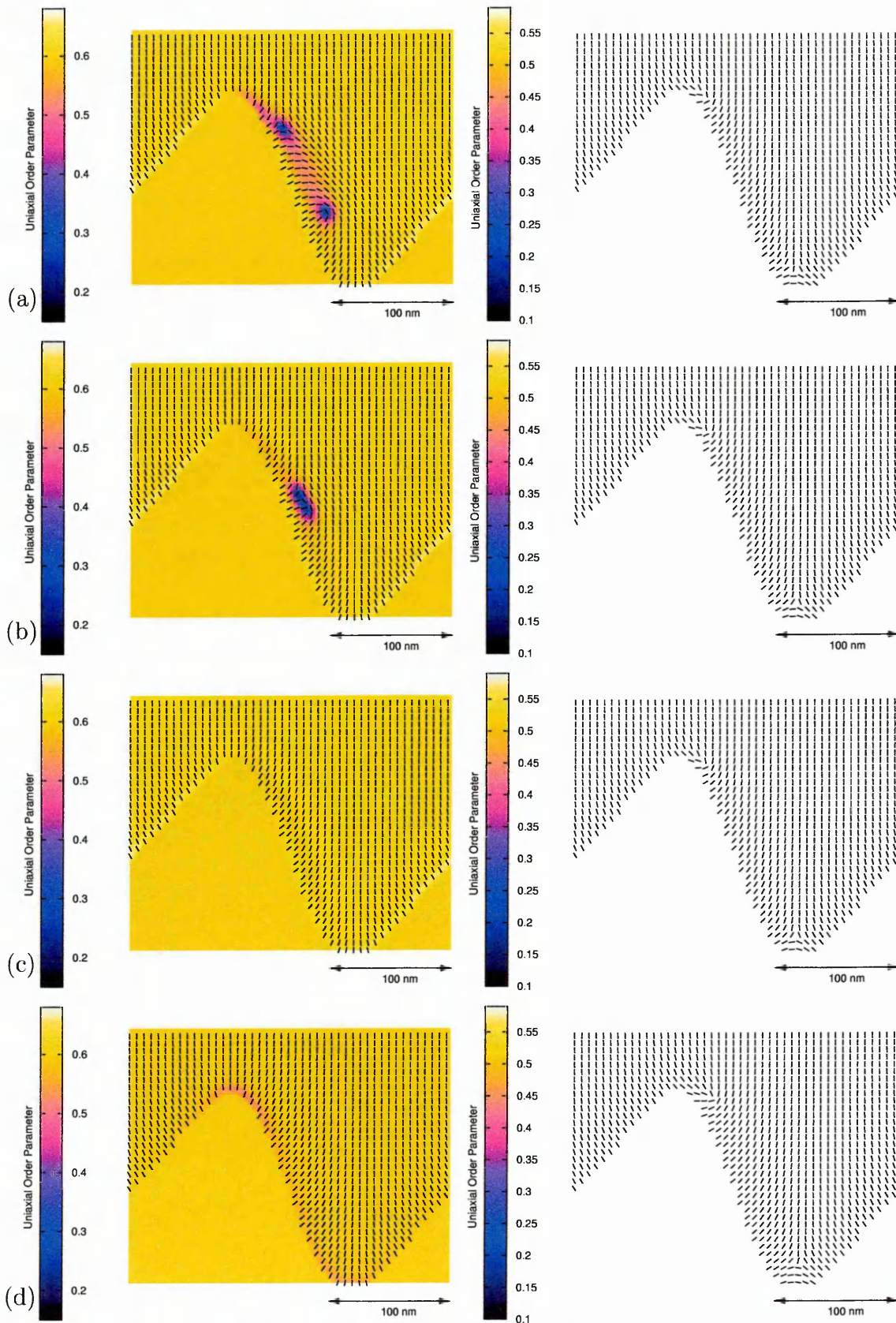


Figure 6.16: Switching from the  $\mathcal{D}$  to  $\mathcal{C}$  state through application of +15 V at  $t = 0$  to  $t = 34.92\mu\text{s}$ . Left (right) indicate calculations from the Q tensor (EL limit). (a)  $t = 13.968\mu\text{s}$ , (b)  $t = 17.46\mu\text{s}$ , (c)  $t = 20.952\mu\text{s}$ , (d)  $t = 38.412\mu\text{s}$ . (Data plotted every other lattice point.)

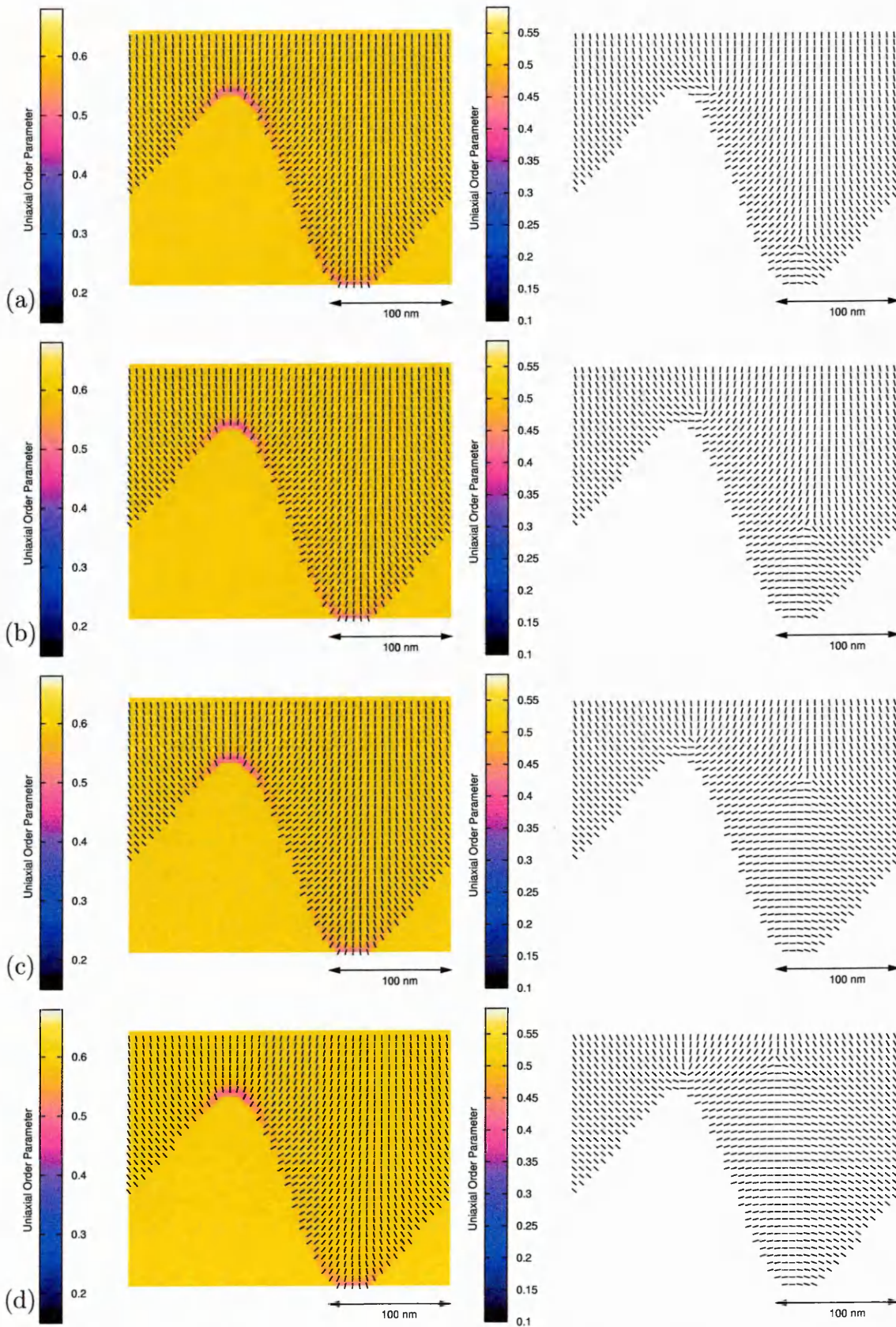


Figure 6.17: Switching from the  $\mathcal{D}$  to  $\mathcal{C}$  state through application of +15 V at  $t = 0$  to  $t = 34.92\mu\text{s}$ . Left (right) indicate calculations from the  $\mathbf{Q}$  tensor (EL limit). (a)  $t = 48.888\mu\text{s}$ , (b)  $t = 83.808\mu\text{s}$ , (c)  $t = 153.648\mu\text{s}$ , (d)  $t = 223.48\mu\text{s}$ . (Data plotted every other lattice point.)

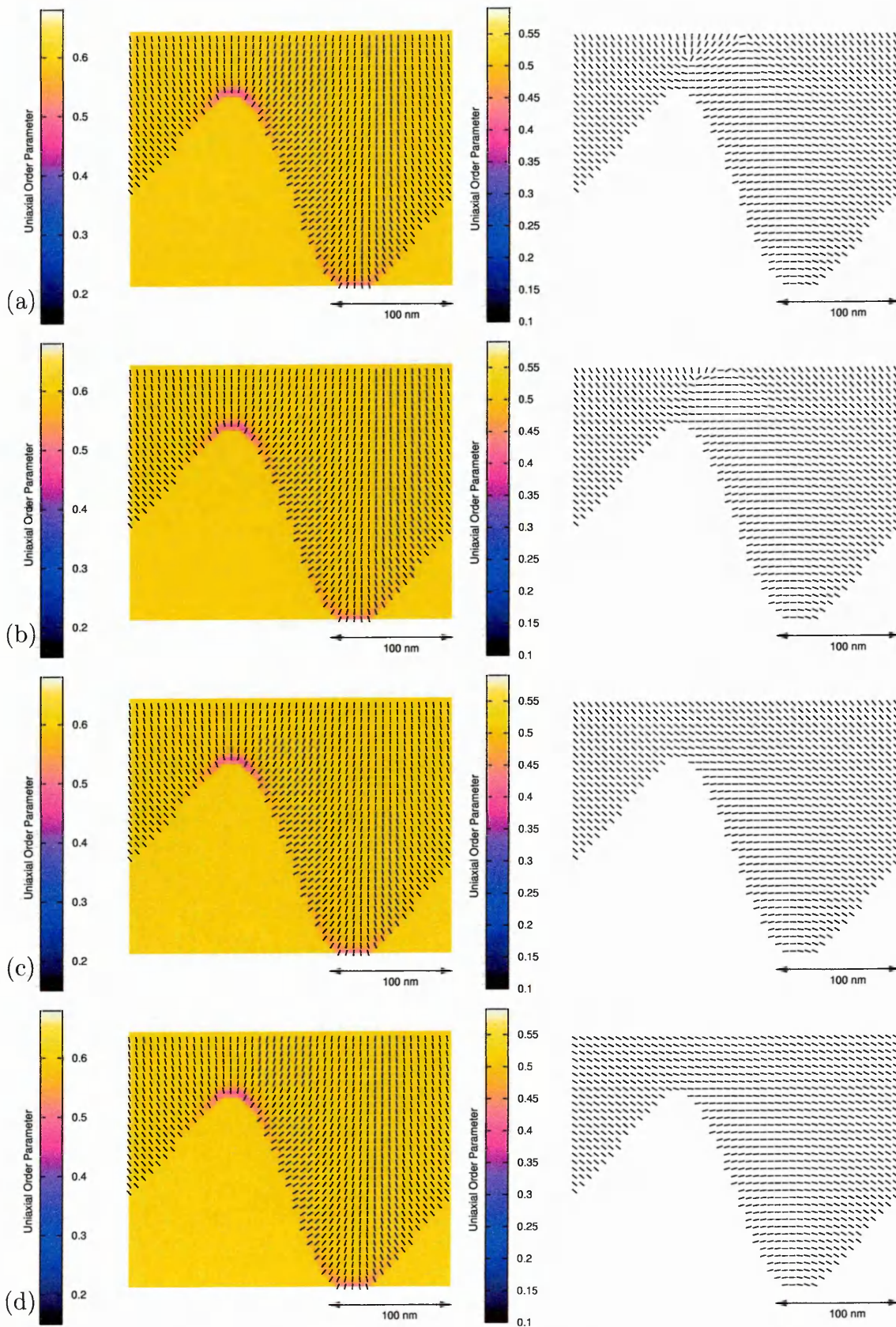


Figure 6.18: Switching from the  $\mathcal{D}$  to  $\mathcal{C}$  state through application of +15 V at  $t = 0$  to  $t = 34.92\mu\text{s}$ . Left (right) indicate calculations from the Q tensor (EL limit). (a)  $t = 258.408\mu\text{s}$ , (b)  $t = 263.646\mu\text{s}$ , (c)  $t = 298.566\mu\text{s}$ , (d)  $t = 1.746\text{ms}$ . (Data plotted every other lattice point.)

$m = +1/2$  defect. So the system has returned to the initial  $\mathcal{D}$  state.

This switching process is summarised in figure 6.19 where the average director angle is plotted in time. Figure 6.19a corresponds to the previous figures in which the final states for the two calculations are opposite. Figure 6.19b shows that it is possible to switch from the  $\mathcal{D}$  to  $\mathcal{C}$  in the EL limit if we apply a voltage for a much larger period of time.

At higher applied voltages in the  $Q$  tensor method the defect motions are altered. The original defects are still projected off the surfaces but in addition two  $m = \pm 1/2$  defects are created at around  $h/2$  in the high distortion region of figure 6.15c. The  $m = +1/2$  defect then moves upwards to meet the  $m = -1/2$  defect from the grating peak. The  $m = -1/2$  defect moves downwards to meet the  $m = +1/2$  defect from the grating trough.

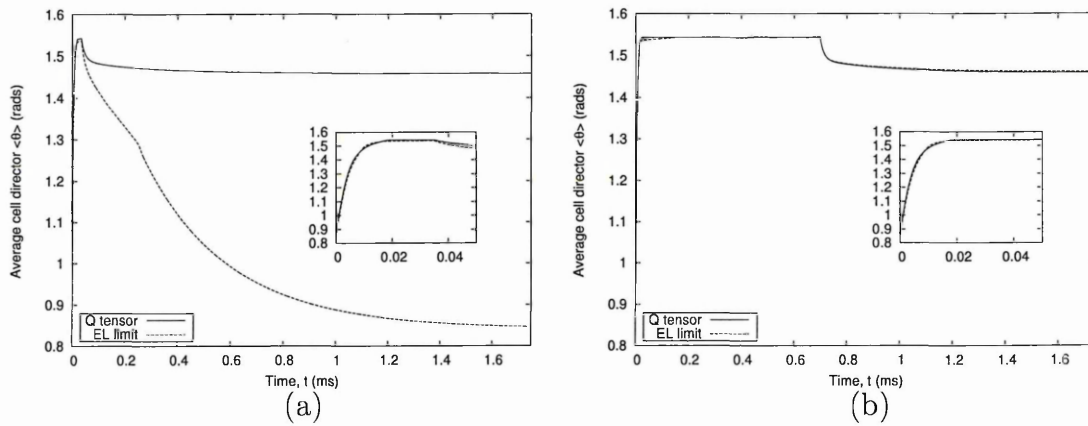


Figure 6.19: Graphs showing the cell average director angle during the switching  $\mathcal{D}$  to  $\mathcal{C}$  (a) voltage applied for  $t = 34.92\mu\text{s}$ , (b) voltage applied for  $t = 698.4\mu\text{s}$ . Inset graphs zoom in on the  $t = 0$  region to identify the initial state. Note average cell director is measured with respect to the  $x$ -axis.

### 6.3.2 $\mathcal{C}$ to $\mathcal{D}$ State Switching

Starting from the calculated  $\mathcal{C}$  states we apply  $\phi = -15$  volts (positive  $\underline{E}$ ) until the system reaches steady state and then turn it off  $\phi = 0$  volts. The switching process is depicted in figures 6.20 to 6.23.

For the  $Q$  tensor method the bulk directors align quickly with the field. The opposite polarisation now occurs at the surface causing the order parameter to lower. The surface directors then rotate to form the ‘frustrated’ state of the beginning of

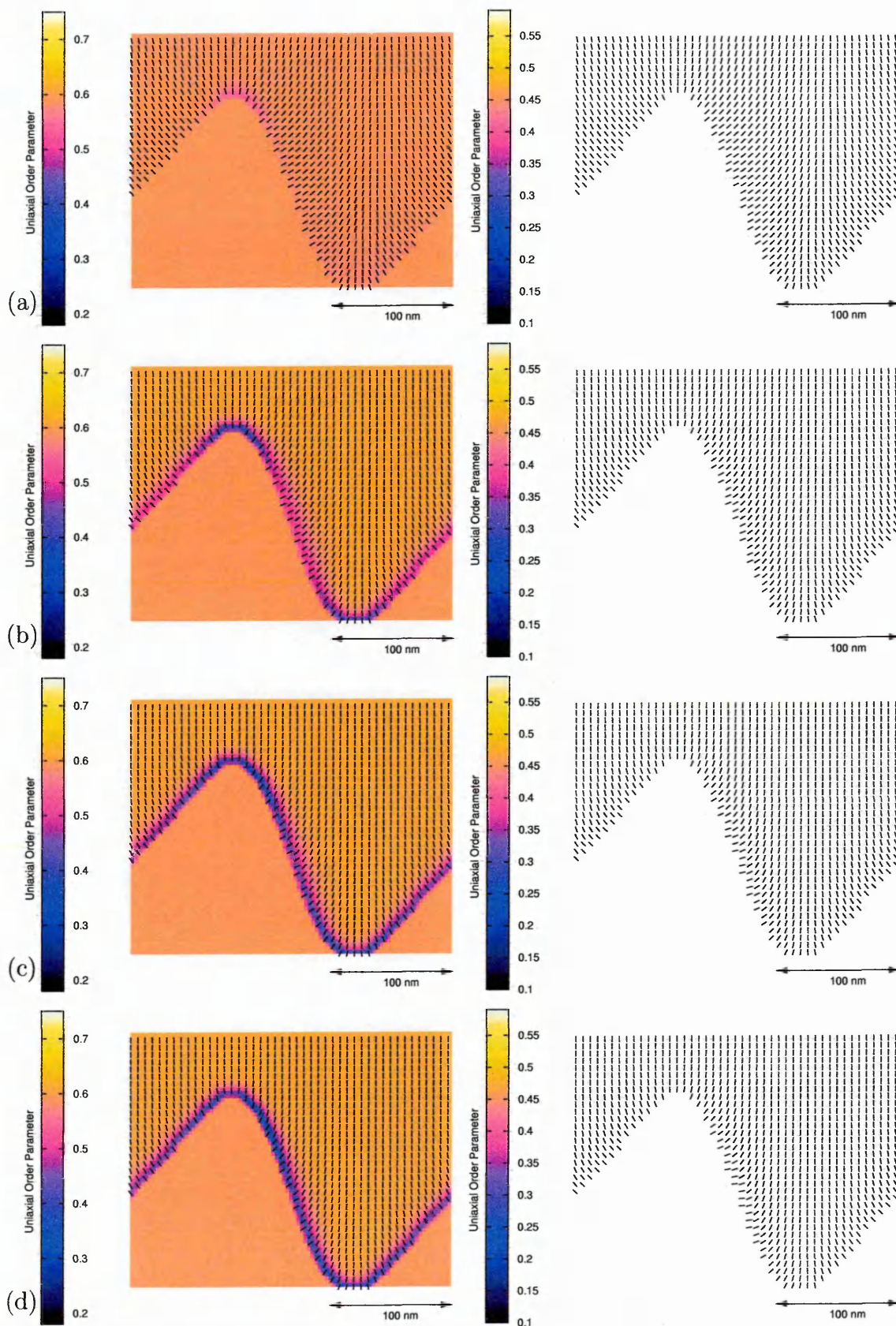


Figure 6.20: Switching from the  $C$  to  $D$  state through application of  $-15$  V at  $t = 0$  to  $t = 349.2\mu\text{s}$ . Left (right) indicate calculations from the  $Q$  tensor (EL limit). (a)  $t = 0\text{s}$ , (b)  $t = 3.492\mu\text{s}$ , (c)  $t = 17.46\mu\text{s}$ , (d)  $t = 34.92\mu\text{s}$ . (Data plotted every other lattice point.)

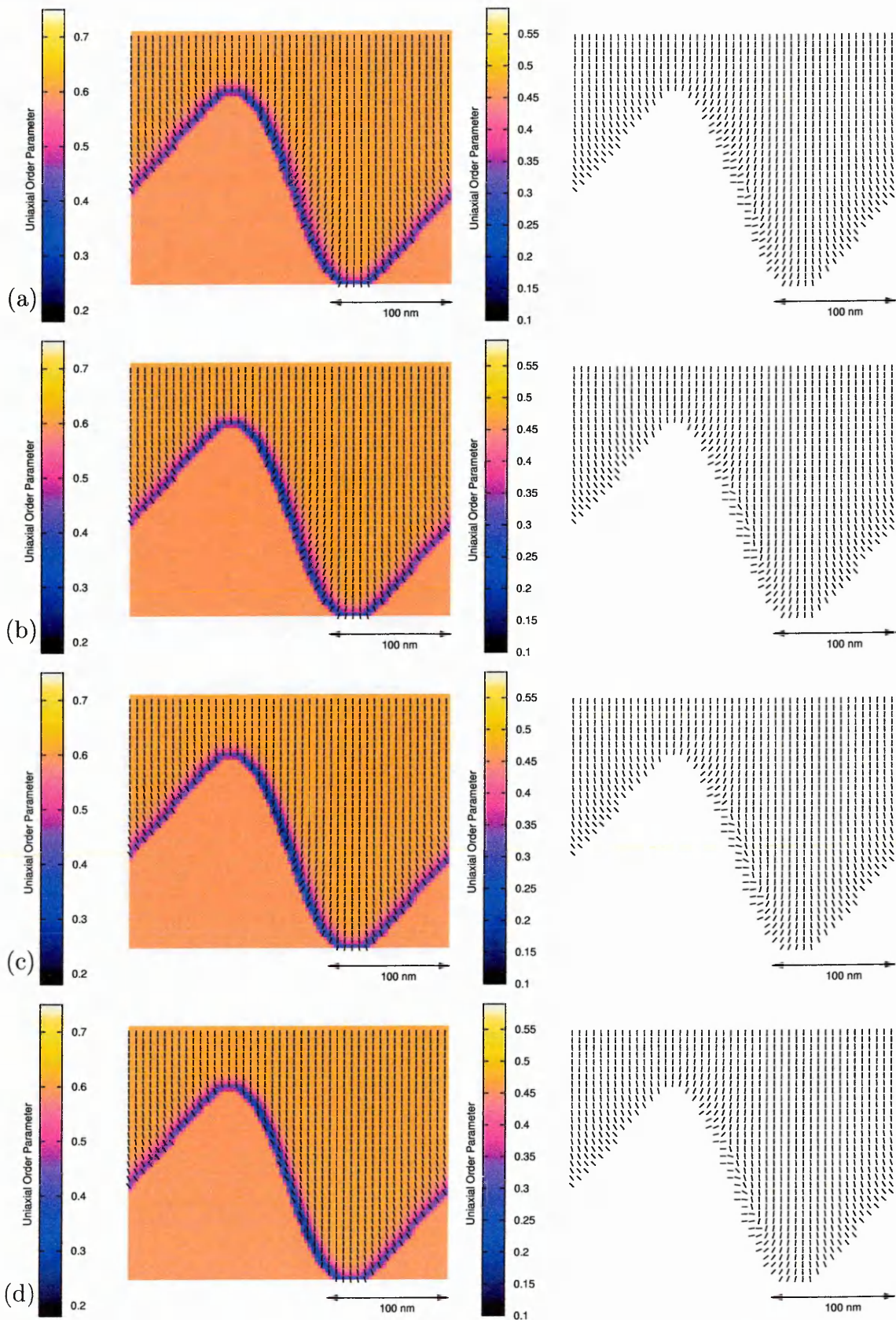


Figure 6.21: Switching from the  $\mathcal{D}$  to  $\mathcal{C}$  state through application of  $-15$  V at  $t = 0$  to  $t = 349.2\mu\text{s}$ . Left (right) indicate calculations from the Q tensor (EL limit). (a)  $t = 41.904\mu\text{s}$ , (b)  $t = 52.38\mu\text{s}$ , (c)  $t = 69.84\mu\text{s}$ , (d)  $t = 87.3\mu\text{s}$ . (Data plotted every other lattice point.)

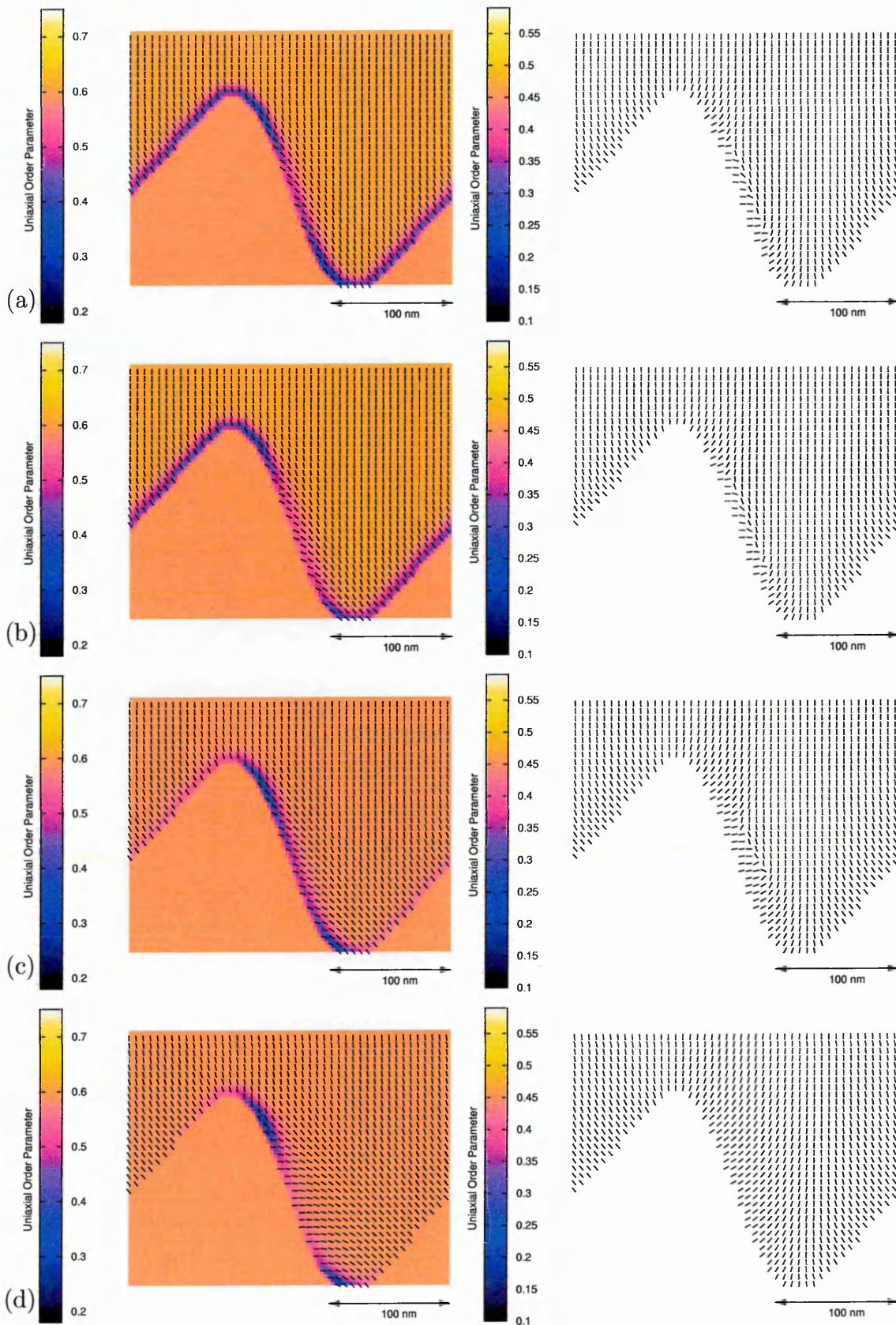


Figure 6.22: Switching from the  $\mathcal{D}$  to  $\mathcal{C}$  state through application of  $-15$  V at  $t = 0$  to  $t = 349.2\mu\text{s}$ . Left (right) indicate calculations from the Q tensor (EL limit). (a)  $t = 104.76\mu\text{s}$ , (b)  $t = 314.28\mu\text{s}$ , (c)  $t = 352.692\mu\text{s}$ , (d)  $t = 366.66\mu\text{s}$ . (Data plotted every other lattice point.)

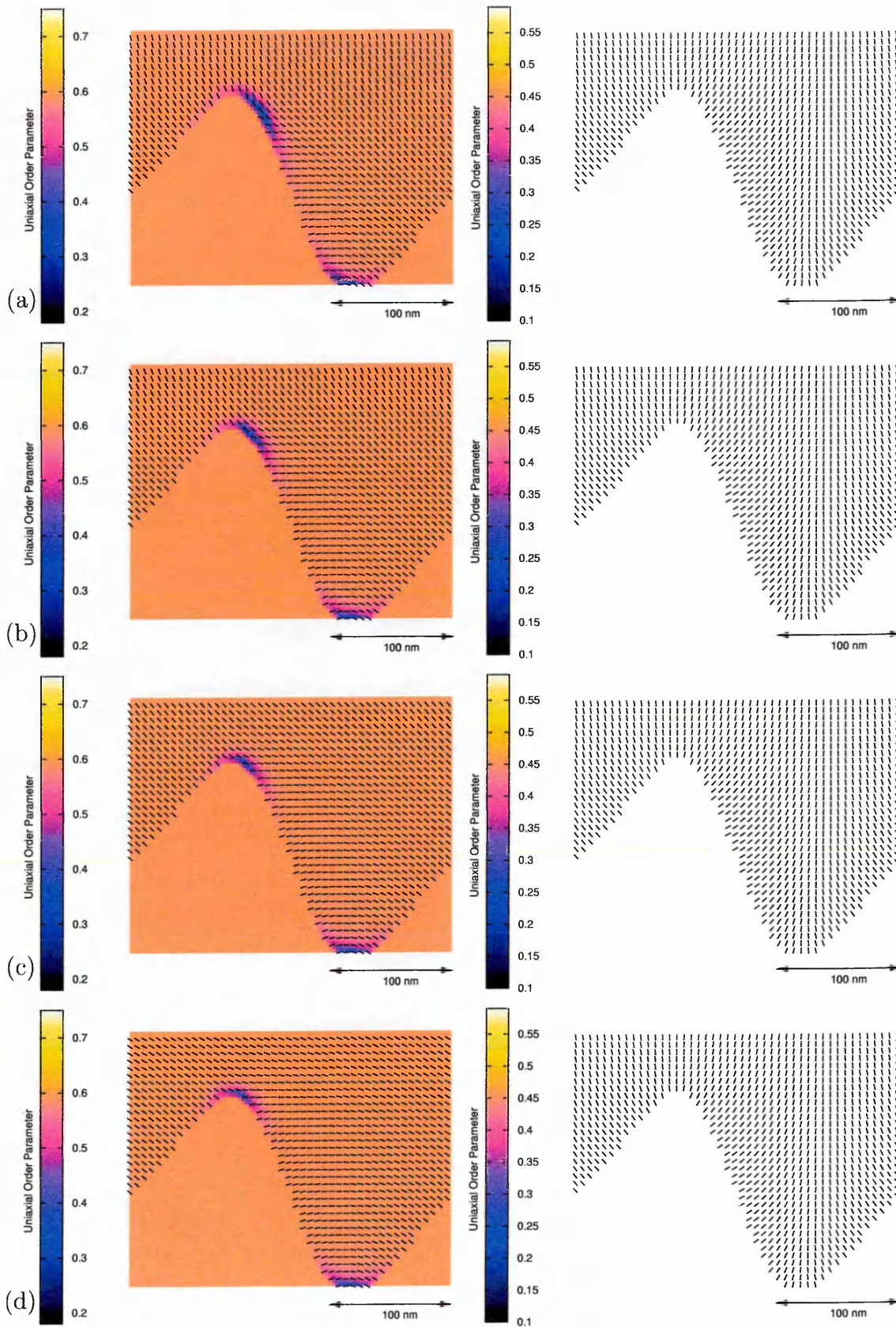


Figure 6.23: Switching from the  $\mathcal{D}$  to  $\mathcal{C}$  state through application of  $-15$  V at  $t = 0$  to  $t = 349.2\mu\text{s}$ . Left (right) indicate calculations from the  $\mathbf{Q}$  tensor (EL limit). (a)  $t = 384.12\mu\text{s}$ , (b)  $t = 419.04\mu\text{s}$ , (c)  $t = 523.8\mu\text{s}$ , (d)  $t = 1.746\text{ms}$ . (Data plotted every other lattice point.)

$m = \pm 1/2$  defects and the system reaches a steady state (6.22b). Turning off the field reduces the surface polarisation. The homeotropic anchoring then aids the formation of the defects. When established the defects move to their minimum free energy positions at the grating peaks and troughs. This process is slow and in doing so it rotates the bulk directors to the more tilted state.

For the EL limit method the directors, as usual, align quickly to the field. The directors at the steeper grating edge then rotate clockwise. This causes a conflict with the bulk alignment and two defects are formed just away from the surface. These defects separate slightly and then remain as the steady state is reached. Upon turning off the field the two bulk defects annihilate. The system then relaxes back to the initial  $\mathcal{C}$  state.

This switching process is summarised in figure 6.24 where the average director angle is plotted in time. Figure 6.24a corresponds to the previous figures where opposite outcome states occur. Figure 6.24b shows through application of a much larger voltage it is possible to switch between  $\mathcal{C}$  and  $\mathcal{D}$  states in the EL limit.

Even though the above simulations ( $Q$  tensor and EL limit) have used the same resolutions we may observe the associated correlation lengths of the two methods. Figure 6.25 is a grey level plot of the director angle during the formation of the defects in switching  $\mathcal{C}$  to  $\mathcal{D}$ . At the defect locations next to the wall, the thickness of the black band is an indication of the differences in correlation length. The  $Q$  tensor method having length  $\xi \sim \sqrt{L_1/\alpha_F}$  and the EL limit having a larger length

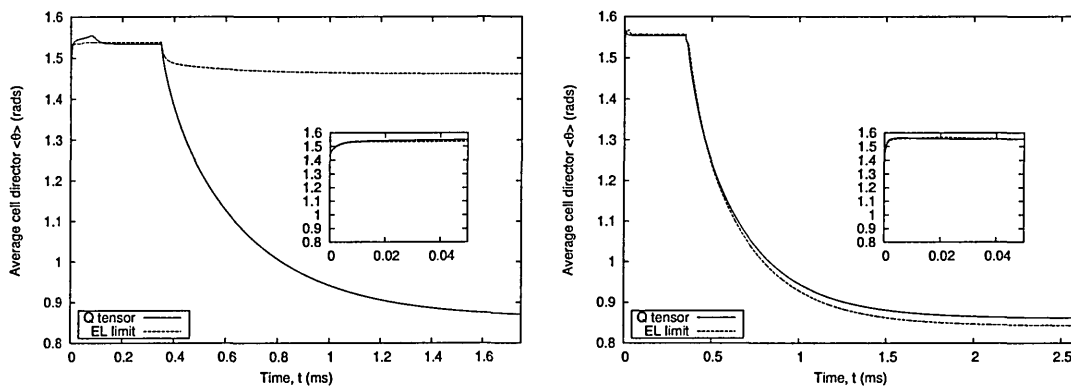


Figure 6.24: Graphs showing the cell average director angle during the switching  $\mathcal{C}$  to  $\mathcal{D}$ , voltages applied for  $t = 349.2\mu\text{s}$  (a)  $V = -15\text{V}$ , (b)  $V = -35\text{V}$ . Inset graphs zoom in on the  $t = 0$  region to identify the initial state. Note average cell director is measured with respect to the  $x$ -axis.

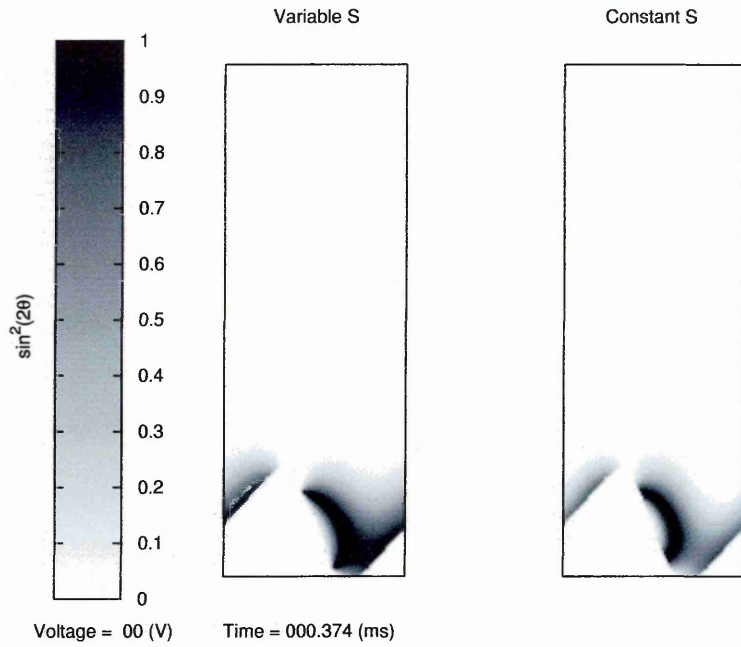


Figure 6.25: Grey levels plot of the director during switching from  $\mathcal{C}$  to  $\mathcal{D}$  for both  $Q$  tensor and EL theories. Black (white) levels are directors at  $\pm 45^\circ$ , ( $0^\circ$  and  $90^\circ$ ). The  $Q$  tensor method captures better the defects core and its length indicated by the narrower black region at the steeper grating surface in comparison to the EL method.

at  $\xi \sim (1/|E|)\sqrt{L_1/\epsilon_0\Delta\epsilon_a^{max}}$ .

We have shown the switching between both bistable states. The switching was driven by a surface flexoelectric term only. The  $Q$  tensor and EL calculations shows marked differences when considering the dynamic evolution of defects. The EL simulations also make a distinction between surface and bulk defects. The  $Q$  tensor simulations can avoid the formation of multiple defects through the lowering (raising) of the order parameters. As the  $Q$  tensor method is the more complete theory it is expected the dynamics are more reliable than the EL calculations and we may conclude the EL limit cannot be used for simulations of defect dynamics but may be used as a slightly quicker qualitative only estimate of equilibrium structures.

### 6.3.3 Comparison of Simulation to Experimental Work

Jones [31] examines the switching characteristics of the real ZBD and finds that to switch from the  $\mathcal{D}$  to  $\mathcal{C}$  states a negative field directed into the grating surface is required. To switch from the  $\mathcal{C}$  to  $\mathcal{D}$  states a positive electric field directed out of the grating surface is required. Jones [29] also states this sign dependence holds for all materials tested in their devices.

Throughout this chapter our calculations have assumed a positive value for the quadrupolar flexoelectric coefficient. In doing this we calculated switching from the  $\mathcal{D}$  to  $\mathcal{C}$  states requires a negative electric field directed into the grating surface. To switch from the  $\mathcal{C}$  to  $\mathcal{D}$  states requires a positive electric field directed out of the grating.

The simulated behaviour agrees with what is seen experimentally: the correct sign dependence of switching is recovered. This implies that the  $E_{13}$  value for nematics is positive. Using a negative value of  $E_{13}$  in the simulations would lead to the identical dynamics of the previous sections but with the opposite voltages. We can thus conclude in the limit of surface flexoelectric switching the quadrupolar coefficient is positive.

## 6.4 The Effect of Flexoelectric and Dielectric Contributions upon Switching.

Here we investigate the effect of some material properties upon the dynamic switching of the  $\mathcal{D}$  to  $\mathcal{C}$  state. It is reported [158] that increased flexoelectric coefficients would increase the switching speeds and in [31] they report increased switching speeds for materials of larger  $\Delta\epsilon_a$  and larger voltages.

The following calculations have been carried out with a positive  $E_{13}$ . In figure 6.26 we start calculations in the  $\mathcal{D}$  state and apply +15 volts. The resultant defect trajectories are shown in the grating region of the device at various values of  $E_{13}$  that are proposed in the literature [4]. For  $E_{13} = 0$  (i.e. no flexoelectricity) the defects move along the surface and annihilate. As  $E_{13}$  is increased we increase the surface polarisation and order parameter which pushes the defects further out into the bulk to annihilate. The inset graph plots the time taken for the defects to annihilate (an indication of the time at which the voltage may be turned off). It is found increasing  $E_{13}$  does increase the switching speed but tends to saturate at  $E_{13} > 5 \times 10^{-11} \text{ A s m}^{-1}$ .

It is also worth pointing out that a comparison of this annihilation time to experimental data on the time dependence of light transmission would provide a route to determine not only the sign but also the magnitude of the flexoelectric coefficient. This is because one can expect a ‘ripple’ in the orders of transmission

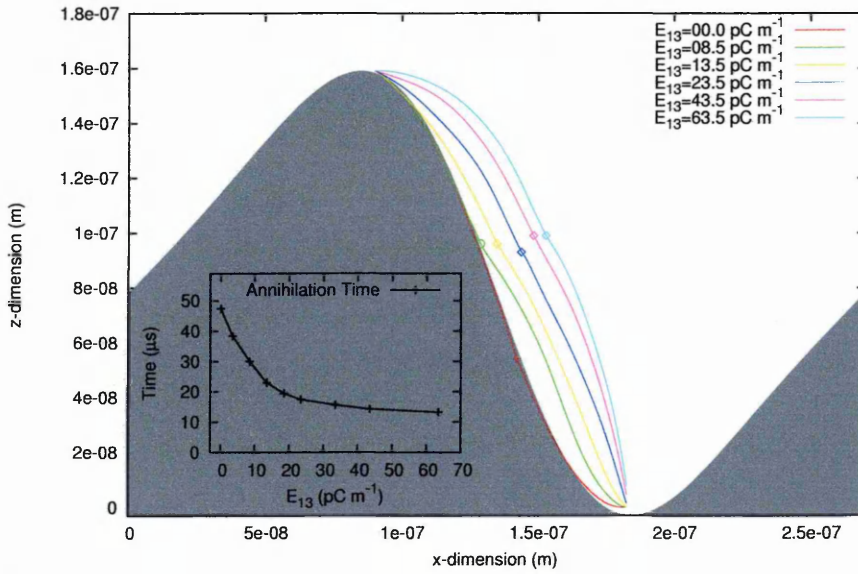


Figure 6.26: Defect trajectories during the  $\mathcal{D}$  to  $\mathcal{C}$  switching for various  $E_{13}$  values. Points indicate location of the annihilation. The inset figure indicates the time at which defects annihilate from the turn on of the voltage.

as the defects annihilate (see appendix C for further details).

Alternatively we keep  $E_{13}$  constant and vary the dielectric anisotropy,  $\Delta\epsilon_a$ , see figure 6.27. For decreasing  $\Delta\epsilon_a$  this effectively increases flexoelectric contributions

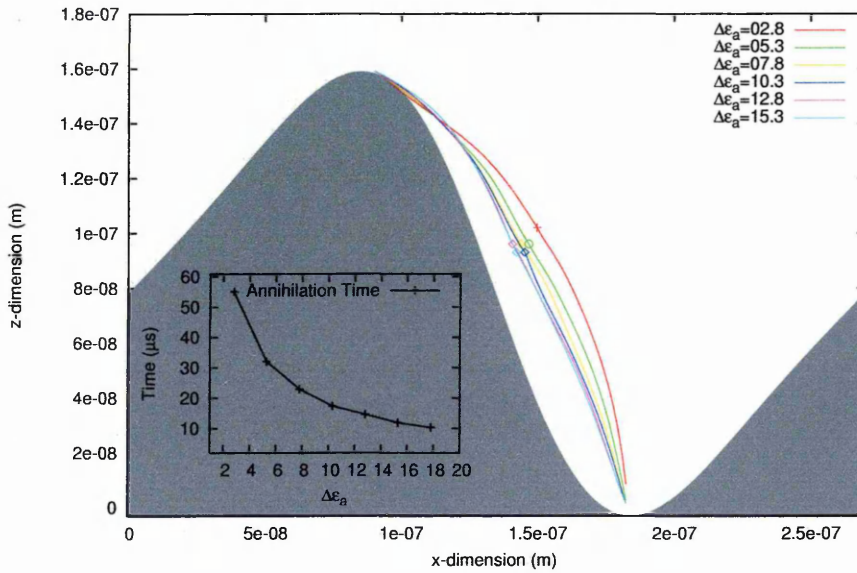


Figure 6.27: Defect trajectories during the  $\mathcal{D}$  to  $\mathcal{C}$  switching for various  $\Delta\epsilon_a$  values. Points indicate location of the annihilation. The inset figure indicates the time at which defects annihilate from the turn on of the voltage.

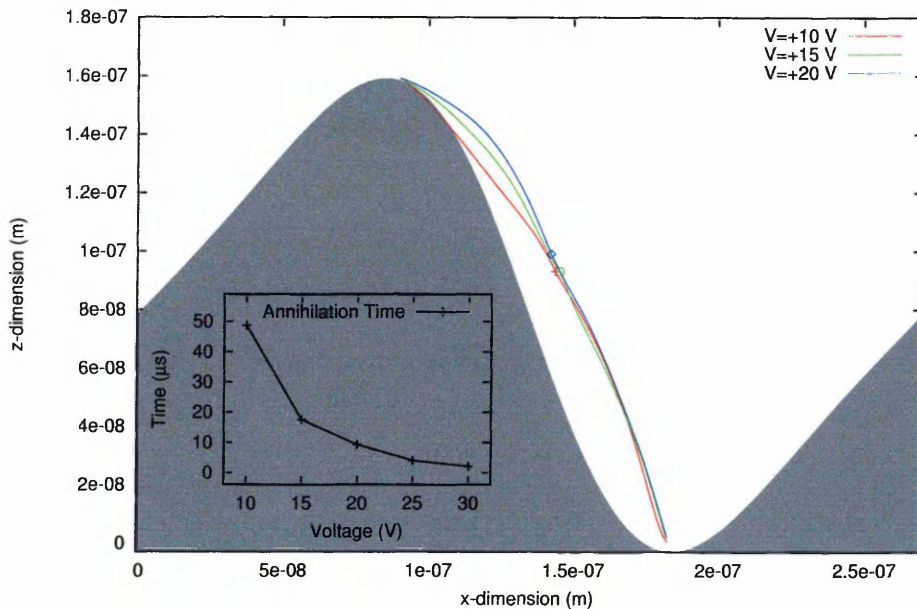


Figure 6.28: Defect trajectories during the  $\mathcal{D}$  to  $\mathcal{C}$  switching for various  $\phi$  values. Points indicate location of the annihilation. The inset figure indicates the time at which defects annihilate from the turn on of the voltage.

(remember the electrical free energy:  $F = -\frac{1}{3}\epsilon_0\Delta\epsilon_a E_\alpha Q_{\alpha\beta} E_\beta - C_1 E_\alpha \partial_\gamma Q_{\alpha\gamma}$ ) to the nematic, this increases the surface polarisation that pushes the defects further into the bulk of the device. Increasing  $\Delta\epsilon_a$  effectively reduces the flexoelectric contributions to switching and the defects do not travel as far into the bulk. Also increasing  $\Delta\epsilon_a$  tends to decrease the switching time.

For increasing applied voltage whilst keeping  $\Delta\epsilon_a$  and  $E_{13}$  constant contributes to both flexoelectric and dielectric terms. The defect trajectories are shown in figure 6.28. There is no significant alteration to the trajectories but as expected for most LCD devices the increased voltage speeds up the device switching time.

## 6.5 Conclusions.

We have applied the LB solver to a real LC device of current and important interest. It has been shown that flexoelectric properties are able to control the way in which the ZBD device switches between bistable states. We have shown creation and annihilation of defects on a grating surface which appears more correct than previous studies [146, 164, 161]. EL type theories can reproduce qualitatively defects at

equilibrium but cannot capture the correct dynamics of the defects. We show how the speed and defect trajectories vary for a range of changing  $\Delta\epsilon_a$ ,  $E_{13}$  and  $\phi$ . We find through comparison to experimental switching behaviour a method to determine the sign of the flexoelectric coefficient  $E_{13}$  which is positive in the limit that quadrupolar ( $C_2 = 0$ ) flexoelectricity is used. Some comparisons to experimental data may provide a route to determine the magnitude of this value.

# Chapter 7

## Further Modelling of the Zenithal Bistable Device

This chapter reports further investigation of the ZBD device. In chapter 6 we reduced the detail of the calculations to identify what can cause the device to be bistable. In this chapter we examine device switching with a more complete description that includes hydrodynamics and electrostatics solutions. Some grating surface properties are briefly examined and the effect of a temperature change also considered.

### 7.1 The Hydrodynamic Effects

The dynamics of ZBD device switching reported in chapter 6 were purely rotational, ignoring the hydrodynamic effect. However in some bistable LCD's [29] the hydrodynamics act as a selection mechanism between bistable states and as such must be included in calculations to reproduce what happens. In the ZBD the effect of hydrodynamics is less clear. It is found [158] that the device has an extremely high mechanical shock threshold and cells can undergo large deformations yet still retain their image. This suggests the hydrodynamic influences do not play an important part in the bistable states. However during the switching process in which large voltages are used, we may expect large hydrodynamic forces, particular in the  $\mathcal{D}$  to  $\mathcal{C}$  switching case; this may give rise to different dynamics than that considered in the previous chapter. We now include the hydrodynamics through the LB solver to see its effect upon switching. Material and device parameters are the same as in the previous chapter, hence enabling direct comparisons. Additionally the  $\alpha_{ii}$  are the same as in chapter 5.

### 7.1.1 $\mathcal{D}$ to $\mathcal{C}$ State Switching

Starting in the  $\mathcal{D}$  state (see figure 6.4) we apply a  $\phi = +15$  volts until the system reaches steady state and then turn it off ( $\phi = 0$  volts). The resulting director and flow fields are shown in figures 7.1 to 7.4. In these figures we display several pieces of information. The left hand figures display vectors indicating the velocity vectors of the flow field, the colour representing the order parameter to indicate the defect locations. The right hand figures display the director structure, the colour representing the magnitude of the velocity.

Initially a large flow field in the negative  $x$ -direction occurs in the bulk of the device (figure 7.1a). This serves to aid vertical director alignment in the upper half of the cell and hinder alignment in the bottom half. The grating region flow field remains small due to the large surface area in which non-slip viscous boundary conditions are applied. The bulk flow then reverses to the positive  $x$ -direction initiating some recirculation (figure 7.1b and 7.1c). This positive flow field then aids director alignment in the lower half of the cell. The alignment of the director in figure 7.1d has a high viscosity and dampens out bulk flows quickly.

The defects that are projected off the surfaces due to polarisations then start to induce flow. The flow associated with the  $m = +1/2$  defect being twice as large as those of the  $m = -1/2$  defect. This feature being typical of  $m = \pm 1/2$  annihilation process [64, 145]. Comparing figures 7.2d with figure 6.16a it can be seen the flow has served to accelerate the path of the  $m = +1/2$  defect. Consequently the annihilation time is decreased by  $\sim 3\mu\text{s}$  compared to the case without hydrodynamics.

After the system reaches steady state the electric field is released (figure 7.4a) causing only minor flows as the director does not have far to relax to the  $\mathcal{C}$  state.

Figure 7.5 compares the average director angle in the cell during the switching process for the case with and without hydrodynamics. It is seen there are only minor differences between the corresponding calculations.

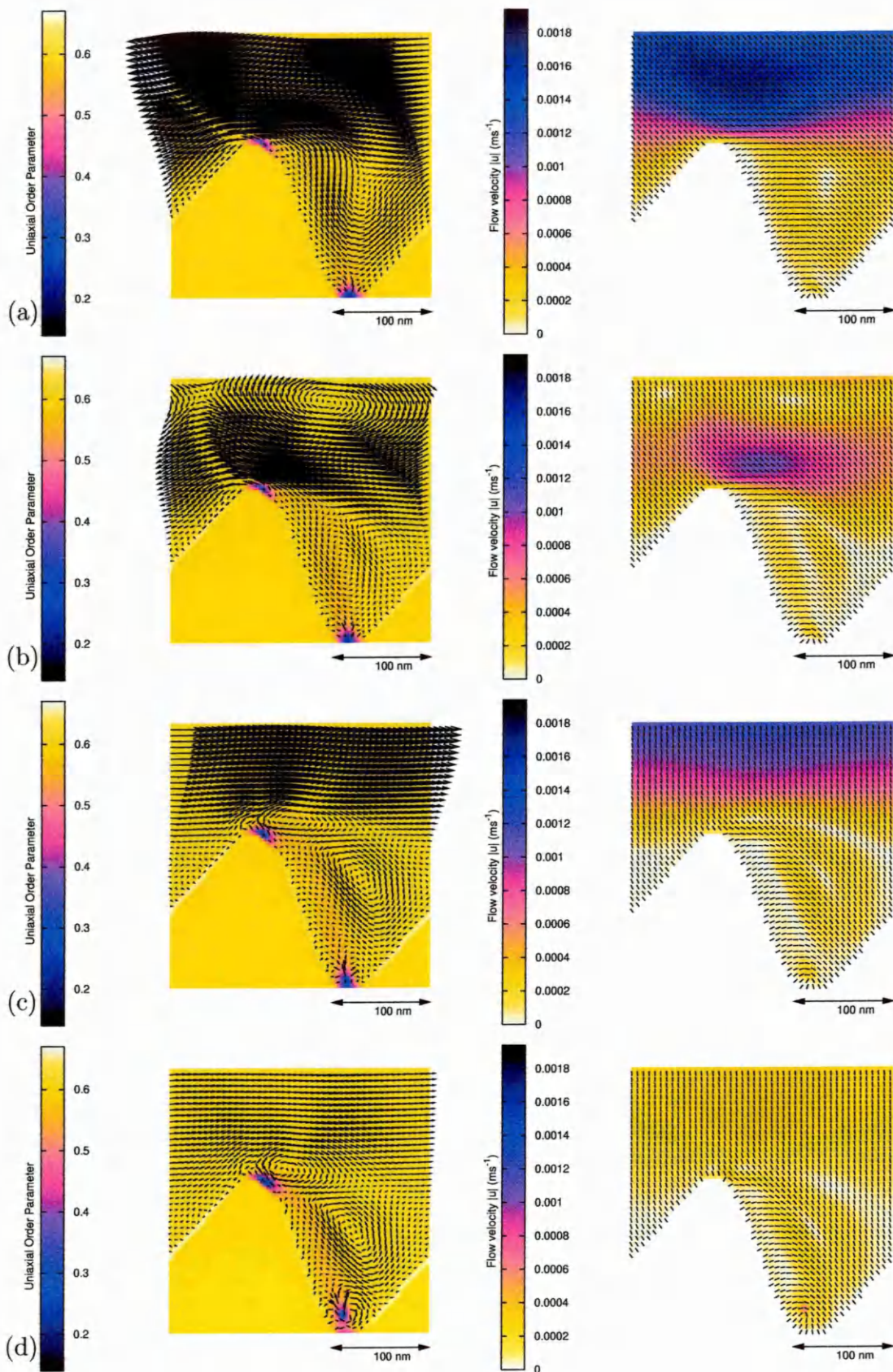


Figure 7.1: Switching from the  $D$  to  $C$  state through application of  $+15$  V at  $t = 0$  to  $t = 87.3\mu\text{s}$ . Left (right) indicate order parameter and flow fields (director and flow fields). (a)  $t = 1.746\mu\text{s}$ , (b)  $t = 3.492\mu\text{s}$ , (c)  $t = 5.238\mu\text{s}$ , (d)  $t = 6.984\mu\text{s}$ . (Data plotted every other lattice point, velocity scale =  $60\mu\text{m s}^{-1}$  between plotted points.)

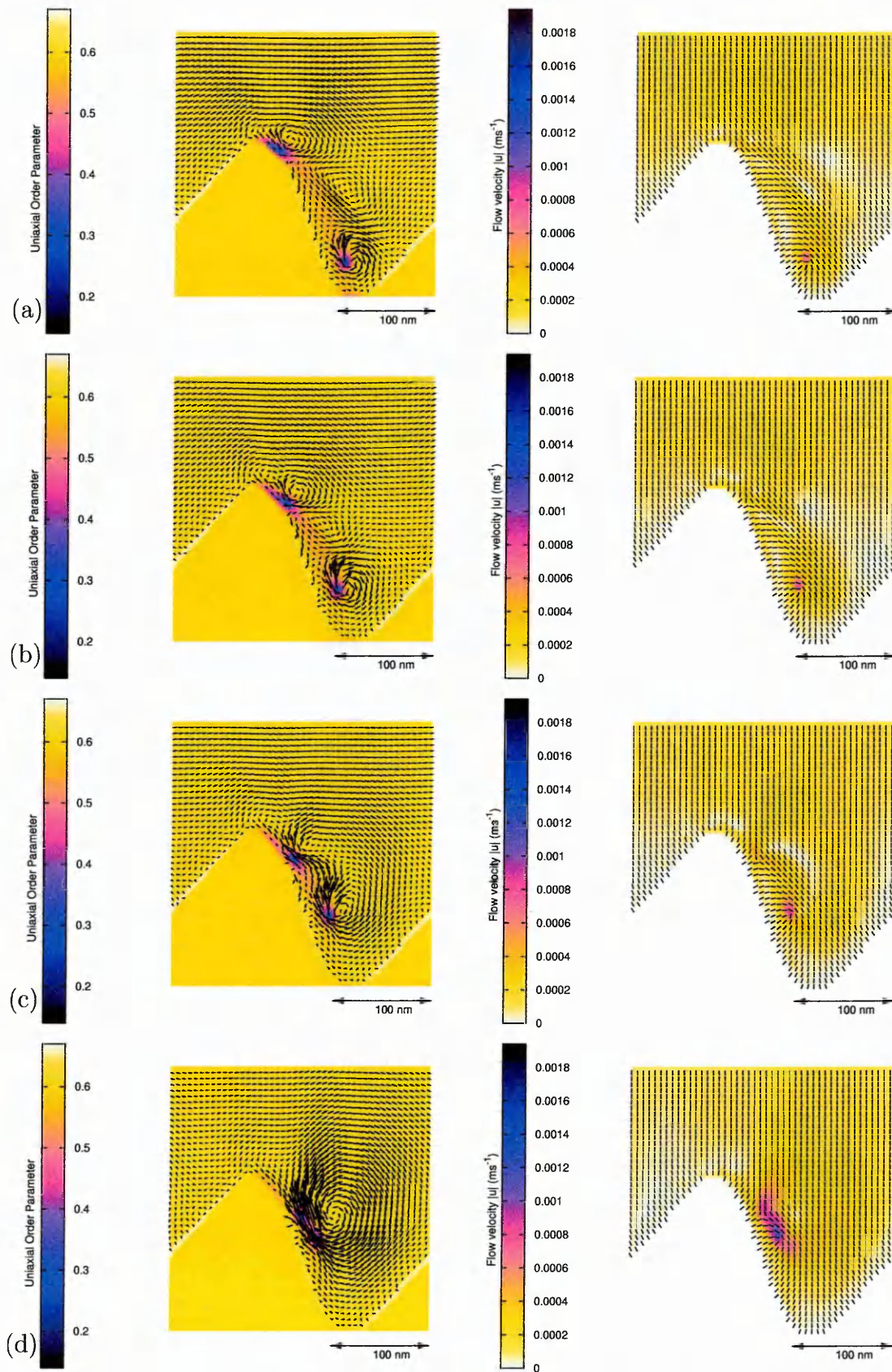


Figure 7.2: Switching from the  $\mathcal{D}$  to  $\mathcal{C}$  state through application of +15 V at  $t = 0$  to  $t = 87.3\mu\text{s}$ . Left (right) indicate order parameter and flow fields (director and flow fields). (a)  $t = 8.73\mu\text{s}$ , (b)  $t = 10.476\mu\text{s}$ , (c)  $t = 12.222\mu\text{s}$ , (d)  $t = 13.968\mu\text{s}$ . (Data plotted every other lattice point, velocity scale =  $60\mu\text{m s}^{-1}$  between plotted points.)

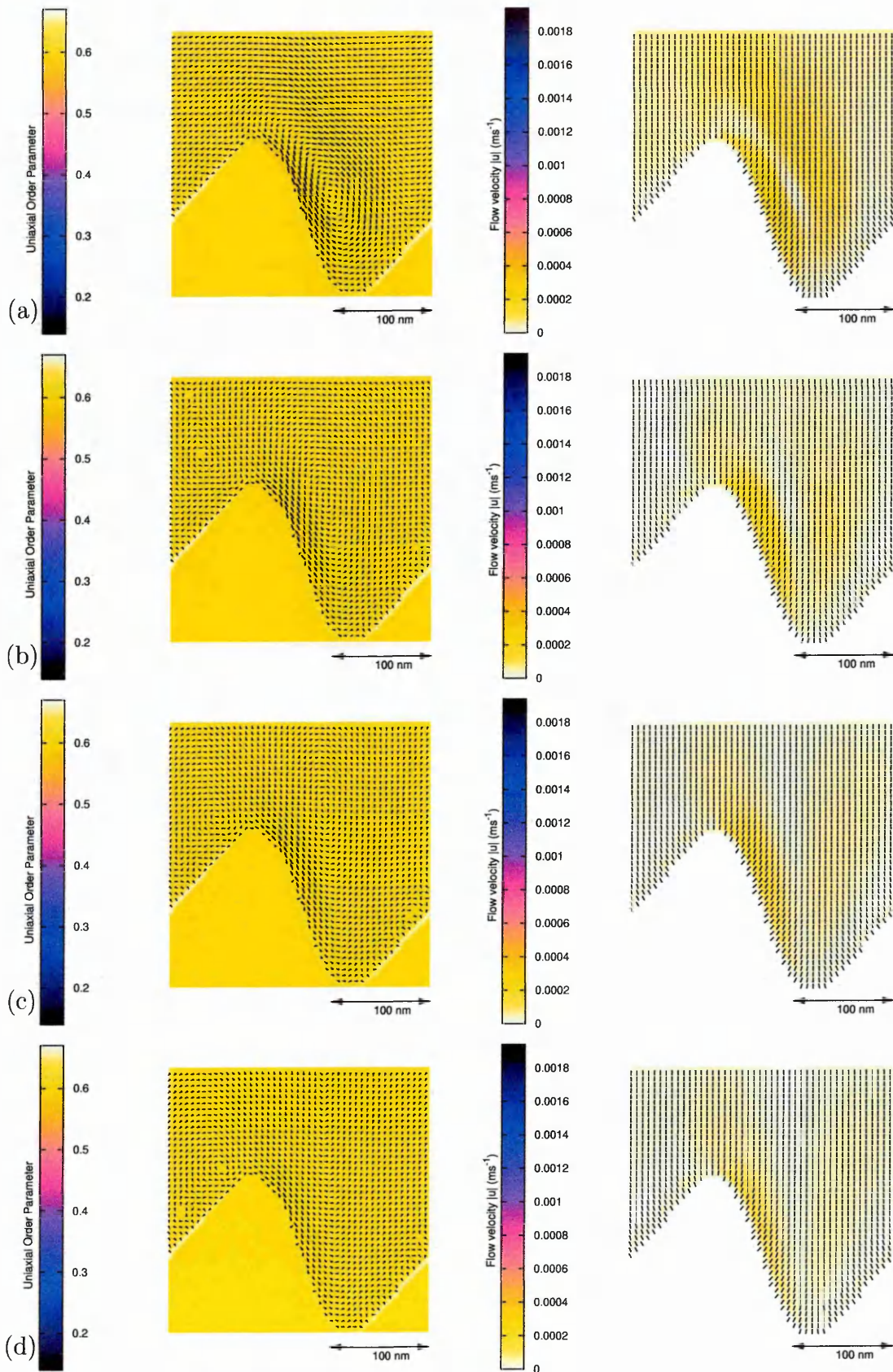


Figure 7.3: Switching from the  $D$  to  $C$  state through application of  $+15$  V at  $t = 0$  to  $t = 87.3\mu\text{s}$ . Left (right) indicate order parameter and flow fields (director and flow fields). (a)  $t = 15.714\mu\text{s}$ , (b)  $t = 17.46\mu\text{s}$ , (c)  $t = 19.206\mu\text{s}$ , (d)  $t = 85.554\mu\text{s}$ . (Data plotted every other lattice point, velocity scale =  $60\mu\text{m s}^{-1}$  between plotted points.)

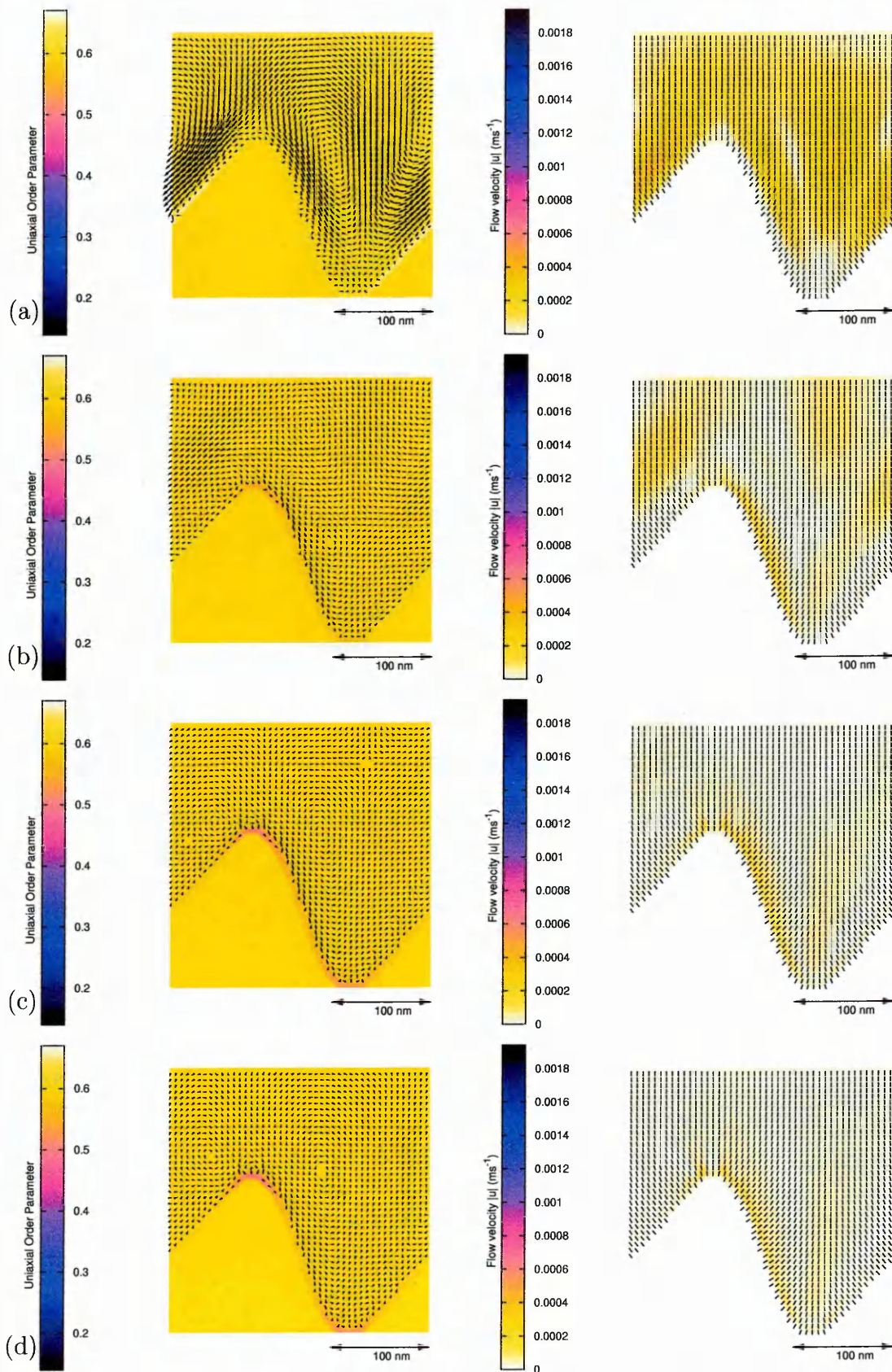


Figure 7.4: Switching from the  $D$  to  $C$  state through application of  $+15$  V at  $t = 0$  to  $t = 87.3\mu\text{s}$ . Left (right) indicate order parameter and flow fields (director and flow fields). (a)  $t = 87.3\mu\text{s}$ , (b)  $t = 89.046\mu\text{s}$ , (c)  $t = 96.03\mu\text{s}$ , (d)  $t = 104.76\mu\text{s}$ . (Data plotted every other lattice point, velocity scale =  $60\mu\text{m s}^{-1}$  between plotted points.)

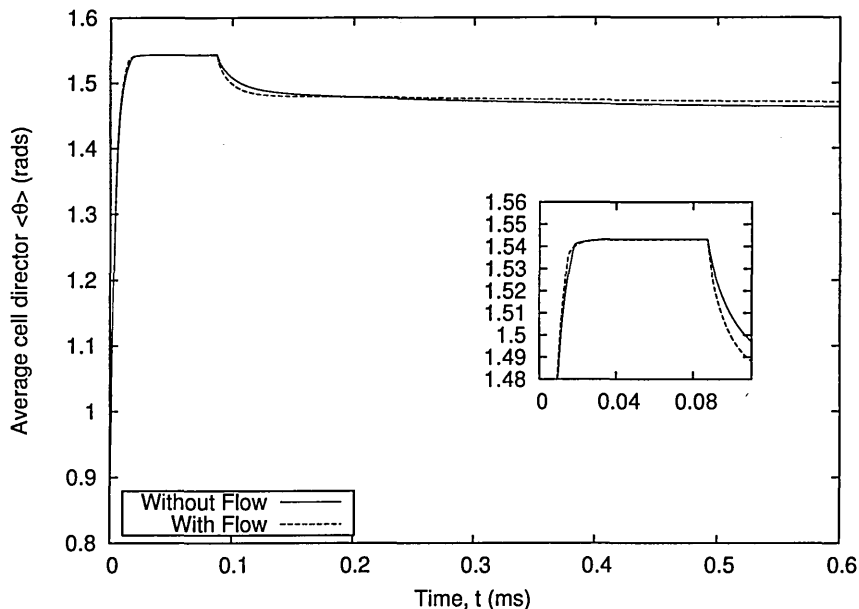


Figure 7.5: Graph showing the cell average director angle during the switching  $\mathcal{D}$  to  $\mathcal{C}$ , for flow and no-flow calculations. Inset graphs zoom in on the  $t = 0$  region to identify the initial state. Note average cell director is measured with respect to the  $x$ -axis.

### 7.1.2 $\mathcal{C}$ to $\mathcal{D}$ State Switching

Starting in the  $\mathcal{C}$  state (see figure 6.3) we apply a  $\phi = -15$  volts until the system reaches steady state and then turn it off  $\phi = 0$  volts. The resulting director and flow fields are shown in figures 7.6 to 7.9.

Turning on the electric field (figure 7.6a) does not generate large flow fields as the  $\mathcal{C}$  state director is already mostly vertically aligned. Small currents are induced from the immediate grating surface as the directors rotate (figures 7.6c to 7.7d) to form the ‘frustrated’ states in which the defects start to form.

Upon turning off the electric field (figure 7.8c) the homeotropic anchoring drives the initial flow causing a negative  $x$ -direction flow. This flow profile is plotted at various cross-sections of the device in figure 7.11 and persists, with decreasing magnitude through to the final  $\mathcal{D}$  state. The negative velocity gradient region aids director rotation towards the  $\mathcal{D}$  state in the lower half of the cell but the positive velocity gradient region hinders director rotation to the  $\mathcal{D}$  state in the upper half of the cell.

Figure 7.10 compares the average director angle in the cell during the switching process for the case with and without hydrodynamics. It is seen the calculation

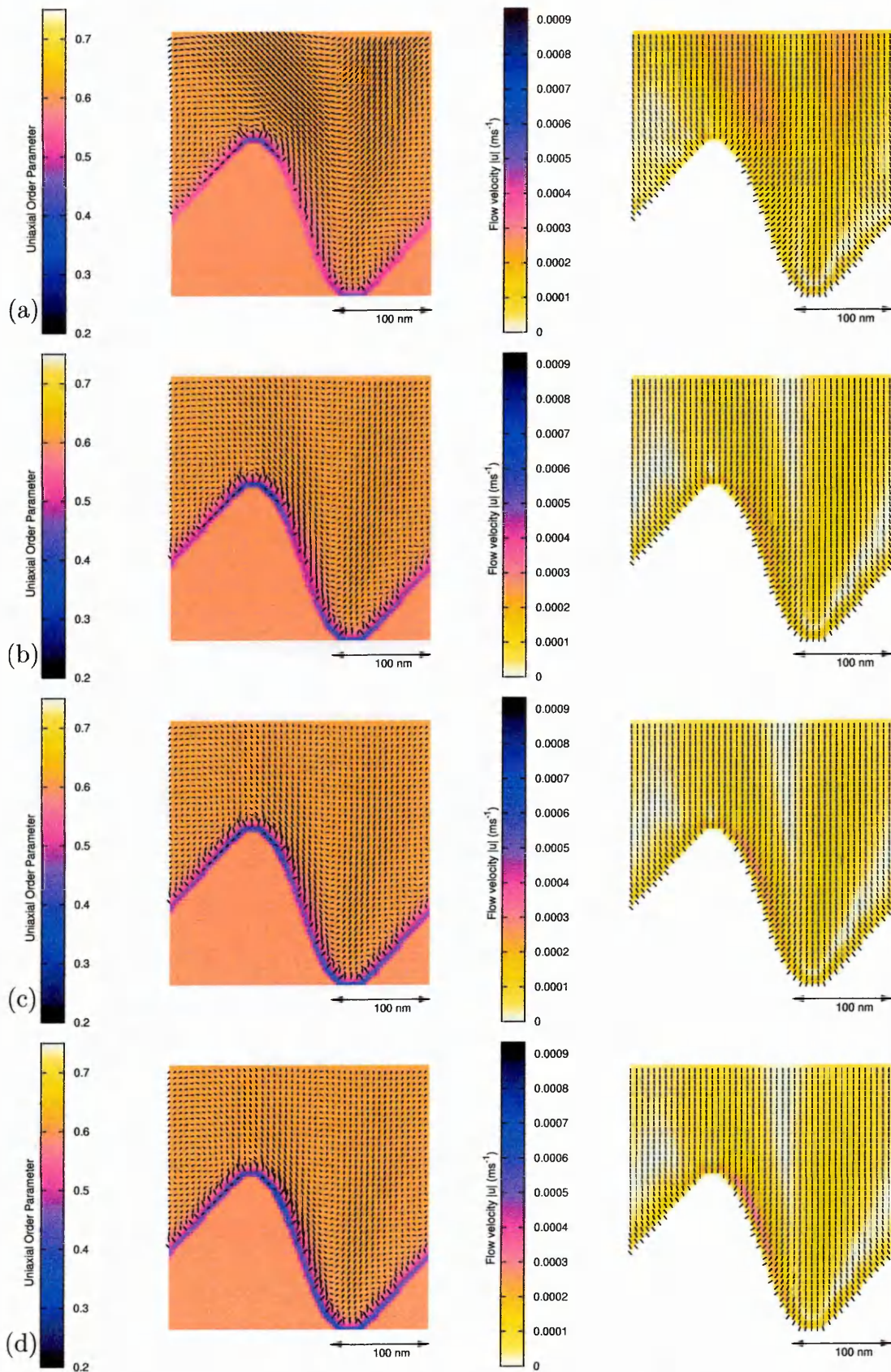


Figure 7.6: Switching from the  $D$  to  $C$  state through application of  $-15$  V at  $t = 0$  to  $t = 209.52\mu\text{s}$ . Left (right) indicate order parameter and flow fields (director and flow fields). (a)  $t = 1.746\mu\text{s}$ , (b)  $t = 5.238\mu\text{s}$ , (c)  $t = 8.73\mu\text{s}$ , (d)  $t = 15.714\mu\text{s}$ . (Data plotted every other lattice point, velocity scale =  $60\mu\text{m s}^{-1}$  between plotted points.)

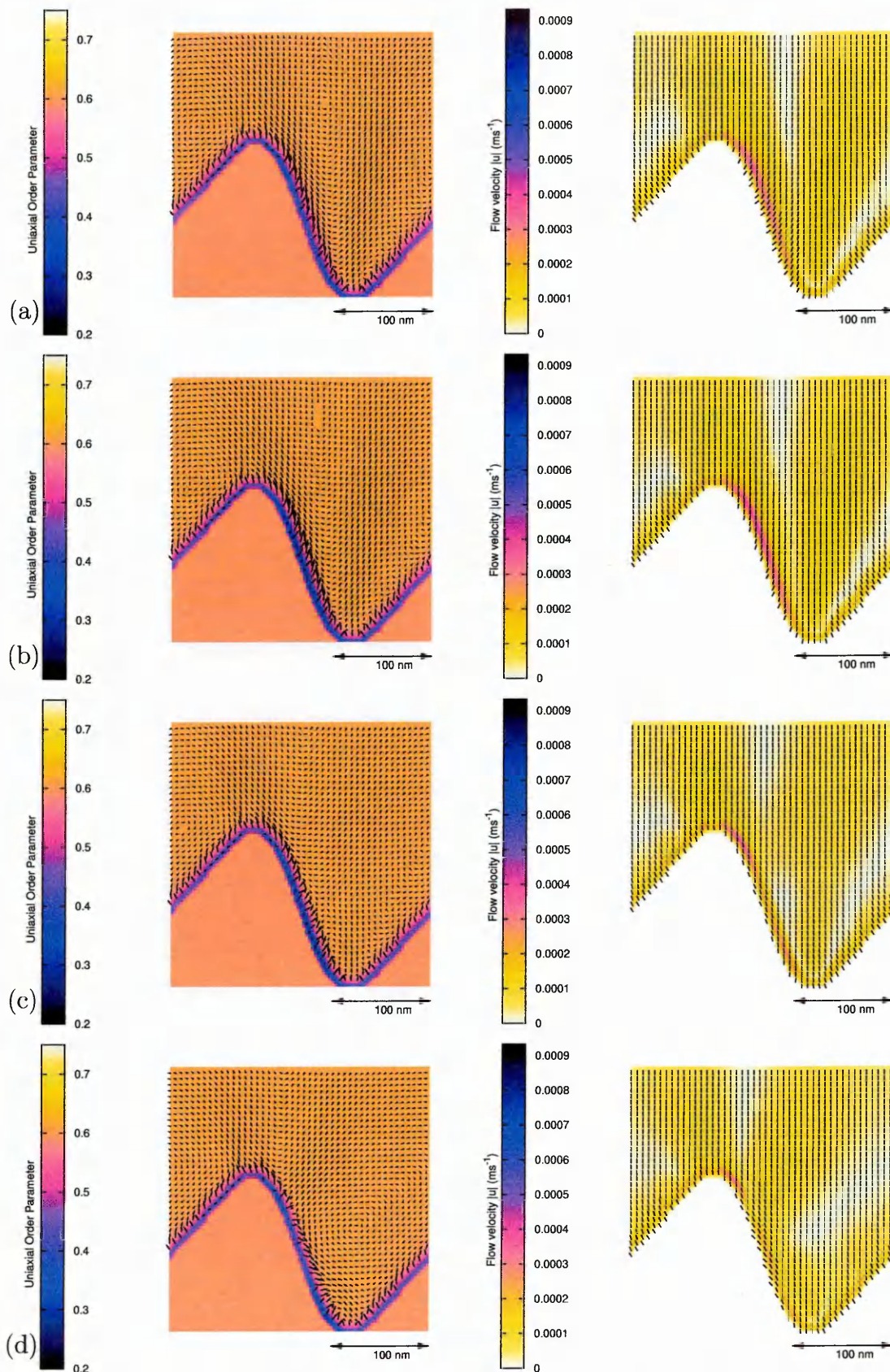


Figure 7.7: Switching from the  $D$  to  $C$  state through application of  $-15$  V at  $t = 0$  to  $t = 209.52\mu\text{s}$ . Left (right) indicate order parameter and flow fields (director and flow fields). (a)  $t = 22.698\mu\text{s}$ , (b)  $t = 41.904\mu\text{s}$ , (c)  $t = 52.38\mu\text{s}$ , (d)  $t = 61.11\mu\text{s}$ . (Data plotted every other lattice point, velocity scale =  $60\mu\text{m s}^{-1}$  between plotted points.)

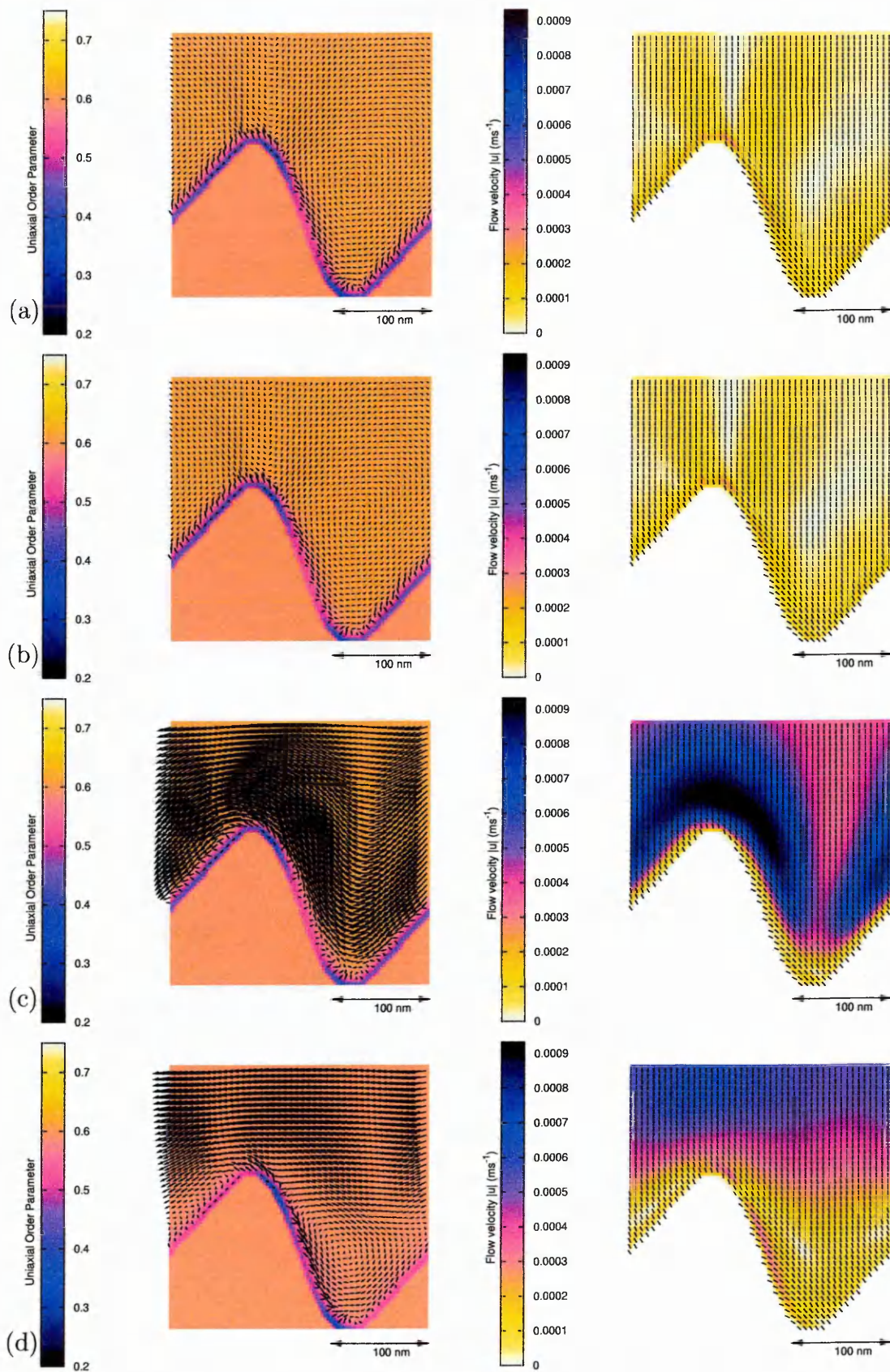


Figure 7.8: Switching from the  $D$  to  $C$  state through application of  $-15$  V at  $t = 0$  to  $t = 209.52\mu\text{s}$ . Left (right) indicate order parameter and flow fields (director and flow fields). (a)  $t = 87.3\mu\text{s}$ , (b)  $t = 207.774\mu\text{s}$ , (c)  $t = 209.52\mu\text{s}$ , (d)  $t = 211.266\mu\text{s}$ . (Data plotted every other lattice point, distance between points corresponds to  $60\mu\text{m s}^{-1}$ .)

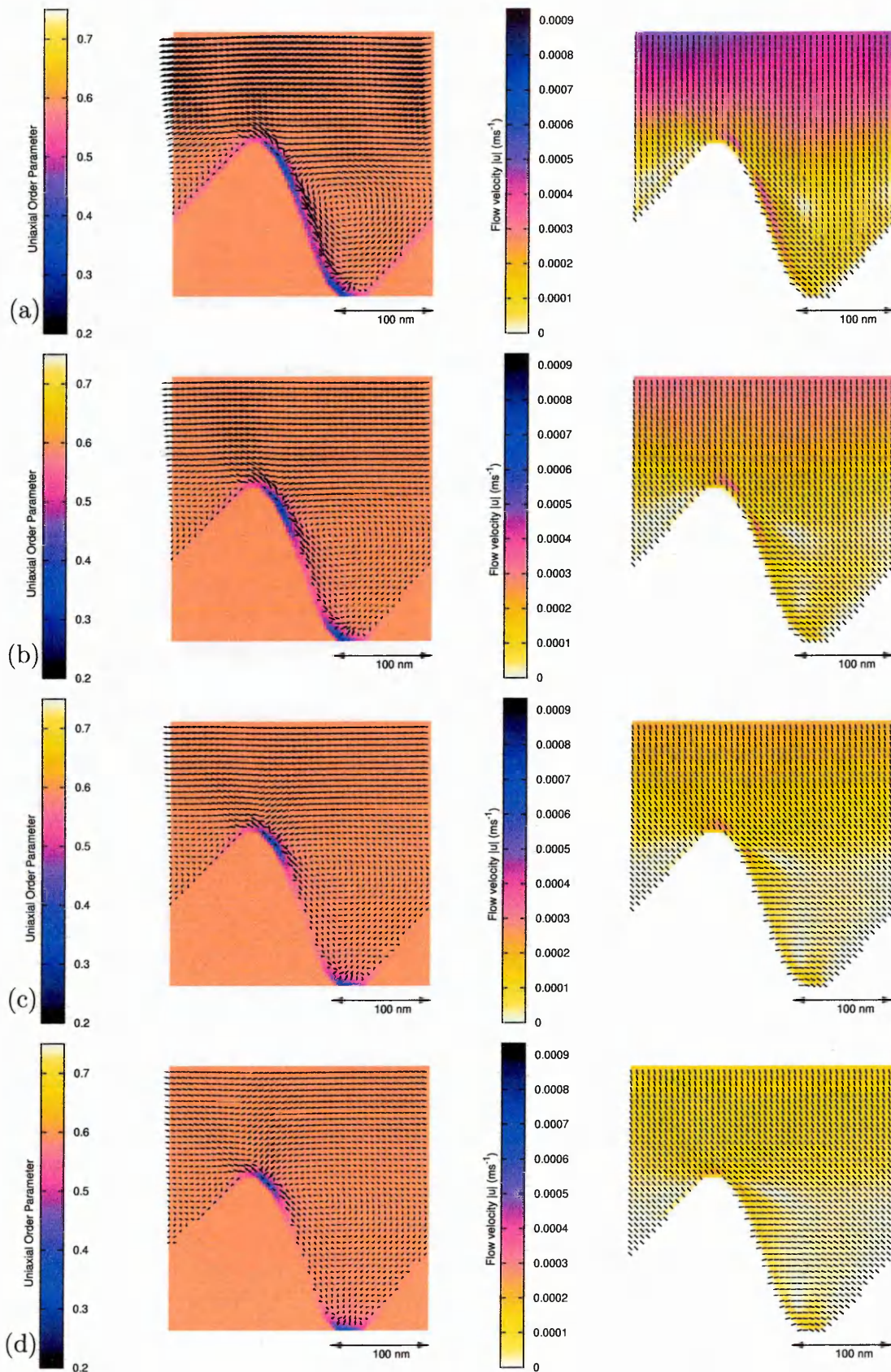


Figure 7.9: Switching from the  $D$  to  $C$  state through application of  $-15$  V at  $t = 0$  to  $t = 209.52\mu\text{s}$ . Left (right) indicate order parameter and flow fields (director and flow fields). (a)  $t = 214.758\mu\text{s}$ , (b)  $t = 225.234\mu\text{s}$ , (c)  $t = 242.694\mu\text{s}$ , (d)  $t = 260.154\mu\text{s}$ . (Data plotted every other lattice point, velocity scale =  $60\mu\text{m s}^{-1}$  between plotted points.)

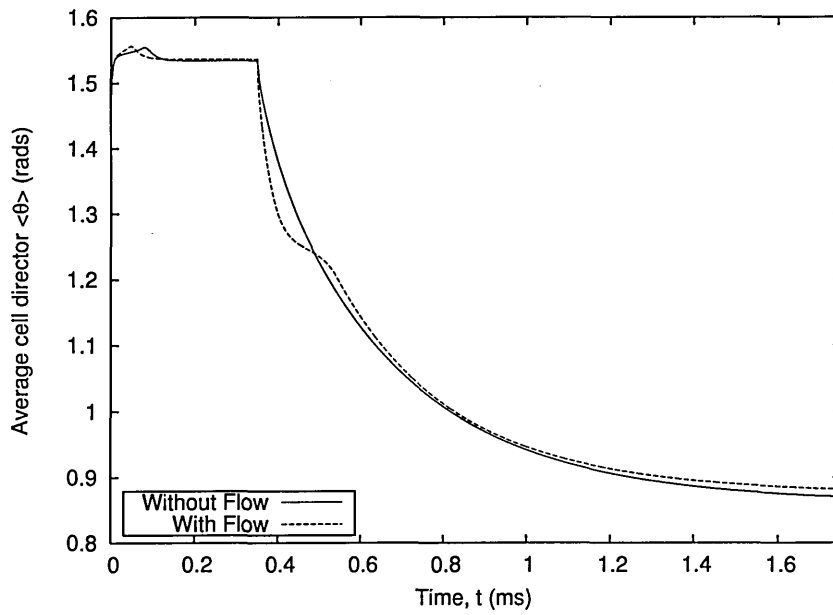


Figure 7.10: Graph showing the cell average director angle during the switching  $\mathcal{C}$  to  $\mathcal{D}$ , for flow and no-flow calculations. Note average cell director is measured with respect to the  $x$ -axis.

with flow does initially speed up the relaxation to the  $\mathcal{D}$  state but at  $t \sim 0.4$ ms, the calculation with flow slows down the switching process. This being attributed to the region of positive velocity gradient as seen in figure 7.11. The overall outcome

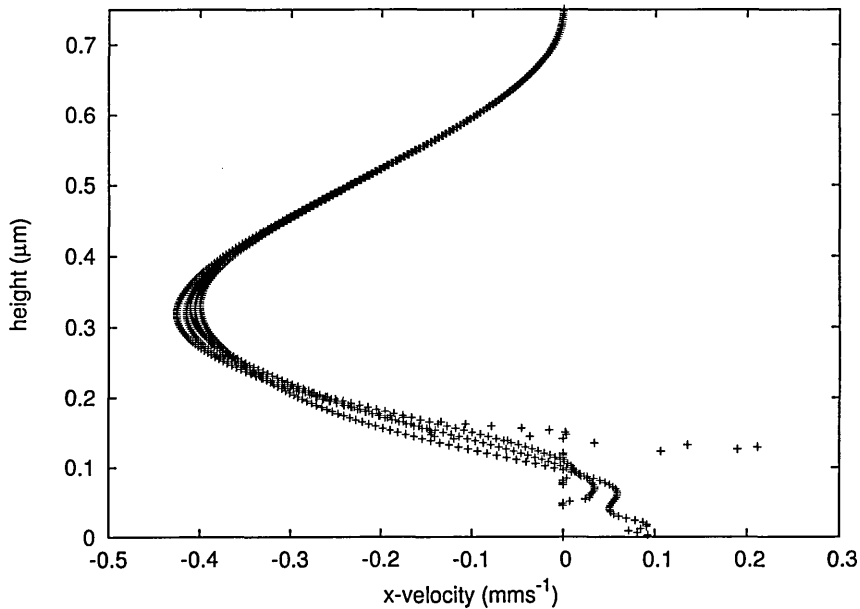


Figure 7.11: Graph shows the flow profile at various cross-sections in the cell at a time  $t = 357.93 \mu\text{s}$ . The profile remains but reduces in magnitude as the cell relaxes to the  $\mathcal{D}$  state.

again showing not much difference between the calculations in terms of the time taken between states.

Comparing the two directions of switching we see the maximum velocity induced for the  $\mathcal{D}$  to  $\mathcal{C}$  switch is twice as large as that of the  $\mathcal{C}$  to  $\mathcal{D}$  switch. The grating region has a large surface area imposing the non-slip boundary condition and because both switching cases are determined by the annihilation or creation of defects within this region, the hydrodynamics does not play an important part in device switching. What determines the switched state is the formation and annihilation of the defects. This shows that we may model the ZBD device to a very good approximation using just rotational dynamics.

In both cases of switching, the calculated flow profiles should be treated as a first qualitative estimate. This is firstly because the grating profile has been modelled on discrete lattice sites and as such has stair-case boundaries (square lattice). Secondly due to the large gradients in  $\mathbf{Q}$  that occur at the surfaces (c.f. §4.2.3 and §4.4.4). Future improvements to the calculation of the flow dynamics would be in the use of finer grid resolutions through multi-grid methods and to model the boundary as a continuous surface.

## 7.2 The Electrostatic Effects

The electric field in the switching dynamics of chapter 6 was treated as a constant. In this case the flexoelectric effect arises from gradients in  $\mathbf{Q}$  alone and as such is mainly a surface contribution. As a consequence of the dielectric properties of LC's the electric field varies with the director alignment. Here we include the correct treatment of the electric field, allowing it to vary in order to investigate how it effects the calculated switching dynamics. Now, the flexoelectric effect is a combination of gradients in  $\mathbf{Q}$  and  $\mathbf{E}$  (see equation 4.8). In this work we modify the device geometry so as to place the electrodes in a more realistic position away from the liquid crystal region allowing for the alignment and structure layers [57], this is shown in figure 7.12. We consequently now apply  $\phi = \pm 18$  V in order to switch between states, this is chosen to keep the cell electric field strength the same ( $E = -V/d$ , with  $d$  being the distance between electrodes). All other device and material parameters remain the same. We also choose to omit the hydrodynamic

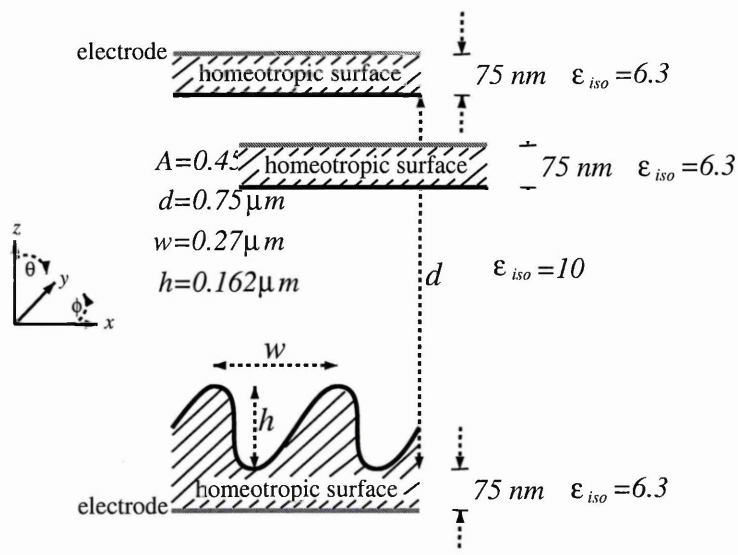


Figure 7.12: Schematic of the two dimensional ZBD geometry over two grating pitches,  $w$ . Homeotropic boundary conditions serve to cause bistability. Electrodes now positioned at  $z = 0$  (earth  $\phi = 0$ ) and  $z = 0.9\mu m$ .

effects in the calculations as evidence from the preceding section shows these to be of little importance to the switching process.

We point out that even for no externally applied potentials there will be an internal electric field generated from the flexoelectric polarisation that occurs in the distortion region of the grating. For this reason we recalculate the main equilibrium  $\mathcal{D}$  and  $\mathcal{C}$  states of the device. These states are shown in figures 7.13a and 7.16a respectively. In both cases the presence of the internal electric field contributes to the electric free energy and consequently we see in both the  $\mathcal{D}$  and  $\mathcal{C}$  states the cell averaged director is more vertically aligned.

Upon applying an external field to this device similar, but not identical, steady state director configurations are obtained as in §6.2.4. The main difference being in the  $\phi =$  positive case. The ‘frustrated’ region forming on the surface is reduced: contributions due to the dielectric free energy serve to align the director more vertically, the directors at the steeper surface are now parallel to it. Upon turning off the applied field the system relaxes to the  $\mathcal{C}$  state and we have lost the ability to recover a bistable device. This may be overcome by increasing the flexoelectric coefficient to values of  $\gtrsim 5 \times 10^{-10} \text{ A s m}^{-1}$  but this is at least an order of magnitude higher than values reported in the literature and leads to extraneous values of the order parameter in the surface region. It is better overcome by moving away from

using the quadrupolar picture as the main source of flexoelectricity and towards LC molecules that can contain both longitudinal and lateral dipoles (now  $C_2 \neq 0$ ). Hence, we recover bistable switching easily through an appropriate choice of  $e_{11}$  and  $e_{33}$ . We find values of  $e_{11} = 1.35 \times 10^{-11} \text{ A s m}^{-1}$  and  $e_{33} = -2.35 \times 10^{-11} \text{ A s m}^{-1}$  ( $E_{13} = -5 \times 10^{-12} \text{ A s m}^{-1}$ ) recover very easily the bistability of the device.

### 7.2.1 $\mathcal{D}$ to $\mathcal{C}$ State Switching

Starting in the  $\mathcal{D}$  state we apply  $\phi = +18$  volts until the system reaches steady state and then turn it off  $\phi = 0$  volts. The resulting dynamics are shown in figures 7.13 and 7.14.

Upon turning on the applied field the bulk directors align quickly to the main field direction. The original defects do not leave the surfaces despite the surface polarisation raising the surface order parameter. A large distortion region just to the right of the grating peak causes the creation of two defects  $m = \pm 1/2$  (figure 7.13d). The  $m = +1/2$  defect annihilates with the  $m = -1/2$  defect at the peak (figure 7.13e), the  $m = -1/2$  defect annihilates with the  $m = +1/2$  defect at the grating trough. The overall time to steady state applied field is no different to the case without the electrostatic solver (figure 7.14a). Turning off the applied field relaxes the system to the  $\mathcal{C}$  state (figure 7.14c-h).

The switching process is summarised in figure 7.15 where the averaged director angle over the cell is plotted in time. Both the case with and without the electrostatic solver is shown. It is seen that with the more accurate electric field, the director is generally more vertically aligned throughout the switching process and more so in the  $\mathcal{C}$  state. The relaxation to the final state also appears to occur more quickly for case with the more accurate electric field.

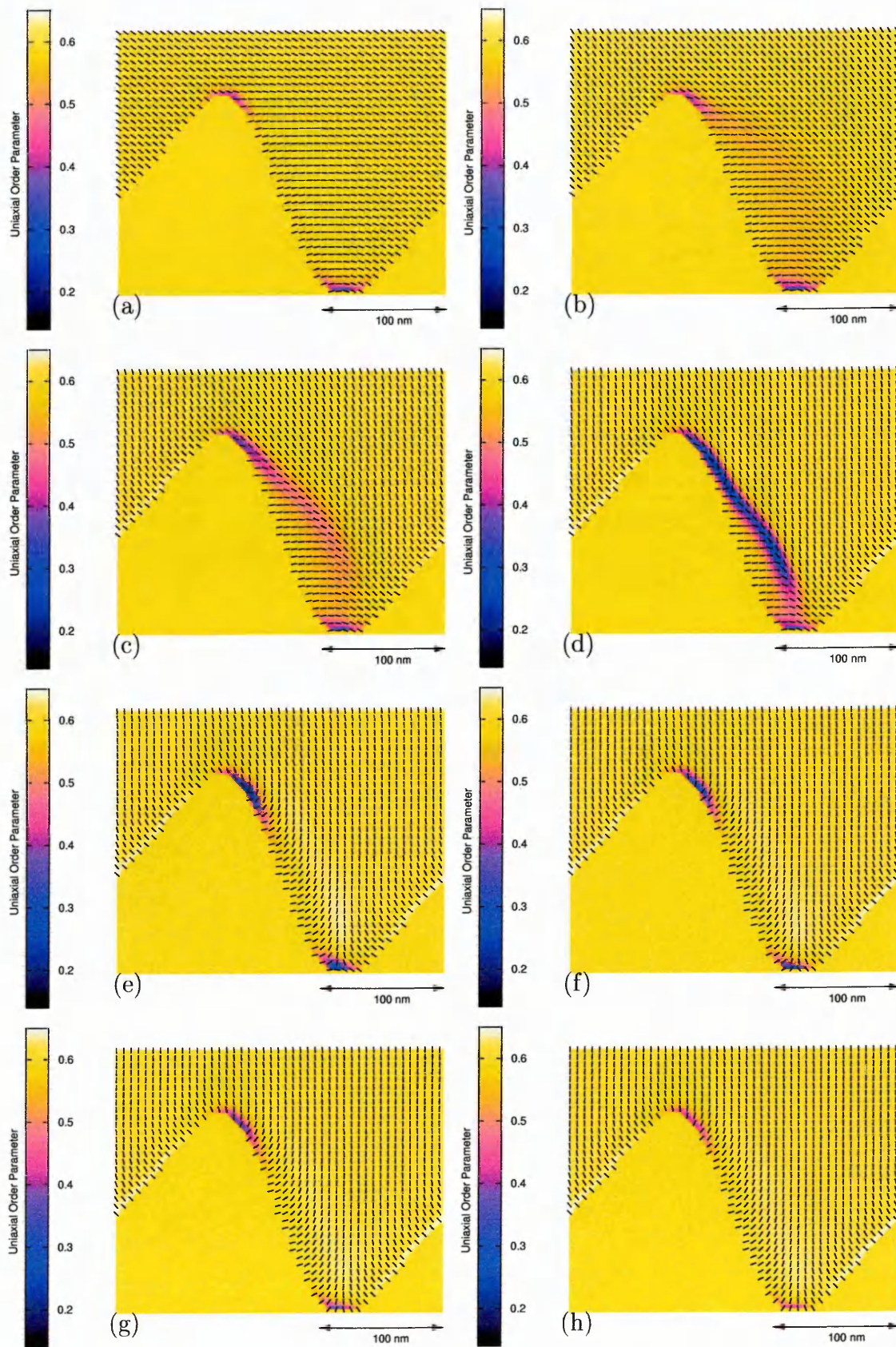


Figure 7.13: Switching from the  $D$  to  $C$  state through application of +18 V at  $t = 0$  to  $t = 349.2 \mu\text{s}$ . (a)  $t = 0 \mu\text{s}$ , (b)  $t = 1.746 \mu\text{s}$ , (c)  $t = 3.492 \mu\text{s}$ , (d)  $t = 5.238 \mu\text{s}$ , (e)  $t = 6.984 \mu\text{s}$ , (f)  $t = 8.73 \mu\text{s}$ , (g)  $t = 10.476 \mu\text{s}$ , (h)  $t = 12.222 \mu\text{s}$ . (Data plotted every other lattice point.)

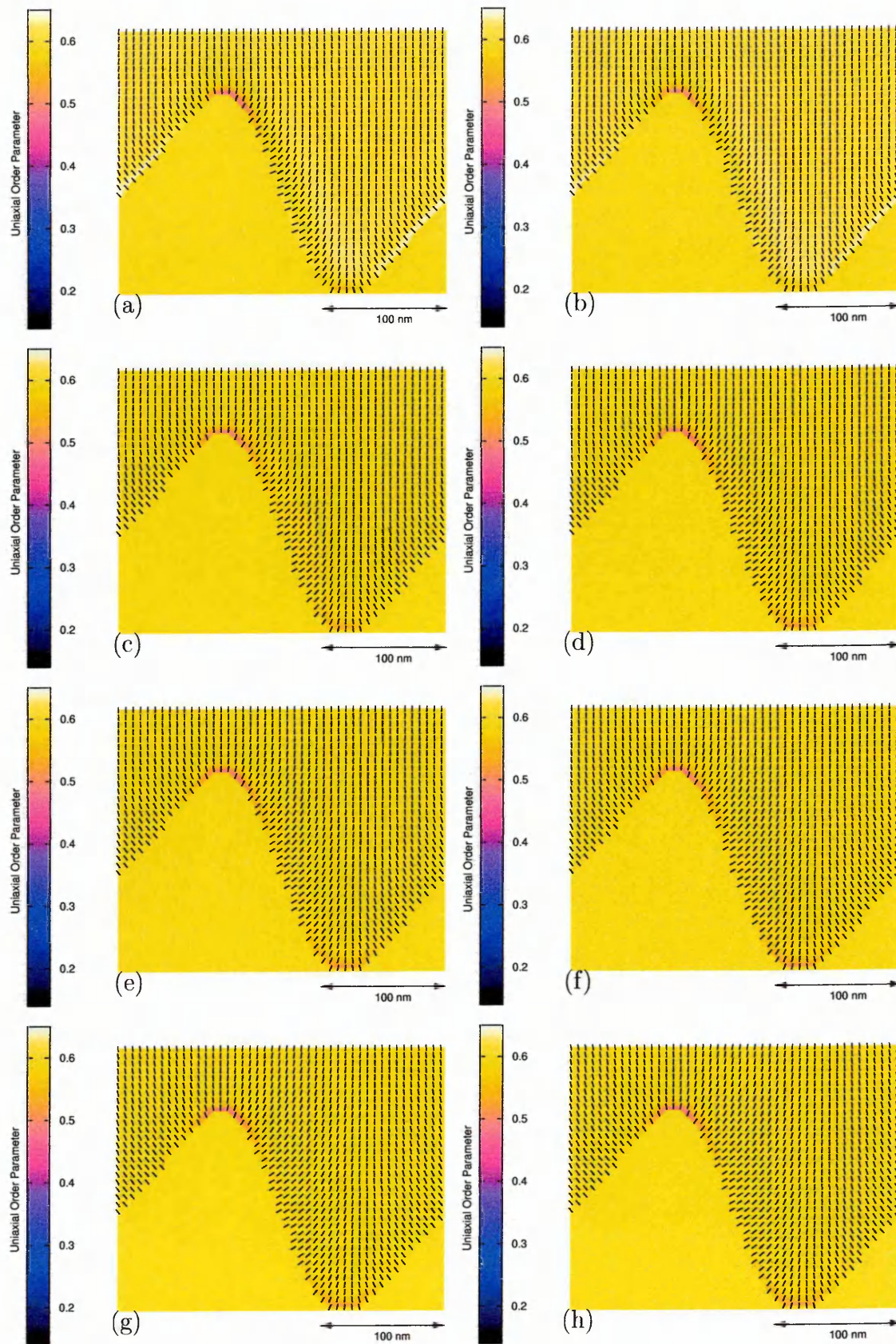


Figure 7.14: Switching from the  $D$  to  $C$  state through application of  $+18$  V at  $t = 0$  to  $t = 349.2\mu\text{s}$ . (a)  $t = 17.46\mu\text{s}$ , (b)  $t = 139.68\mu\text{s}$ , (c)  $t = 350.946\mu\text{s}$ , (d)  $t = 352.692\mu\text{s}$ , (e)  $t = 354.438\mu\text{s}$ , (f)  $t = 356.184\mu\text{s}$ , (g)  $t = 373.644\mu\text{s}$ , (h)  $t = 1047.6\mu\text{s}$ . (Data plotted every other lattice point.)

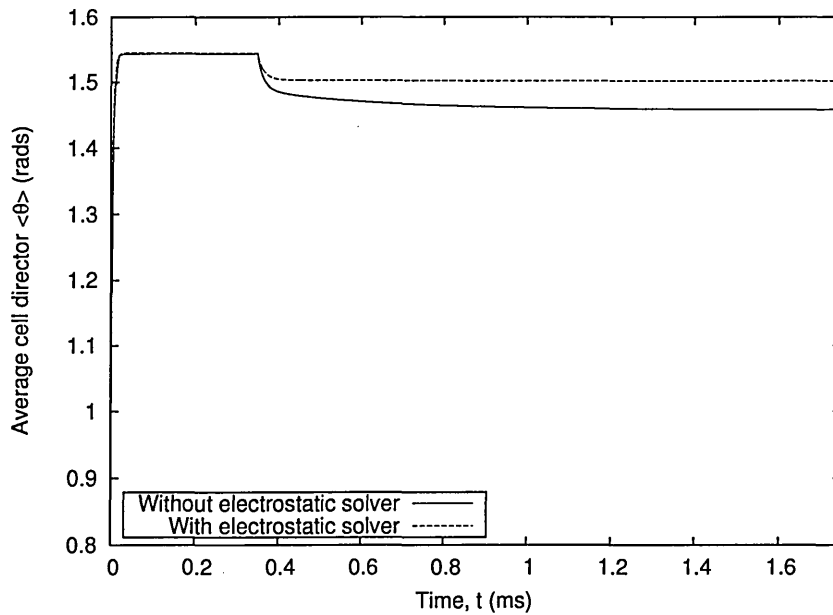


Figure 7.15: Graph showing the cell average director angle during the switching  $\mathcal{D}$  to  $\mathcal{C}$ , for calculations with and without electrostatics. Note average cell director is measured with respect to the  $x$ -axis.

## 7.2.2 $\mathcal{C}$ to $\mathcal{D}$ State Switching

Starting in the  $\mathcal{C}$  state we apply  $\phi = -18$  volts until the system reaches steady state and then turn it off  $\phi = 0$  volts. The resulting dynamics are shown in figures 7.16 and 7.17.

Upon turning on the applied field the bulk directors align quickly to the main field direction. The opposite polarisation lowers the order parameter at the grating surface in which the directors can rotate round to form the ‘frustrated’ state as with the case without the electrostatic solver. The system reaches its steady state (figure 7.16h). This figure can be contrasted with figure 6.22b for the steady state director profiles without the electrostatic solver. The region between the defect areas with the electrostatic solver on is more homeotropic than in the case without. This is because we have made the dipole across the short axis of the molecule ( $|e_{33}|$ ) larger than that of the long axis of the molecule ( $|e_{11}|$ ). Upon turning off the applied field the defects slowly move the short distance to the grating peaks and troughs. The director in the grating region slowly rotates round to form the higher tilted defect state.

The switching process is summarised in figure 7.18 where the averaged director

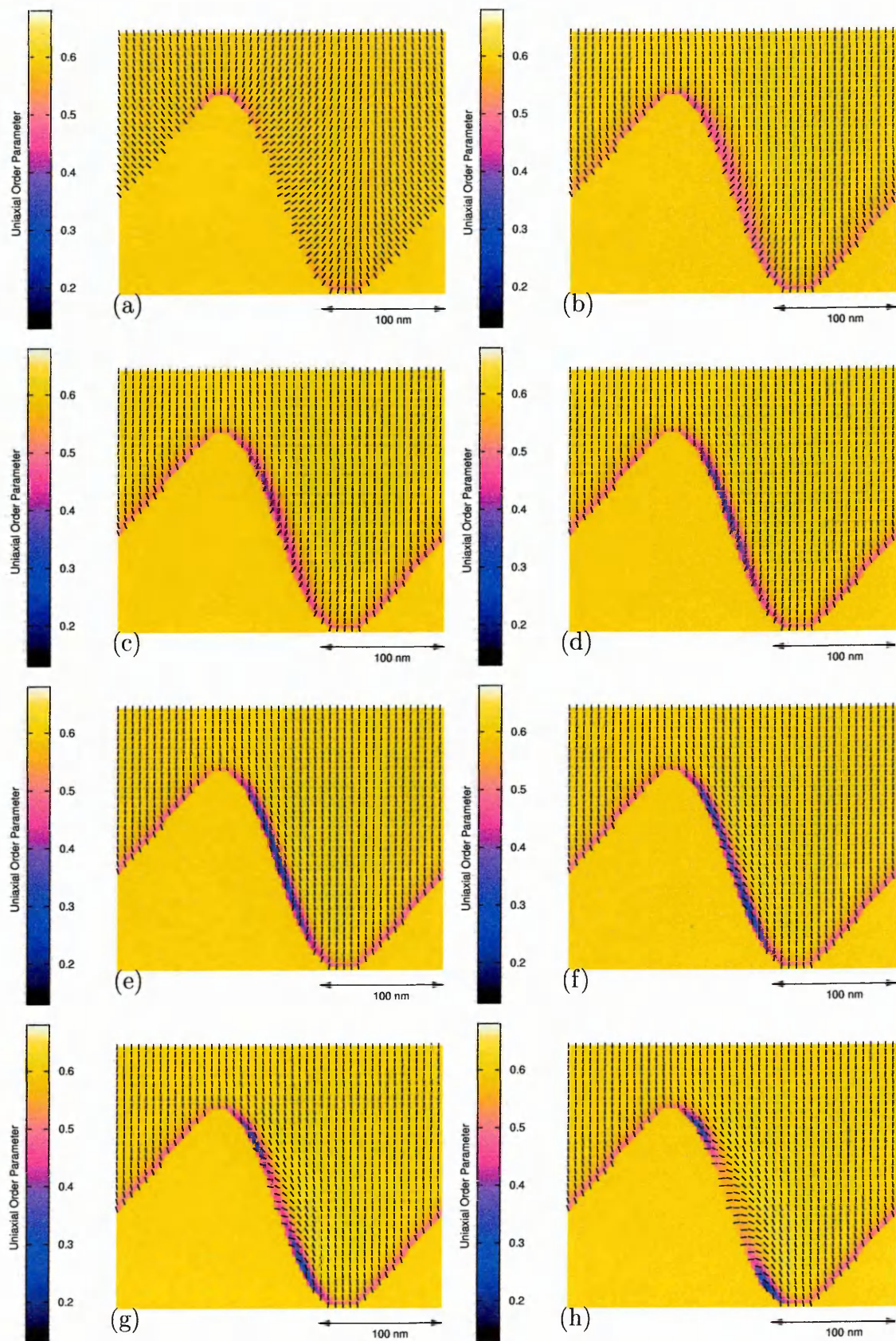


Figure 7.16: Switching from the  $C$  to  $D$  state through application of  $-18$  V at  $t = 0$  to  $t = 349.2\mu\text{s}$ . (a)  $t = 0\mu\text{s}$ , (b)  $t = 5.238\mu\text{s}$ , (c)  $t = 10.476\mu\text{s}$ , (d)  $t = 17.46\mu\text{s}$ , (e)  $t = 27.936\mu\text{s}$ , (f)  $t = 41.904\mu\text{s}$ , (g)  $t = 52.38\mu\text{s}$ , (h)  $t = 174.6\mu\text{s}$ . (Data plotted every other lattice point.)

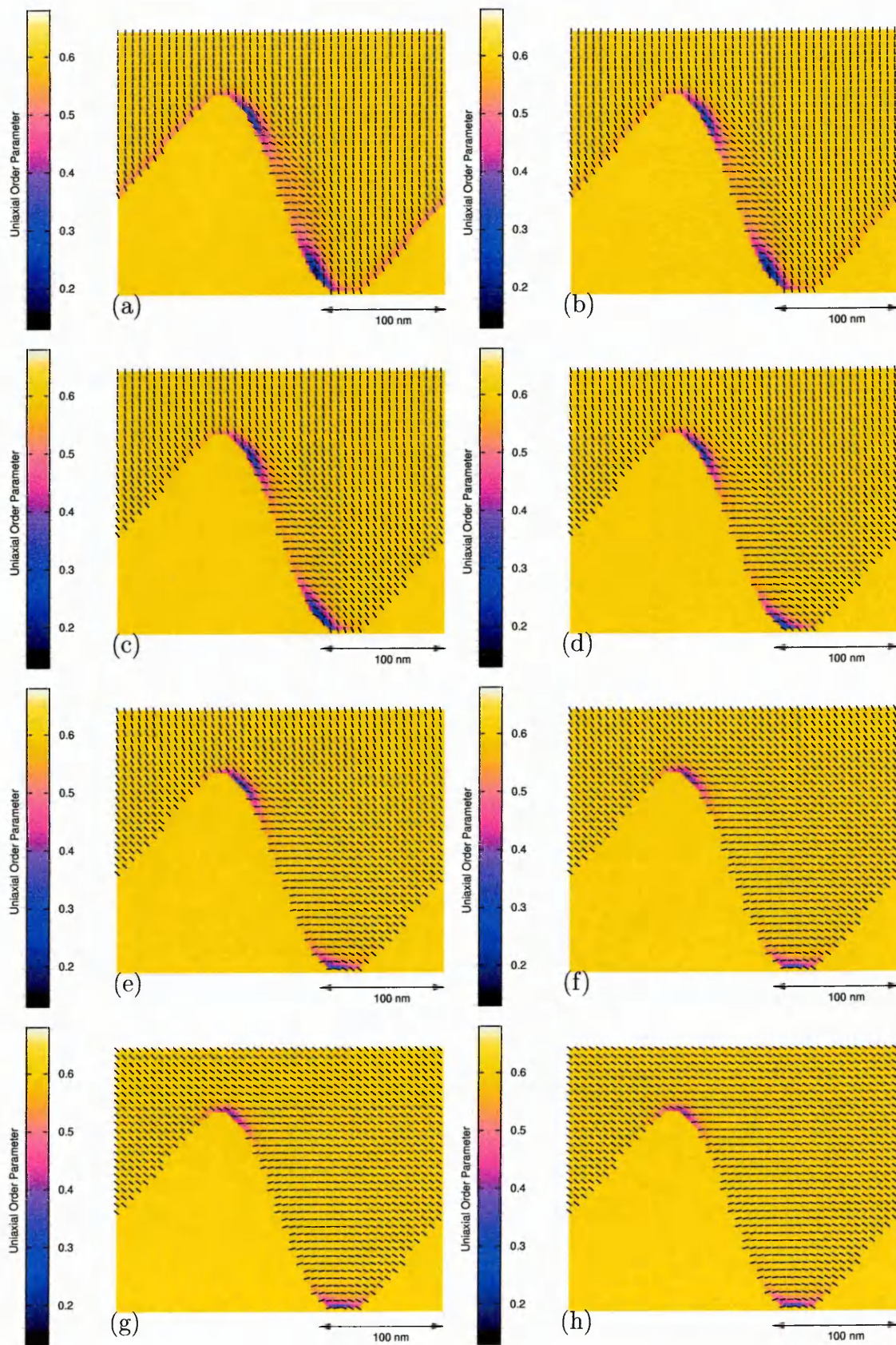


Figure 7.17: Switching from the  $C$  to  $D$  state through application of  $-18$  V at  $t = 0$  to  $t = 349.2\mu\text{s}$ . (a)  $t = 350.946\mu\text{s}$ , (b)  $t = 354.438\mu\text{s}$ , (c)  $t = 361.422\mu\text{s}$ , (d)  $t = 375.39\mu\text{s}$ , (e)  $t = 392.85\mu\text{s}$ , (f)  $t = 453.96\mu\text{s}$ , (g)  $t = 628.56\mu\text{s}$ , (h)  $t = 2619.0\mu\text{s}$ . (Data plotted every other lattice point.)

angle over the cell is plotted in time. Both the case with and without the electrostatic solver is shown. It is seen that with the electrostatic solver on the director is generally more vertically aligned throughout the switching process than without it. The relaxation to the steady state voltage-on case happens slightly quicker with the more accurate electric field. The relaxation into the  $\mathcal{D}$  state also appears to occur slightly more quickly for case with the more accurate electric field.

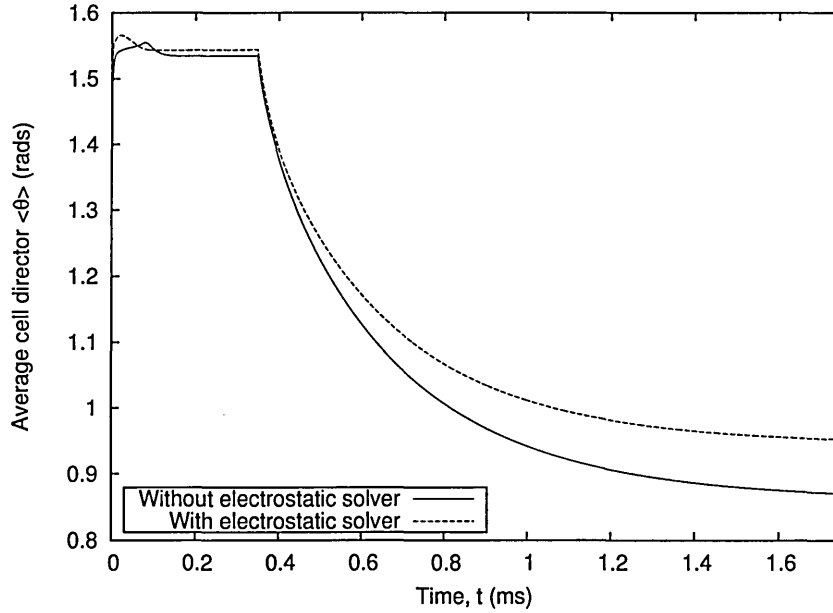


Figure 7.18: Graph showing the cell average director angle during the switching  $\mathcal{C}$  to  $\mathcal{D}$ , for calculations with and without electrostatics. Note average cell director is measured with respect to the  $x$ -axis.

In figures 7.19 we show the lines of constant iso-potential throughout the cell for both applied voltage on and off cases at steady state. These show why it is important to calculate the correct electric field distribution across the cell ( $E_\beta(\underline{x}) = -\partial_\beta\phi(\underline{x})$ ) particularly for flexoelectric materials. It also shows that there is an internal electric field distribution in the  $\mathcal{C}$  and  $\mathcal{D}$  states causing them to be more vertical due to dielectric contributions. For both the  $\mathcal{C}$  and  $\mathcal{D}$  states the maximum potential occurs at the grating peaks and troughs corresponding to the larger director and order distortions and hence flexoelectric and order electric polarisation, further distortion is caused by the dielectric permittivity differences between surface and nematic regions. For the voltage on cases the uniform lines indicate the electric field is both vertical and constant in the upper centre portion of the cell but towards the grating surface the lines are a little distorted and hence the electric field varies due to the

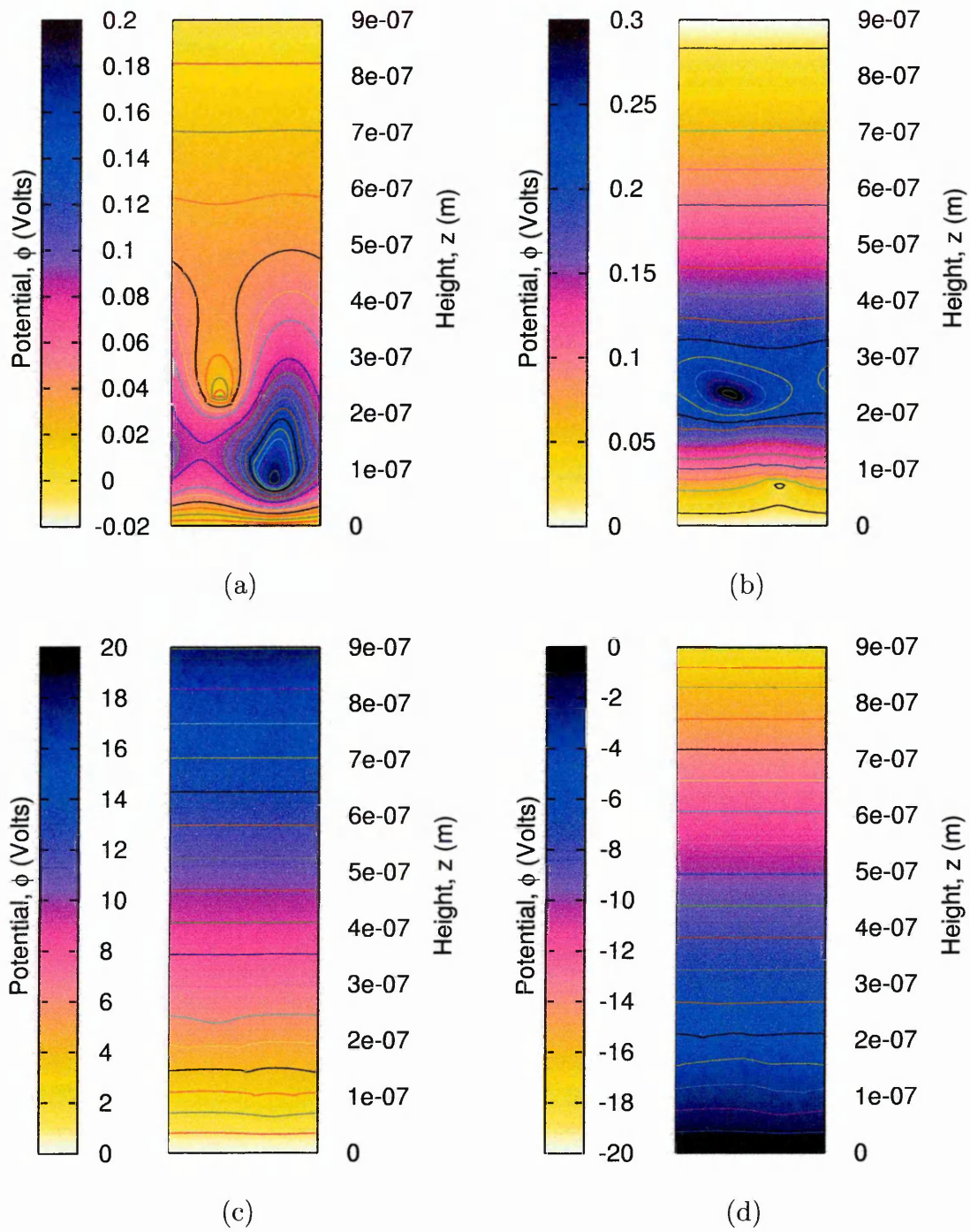


Figure 7.19: Distortion of the lines of constant iso-potential across the device due to dielectric and flexoelectric effects. (a)  $\mathcal{C}$  state, (b)  $\mathcal{D}$  state, (c) applying  $\phi = +18\text{V}$ , (d) applying  $\phi = -18\text{V}$ .

polar flexoelectric effect and dielectric mismatch of bulk and grating permittivities.

With the inclusion of the correct calculations of the electric field we found it was required to choose more suitable flexoelectric coefficients to achieve device switching.

This implies that the electrostatic calculations must be used in simulating this type of device. The  $m = \pm 1/2$  defects do not get projected off the surface but remain at the grating surface during the  $\mathcal{D}$  to  $\mathcal{C}$  switching. The director structures of the equilibrium states are also more tilted towards vertical alignment. The inclusion of a larger  $e_{33}$  flexoelectric coefficient (that is  $e_{33} > -e_{11}$ ) helped the formation of the defects. Further work into investigating the switched states for varying  $e_{11}$  and  $e_{33}$  independently would aid the selection of appropriate nematic materials for use in the ZBD devices and will be done in future work, however this will require development of experimental techniques in the measurement of these values and in the manufacturing of appropriate materials.

### 7.3 A First Step to Quantifying Device Operation

We have seen that the switching time for the  $\mathcal{D}$  to  $\mathcal{C}$  switching are relatively quick and that the  $\mathcal{C}$  to  $\mathcal{D}$  switching times are relatively slow. It is also required to apply comparatively large voltages (that is comparative to handheld devices such as phones) in order to break the free energy barrier that exists between the bistable states. A decrease in both time and switching thresholds would make these devices more commercially attractive within the display markets.

Through computer simulations we have a route to systematically characterise both the display and the material properties of this device. For the 25 or so dimensional parameter space and countless grating shapes that may be considered this is a very time-consuming process and as such will not be considered in this work. We do however make some initial qualitative tests upon device operation. As it is the  $\mathcal{C}$  to  $\mathcal{D}$  switching relaxation time that takes the longest we concentrate on how properties can effect this particular process.

The simulation parameters are as in the previous section unless otherwise stated; the electrostatic solver is included in simulations but the hydrodynamic part is not. All simulations have started with a uniform configuration,  $\theta = \pi/2$ , then we apply a negative voltage until steady state and the subsequent relaxation process is monitored. The relaxation is monitored by following the cell averaged director angle in time. A high value ( $\pi/2$ ) corresponds to continuous states and a lower value to defect states.

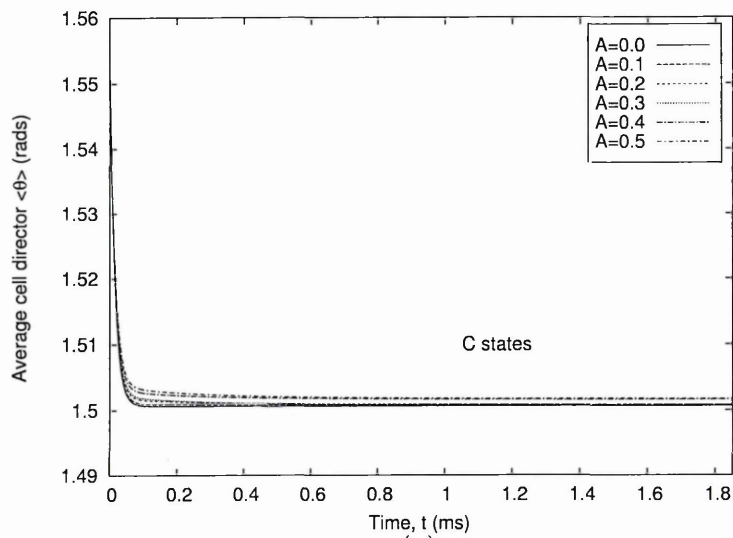
Figures 7.20 show how a change in the grating asymmetry factor,  $A$ , effects the relaxation of the device. First we observe the switched  $\mathcal{D}$  state has different equilibrium position. The more symmetric the grating the higher the tilt at the lower surface. Changes in the grating asymmetry do not significantly effect the speed of relaxation for the modelled profile dimensions. For symmetric gratings ( $A = 0$ ) it was not possible to form the  $\mathcal{D}$  state for the range of voltages tested.

We can also say from comparing figures 7.20 that the voltage required to switch to the  $\mathcal{D}$  state is larger the more symmetric the grating. As a larger asymmetry corresponds to steeper surface features we may postulate that steeper surface features can reduce the voltage requirements upon switching. From figures 7.21 we plot the time taken at constant  $A$  and varying the applied voltage. In figure 7.21a, the more symmetric grating, we require larger voltages to switch (only  $\phi = -18\text{V}$  switched to the  $\mathcal{D}$  state). In figure 7.21b, the most asymmetric grating, we require lower voltages to switch (both  $\phi = -18\text{V}$  and  $\phi = -14\text{V}$  switched to the  $\mathcal{D}$  state). Changing the applied voltage does not effect the relaxation time.

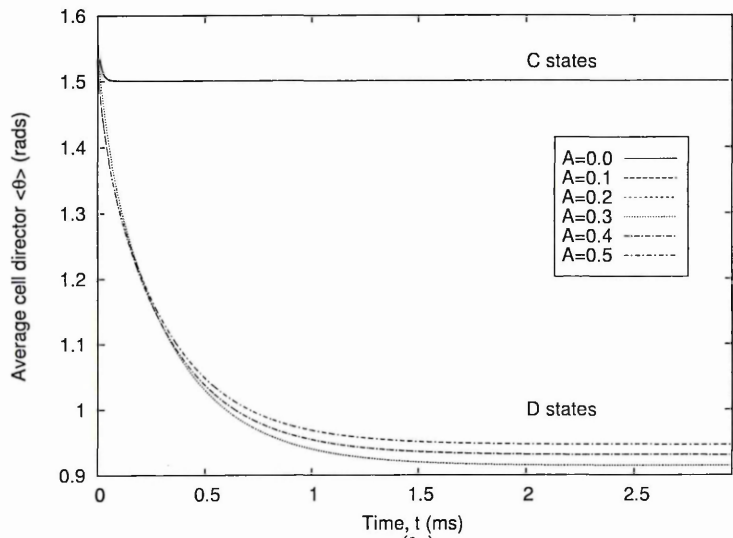
In figure 7.22 the surface homeotropic anchoring energy is varied. The figure shows there is a complex relationship between the anchoring strength and flexoelectric distortion as to which state is selected during switching. At  $W = 0.5 \times 10^{-4} \text{ kg s}^{-2}$  and  $W = 5.0 \times 10^{-4} \text{ kg s}^{-2}$  the  $\mathcal{D}$  state is achieved. It is the larger of these two values that has the faster relaxation time. At  $W = 1.0 \times 10^{-4} \text{ kg s}^{-2}$  and  $W = 10.0 \times 10^{-4} \text{ kg s}^{-2}$  the  $\mathcal{C}$  state is achieved. The larger of these two is such that the flexoelectric polarisation has little effect upon the surface. On account of changes in temperature shown in the following section we may prefer the lower of these two values despite the larger relaxation time.

In figure 7.23 we vary the  $h$  parameter of the grating shape corresponding to the height of the grating features. At small values ( $h = 0.3w$ ) the device is not bistable, the  $\mathcal{C}$  state is the only state. Increasing  $h$  reduces the relaxation times quite significantly into the  $\mathcal{D}$  state. Also the smaller the value of  $h$  the more vertically aligned the system.

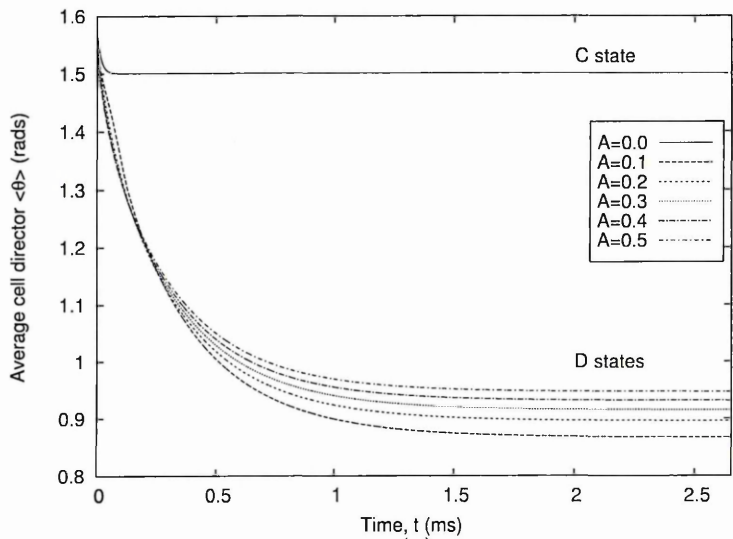
Figure 7.24 shows the change that occurs for different values of the elastic constants whilst keeping the characteristic elastic constant,  $(K_{11} + K_{33})/2$  constant. A larger difference between  $K_{11}$  and  $K_{33}$  increases, slightly, the relaxation time in to



(a)



(b)



(c)

Figure 7.20: Graphs showing the cell average director angle during relaxation from applying a negative potential for various blaze factors  $A$  and with voltages: (a)  $-10V$ , (b)  $-14V$  and (c)  $-18V$ . Note average cell director is measured with respect to the  $x$ -axis.

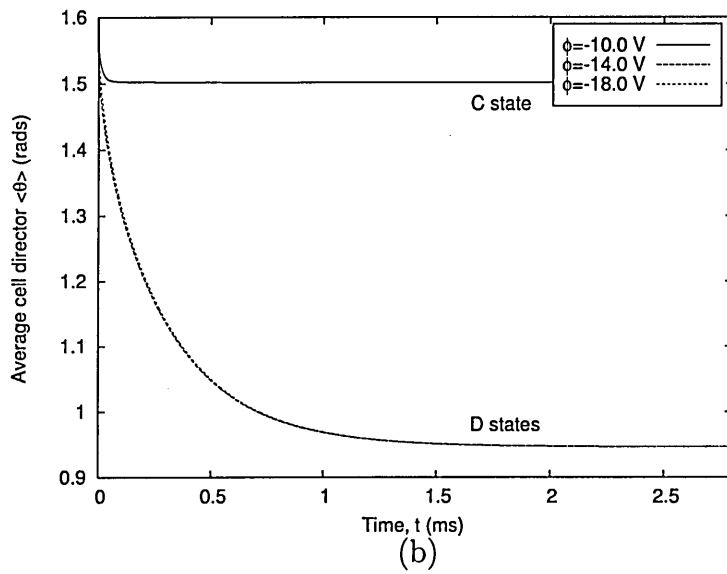
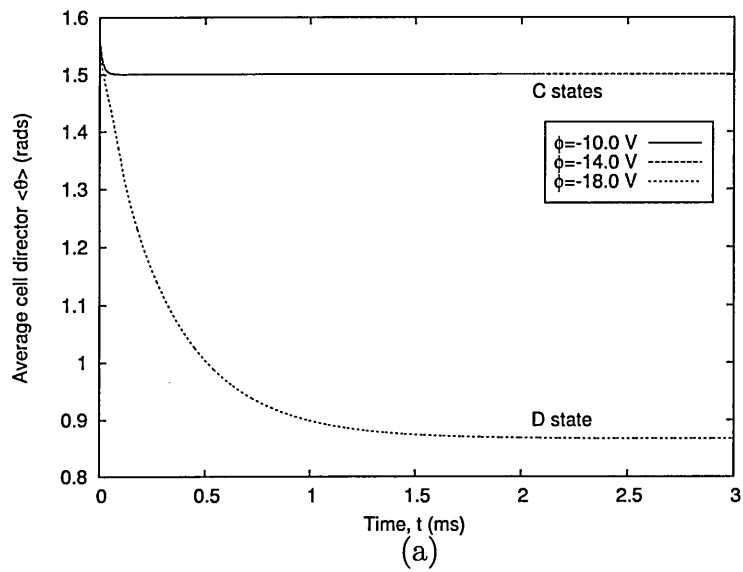


Figure 7.21: Graph showing the cell average director angle during relaxation from applying various negative potentials for calculations with blaze factors (a)  $A = 0.1$  and (b)  $A = 0.5$ . Note average cell director is measured with respect to the  $x$ -axis.

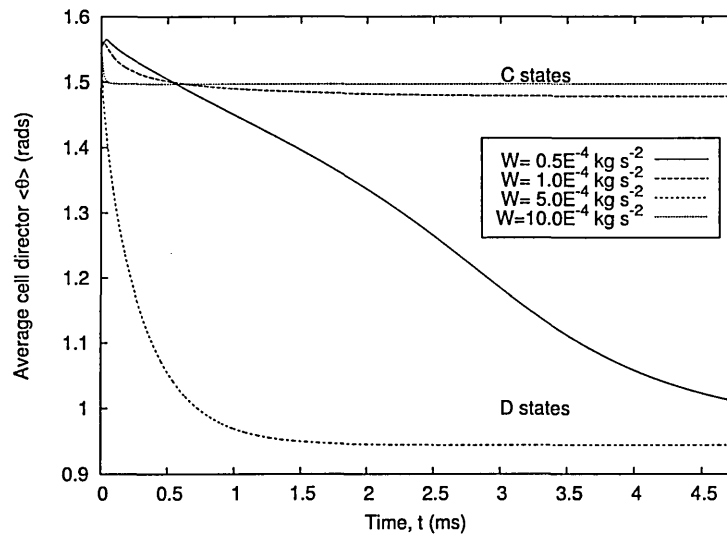


Figure 7.22: Graph showing the cell average director angle during the relaxation from applying a  $\phi = -14V$  potential for calculations with varying anchoring strength and  $A = 0.45$ . Note average cell director is measured with respect to the  $x$ -axis.

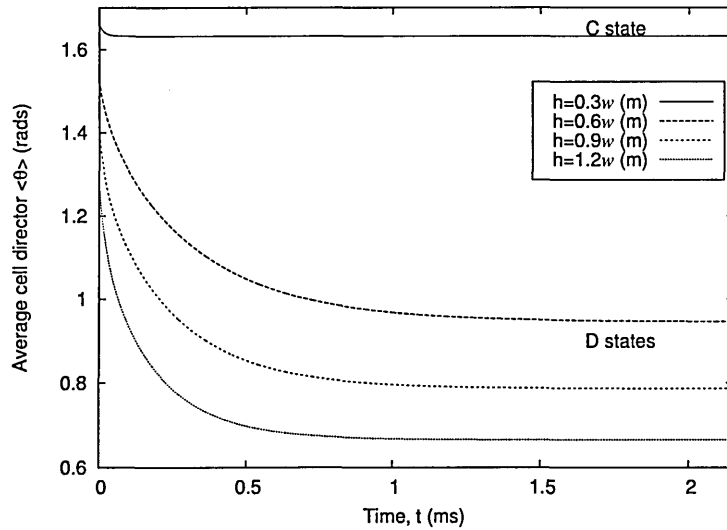


Figure 7.23: Graph showing the cell average director angle during the relaxation from applying a  $\phi = -14V$  potential for calculations with varying grating height,  $h$ , and  $A = 0.45$ . Note average cell director is measured with respect to the  $x$ -axis.

the  $\mathcal{D}$  state. A larger difference also gives a more vertically aligned director.

These investigations are by no means exhaustive. They provide an initial look as to how some parameters effect the device and as to what may need to be considered for a future quantitative parameterisation of the device.

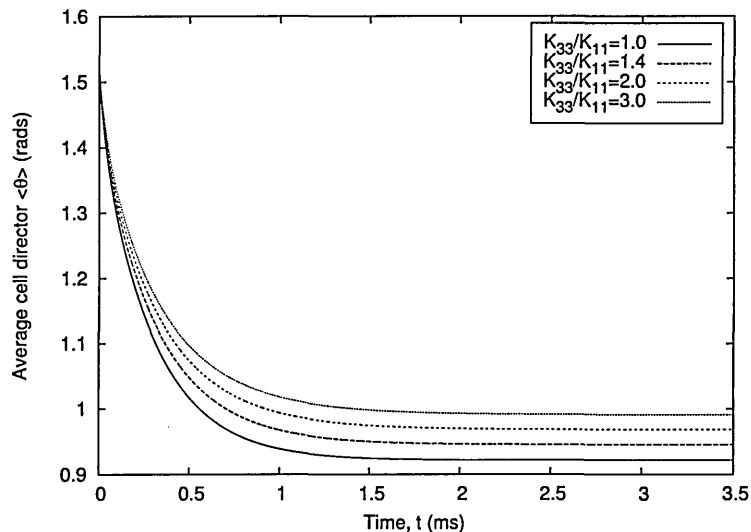


Figure 7.24: Graph showing the cell average director angle during the relaxation from applying a  $\phi = -14V$  potential for calculations with varying elastic constants,  $K_{11}$  and  $K_{33}$  in which  $(K_{11} + K_{33})/2 = 12 \times 10^{-12} \text{ kg m s}^{-2}$  and  $A = 0.45$ . Note average cell director is measured with respect to the  $x$ -axis.

## 7.4 A Temperature Variation

When searching for the equilibrium states of this device we found upon cooling into the nematic phase from the isotropic phase the  $\mathcal{D}$  state is always found. This suggests that near  $T_{IN}$  the  $\mathcal{D}$  state has a lower free energy state. In this section we show the reverse behaviour by starting in the nematic phase and increasing the temperature.

Starting in the calculated equilibrium  $\mathcal{D}$  state of §7.2 it is found the device remains in this state whilst increasing the temperature through to the isotropic phase. Starting in the calculated equilibrium  $\mathcal{C}$  state of §7.2 we find as the temperature increases the device jumps into the  $\mathcal{D}$  state when the temperature reaches  $T^* < T < T_{IN}$ . For these calculation we have not included the hydrodynamic part of the solver and no external electric or magnetic fields are applied. Figures 7.25 to 7.27 show such a process.

For these figures we have started in the  $\mathcal{C}$  state at  $T = T_{IN} - 4(T_{IN} - T^*)$  (K) and we increase the temperature to  $T = T_{IN} - 4(T_{IN} - T^*) + 4.403$  (K) at time  $t = 0$ . The boundary condition remains as with the previous sections: uniaxial, homeotropic and with the preferred order parameter  $S_0 = 0.591$ .

Almost immediately the order parameter drops to a value appropriate to the new

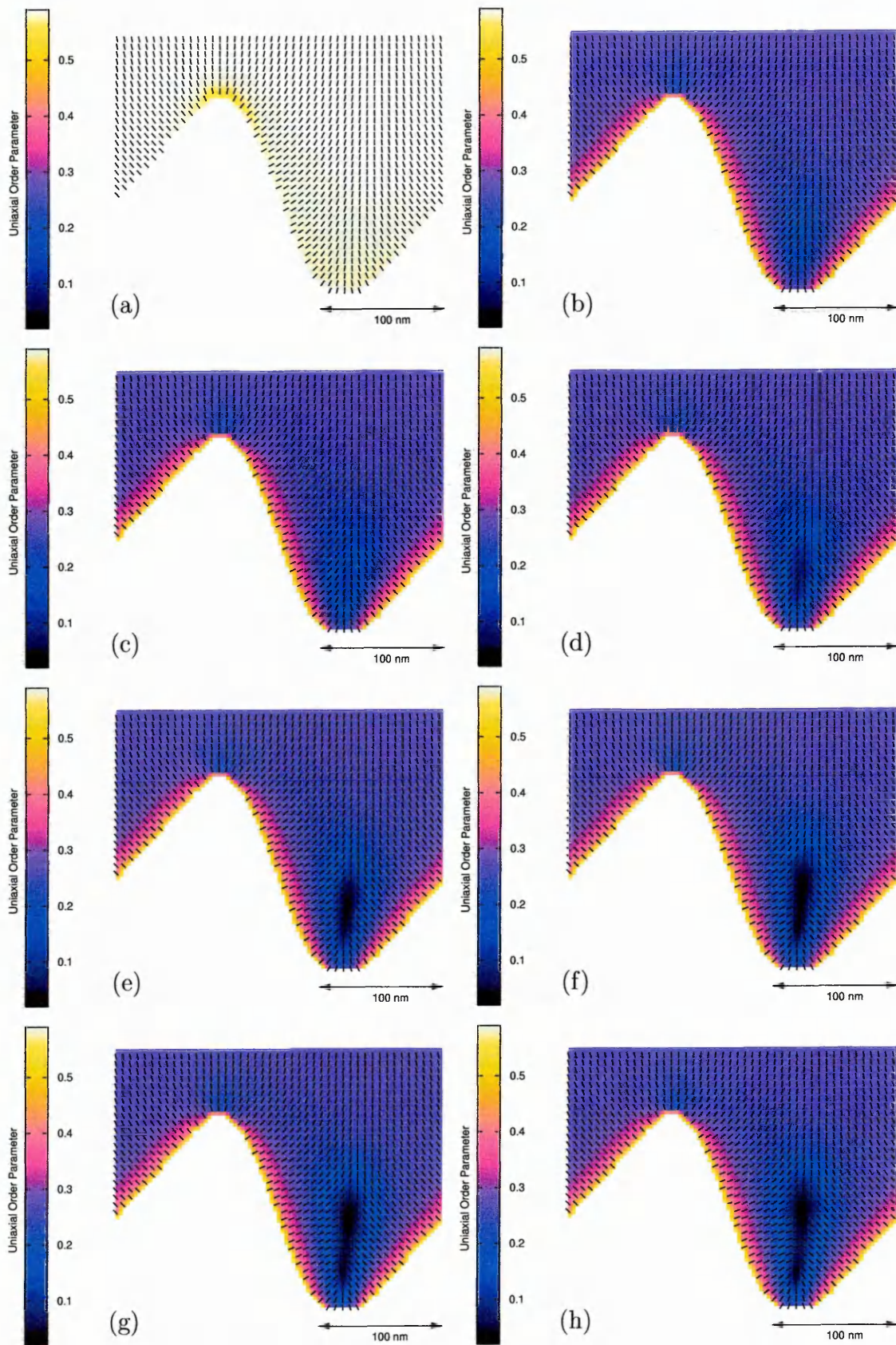


Figure 7.25: Temperature induced switching from an initial  $\mathcal{C}$  state at  $T = T_{IN} - 4(T_{IN} - T^*)$  (K) increased to  $T = T_{IN} - 4(T_{IN} - T^*) + 4.403$  (K) at  $t = 0$  (No external fields). (a)  $t = 0\mu\text{s}$ , (b)  $t = 13.968\mu\text{s}$ , (c)  $t = 27.936\mu\text{s}$ , (d)  $t = 41.904\mu\text{s}$ , (e)  $t = 55.872\mu\text{s}$ , (f)  $t = 69.84\mu\text{s}$ , (g)  $t = 83.808\mu\text{s}$ , (h)  $t = 97.776\mu\text{s}$ . (Data plotted every other lattice point.)

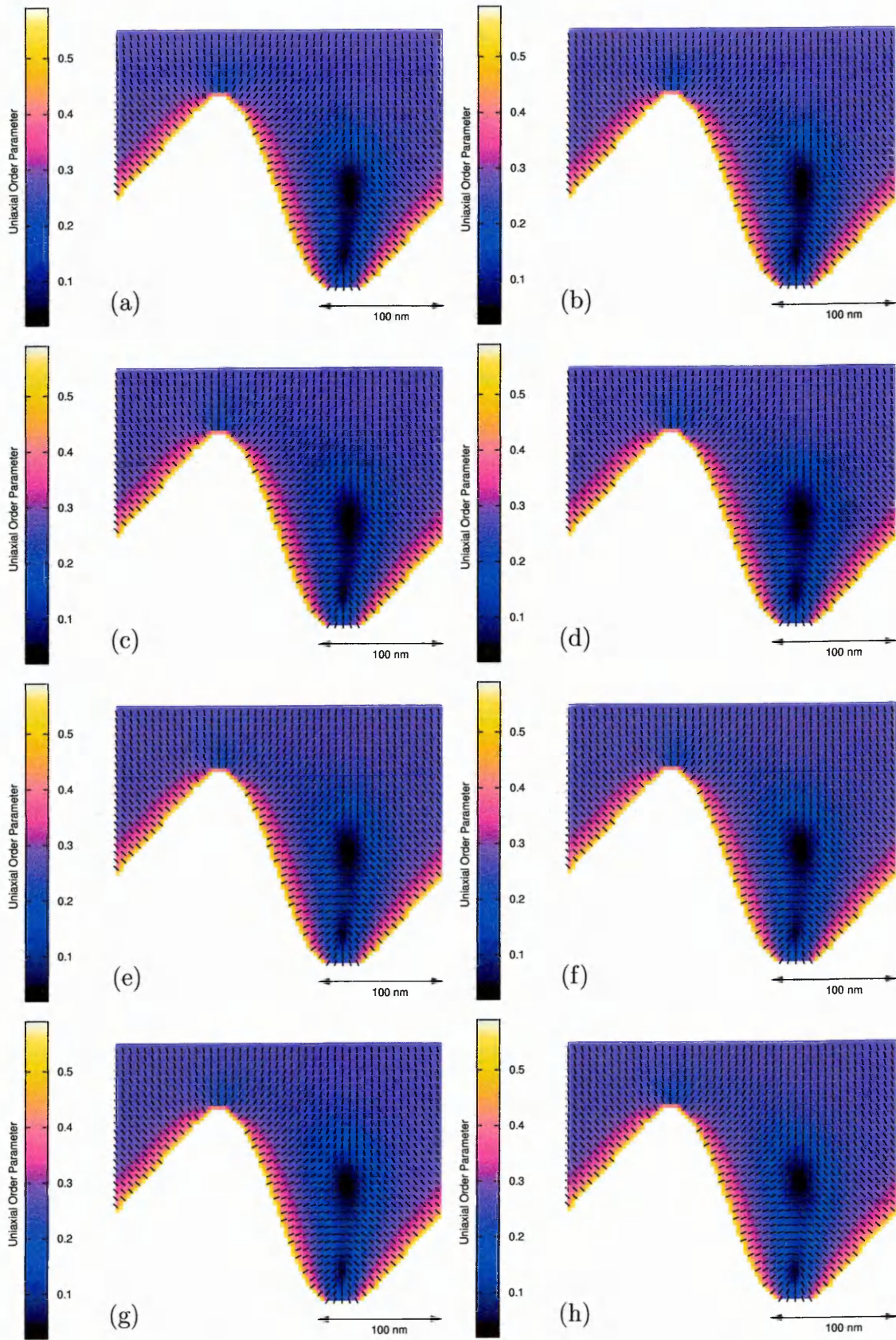


Figure 7.26: Temperature induced switching from an initial  $C$  state at  $T = T_{IN} - 4(T_{IN} - T^*)$  (K) increased to  $T = T_{IN} - 4(T_{IN} - T^*) + 4.403$  (K) at  $t = 0$  (No external fields). (a)  $t = 111.744\mu\text{s}$ , (b)  $t = 125.712\mu\text{s}$ , (c)  $t = 139.68\mu\text{s}$ , (d)  $t = 181.584\mu\text{s}$ , (e)  $t = 209.52\mu\text{s}$ , (f)  $t = 251.424\mu\text{s}$ , (g)  $t = 307.296\mu\text{s}$ , (h)  $t = 349.2\mu\text{s}$ . (Data plotted every other lattice point.)

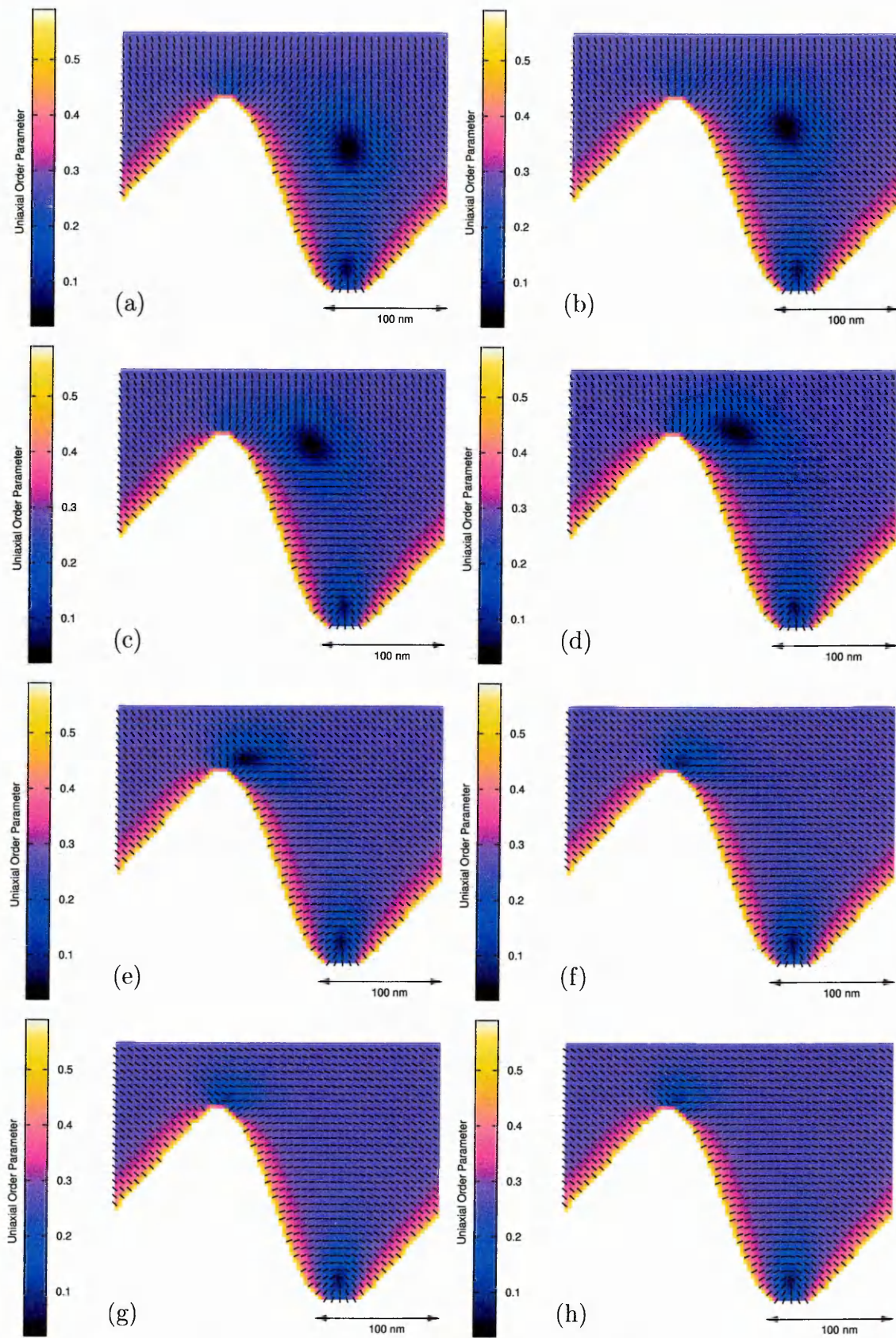


Figure 7.27: Temperature induced switching from an initial  $C$  state at  $T = T_{IN} - 4(T_{IN} - T^*)$  (K) increased to  $T = T_{IN} - 4(T_{IN} - T^*) + 4.403$  (K) at  $t = 0$  (No external fields). (a)  $t = 460.944\mu\text{s}$ , (b)  $t = 600.624\mu\text{s}$ , (c)  $t = 782.208\mu\text{s}$ , (d)  $t = 879.984\mu\text{s}$ , (e)  $t = 977.76\mu\text{s}$ , (f)  $t = 1131.408\mu\text{s}$ , (g)  $t = 2039.328\mu\text{s}$ , (h)  $t = 3142.8\mu\text{s}$ . (Data plotted every other lattice point.)

temperature of the system (figure 7.25a). As the elastic constants of the nematic are  $\propto S^2$  there is a decrease in the elastic energy of the system. The strong homeotropic anchoring now induces a large melted region within the grating trough in which two  $m = \pm 1/2$  defects emerge (figure 7.25f). The  $m = +1/2$  defect is formed below the  $m = -1/2$  defect. Once established the  $m = -1/2$  defect is pushed out of the grating trough by the homeotropic anchoring and moves to the minimum energy position in the cell which corresponds to the  $\mathcal{D}$  state (figure 7.27h).

For the surface modelled in this section, towards the transition temperature the LC cell is now monostable. For a device this means any written image/data would be lost. In the competitive display market products typically have stringent operational requirements of  $-20^\circ\text{C} \lesssim T \lesssim 65^\circ\text{C}$  for which the upper end of this range corresponds to  $T_{IN}$  for commonly used display materials. This identifies a significant feature to consider in the design of a grating surface for the ZBD displays.

For the surface chosen here it has a limited temperature operational range and we must modify the surface or device properties in order to maximise the device bistability temperature range. These changes may include weaker anchoring strengths, larger pitch ( $w$ ) of the grating pattern, larger grating trough angle such that it is  $\gtrsim 90^\circ$  or new nematic material selection. The effect of making any such changes on the overall operating features of this device, as seen in §7.3, are less clear.

## 7.5 Conclusions

Further theoretical modelling of the ZBD device has shown hydrodynamic forces do not play an important part in order to achieve dynamic switching of the device. A switched state is determined solely by the time at which defects have annihilated or created. The inclusion of an electrostatic solver makes significant changes to time dynamics, equilibrium states and path of defects and thus must be included in any simulation. Switching is better achieved through the selection of more suitable flexoelectric coefficients in which  $e_{33} \neq e_{11}$ . The energy of the two equilibrium states are not equal over a wide temperature range: the  $\mathcal{D}$  state being the only stable state at temperatures near  $T_{IN}$  for the surface modelled here. The grating shape and dimension have many effects upon device operation and as such require further systematic investigation.

# Chapter 8

## Discussion, Conclusions and Further Work

### 8.1 Discussion

In this thesis we have described the development of a lattice Boltzmann based solver for liquid crystals and liquid crystal displays. The method recovers the hydrodynamic, director and order variations of liquid crystals in a confined geometry and subject to external magnetic or electric fields. The flexoelectric properties of nematic liquid crystal display devices was also investigated. The solver may be of particular interest to device engineers.

After introducing liquid crystal properties and liquid crystal display technology in chapter 1 we reviewed the Q-tensor theory for liquid crystals in chapter 2. The free energy appropriate for thermotropic nematic and chiral nematics is identified including unequal elastic constants, chirality, flexoelectric, electric, magnetic and surface anchoring effects. The nemato-dynamic equations presented by Qian [40] are identified as the target macroscopic equations to be recovered by our solver as they retain the independence of material coefficients and thus allow all the experimentally known material values to be used.

In chapter 3 we cover the lattice Boltzmann method for isotropic fluid dynamics that recovers the Navier-Stokes equations. A brief study of isotropic pressure-driven laminar flows over a backward facing step is undertaken using two methods: a uniform body forced lattice Bhatnagar Gross Krook method and a pressure evolved exactly incompressible lattice Bhatnagar Gross Krook method. Measurements of the steady state velocity profiles and reattachment length have been undertaken for

a range of *Reynolds* numbers. The results are directly compared to experimental measurements made by Denham [76] with a good level of agreement. For many engineering computational flows in the lattice Boltzmann literature flow is induced via a uniform body forced method. Our results suggest that if only velocity information is required this method can be used with confidence and, with an appropriate adjustment, can be made to produce a qualitative representation of the pressure field.

The proposed lattice Boltzmann solver for  $Q$ -tensor nemato-dynamics is presented in chapter 4. The solver is validated against a number of test cases including temperature behaviour, electric field, flow alignment, Miesowicz viscosities and a ‘kick-back’ cell. Comparison of results to simple analytical calculations show excellent agreement; however these analytical results are for uniformly bulk aligned systems.

In chapter 5 we investigate a one-dimensional model of a bistable liquid crystal display cell developed by Davidson [2]. Numerical solutions from the lattice Boltzmann solver for the statics of this model compare well to Davidson’s calculations using an Ericksen-Leslie model which lends further support to the solver. We then use the lattice Boltzmann solver to investigate more completely the statics of the device adding unequal elastic constants and the electrostatic solver for the electric field. Marked differences are found when including the electrostatic solver that imply such omissions of this effect should not be made for quantitative dynamics of a cell. The addition of our variable order method allows us to better evaluate flexoelectric and, in particular, order electric polarisation which is found to contribute significantly to the electric polarisation at the limiting surfaces of the cell.

The dynamic behaviour of the model, as found by Davidson [2], is completely dependent upon the value of the surface viscosity. Tuning the surface viscosity for a particular cell could allow time evolution of the model to match experiment but does not allow any further quantitative features of a bistable cell to be seen.

It is found in the modelling of such a model that a pre-tilt is required to avoid reverse tilts and out of plane director rotation. A pre-tilt of  $\geq 5^\circ$  can avoid out of plane rotation and a pre-tilt of  $\geq 9^\circ$  will optimise switching times. The effect of hydrodynamic flow upon the device is negligible for small and large surface viscosities

but it is possible to choose a value at which the flow becomes important in order to calculate the final bistable state selected.

Chapter 6 investigates the zenithal bistable display device. We show how flexoelectric properties of nematics provide a source of bistability in this cell. The switching behaviour can be qualitatively reproduced using simpler equations that ignore the hydrodynamic and electrostatic effects. The defect creation and annihilation processes are shown and these appear to be more correct than in previous studies. It is shown through comparison to Ericksen-Leslie type simulations that a variable order parameter scheme is essential in calculations that deal with defect dynamics. It is also shown that if the quadrupolar model of flexoelectricity is used then the sign of the flexoelectric coefficient is positive. Increasing values of this coefficient will decrease switching times and cause the defects to annihilate further away from the device surfaces. A method for calculating the magnitude of the flexoelectric coefficient is proposed.

In chapter 7 further qualitative features are added to the simulations of the zenithal bistable display. The hydrodynamics during switching are shown. It is found that in the region where the defects exist the grating surface serves to reduce the hydrodynamic flows and thus they do not play an important role in device bistability.

The addition of the electrostatic solver required that we choose more suitable flexoelectric coefficients in order to reproduce switching behaviour. Values that obey  $e_{11} > 0$  and  $e_{33} < -e_{11}$  recover bistable properties well. The main effect of the electrostatics was to show a large residual potential exists within the device near the distorted grating regions. This in turn generates higher director tilts throughout the cell due to the dielectric effect. During the switching process it is found its effect is to confine the  $\pm 1/2$  defects to the grating surfaces. The potential calculated in the device is limited by the omission of ion concentrations and the smaller device dimensions used.

Further simulations of the slow continuous to defect state relaxation switching suggest:

- A steeper surface feature can reduce the switching voltage.
- A stronger anchoring coefficient can decrease switching times.

- There are windows of anchoring strengths that can achieve bistable switching.
- A larger grating depth also reduces switching times.
- Larger differences in the splay-bend elastic constants tend to increase the switching times to the defect state.
- At higher temperatures near  $T_{IN}$  the strong surface anchoring properties make the defect state the only stable state; the device is no longer bistable.

Individually these simulations all provide a useful insight into the zenithal bistable display operation however further systematic investigation is required because the optimisation of one parameter may hinder the operation in other areas of the display. For the large parameter space and including the surface shape variations of these displays an optimisation process will be a very time consuming. It should also be highlighted that real zenithal bistable display device dimensions are twice those used in this study. This obviously has an effect on the quantitative applicability of the calculations but qualitatively no changes are expected.

## 8.2 Conclusions

We have undertaken the development of a full device solver for liquid crystals and liquid crystal displays. The lattice Boltzmann method is chosen as the numerical tool to solve the governing  $Q$ -tensor equations of nemato-dynamics. A Chapman-Enskog analysis demonstrates that the algorithm recovers the target macroscopic equations. Simple test simulations validate the method for the evolving momentum, director and order parameter fields. The  $Q$ -tensor method yields a fuller description of boundaries in terms of flexoelectric polarisation properties and in the simulation of defect dynamics.

The succesful use of the lattice Boltzmann method in the simulation of a non-Newtonian liquid crystalline fluids suggests that these methods can readily be adapted and used in the simulation of other types of complex fluids. In doing so we may exploit the advantages of lattice Boltzmann methods such as the ease of use, particle suspensions, multi-component flows and for complex boundaries.

Simulations of the zenithal bistable display have been undertaken. It is shown that flexoelectric properties of nematics can provide a route to recover the bistability of the device. The defect creation and annihilation process has been shown. A method to determine the sign and magnitude of the flexoelectric coefficients is proposed. The operational performance of the zenithal bistable display has been examined for varying material and surface properties and preliminary results are shown for device optimisation. A complete optimisation would involve a lengthy series of simulations to investigate fully the parameter space, a task which is possible through the presently developed device solver.

### 8.3 Further Work

There are a number of areas of further work that stem from this study. Firstly there are a number of improvements to the lattice Boltzmann solver that would be worthwhile. A modified forcing term to eliminate the non-negligible Landau terms of the molecular field should provide more accurate calculation and stability of parameters near to surfaces and defects. Simulations suggest their effect is felt in the velocity profiles near to wall regions when a weak anchoring condition is used. The introduction of a lattice Boltzmann boundary condition for the order tensor may also increase the accuracy of simulations. A parallelisation of the solver would increase the productivity of simulations (lattice Boltzmann codes report good linear scaling with the number of processors) and allow for real device dimensions and make real device optimisation a feasible undertaking. The development of an electro-dynamics theory for ion convection within the Q-tensor frame may provide further quantitative applicability of the solver.

In order to investigate bounding surfaces and defect structures more accurately in liquid crystal devices a hybrid scheme could be developed that combines our lattice Boltzmann method with molecular dynamics simulation methods. Through molecular dynamics a more accurate representation of boundary and defects can be expected with the shorter time and length scales that are accesible. Constructing a suitable interface with information exchange rules from the different regions may capture fully the correct dynamics of complex situations.

We have shown the solver to be usefully applied to the zenithal bistable display

device. A further systematic investigation of this device over its entire parameter space could help optimise these types of display and perhaps enable further commercialisation in the liquid crystal display market.

It is was proposed through comparison of simulations and experimental data a method to determine the flexoelectric coefficients. These coefficients are hard to determine experimentally particularly in one-dimensional devices. Through the simulations of the zenithal bistable display and sufficient experimental data (e.g. see appendix C) it should be possible to determine these coefficients. Current data for a full set of material coefficients is sparse, particularly there is a lack of Landau coefficient data available. Measurement of the complete set of parameters for a range of materials would enable wider applicability of the solver.

Taking advantage of particle methods in the lattice Boltzmann method it should be possible to introduce colloidal particles into simulations as an area of futher study. In particular there is experimental interest into the effects of adding spherical particles to liquid crystal mixtures. More recently experiments have inserted carbon nano tubes into liquid crystal mixtures in order to align the nano tubes. Through simulations we will be able explore further the use of such nano tubes.

# Appendix A

## EILBGK Model

The compressibility error of the LBGK method (§ 3.1) may be overcome. The Exactly Incompressible EILBGK model of Zou [166] and Lin [167] makes a slight change to the interpretation of the distribution function  $f_i$  in order to make the macroscopic dynamics much more incompressible, but at the expense of the accuracy of its time variation. Applications of the EILBGK are therefore restricted to steady state solutions and to flows with slow variation. However, EILBGK allows for a more accurate treatment of pressure boundary conditions. What changes is the equilibrium distribution function and the definition of velocity; for the D2Q9 lattice these being:

$$f_i^{(eq)} = t_i \left( \rho + \frac{\mathbf{e}_i \cdot \mathbf{u}}{c_s^2} + \frac{(\mathbf{e}_i \cdot \mathbf{u})^2}{2c_s^4} - \frac{\mathbf{u} \cdot \mathbf{u}}{2c_s^2} \right) \quad (\text{A.1})$$

with

$$c_s^2 = \frac{1}{3}, \quad t_0 = \frac{4}{9}, \quad t_1 = t_2 = t_3 = t_4 = \frac{1}{9}, \quad t_5 = t_6 = t_7 = t_8 = \frac{1}{36} \quad (\text{A.2})$$

and the density and velocity are then defined:

$$\left. \begin{aligned} \sum_i f_i^{(eq)} &= \rho \\ \sum_i f_i^{(eq)} e_{i\alpha} &= u_\alpha \\ \sum_i f_i^{(eq)} e_{i\alpha} e_{i\beta} &= \Pi_{\alpha\beta}^{(0)} \end{aligned} \right\} \quad (\text{A.3})$$

Using the Chapman-Enskog analysis one can obtain the following dynamics:

$$\left. \begin{aligned} \partial_\alpha u_\alpha &= 0 \\ \partial_\beta (u_\alpha u_\beta) &= -c_s^2 \partial_\alpha \rho + \nu \partial_\beta \partial_\beta u_\alpha \end{aligned} \right\} \quad (\text{A.4})$$

which are the exact steady state incompressible NS equations with constant density  $\rho_0$ . In this model the effective pressure and viscosity are given by:

$$\frac{P}{\rho_0} = c_s^2 \rho, \quad \nu = \frac{\Delta t c_s^2}{2} (2\tau - 1) \quad (\text{A.5})$$

Note the continuity and NS equations are exactly incompressible, while the form of the diffusive term is preserved at the cost of the time derivative. In general EILBGK schemes are not able to achieve the *Re* numbers of the LBGK simulations due to the stricter incompressibility constraints.

\* \* \* \* \*

# Appendix B

## Ericksen-Leslie EL Theory

The EL equations governing uniaxial, constant order parameter dynamics of incompressible isothermal nematics are [46, 40]:

$$\partial_\alpha u_\alpha = 0 \quad (\text{B.1})$$

$$\rho \dot{u}_\alpha = \partial_\beta (-P \delta_{\alpha\beta} + \sigma_{\alpha\beta}^d + \sigma_{\alpha\beta}^{em} + \sigma_{\alpha\beta}^v) \quad (\text{B.2})$$

$$I \ddot{\hat{n}}_\alpha = h_\alpha + h_\alpha^v - \lambda \hat{n}_\alpha \quad (\text{B.3})$$

where symbols are defined as:

$$\sigma_{\alpha\beta}^d = - \left( \frac{\partial F}{\partial (\partial_\alpha \hat{n}_\gamma)} \right) \partial_\beta \hat{n}_\gamma \quad (\text{B.4})$$

$$h_\beta = - \frac{\partial F}{\partial \hat{n}_\beta} + \partial_\alpha \left( \frac{\partial F}{\partial (\partial_\alpha \hat{n}_\beta)} \right) \quad (\text{B.5})$$

$$\begin{aligned} \sigma_{\alpha\beta}^v = & \alpha_1 \hat{n}_\alpha \hat{n}_\beta \hat{n}_\nu \hat{n}_\mu A_{\mu\nu} + \alpha_4 A_{\alpha\beta} + \alpha_5 \hat{n}_\alpha \hat{n}_\mu A_{\mu\beta} + \alpha_6 \hat{n}_\beta \hat{n}_\mu A_{\mu\alpha} \\ & + \alpha_2 \hat{n}_\alpha N_\beta + \alpha_3 \hat{n}_\beta N_\alpha \end{aligned} \quad (\text{B.6})$$

$$h_\alpha^v = -\gamma_2 \hat{n}_\beta A_{\beta\alpha} - \gamma_1 N_\alpha \quad (\text{B.7})$$

$$N_\alpha = \dot{\hat{n}}_\alpha - \varepsilon_{\alpha\beta\gamma} \omega_\beta \hat{n}_\gamma \quad (\text{B.8})$$

$$\gamma_1 = \alpha_3 - \alpha_2 \quad \gamma_2 = \alpha_3 + \alpha_2 = \alpha_6 - \alpha_5 \quad (\text{B.9})$$

$$\sigma_{\alpha\beta}^{EM} = \frac{1}{2} (H_\alpha B_\beta + H_\beta B_\alpha) - \frac{H_\gamma B_\gamma}{2} \delta_{\alpha\beta} + \frac{1}{2} (E_\alpha D_\beta + E_\beta D_\alpha) - \frac{E_\gamma D_\gamma}{2} \delta_{\alpha\beta} \quad (\text{B.10})$$

In the limit of equation 2.8 the  $Q$  tensor governing equations seen in §2.4.1 reduces exactly to those seen above. The form of the director free energy is given in chapter 2.

\*\*\*\*\*

# Appendix C

## Measurement of the Flexoelectric Coefficients.

Comparison of the sign dependence of switching in the ZBD device in chapter 6 showed that the flexoelectric coefficient  $E_{13}$  was positive. Here we show evidence that may determine the magnitude of this coefficient. Figure C.1 is taken from Edwards [168] recent work to measure light transmission levels through a ZBD during switching. The figure shows the voltage ('driver') pulse waveform used and the two

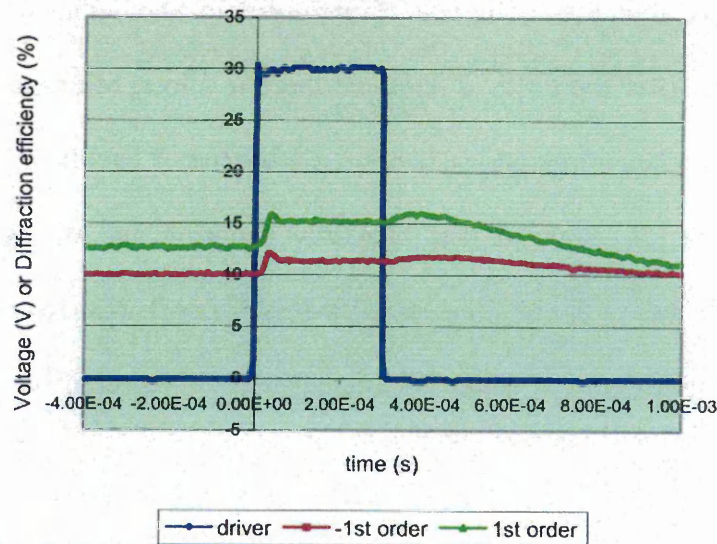


Figure C.1: Figure 7.5a page 118 of [168] showing the diffracted transmission orders during  $\mathcal{D}$  to  $\mathcal{C}$  state switching and the voltage applied to the cell.

$\pm 1^{st}$  order diffracted transmission light levels. A ripple occurs in both orders at around the  $\sim 30\mu\text{s}$  time. Comparing this time to the annihilation time in figure 6.26 we may read of a value for the flexoelectric coefficient, which from figure 6.26 we get  $E_{13} \sim 8 \times 10^{-12} \text{ C m}^{-1}$  (note the simulation and material parameters are not

identical). This is a typical magnitude to those currently reported in the literature and through matching simulation to experimental parameters may improve this measurement.

\* \* \* \* \*

# A many-component lattice Boltzmann equation simulation for transport of deformable particles

BY M. M. DUPIN, T. J. SPENCER, I. HALLIDAY AND C. M. CARE

*Materials Research Institute, Sheffield Hallam University, Howard Street,  
Sheffield S1 1WB, UK (mriih@exchange.shu.ac.uk)*

*Published online 16 July 2004*

We review the analysis of single and  $N$ -component lattice Boltzmann methods for fluid flow simulation. Results are presented for the emergent pressure field of a single phase incompressible liquid flowing over a backward-facing step, at moderate Reynolds Number, which is compared with the experimental data of Denham & Patrick (1974 *Trans. IChE* **52**, 361–367). We then assess the potential of the  $N$ -component method for transport of high volume fraction suspensions of deformable particles in pressure-driven flow. The latter are modelled as incompressible, closely packed liquid drops. We demonstrate the technique by investigating the particles' transverse migration in a uniform shear ('lift'), and profile blunting and chaining.

**Keywords:** lattice Boltzmann;  $N$ -component flow; blunting; pressure-driven flow

## 1. Introduction

The expanding literature on the lattice Boltzmann method (hereafter LBM) may be classified into general model development (use) in simple (complex) geometry, turbulence, thermohydrodynamics and complex,  $N$ -component fluids. Simple geometries are used for quantitative comparisons or qualitative tests of new schemes. Typical of the latter, Hou *et al.* (1995) and Hou (1995) compare LBM and computational fluid dynamics (hereafter CFD) results for lid-driven cavity flow for a range of Reynolds numbers  $10 \leq Re \leq 10^5$ . Other geometries include backward-facing steps and arrays of cylinders (Qian *et al.* 1996; He & Luo 1997*a*; Chen *et al.* 1997), for both creeping and vortex shedding. Several informative reviews can be found (see, for example, Wagner 1994; Higuera & Luo 1989; Mei *et al.* 2000). Relative ease of boundary implementation makes LBM well suited for complex geometries. Typical of this application is work by He & Doolen (1997*a, b*), who also use an irregular lattice and an interpolation system. In porous media, the LBM's application to the problem of the emergence of macroscopic transport coefficients from microscopic dynamics has demonstrated its mesoscale credentials. Darcy's law has been confirmed in LBM schemes by Succi *et al.* (1989), Cali *et al.* (1992) and Ferreol & Rothman (1995). Fundamental LBM development is now a large area of research encompassing boundary models, numerical stability (Reider & Sterling 1995), non-uniform grids (He & Doolen 1997*a, b*; Filippova & Hänel 1998; Tölke *et al.* 1998) and spurious dynamics (Qian & Zhou

One contribution of 12 to a Theme 'Discrete-element modelling: methods and applications in the environmental sciences'.

1998). Several turbulence models are currently available (Martinez *et al.* 1994; Succi *et al.* 1991; Hou *et al.* 1996) and these may be coupled with thermohydrodynamic models (see below). Further afield, LBM models for the Schrödinger equation are under development (Succi 2002; Boghosian & Taylor 1997).

LBMs for fluids with an energy mode were initially developed by Alexander *et al.* (1993), to model monotonic gases. Subsequent improvements (Chen *et al.* 1994) have produced a model which agrees well with analytical results for Couette and Poiseuille flows. However, these thermohydrodynamic LBM models only allow small temperature variations, due to their limited stability arising from the lack of an H-theorem.

Simulating complex fluids is a strength of the LBM. Colloids have been considered with algorithmic generalizations to represent suspended particles (Ladd 1994), and other LBM models include magnetohydrodynamics (Chen *et al.* 1991), bubble growth (Yang *et al.* 2001) and granular flows (Luo *et al.* 1997). Most importantly for this work, two-phase fluids with spontaneous interface formation have been developed to model immiscible fluids (Swift *et al.* 1995; Gunstensen *et al.* 1991; Shan & Chen 1994; Halliday *et al.* 1998; Lishchuk *et al.* 2003), and, for  $N$  immiscible components ( $N \gg 2$ ) by Dupin *et al.* (2003). It is on this area that we shall now concentrate.

Currently, LBM models fluid mixtures using two strategies, broadly termed ‘bottom up’ and ‘top down’. On one hand, top-down strategies are adopted when appropriate behaviour may be postulated for the model: the system considered (often mesoscale) has an interface with a known equilibrium state. Free-energy LBM interface models (Swift *et al.* 1995) capture the kinematics and hydrodynamics of phase separation, for example. On the other hand, bottom-up strategies are adopted where hydrodynamics alone defines a continuum problem (as in the present work), or where, for very complicated systems, an equilibrium state of the interface is not known. In the latter case simpler LBM interface algorithms are equally valid (Do-Quang *et al.* 2000) and desirable from several points of view: computational efficiency (Dupin *et al.* 2003), their ability to embed additional physics directly and their ability to produce a sharp fluid–fluid interface which impacts minimally on the continuum length-scales of the application. A range of techniques has been developed to model such fluid interfaces with, perhaps, the Shan & Chen (1994) approach being the most popular. More details can be found in reviews by Benzi *et al.* (1992) and Chen & Doolen (1998).

In continuum hydrodynamics, the boundary between immiscible fluids should have no structure. However, surface tension in the (*mesoscale*) LBM is activated by methods which are *microscopic* and as a consequence, the emergent LBM interface has artefacts: small but spurious velocities or micro-currents and a finite thickness. It should be noted that another scheme for imposing surface tension by Lishchuk *et al.* (2003) has a greatly reduced micro-current activity. Here we aim to illustrate the potential of the two-dimensional  $N$ -component LBM applied to the transport of high-volume-fraction suspensions of deformable particles in internal pressure-driven flow. We model the latter particles as mutually immiscible, relatively viscous drops of incompressible liquid.

The paper is essentially divided into three further parts. We firstly review the core LBM method (§ 2). Secondly, we present an appropriate generalization, inserting practical immiscibility between a large number of drop species, in § 3. Finally, in § 4, we validate pressure-driven single-component flow with experimental evidence and

proceed to consider  $N$ -component problems such as transverse migration on single, deformable drops in a linear shear and the transport of dense suspensions. For the experienced reader, all new results/analysis are to be found there.

## 2. The Lattice Boltzmann equation for single-component fluids

There are several approaches to the modelling of fluid systems. Microscopic approaches ( $<10^{-9}$  m) include molecular dynamics (MD) and non-equilibrium molecular dynamics (NEMD), mesoscale approaches ( $<10^{-6}$  m) include lattice gas cellular automaton (LGCA) and lattice Boltzmann and macroscopic approaches ( $>10^{-9}$  m) include the broad family of traditional CFD. This section proposes briefly to set the LBM into context and length-scale. For more detail the reader is directed to excellent, comprehensive reviews by Succi (2001), Chen & Doolen (1998) and Luo (2000).

### (a) Practical context of the lattice Boltzmann simulation

At the microscopic scale, MD and NEMD (Goodfellow 1991; Allen & Tildesley 1997) solve numerically the Newtonian equations of motion for a set of explicitly modelled molecules. Both of these techniques show great potential but are impractical for continuum systems: current computer ability limits simulations to only  $\sim 10^5$  molecules, *far* short of continuum scales. To bridge the gap, mesoscale methods like dissipative particle dynamics (DPD), Stokesian and Brownian dynamics and LGCA and LBM have evolved.

DPD simulation (Groot & Warren 1997; Español 2002) was originally developed by Hoogerbrugge & Koelman (1992) to avoid the lattice artefacts of LGCA (§ 2 *e*), while accessing hydrodynamic time- and space-scales. In DPD, point-like ‘particles’ move and interact with each other through prescribed conservative, repulsive, dissipative and stochastic forces whose amplitudes are governed by a fluctuation-dissipation theorem. These particles represent a population of molecules moving coherently. DPD is effectively a coarse graining of MD to a hydrodynamic mesoscale which can accommodate additional microphysics (possibly in the form of potentials) in the interest of multi-phase flows, colloids, and polymers. However, like MD, DPD is computationally expensive. Moreover, problems remain regarding its equation of state, diffusion coefficients and length-scale separations.

The LBM (Chen & Doolen 1998; Succi 2001) uses a discretized Boltzmann equation (§ 2 *g*) with fully discretized space, time and therefore velocity. Distributed groups of particles (hereafter densities) with the same discrete velocity move along links of a lattice and are redistributed at nodes, according to local collision rules. This locality brings decisive advantages to LBM: it is massively parallelizable, complex geometries are made trivial, and additional physics can be included.

In fact the LBM can be used, as in this paper, at continuum scales. However, by far the most popular single-component continuum-scale method remains CFD (Anderson 1995; Conner & Brebbia 1976).

### (b) Hydrodynamics of the lattice Boltzmann method

We shall see that the macroscopic dynamics describing a standard LBM is a weakly compressible form of the Navier–Stokes (Landau & Lifshitz 1995) and continuity

equations

$$\partial_t(\rho) + \partial_\beta(\rho u_\beta) = 0, \quad (2.1)$$

$$\partial_t(\rho u_\alpha) + \partial_\beta(\rho u_\alpha u_\beta) = -\partial_\alpha P + \partial_\beta(2\nu\rho S_{\alpha\beta}) + \rho a_\alpha, \quad (2.2)$$

where  $a_\alpha$  is a uniform acceleration acting on the lattice fluid,  $\nu$  its kinematic viscosity,  $P$  the lattice fluid pressure,  $\rho$  the lattice fluid's density,  $S_{\alpha\beta} = \frac{1}{2}(\partial_\beta u_\alpha + \partial_\alpha u_\beta)$  the rate of strain tensor and  $\mathbf{u}$  the lattice fluid's velocity (see equation (2.20) for the definition of  $\rho$  and  $\mathbf{u}$ ). The LBM has an ideal gas equation of state,

$$P = c_s^2 \rho, \quad (2.3)$$

where  $c_s^2$  is the speed of sound squared. Equations (2.1) and 2.2 have solutions parametrized by a single dimensionless number, based on a characteristic lattice velocity  $U_0$ , lattice dimension  $L_0$  and the LBM's kinematic viscosity  $\nu$ : the lattice Reynolds number

$$Re = \frac{U_0 L_0}{\nu}, \quad (2.4)$$

which quantity may be directly compared with the Reynolds number of the flow under study. Note that, for LBM, the speed of sound  $c_s$  is only  $O(1)$ , which induces some problems for high- $Re$  applications of the standard LBM.

### (c) Theoretical foundations of the lattice Boltzmann method

The earliest example of LBM (*ca.* 1988) was essentially an attempt to address statistical noise inherent in LGCA (Succi 2001). Subsequently, the essential theoretical basis of the LBM has been shown to derive from non-equilibrium statistical mechanics (Succi 2001, 2002) so its theoretical analysis has two distinct routes. One, heuristic, follows LBM's advent from LGCA's, the other a formal discretization of the exact Boltzmann transport equation (He & Luo 1997*b*; Abe 1966). We detail the former here.

Boltzmann made stringent assumptions (Liboff *et al.* 2003) to close the description of dilute systems obtained from kinetic theory. For dilute systems the macroscopic observables of interest only depend on one- or two-body distributions, so the  $6N$  variables were reduced to just  $M = 1, 2$ . The Boltzmann equation

$$\partial_t f + \mathbf{v} \cdot \partial_{\mathbf{x}} f + \mathbf{a} \cdot \partial_{\mathbf{v}} f = C_2\{f_2\} \quad (2.5)$$

then follows, where  $f = f_1(\mathbf{x}, \mathbf{v}, t)$  is the one-body distribution representing the probability density of finding a particle at position  $\mathbf{x}$ , with particle velocity  $\mathbf{v}$  at time  $t$ .  $f_2$  is a two-body distribution (see below) and  $C_2$  is the two-body-collision operator. It should be noted that, for dense systems, the validity of this reduction is less clear and, at the time of writing, there are attempts to formulate lattice BBGKY equations (after Bogolyubov, Born, Green, Kirkwood and Yvon), which may be better adapted to the simulation of denser fluids. The left-hand side of equation (2.5) represents the free steaming of particles in phase space; the collision operator,  $C_2\{f_2\}$ , henceforth denoted  $C(f, f)$ , on the right, represents the effects of collisions. In the dilute-gas limit (where binary collisions alone are significant) the gas is considered to be subjected to molecular chaos (molecules entering a binary collision have uncorrelated motion):

$$f_2(\mathbf{x}_1, \mathbf{v}_1, \mathbf{x}_2, \mathbf{v}_2, t) = f(\mathbf{x}_1, \mathbf{v}_1, t)f(\mathbf{x}_2, \mathbf{v}_2, t). \quad (2.6)$$

This allowed Boltzmann to write down an integral expression for the  $C_2\{f_2\}$  (Liboff *et al.* 2003). In fact He & Luo (1997a) have shown that one particular LBE algorithm may be obtained by a systematic discretization of equation (2.5).

(d) *Solving the Boltzmann equation: Chapman–Enskog analysis*

The Chapman–Enskog procedure is used to solve the Boltzmann equation (2.5) by means of recursive perturbation techniques (Chapman & Cowling 1970). A variant of this method might be better known as ‘successive approximation’, ‘multi-scale expansion’ or ‘Hilbert expansion’. It is used to obtain the behaviour of hydrodynamic modes in the LBM, although crucially, it may miss other, kinetic, modes. The expansion is parametrized by a small dimensionless Knudsen number,  $Kn$ , introduced into the collision term of the Boltzmann equation (2.5) without the forcing term (Liboff *et al.* 2003):

$$\partial_t f + v_\alpha \partial_\alpha f = \frac{1}{\varepsilon} C(f, f), \quad \varepsilon \equiv Kn = \frac{l}{L}. \tag{2.7}$$

The distribution function  $f(\mathbf{x}, \mathbf{v}, t)$  and time derivative are then expanded in terms of  $\varepsilon$  as

$$f = \sum_{n=0}^{\infty} \varepsilon^n f^{(n)}, \quad \partial_t = \sum_{n=0}^{\infty} \varepsilon^n \partial_{t_n}, \tag{2.8}$$

with the constraints that ‘moments’ of the equilibrium distribution  $f^{(0)}$ ,

$$f^{(0)} = f^{(eq)} = \frac{\rho}{(2\pi RT)^{D/2}} \exp\left\{-\frac{(\mathbf{v} - \mathbf{u})^2}{2RT}\right\}, \tag{2.9}$$

alone determine the hydrodynamic quantities

$$\left. \begin{aligned} \int f^{(0)} \begin{bmatrix} 1 \\ \mathbf{v} \\ \frac{1}{2}(\mathbf{v} - \mathbf{u})^2 \end{bmatrix} d\mathbf{v} &= \rho \begin{bmatrix} 1 \\ \mathbf{u} \\ e \end{bmatrix} \\ \int \varepsilon^{(n)} f^{(n)} \begin{bmatrix} 1 \\ \mathbf{v} \\ \frac{1}{2}(\mathbf{v} - \mathbf{u})^2 \end{bmatrix} d\mathbf{v} &= 0, \quad n > 0, \end{aligned} \right\} \tag{2.10}$$

where  $e$  is the energy and  $\mathbf{u}$  is the macroscopic fluid velocity. Importantly, higher-order non-equilibrium parts ( $f^{(n)}$ ,  $n > 0$ ) do not contribute to the hydrodynamic observable. Note, the space/time variation of  $f^{(0)}$  is purely implicit, through, for example,  $f^{(0)} = f^{(0)}(\rho, \mathbf{u}, T)$ . The collision term is also expanded in terms of  $\varepsilon$ ,

$$C(f, f) = \sum_{n=0}^{\infty} \varepsilon^n C^{(n)}, \quad C^{(n)} = \sum_{k+l=n} C(f^{(k)}, f^{(l)}), \tag{2.11}$$

and solutions to the Boltzmann equation may now be obtained by equating powers of  $\varepsilon$  in the expanded equation, obtained from equations (2.7)–(2.11), then solving each order of this recursion hierarchically:

$$\left. \begin{aligned} O(\varepsilon^{-1}) : C(f^{(0)}, f^{(0)}) &= 0, \\ O(\varepsilon^0) : \partial_t f^{(0)} + v_\alpha \partial_\alpha f^{(0)} &= 2C(f^{(0)}, f^{(1)}) \\ &\vdots \end{aligned} \right\} \tag{2.12}$$

By solving to  $O(\varepsilon^{-1})$ , the equilibrium distribution  $f^{(0)}$  is found to be the Maxwell–Boltzmann distribution (Chapman & Cowling 1970). Given this, the  $O(\varepsilon^0)$  equation can, in principle, yield  $f^{(1)}$ , and so on through increasing orders of  $\varepsilon$ .

Hydrodynamic equations are extracted by evaluating moments of the Boltzmann equation with normal solutions (Liboff *et al.* 2003):

$$\int (\partial_t f + v_\alpha \partial_\alpha f - C(f, f)) d\mathbf{v} \begin{bmatrix} 1 \\ \mathbf{v} \\ \frac{1}{2}(\mathbf{v} - \mathbf{u}) \end{bmatrix} = 0. \quad (2.13)$$

The above equations will give the Euler equation (Landau & Lifshitz 1995) for  $f = f^{(0)}$  and the Navier–Stokes equations (2.2) for  $f = f^{(0)} + f^{(1)}$  (Liboff *et al.* 2003).

The Chapman–Enskog procedure is, unsurprisingly, key to extracting the hydrodynamic equations of the LBM and will be used in detail in §2*h*. An important approximation of the Bhatnagar–Gross–Krook (BGK) collision operator (Bhatnagar *et al.* 1954) greatly simplifies solution. The BGK Boltzmann equation is

$$\partial_t f + v_\alpha \partial_\alpha f = -\frac{1}{\tau}(f - f^{(0)}), \quad (2.14)$$

and now the first-order solution  $f^{(1)}$  is easily obtained, from equation (2.12), as

$$f^{(1)} = -\tau(\partial_t f^{(0)} + v_\alpha \partial_\alpha f^{(0)}). \quad (2.15)$$

#### (e) Lattice gas cellular automata

It is instructive to look at the construction of lattice gas cellular automata (LGCA) models, as these are parents to the LBM and operate in a similar vein.

Cellular automata (CA) (von Neumann 1966) and MD for gases (Broadwell 1964) were merged to give rise to the first LGCA. Mono-energetic molecules are confined to move/interact on a lattice and updated by CA rules. Space, velocity and time are all discretized. The first LGCA model (the HPP model) with deterministic rules that reproduce fluid dynamic-like features was introduced by Hardy, de Pazzis and Pomeau (Hardy *et al.* 1973, 1976). This was superseded by the FHP model (proposed by Frisch, Hasslacher and Pomeau (Frisch *et al.* 1986; Wolfram 1986)), which was the first LGCA model shown to map onto the Navier–Stokes equations (2.2). It has discrete velocity and position space and discrete collision rules (Frisch *et al.* 1986), represented in essence in figure 1, which shows two sequential lattice states.

Notwithstanding, evolution of the LGCA models is very simple and consists of two main repeated steps: collision and streaming (see figure 1), the time-order of which is irrelevant. Collisions are very simple but must conserve particle number, momenta and energy (only). Evolution is represented by a lattice-species Boltzmann equation

$$n_i(\mathbf{x} + \mathbf{c}_i, t + 1) - n_i(\mathbf{x}, t) = C_i(n_1, n_2, \dots), \quad (2.16)$$

where  $n_i(\mathbf{x}, t)$  is the number  $\in \{0, 1\}$  of particles with particle velocity  $\mathbf{c}_i$ ,  $n_i \in \{0, 1\}$ ; the subscripts  $i$  and  $j$  denote discrete velocities  $i, j \in \{1, 2, \dots, b\}$ ,  $b$  is the size of the lattice velocity basis and  $\mathbf{c}_i$  is a ‘Boolean’ function of the  $n_i$  values which expresses the possible collisions.

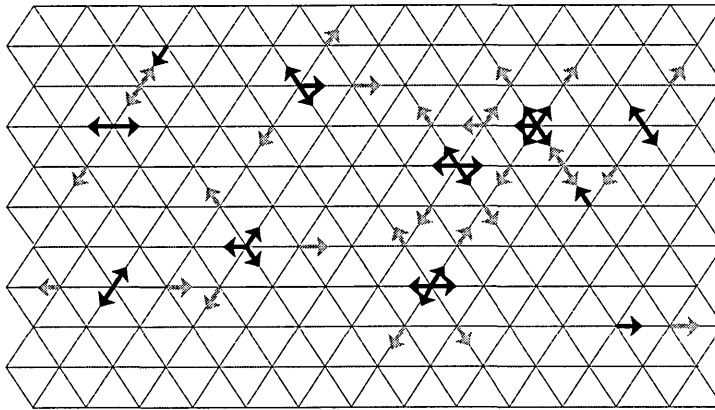


Figure 1. Lattice structure and evolution of the FHP-I LGA model. Solid (hollow) arrows represent particles with the velocities corresponding to time  $t$  ( $t+$ ). Hollow arrows therefore represent post collision, post propagation evolution.

The LGCA may be viewed as a maximally discretized MD model. Variants with increased stability on more complicated lattices have been developed: essentially, all give the same general hydrodynamic equations but with different values for, e.g., the speed of sound squared  $c_s^2$  and lattice fluid viscosities  $\nu$  and  $\eta$ . The key advantages of LGCA are their unconditional stability, optimal use of computer memory, and localization, allowing for massive parallelization and dedicated computers. In fact it has been shown that isothermal LGCA models admit both a local and global H-theorem (Frisch *et al.* 1986), confirming the unconditional stability—a decisive advantage in the computation of turbulence. Further information on LGCA and its applications may be found in Succi (2001), Wolfram (1986), He *et al.* (1997a), McNamara & Zanetti (1988), D’Humières *et al.* (1989), Rothmann & Zaleski (1994) and Benzi *et al.* (1992).

LGCA simulation has now been largely superseded by the LBM, for the above advantages are accompanied by a number of limitations. Certainly, early models were limited to relatively low Reynolds numbers (see equation (2.4)) due to high momentum diffusivity (viscosity  $\nu$ ) and the LGCA’s lack of Galilean invariance.

#### (f) Lattice Boltzmann models

McNamara & Zanetti (1988) realized that equation (2.16) can be re-expressed as a Boltzmann equation for LGCA ensemble averages. Defining

$$f_i(\mathbf{x}, t) \equiv \langle n_i(\mathbf{x}, t) \rangle, \quad 0 \leq f_i \leq 1, \quad i = 1, \dots, b, \quad (2.17)$$

where  $f_i(\mathbf{x}, t)$  are real continuous functions representing the probability distribution of finding particles with discrete velocities and space. Their evolution may be expressed after equation (2.16) as

$$f_i(\mathbf{x} + \mathbf{c}_i, t + 1) - f_i(\mathbf{x}, t) = \Delta_i(f_0, f_1, f_2, \dots), \quad (2.18)$$

the collision term  $\Delta_i(f_i)$  being essentially the  $C_i$  of the LGCA but with the ensemble averages  $f_i$  replacing the  $n_i$  (Frisch *et al.* 1986). In fact, there are several variants of the lattice Boltzmann method (e.g. Succi 2002); we shall focus on the simplest.

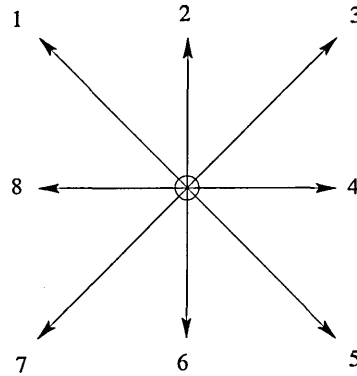


Figure 2. The D2Q9 model lattice structure showing a regular repeating structure with nine distributions located at each lattice node.

(g) *Lattice BGK (LBGK) models*

It was Qian *et al.* (1992) and Chen *et al.* (1992) who realized that  $\Delta_i$  in (2.17) could be further simplified by assuming a single relaxation time  $\tau$ :

$$f_i(\mathbf{x} + \delta \mathbf{c}_i, t + \delta) = f_i(\mathbf{x}, t) - \frac{1}{\tau}(f_i(\mathbf{x}, t) - f_i^{(\text{eq})}) + F_i, \quad 0 \leq \frac{1}{\tau} \leq 2, \quad (2.19)$$

in which we have added a ‘forcing term’,  $F_i$ , to which we shall return, taking  $F_i = 0$  for the moment. Note that equation (2.19) has a relaxation form.

Equation (2.19) and its appropriate equilibrium distribution function (see below) together comprise the so-called LBGK model. Setting  $\tau = 1$  in equation (2.19), the momentum densities,  $f_i$ , relax immediately to local equilibrium  $f_i^{(\text{eq})}$ , on the scale of the propagation length  $\delta c_{i\alpha}$ , which is determined by the time-of-flight parameter  $\delta$ . With  $c_{i\alpha} = O(1)$  it is natural to associate the duration  $\delta$  with the mean free path, or Knudsen number. In other words, we take  $\delta = \varepsilon$  (see equation (2.7)) for the purposes of extracting the model’s dynamics.

When LBM is used for two-dimensional fluid dynamics simulations, the LBGK model is the one most commonly used and, in particular, the one with nine velocities in two dimensions (D2Q9). Section 2*h* details an analysis for extracting its hydrodynamics. The shortcomings of the LBGK models include spurious invariant quantities when  $1/\tau$  reaches its limits, and round-off errors which can cause instability, due to floating point algebra. At present no local or global H-theorem for LBM models has been found (Succi 2002). However, it is anticipated that this will change in the near future. This will allow the stability boundaries for these methods to be determined.

(h) *Hydrodynamics of the LBGK method*

Our method of manipulating the macroscopic dynamics differs from that of others (e.g. Hou *et al.* 1995) in that, for adaptability, it treats the role of the lattice in a general way. However, we focus on the slow, hydrodynamic modes in the usual way, by using a Chapman–Enskog analysis to develop the LBGK evolution equation, (2.19). The requirements on  $f_i^{(n>0)}$  are as discussed previously, but we have an additional

requirement that the second moment of  $f_i^{(1)}$  relates directly to the viscous stress  $\Pi_{\alpha\beta}^{(1)}(x_\alpha, t)$ :

$$\left. \begin{aligned} \sum_i f_i^{(\text{eq})} \begin{bmatrix} 1 \\ c_{i\alpha} \\ c_{i\alpha}c_{i\beta} \end{bmatrix} &= \begin{bmatrix} \rho(x, t) \\ \rho u_\alpha(x, t) \\ \Pi_{\alpha\beta}^{(0)}(x, t) \end{bmatrix}, \\ \sum_i f_i^{(n)} \begin{bmatrix} 1 \\ c_{i\alpha} \\ c_{i\alpha}c_{i\beta} \end{bmatrix} &= \begin{bmatrix} 0 \\ 0 \\ \Pi_{\alpha\beta}^{(n)}(x, t) \end{bmatrix}, \quad n > 0. \end{aligned} \right\} \quad (2.20)$$

In fact LBGK equilibrium  $f_i^{(\text{eq})}$  approximates a uniformly translating Maxwell-Boltzmann distribution in the peculiar velocity  $(c_{i\alpha} - u_\alpha)$ :

$$\left. \begin{aligned} f_i^{(\text{eq})} &= \frac{\rho}{(2\pi RT)^{D/2}} \exp\left\{-\frac{(c_{i\alpha} - u_\alpha)^2}{2RT}\right\} = \rho t_i \exp\left\{\frac{u_\alpha c_{i\alpha}}{RT}\right\} \exp\left\{-\frac{u^2}{2RT}\right\}, \\ t_i &\equiv \exp\left\{\frac{c_{i\alpha}c_{i\alpha}}{RT}\right\} \frac{1}{(2\pi RT)^{D/2}}, \end{aligned} \right\} \quad (2.21)$$

by making a Taylor expansion to  $O(u^2)$  in equation (2.21):

$$f_i^{(\text{eq})} = \rho t_i \left( 1 + \frac{c_{i\alpha}u_\alpha}{RT} + \frac{c_{i\alpha}c_{i\beta}u_\alpha u_\beta}{2(RT)^2} - \frac{u^2}{2RT} \right).$$

For isothermal flows  $R$  and  $T$  are constant and we therefore may simplify  $f_i^{(\text{eq})}$ :

$$f_i^{(\text{eq})} = t_i(A + Bc_{i\alpha}u_\alpha + Cc_{i\alpha}c_{i\beta}u_\alpha u_\beta + Du^2), \quad (2.22)$$

in which  $t_i$ ,  $A$ ,  $B$ ,  $C$  and  $D$  are taken as constants yet to be determined (not all of which are independent). This form of the equilibrium distribution is less general than that of Hou *et al.* (1995), because it is predicated, from the outset, on a uniformly translating Maxwell-Boltzmann. However, any attempt to depart significantly from that form (i.e. that of equation (2.22)) quickly leads to instabilities. In the limit of small  $Re$ , an increased freedom of choice around the coefficients in equation (2.22) is a means of embedding different physical effects. Our discrete velocity set  $c_i$  is that of the most popular in the literature, classified D2Q9 (two dimensions and nine discrete velocities; see figure 2). Here we derive parameters for D2Q9, though it is trivial to adapt this derivation to fit any of the models listed at the end of this section.

To close the equilibrium distribution  $f_i^{(\text{eq})}$  of our D2Q9 model (and effectively determine the whole of the model's dynamics) we Taylor expand the left-hand side of the LBGK evolution equation (2.19) to second order in  $\delta = \varepsilon$  as

$$\varepsilon[\partial_t + c_{i\alpha}\partial_\alpha]f_i + \frac{1}{2}\varepsilon^2[\partial_t + c_{i\alpha}\partial_\alpha]^2f_i + O(\varepsilon^3) = -\frac{1}{\tau}(f_i - f_i^{(\text{eq})}). \quad (2.23)$$

The terms of  $O(\varepsilon)$  already correspond to the Boltzmann transport equation (2.14). We now substitute the Knudsen number  $\varepsilon$ -expansions of equations (2.8) (for  $f_i$  about equilibrium  $f_i^{(\text{eq})}$  and for the time derivative  $\partial_t$  about  $\partial_{t_0}$ ) into equation (2.23) and retain terms to  $O(\varepsilon^2)$ . Separating orders of  $\varepsilon$ , we have, at  $O(\varepsilon)$ ,

$$(\partial_{t_0} + c_{i\alpha}\partial_\alpha)f_i^{(0)} = -\frac{1}{\tau}f_i^{(1)}, \quad (2.24)$$

and, at  $O(\varepsilon^2)$ , using the result at  $O(\varepsilon)$  in equation (2.24),

$$\partial_{t_1} f_i^{(0)} + (\partial_{t_0} + c_{i\alpha} \partial_\alpha) \left( 1 - \frac{1}{2\tau} \right) f_i^{(1)} = -\frac{1}{\tau} f_i^{(2)}. \quad (2.25)$$

We proceed to tune the discrete moments of equations (2.24) and (2.25) onto hydrodynamic behaviour. Summing equation (2.20) on link index  $i$ :

$$\partial_{t_0} \sum_i f_i^{(0)} + \partial_\alpha \sum_i c_{i\alpha} f_i^{(0)} = -\frac{1}{\tau} \sum_i f_i^{(1)},$$

from which it is evident that the model's macroscopic dynamics are described by the continuity equation on its shortest time scales  $t_0$ :

$$\partial_{t_0} \rho + \partial_\alpha \rho u_\alpha = 0. \quad (2.26)$$

The first moment of equation (2.24) is obtained by multiplying it by  $c_{i\alpha}$  prior to summing on  $i$ :

$$\partial_{t_0} \sum_i c_{i\alpha} f_i^{(0)} + \partial_\beta \sum_i c_{i\alpha} c_{i\beta} f_i^{(0)} = -\frac{1}{\tau} \sum_i c_{i\alpha} f_i^{(1)}.$$

Hence, we obtain an Euler equation for the momentum,

$$\partial_{t_0} \rho u_\alpha + \partial_\beta \Pi_{\alpha\beta}^{(0)} = 0, \quad (2.27)$$

where  $\Pi_{\alpha\beta}^{(0)}$  is that defined in equation (2.20). To extract the longer-time dissipative modes it is necessary to proceed to longer times. Take moments in the  $O(\varepsilon^2)$  equation (2.25) and use the identities given by equation (2.20). The zeroth moment immediately yields

$$\partial_{t_1} \rho = 0, \quad (2.28)$$

and, using equations (2.20), its first moment (with  $c_{i\alpha}$ ) yields

$$\left( 1 - \frac{1}{2\tau} \right) \partial_\beta \Pi_{\alpha\beta}^{(1)} + \partial_{t_1} \rho u_\alpha = 0. \quad (2.29)$$

The Chapman–Enskog expansions need to be recombined, in the case of equations (2.27), (2.29) to give the Navier–Stokes equation. To obtain the desired result from this the process we clearly need to control the form  $\Pi_{\alpha\beta}^{(0)}$  and  $\Pi_{\alpha\beta}^{(1)}$ . This is best achieved by expressing the latter directly in terms of the parameters  $t_i$ ,  $A$ ,  $B$ ,  $C$  and  $D$  of  $f_i^{(\text{eq})}$ , resulting in expressions which contain ‘tensors’ such as  $\sum_i t_i c_{i\alpha} c_{i\beta}$ , for it is possible to show that  $\Pi_{\alpha\beta}^{(0)}$  and  $\Pi_{\alpha\beta}^{(1)}$  take appropriate form when such tensors are isotropic.

After Wolfram (1986) and C. M. Care (2003, personal communication), we seek

- (i) a set of isotropic tensors  $E^n$  with order  $O(n)$  of the discrete velocity basis ( $c_{i\alpha}$ , figure 2),
- (ii) the appropriate weight of link  $i$ ,  $t_i$ .

The latter tensors appear in the expressions for  $\Pi_{\alpha\beta}^{(0)}$  and  $\Pi_{\alpha\beta}^{(1)}$ . We define and evaluate the following tensors:

$$\left. \begin{aligned} E^{(0)} &\equiv \sum_i t_i = t_0 + 4t_1 + 4t_2, \\ E_{\alpha}^{(1)} &\equiv \sum_i t_i c_{i\alpha} = 0, \\ E_{\alpha\beta}^{(2)} &\equiv \sum_i t_i c_{i\alpha} c_{i\beta} = (2t_1 + 4t_2)\delta_{\alpha\beta}, \\ E_{\alpha\beta\gamma}^{(3)} &\equiv \sum_i t_i c_{i\alpha} c_{i\beta} c_{i\gamma} = 0, \\ E_{\alpha\beta\gamma\delta}^{(4)} &\equiv \sum_i t_i c_{i\alpha} c_{i\beta} c_{i\gamma} c_{i\delta} = (2t_1 - 8t_2)\delta_{\alpha\beta\gamma\delta} + 4t_2(\delta_{\alpha\beta}\delta_{\gamma\delta} + \delta_{\alpha\gamma}\delta_{\beta\delta} + \delta_{\alpha\delta}\delta_{\beta\gamma}), \end{aligned} \right\} \quad (2.30)$$

as may be checked by direct computation, using the D2Q9 basis. Note that odd-order tensors  $E^{(2n+1)}$  are zero. Only fourth-order tensors are necessary for hydrodynamics. Wolfram shows that the  $E_{\alpha\dots}^n$  will be isotropic if

$$E_{\alpha\dots}^{2n+1} = 0, \quad E_{\alpha\dots}^{2n} = T^{2n} \Delta_{\alpha\dots}^{2n}, \quad (2.31)$$

where tensor  $\Delta_{\alpha\dots}^{2n}$  is defined as (Wolfram 1986)

$$\Delta^0 = 1, \quad \Delta_{\alpha\beta}^2 = \delta_{\alpha\beta}, \quad \Delta_{\alpha\beta\gamma\theta}^4 = \delta_{\alpha\beta}\delta_{\gamma\theta} + \delta_{\alpha\gamma}\delta_{\beta\theta} + \delta_{\alpha\theta}\delta_{\beta\gamma}. \quad (2.32)$$

Comparing equations (2.32) and definitions (2.30), we obtain

$$T^0 = t_0 + 4t_1 + 4t_2, \quad T^2 = 2t_1 + 4t_2, \quad T^4 = 4t_2, \quad t_2 = \frac{1}{4}t_1. \quad (2.33)$$

With equations (2.33), we return to the task of manipulating the emerging macroscopic equations into an appropriate form. We evaluate the requisite moments of the equilibrium distribution (equation (2.20)) by inserting the form of  $f_i^{(eq)}$  (2.22) and using equations (2.33). For example, the moment  $\sum_i f_i^{(0)} = \rho$  gives

$$-\rho + A \sum_i t_i + Bu_{\alpha} \sum_i t_i c_{i\alpha} + Cu_{\alpha}u_{\beta} \sum_i t_i c_{i\alpha} c_{i\beta} + Du_{\alpha}u_{\alpha} \sum_i t_i = 0, \quad (2.34)$$

which, on substituting for the tensors from equation (2.22), yields

$$-\rho + AT^0 + Cu^2T^2 + Du^2T^0 = 0 \quad (2.35)$$

after a little algebra. Similarly, the first moment

$$\sum_i f_i^{(0)} c_{i\gamma} = \rho u_{\gamma}$$

and the ‘momentum flux’ moment

$$\sum_i f_i^{(0)} c_{i\gamma} c_{i\theta} = P\delta_{\gamma\theta} + \rho u_{\gamma}u_{\theta},$$

give, respectively,

$$\left. \begin{aligned} -\rho u_{\gamma} + Bu_{\gamma}T^2 &= 0, \\ -P\delta_{\gamma\theta} - \rho u_{\gamma}u_{\theta} + AT^2\delta_{\gamma\theta} + T^4Cu^2\delta_{\gamma\theta} + 2T^4Cu_{\gamma}u_{\theta} + Du^2T^2\delta_{\gamma\theta} &= 0. \end{aligned} \right\} \quad (2.36)$$

Noting that the equations (2.34)–(2.36) must be true for all  $\rho, u_\alpha$ , we obtain the following six equations:

$$\left. \begin{aligned} -\rho + AT^0 &= 0, & CT^2 + DT^0 &= 0, & -\rho + BT^2 &= 0, \\ -P + AT^2 &= 0, & 2CT^4 - \rho &= 0, & CT^4 + DT^2 &= 0, \end{aligned} \right\} \quad (2.37)$$

and, recalling that  $A = \rho$ , we have a closed system of simultaneous equations with a non-trivial solution:

$$\left. \begin{aligned} A &= \rho, & T^0 &= 1, & t_0 &= \frac{4}{9}, \\ B &= 3\rho, & T^2 &= \frac{1}{3}, & t_1 &= \frac{1}{9}, \\ C &= \frac{9}{2}\rho, & T^4 &= \frac{1}{9}, & t_2 &= \frac{1}{36}, \\ D &= -\frac{3}{2}\rho, & P &= \frac{1}{3}\rho. \end{aligned} \right\} \quad (2.38)$$

We may identify the  $\frac{1}{3}$  in the equation of state as the speed of sound squared ( $c_s^2$ ), in terms of which the equilibrium is often written

$$f_i^{(eq)} = \rho t_i \left( 1 + \frac{c_{i\alpha} u_\alpha}{c_s^2} + \frac{c_{i\alpha} c_{i\beta} u_\alpha u_\beta}{2c_s^4} - \frac{u^2}{2c_s^2} \right). \quad (2.39)$$

Finally, we demonstrate an appropriate form for ‘viscous stress’ moment  $\Pi_{\alpha\beta}^{(1)}$ . We need an expression for  $f_i^{(1)}$ , obtained by rearranging equation (2.24) as

$$\left. \begin{aligned} \Pi_{\gamma\theta}^{(1)} &= \sum_i c_{i\gamma} c_{i\theta} f_i^{(1)} \\ &= -\tau \sum_i c_{i\gamma} c_{i\theta} (\partial_{t_0} + c_{i\lambda} \partial_\lambda) f_i^{(eq)} \\ &= -\tau [-c_s^2 u_\gamma \partial_\theta \rho - c_s^2 u_\theta \partial_\gamma \rho - \partial_\lambda \rho u_\gamma u_\theta u_\lambda + \partial_\lambda \rho u_\gamma c_s^2 \delta_{\lambda\theta} + \partial_\lambda \rho u_\theta c_s^2 \delta_{\gamma\lambda}], \end{aligned} \right\} \quad (2.40)$$

where identity  $[\partial_{t_0} \rho u_\gamma u_\theta = -c_s^2 u_\gamma \partial_\theta \rho - c_s^2 u_\theta \partial_\gamma \rho - \partial_\lambda \rho u_\gamma u_\theta u_\lambda]$  and the continuity equation have been used.

We recombine the four Chapman–Enskog moment expansions. First the  $O(\varepsilon^1)$  and  $O(\varepsilon^2)$  continuity equations (2.26), (2.28):

$$(\varepsilon \partial_{t_0} + \varepsilon^2 \partial_{t_1}) \rho + \varepsilon \partial_\alpha \rho u_\alpha = 0 \quad \Rightarrow \quad \partial_i \rho + \partial_\alpha \rho u_\alpha = 0. \quad (2.41)$$

Combining the ‘ $c_{i\alpha}$  moment’  $O(\varepsilon^1)$  and  $O(\varepsilon^2)$  (equations (2.27) and (2.29)) gives

$$\partial_i \rho u_\alpha + \partial_\beta \rho u_\alpha u_\beta = -\partial_\alpha c_s^2 \rho + \varepsilon \frac{1}{2} c_s^2 (2\tau - 1) \partial_\beta 2\rho S_{\alpha\beta} - (\tau - \frac{1}{2}) \partial_\beta \partial_\gamma \rho u_\alpha u_\beta u_\gamma,$$

where  $S_{\alpha\beta} = \frac{1}{2}(\partial_\alpha u_\beta + \partial_\beta u_\alpha)$  is the rate of strain. Defining the viscosity as

$$\nu \equiv \frac{1}{2} \varepsilon c_s^2 (2\tau - 1), \quad (2.42)$$

we note an ideal-gas equation of state, with  $c_s^2$  only of the order of 1. Retaining terms to  $O(u^2)$ ,

$$\partial_i \rho u_\alpha + \partial_\beta \rho u_\alpha u_\beta = -\partial_\alpha P + \partial_\beta (2\nu \rho S_{\alpha\beta}). \quad (2.43)$$

Equations (2.41) and (2.43) are a weakly compressible form of the Navier–Stokes and continuity equations. The procedure by which they have been derived may be applied

Table 1. LBGK lattice parameters for a selection of commonly used models indicating the lattice shape, velocity directions and equilibrium distribution weights

model	unit cell	$t_0$ 0	$t_1$ 1	$t_2$ $\sqrt{2}$	$t_3$ $\sqrt{3}$	$t_4$ 2	$c_s^2$ $c_s^2$	order of isotropy
D1Q3	line	$\frac{2}{3}$	$\frac{1}{6}$	0	0	0	$\frac{1}{3}$	4
D1Q5	line	$\frac{1}{2}$	$\frac{1}{6}$	0	0	$\frac{1}{12}$	1	6
D2Q7	hexagonal	$\frac{1}{2}$	$\frac{1}{12}$	0	0	0	$\frac{1}{4}$	4
D2Q9	square	$\frac{4}{9}$	$\frac{1}{9}$	$\frac{1}{36}$	0	0	$\frac{1}{3}$	4
D2Q13	hexagonal	$\frac{11}{25}$	$\frac{9}{100}$	0	$\frac{1}{300}$	0	$\frac{3}{10}$	6
D3Q15	cubic	$\frac{2}{9}$	$\frac{1}{9}$	0	$\frac{1}{72}$	0	$\frac{1}{3}$	4
D3Q19	cubic	$\frac{1}{3}$	$\frac{1}{18}$	$\frac{1}{36}$	0	0	$\frac{1}{3}$	4
D3Q27	cubic	$\frac{8}{27}$	$\frac{2}{27}$	$\frac{1}{54}$	$\frac{1}{216}$	0	$\frac{1}{3}$	4
D4Q25	FCHC	$\frac{1}{3}$	0	$\frac{1}{36}$	0	0	0	4

to the other lattices summarized in terms of their velocity basis and corresponding weights (table 1). It differs from other derivations (Hou *et al.* 1996) simply in that the isotropy of lattice basis tensors is programmed-in explicitly, which is a procedural advantage when inserting additional microphysics. In considering table 1, it should be noted that the analysis of three speed models produces a sufficient number of constraints to solve the coefficients of the equilibrium distribution. However, our method is not the only path to the LBGK equilibrium. He & Luo (1997*b*) give an *a priori* derivation applicable to any lattice structure. Luo integrates the Boltzmann transport equation, via the method of characteristics, to derive the LBGK evolution equation. A Taylor expanded Maxwell–Boltzmann equilibrium distribution has its weights ( $t_i$ ) and lattice calculated by a numerical integration, the number of velocities reflecting the order and choice of the polynomial used in the quadrature. Following this route leads to a number of enhanced models with flexible lattice structures (Luo 1998; Mei *et al.* 2000; He *et al.* 1997*a*), and it allows one to add physics directly from kinetic theory and the Boltzmann equation.

#### (i) Boundaries in lattice models

The Navier–Stokes equation is an elliptic equation: it requires the boundary velocity field to be closed to have any solution. This velocity information can be set in equivalent terms, especially at open boundaries, using, for example, pressure and flux conditions. One problem with LBM lattice closure is that the velocity distribution gives  $D$  conditions which are not necessarily sufficient to determine appropriate values for all the  $f_i$  at a boundary.

Consider first the no-slip zero velocity boundary condition. The velocity of the fluid matches that assumed for the boundary, often zero. Wolfram (1986) showed the simplest operation to reproduce a zero in velocity is the bounce-back condition.  $f_i$  which stream onto a wall site have their velocities inverted for the next streaming step. This robust process clearly inserts friction into the fluid and conserves mass but it is only first-order accurate (Kadanoff *et al.* 1989).

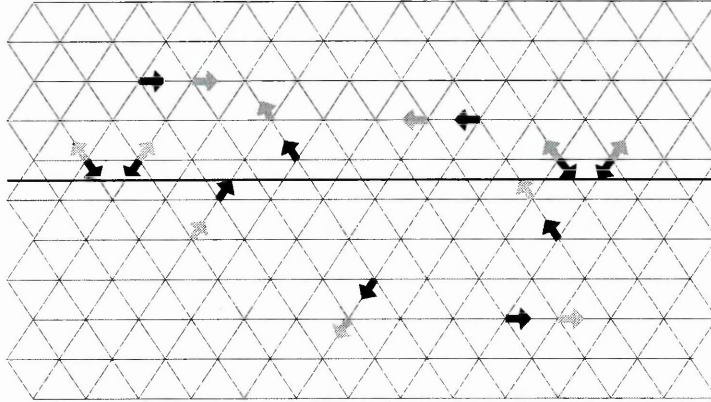


Figure 3. Simplified mid-link bounce-back method on a hexagonal lattice. The heavier line represents the wall position, note it is positioned exactly halfway between lattice nodes. Solid (hollow) arrows represent particle distribution functions at time  $t$  ( $t + 1$ ). In one time-step the distribution function effectively travels half a link then bounces back in the reverse direction so as to introduce non-slip boundaries. Both mass and momentum are conserved. To interact with the wall, particles moving in direction  $i$ , at the end of time step  $t$ , propagate, to re-appear at the same position, moving in direction  $i \oplus Q$  (addition modulo  $Q$ ) at time  $t + 1$ .

The mid-link bounce-back boundary condition retains simplicity of implementation, providing a balance between robustness and accuracy (see figure 3). The zero velocity is located a distance of exactly half a link from the lattice node on which it obtains. It is shown (He *et al.* 1997b; Maier *et al.* 1996; Skordos 1993) to be second-order accurate in space but first-order accurate in time, i.e. not necessarily instantaneously accurate. Note that bounce-back methods are not applicable to open boundaries or moving boundaries.

Halliday *et al.* (2002) proposed strategies for instantaneously accurate lattice closure, for plane boundaries with any known distribution of velocity. Several other sophisticated methods have been developed to overcome the closure problem, all involving velocity gradients (Skordos 1993; Noble *et al.* 1995). All the results presented here use mid-link bounce-back.

For internal pressure-driven flow, pressure and flux conditions often apply at open boundaries. LBM's inherent compressibility error (recall the  $O(1)$  speed of sound) allows one to impose internal pressure gradients as gradients in density. This strategy is valid even at modest  $Re$  (i.e. when the pressure gradient is large). In isothermal LBM, a simple method of combating compressibility and imposing pressure boundary conditions is to approximate the pressure field to a uniform gradient, which is then represented as a body force (Halliday *et al.* 2001).

More precisely, a uniform body force or acceleration  $\rho a_\alpha$  may be used to approximate the principal part of a pressure gradient. Such an acceleration can arise in the LBM's momentum equation (§ 2b) from the term  $F_i$  in the lattice evolution equation (2.19). For a uniform body force in an isothermal LBGK (Halliday *et al.* 2001),

$$\sum_i F_i = 0, \quad \sum_i F_i c_{i\alpha} = \rho a_\alpha, \quad (2.44)$$

and we have, for body force density (acceleration)  $a_\alpha$ ,

$$F_i = \frac{\rho t_i c_{i\alpha} a_\alpha}{c_s^2}. \tag{2.45}$$

While the above is consistent with Luo’s (1998) general derivation of uniform accelerations from the Boltzmann equation, we note that equation (2.45) is strictly valid only if  $a_\alpha$  is constant throughout the flow domain. In any system without unidirectional flow, the pressure gradient cannot be uniform. In fact, it must solve a Poisson-type equation obtained by taking the divergence of the incompressible Navier–Stokes equations

$$\nabla^2 \left( \frac{P}{\rho} \right) = \partial_\alpha v_\beta \partial_\beta v_\alpha. \tag{2.46}$$

The solution of (2.46) yields the instantaneous pressure for the given velocity distribution (Succi 2001). Spencer *et al.* (2004) designed a ‘two-part’ fictitious body force. The first, conservative, part is designed to correct the pressure field after equation (2.46) (see § 4). The second, non-conservative, part is designed, after the method of Halliday *et al.* (2001), to reduce compressibility effects. For applications like those we shall consider, this conservative component closely corresponds to a uniform body force, as the results we present in § 4 will show.

(j) *The exactly incompressible LBGK (EILBGK) model in D2Q9*

For slowly varying flows, the problem of compressibility error may be overcome. The EILBGK model of Zou *et al.* (1995) and Lin *et al.* (1996) makes a slight change to the interpretation of the distribution function  $f_i$  in order to make the macroscopic dynamics much more incompressible, but at the expense of the accuracy of its time variation. Applications of the EILBGK are therefore restricted to steady-state solutions and to flows with slow variation (low Strouhal number). However, EILBGK allows for a more accurate treatment of pressure boundary conditions. What changes is the equilibrium distribution function and the definition of velocity (other hydrodynamic moments remain unchanged):

$$\left. \begin{aligned} f_i^{(eq)} &= t_i \left( \rho + \frac{c_{i\alpha} u_\alpha}{c_s^2} + \frac{c_{i\alpha} c_{i\beta} u_\alpha u_\beta}{2c_s^4} - \frac{u^2}{2c_s^2} \right), \\ c_s^2 &= \frac{1}{3}, \quad t_0 = \frac{4}{9}, \quad t_1 = \frac{1}{9}, \quad t_2 = \frac{1}{36}, \end{aligned} \right\} \tag{2.47}$$

$$\sum_i f_i^{(eq)} \begin{bmatrix} 1 \\ c_{i\alpha} \\ c_{i\alpha} c_{i\beta} \end{bmatrix} = \begin{bmatrix} \rho(x_\alpha, t) \\ u_\alpha(x_\alpha, t) \\ \Pi_{\alpha\beta}^{(0)}(x_\alpha, t) \end{bmatrix}. \tag{2.48}$$

Using the Chapman–Enskog analysis as in § 2 *h*, one can obtain the following dynamics:

$$\left. \begin{aligned} \partial_\alpha u_\alpha &= 0, \\ \partial_\beta u_\alpha u_\beta &= -\partial_\alpha c_s^2 \rho + \nu \partial_\beta \partial_\beta u_\alpha, \end{aligned} \right\} \tag{2.49}$$

which are the exact steady-state incompressible Navier–Stokes equations with constant density  $\rho_0$ . In this model the pressure and viscosity are given by

$$\frac{P}{\rho_0} = c_s^2 \rho, \quad \nu = \frac{c_s^2}{2} (2\tau - 1), \tag{2.50}$$

in which  $\rho/\rho_0$  is the effective pressure. Note that both the continuity equation and the advective term in the Navier–Stokes equations are exactly incompressible, while the form of the diffusive term is preserved at the cost of the time derivative. In general, EILBGK schemes are not able to achieve the Reynolds numbers of LBGK simulations, due to the stricter incompressibility constraints.

### 3. Lattice Boltzmann equation for $N \geq 2$ immiscible fluids

Here we consider how to insert an appropriate interface between immiscible lattice fluids which are otherwise represented by the D2Q9 model already described. We describe our generalization, to  $N \gg 2$  fluids, of an existing model for binary fluids essentially after Gunstensen *et al.* (1991). Our model provides the means to deal, in the hydrodynamic regime, with a very large number of physically different, non-coalescing fluids.

For definiteness, we shall consider the velocity profile of system of stabilized, suspended drops in pressure-driven internal flow (although, of course, our algorithm can be applied more widely). Accordingly, individual drop masses need each to be conserved. In  $9.0 \times 10^5$  lattice updates of our interface algorithm, the mass of a drop is conserved to better than  $2.0 \times 10^{-3}\%$ . For simplicity we choose to prevent all suspended/advected drops from wetting the solid boundaries.

Our generalization to  $N$  immiscible components assigns each fluid a ‘colour’ superscript,  $\Gamma = 0, 1, 2, 3, \dots, (N - 1)$ . Fluids with different values of  $\Gamma$  can have collision parameters  $\tau_\Gamma$  and, therefore, different viscosity  $\nu_\Gamma$ . Now, for  $N$  different species, the  $N$ -component LBM quickly demands impractical amounts of computer storage, as  $N$  increases. But for relatively small, non-evaporating ‘sharp’ drops, the storage (arrays) for  $N$  primary quantities  $f_i^\Gamma(\mathbf{r}, t)$  will be very sparse. Moreover, a natural question arises around the value of attempting to represent, on lattice nodes with  $Q$  links (velocities), more than  $Q$  different colours or species.

To address storage, we record only  $N_Q < Q \ll N$  dominant species at any node. Essentially, we deal with colour difference, as opposed to absolute colour—which generates considerable reduction in the requisite storage. The sharp interfaces from our Gunstensen-type interface method mean minimal mixing and a reduction in the number of different colours found on a node. In practice we take  $N_Q = 5$ . This value is found to be adequate for even the most intimate mono-disperse  $N$ -component flows. Note, however, that this choice reflects the geometry and number of components (colours/drops) in our particular application. Also note that the particular  $N_Q$  dominating colours, or immiscible components, vary between nodes and in time. We assign each colour distribution a superscript  $\alpha$ , identifying their fluid belonging within the fluids ( $\Gamma$ ) of the node.

To guide species segregation, a lattice map of absolute colour, label  $l$ , is needed. However, for such a map, sufficient information can be stored in a five-dimensional integer array with subscript set  $\{x, y, i, \alpha\}$  to identify, for lattice position  $\{x, y\}$  direction  $i$ , the  $n (< N_Q)$  colours present by the value of integer superscript,  $\alpha$ . We have the following limits for the  $f$  and the associated colour label  $l$  values:

$$0 < f(x, y, i, \alpha), \quad 0 < l(x, y, i, \alpha) < N,$$

where, for a system of size  $L \times W$ ,

$$0 < x < L, \quad 0 < y < W, \quad 0 < i < Q, \quad 0 < \alpha < N_Q.$$

By recording only a maximum of  $N_Q$  species at each node, for a total of  $N$  drops (or immiscible components), the dominant (type real) storage requirements ( $f_i^\alpha(\mathbf{r}, t)$ ) are reduced by a factor  $N_Q/N$ , to levels comparable with the diphasic model (Gunstensen *et al.* 1991).

In our  $N$ -phase model, collision is, as in the diphasic model, performed in three steps: mixed fluid collision, perturbation and numerical colour reallocation.

The collision step acts on the mixed fluid's distribution function  $f_i$ ,

$$f_i(\mathbf{r}, t) = \sum_{\alpha=0}^{N_Q-1} f_i^\alpha(\mathbf{r}, t), \quad (3.1)$$

exactly after Zou *et al.* (1995), except with an effective relaxation parameter defined to give a mixed-fluid mean viscosity

$$\nu(\mathbf{r}, t) = \frac{1}{\rho(\mathbf{r}, t)} \sum_{\alpha=0}^{N_Q-1} \rho^\alpha(\mathbf{r}, t) \nu^\alpha,$$

where  $\nu_\alpha$  defines the chosen kinematic viscosity of component  $\alpha$  of the node at  $\mathbf{r}$ , which relates to a particular  $\nu^F$  through the colour map  $l(\mathbf{r}, i, \alpha)$ , and

$$\rho(\mathbf{r}, t) = \sum_{\alpha=0}^{N_Q-1} \rho^\alpha(\mathbf{r}, t), \quad \rho^\alpha(\mathbf{r}, t) \equiv \sum_{i=0}^{Q-1} f_i^\alpha(\mathbf{r}, t).$$

Preventing coalescence amounts to dealing consistently with all possible mixed-node colour states using generalized perturbing and recolouring processes that eliminate mixing between all pairs of species, which may be stated as a need to maximize the work done by a generalized colour flux against a generalized colour gradient. Accordingly, the diphasic Gunstensen colour gradient is generalized for the interface between fluid  $\alpha$  and fluid  $\beta$ , by what we assume to be its local normal (Dupin *et al.* 2003):

$$I_{\alpha\beta}(\mathbf{r}) = \sum_i (\rho^\alpha(\mathbf{r} + \mathbf{c}_i) - \rho^\beta(\mathbf{r} + \mathbf{c}_i)) \mathbf{c}_i. \quad (3.2)$$

This colour gradient is used to perturb the mixed fluids' distribution (equation (3.1)), with a surface tension inducing fluctuation. For the interface between two components  $\alpha$  and  $\beta$  we use a generalized perturbation,

$$\Delta f_i^{\alpha\beta}(\mathbf{r}, t) = \sigma_{\alpha\beta} C_{\alpha\beta}(\mathbf{r}, t) \cos(2(\theta_f(\mathbf{r}) - \theta_i)), \quad (3.3)$$

in which there is no summation on repeated subscripts,  $\sigma_{\alpha\beta}$  is a surface-tension parameter for the  $\alpha\beta$  interface and

$$C_{\alpha\beta}(\mathbf{r}, t) = 1 - \left| \frac{\rho_\alpha(\mathbf{r}, t) - \rho_\beta(\mathbf{r}, t)}{\rho_\alpha(\mathbf{r}, t) + \rho_\beta(\mathbf{r}, t)} \right|, \quad (3.4)$$

is the generalized *concentration factor* for the  $\alpha, \beta$  fluid pair which limits the action of surface tension to multi-coloured nodes (Thompson *et al.* 1999). For a D2Q9 lattice (see figure 2),  $\sigma_{\alpha\beta}$  is modulated by the factor  $\lambda_0$ , so that  $\sigma_{\alpha\beta}$  becomes

$$\sigma_{\alpha\beta}^i = \begin{cases} \lambda_0 \sigma_{\alpha\beta} & i \text{ even,} \\ \sigma_{\alpha\beta} & i \text{ odd,} \end{cases}$$

It has been found that  $\lambda_0 \approx 2.12$  provides the best angular isotropy of the drop (Dupin *et al.* 2003). This maximization of the drop's isotropy ensures that radial interfacial tension is uniform, but has other beneficial effects: the micro-current flow is minimized. To confirm the value 2.12, the qualitative features of the micro-current flow field of an enclosed drop may be predicted: by considering the (angular) directions in which the perturbation (3.3) produces the minimum flow in the near-interfacial region, the factor  $\lambda_0 = 3/\sqrt{2}$  is given (as shown in Dupin *et al.* (2003)).

We now define an 'average' colour gradient which points towards component  $\alpha$  and away from the total of all other components present at the node at position  $\mathbf{r}$ :

$$\begin{aligned} \mathbf{f}^\alpha(\mathbf{r}) &= \sum_i \sum_j \left[ f_j^\alpha(\mathbf{r} + \mathbf{c}_i) - \sum_{\beta \neq \alpha} f_j^\beta(\mathbf{r} + \mathbf{c}_i) \right] \mathbf{c}_i \\ \mathbf{f}^\alpha(\mathbf{r}) &= \sum_i [2\rho^\alpha(\mathbf{r} + \mathbf{c}_i) - \rho(\mathbf{r} + \mathbf{c}_i)] \mathbf{c}_i. \end{aligned} \quad (3.5)$$

The same calculation is repeated for each pair of fluid components  $\alpha\beta$  present at the node, position  $\mathbf{r}$ , the appropriate colour gradient  $\mathbf{f}^\alpha(\mathbf{r})$  (equation (3.5)) being used to 're-colour' (see below) for component  $\alpha$  within each node, essentially in the same way as for a binary fluid but with the order in which components  $\alpha$  are treated begin significant (see below). Accordingly, the total perturbation applied to the mixed fluid at the node at position  $\mathbf{r}$  is

$$\Delta f_i(\mathbf{r}, t) = \sum_{(\alpha, \beta)} \Delta f_i^{\alpha, \beta}(\mathbf{r}, t), \quad (3.6)$$

in which the summation is taken on all possible pairs  $\alpha, \beta$  and  $\Delta f_i^{\alpha, \beta}(\mathbf{r}, t)$  is defined in equation (3.3). Note that calculation of the colour gradient (3.5) requires knowledge of the absolute colour, not just the relative amounts of the different colours present in a local environment. The sum on  $\alpha$  of these individual fields is a measure of the local gradient in the total fluid density and is therefore zero only in a uniform fluid.

The perturbation process produces surface-tension effects in the hydrodynamics but it does not segregate the mixed fluids. To achieve segregation, a process of 're-colouring' is used. The (conserved) masses of the individual colours present at any mixed fluid site are numerically re-allocated to the post-perturbed  $f_i$ , so as to return as much of species  $\alpha$  as possible up the gradient  $\mathbf{f}^\alpha$ , defined in equation (3.5).

In order to achieve optimal colour separation, the order of the reallocation of more than two colours to receptacle  $f_i$  is significant. Different ordering in the re-colouring process can clearly result in small differences in the post-collision, post-segregated state. Careful observation shows that these differences are small but not without consequence. In order to produce optimum segregation (sharp interface), the minority species at a node is given *priority* allocation to its favoured direction. Failure to adopt this scheme results in a relatively large loss of information about the location of minority species, resulting in small but undesirable adhesion between drops in contact.

Target flow applications are, by intention, heavily interface dominated. For the effectively mono-disperse systems we shall consider here, a maximum of five drops and ambient fluid in immediate proximity was allowed (again, simple packing considerations mean this value will increase with increasing poly-dispersity). Resolving

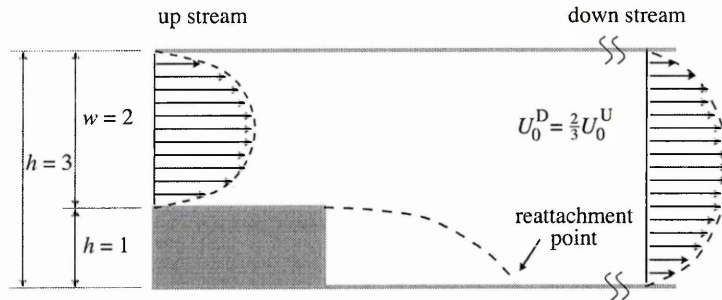


Figure 4. Geometry for a backward-facing step in channel flow with a step to channel width ratio of  $\frac{1}{3}$ . Both upstream and downstream of the step, flow behaves as standard Poiseuille flow. The step region introduces a recirculation zone of length  $L$ , the point of reattachment being when the  $x$ -component of the velocity changes sign. In two dimensions, the  $z$ -direction (into the plane of the paper) is infinite and so does not influence the flow.

five immiscible drops or de-mixing fluids leads to a maximum of  ${}_2P_5 = 10$  possible local interfaces. Having selected a resolution, however, it is crucial to note that we have shown that execution-time and memory requirements scale only weakly with  $N$ , the number of components or drops (Dupin *et al.* 2003).

In high-volume-fraction flows, drops can come close to the simulation boundary and to each other. As an initial step, to avoid the need to postulate sub-lattice lubrication forces, we encourage an explicit layer of ambient liquid always to remain between drops and the boundary. We therefore need to ensure preferential wetting of the boundary and suspended drops by the ambient fluid. This was achieved for the simulations described here (Dupin *et al.* 2004). But the role of lubrication forces is quite possibly important in high-volume-fraction suspensions of deformable particles, for intimate contact is inevitable. As we shall discuss below, the applications considered in the results of figures 8–15 are designed to assist in determining this validity of this assumption.

#### 4. Results: single and $N$ -component pressure-driven flows

We first investigate laminar pressure-driven flow properties of a single-component fluid over a backward-facing step using two different LBM methods. Steady-state results from EILBGK simulation and from body-forced LBGK are compared with experimental data (Denham & Patrick 1974). We proceed to simulate  $N$ -component pressure-driven flow in similar internal geometries, concentrating on issues which relate to the transport of deformable particles, such as lift in a uniform shear and shear banding of a suspension.

##### (a) Laminar flow over a backward-facing step

The backward-facing step geometry (figure 4) produces flow separation at the step and subsequent re-attachment, which is recognized as important within industrial situations.

We consider a ratio of step height to downstream channel width of  $\frac{1}{3}$ , for which there exist two independent experimental investigations approximating two-dimensional flow (Denham & Patrick 1974; Kueny & Binder 1984). Other LBM

simulations originate with Qian *et al.* (1996), who investigate the relationship of the length of the recirculation zone and  $Re$ . Chen *et al.* (1997) give a thorough quantitative comparison of simulation results with experimental data from Kueny & Binder (1984). Here we concentrate on a quantitative comparison with data from Denham & Patrick (1974).

Results were obtained for a range of Reynolds numbers using two methods, both assuming two-dimensional flow. Our first method uses standard LBGK in D2Q9 with second-order accurate mid-link bounce-back ‘solid’ boundaries (figure 4), periodic boundaries in the direction along the pipe and forcing with a conservative body-force to approximate the principal part of the pressure field. No pressure gradient is set explicitly. The overall pressure field is extracted as described below. Using this method the ‘pressure term’ ( $-c_s^2 \partial_\alpha \rho$ ), in the lattice Navier–Stokes equation (2.2), is regarded as a correction to a principal pressure field which is the potential function for the appropriate body force. The body force in the narrow part of the channel is  $\frac{27}{8}$  times that of the wide part of the channel, based upon matching parabolic flow rates. The potential function for this conservative body-force field is

$$\Phi(x) \equiv \begin{cases} -\frac{27}{8}Gx, & x < x_0, \\ -G(x + \frac{27}{8}x_0), & L > x > x_0, \end{cases} \quad (4.1)$$

in which  $G$  is the adjustable force constant and  $x_0$  the step length. The pressure field of the body-forced LBGK (below) is now determined by the expression  $c_s^2 \rho + \Phi$ . Mass is strictly conserved, and pressure across the width of the inlet and outlet throats was held constant. The length of the lattice was chosen to minimize compressibility errors (which may be measured from the velocity divergence in the steady-state continuity equation

$$\partial_\alpha u_\alpha = -\frac{u_\alpha}{\rho} \partial_\alpha \rho$$

but are otherwise ignored here).

Our second method uses the exactly incompressible EILBGK model, which allows pressure and velocity boundary conditions to be applied more accurately at the inlet and outlet throats. Again non-slip boundaries are invoked using mid-link bounce back. Flow is now induced by setting discharge-matched parabolic velocity profiles at inlet and outlet and by fixing the outlet pressure while allowing the inlet pressure to develop to accord with the necessary pressure gradient (itself an observable). Because of direct link between lattice density and pressure, the total mass of this simulation increases asymptotically to a steady-state value.

Using the law of similarity, we compare body-forced LBGK and EILBGK simulations with experimental results from Denham & Patrick (1974), based on Denham’s definition of  $Re$ :

$$Re = \frac{\bar{U}h}{\nu}, \quad (4.2)$$

in which  $\bar{U}$  is the average flow velocity upstream of the step,  $h$  step height and  $\nu$  the kinematic viscosity. Comparison of simulated and experimental data was made by normalizing velocities to the appropriate  $\bar{U}$ , distances to the step height  $h$ . For all our velocity data we note that both the body-forced LBGK and EILBGK results give very similar results for given  $Re$ , so velocity figures are representative of both models

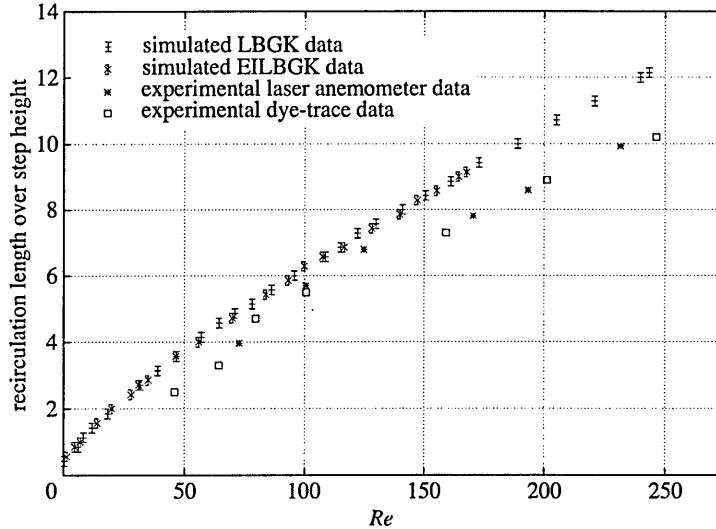


Figure 5. The recirculation length as a function of  $Re$  for the expansion ratio  $\frac{1}{3}$ . Data are compared with experimental values obtained via dye trace and laser anemometer measurements in Denham & Patrick (1974).

used. For all velocity data, flow profiles in the inlet and outlet were in good agreement compared with parabolic flow, supporting the assumption of fully developed flow. All results are analysed in their steady-state solutions, found by measuring the residual

$$R(t) = \sum_{\mathbf{x}} |\mathbf{u}(\mathbf{x}, t)|. \quad (4.3)$$

For the EILBGK system there is an additional condition on the total mass, which must be constant at steady state.

From stream-function data, the recirculation zone was seen to increase with increasing  $Re$ . The position of the vortex centre is given by the coordinates ( $x_c = 0.3L_R, y_c = 0.6h$ ); this is in agreement with the coordinates given by Denham & Patrick (1974).

We define the recirculation length to be the distance  $x$  from the step at  $y = 0$  in which a change in the  $x$ -velocity direction occurs. Figure 5 displays normalized recirculation length against  $Re$  for the step ratio of  $\frac{1}{3}$ . Note that the LBGK data provided in figure 5 are more accurate and cover a greater range of  $Re$  than in previous studies (Qian *et al.* 1996).

Both LBGK and EILBGK data are in good agreement. For given lattice resolution it was observed that the range of accessible  $Re$  for EILBGK is less than those for body-forced LBGK, owing to a more stringent incompressibility constraint. The experimental data points, taken from Denham & Patrick (1974), contain a  $\pm 2\%$  tolerance for measurements of velocity. Including the tolerance limits, experimental results lie just below the simulated points, the discrepancy increasing as  $Re$  increases. But CFD simulations agree with our LBM models.

Velocity profiles obtained at different locations along the simulation are compared with experimental velocity profiles in figure 6. Recall that the agreement between

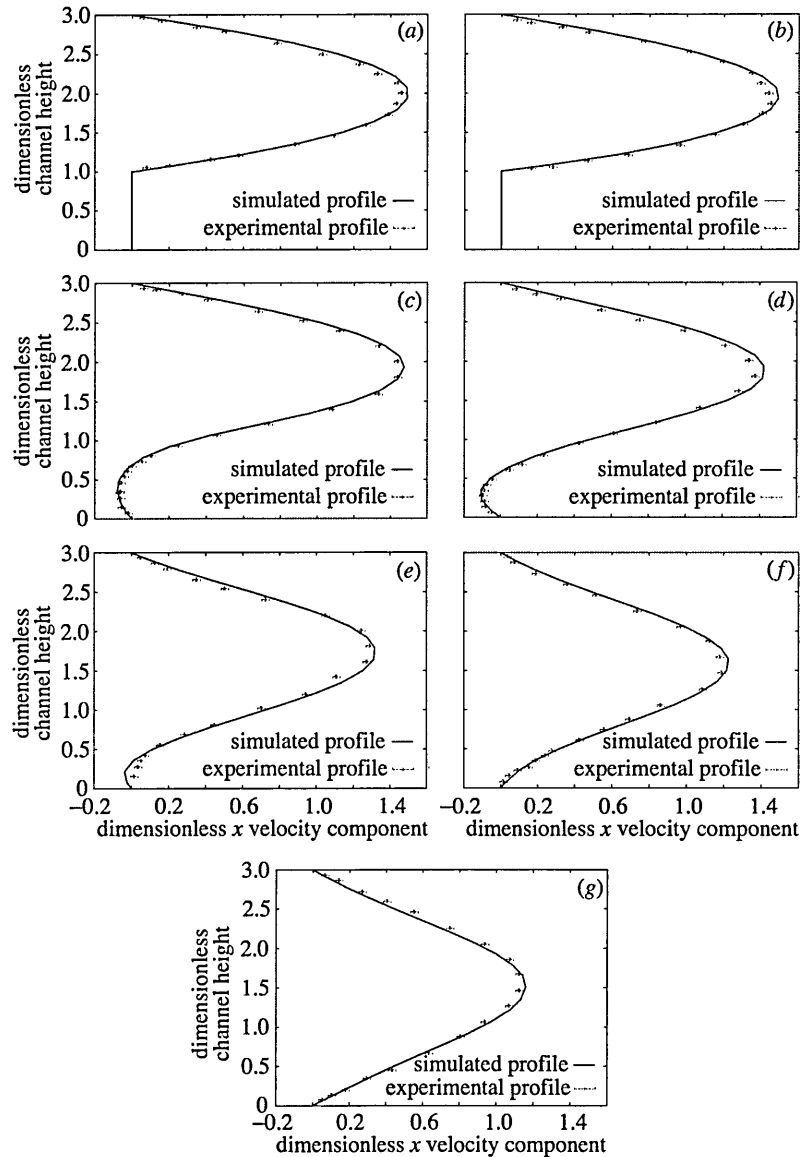


Figure 6. Comparison of simulated velocity profiles with experimental profiles obtained in Denham & Patrick (1974) in the step region at  $Re = 73$  for various dimensionless distances from the step position: (a)  $-1.3$ , (b)  $0.0$ , (c)  $0.8$ , (d)  $2.0$ , (e)  $4.0$ , (f)  $6.0$  and (g)  $8.0$ .

EILBGK and body-forced LBGK data is good and figure 6 shows only one set of simulation data, which agrees satisfactorily with experimental results at  $Re = 73$ . Upstream of the step, discrepancies are probably due to an inadequate development length in the experimental inlet (Denham & Patrick 1974). At higher  $Re$ , there emerge further discrepancies throughout the length of the system, probably due to

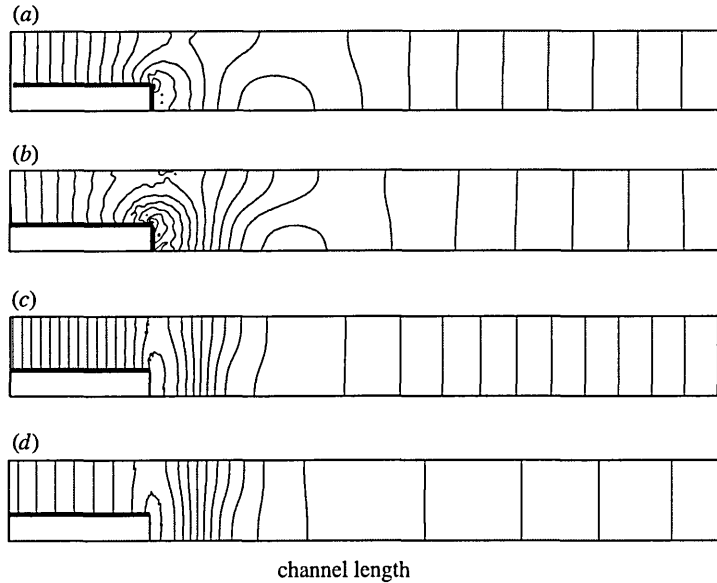


Figure 7. Pressure contours for (a), (b)  $Re = 31$  and (c), (d)  $Re = 174$  for (b), (d) body-forced LBGK and (a), (b) pressure-driven EILBGK. Both simulations used identical velocity boundary conditions (refer to text) but only in the EILBGK simulation does inlet pressure develop freely. There is qualitative agreement between the pressure fields (e.g. minimum pressure occurring in the recirculation zone for both simulations).

three-dimensional effects (Denham & Patrick 1974). More recent experiments on a backward-facing step with a step ratio of  $\frac{1}{2}$  (Armely *et al.* 1983) support this conclusion.

Figure 7 shows steady-state pressure contours (with constant increment, in arbitrary units) for different  $Re$ , for body-forced LBGK and pressure-driven EILBGK. The step height is one-third of the width of the channel. The lattice size is  $60 \times 600$ . Recall that it is EILBGK which accommodates pressure boundary conditions, with inlet pressure developing freely. Qualitative agreement is good, with the minimum pressure occurring in the recirculation zone for both simulations. Notwithstanding this, there are small quantitative differences between these pressure fields of the same order as those which routinely appear between CFD solutions obtained by different methods. Unfortunately, no experimental information on the pressure exists.

As can be seen from figure 7, our two methods produce slightly different pressure contours. However, given their very different representations of a pressure field, the correspondence between the results is highly reassuring. Body-forced LBGK implementation essentially assumes a uniform gradient of pressure which is perturbed. While intuitively valid at most points in the simulation domain, this assumption is weak in the step region, where forced LBGK and EILBGK show differences.

(b) *Suspensions of deformable particles*

We proceed to consider pressure-driven flow of deformable particles, modelled as incompressible liquid drops, of varying volume fraction. The solid properties of our

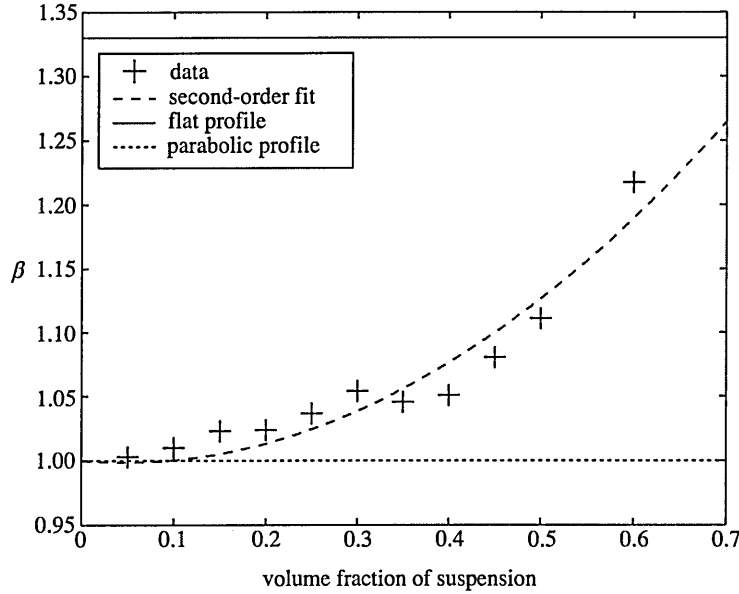


Figure 8. The increased blunting of a dense, monodisperse suspension's velocity profile with increased volume fraction  $\phi$ , with fixed drop deformability. The latter is quantified by surface tension (parameter  $\sigma = 0.01$ ) and viscosity ratio  $\Lambda = 30$  and fixed flow rate (pressure gradient).  $\phi$  varies over the range 0.1–0.6. The latter value is determined by packing and lubrication considerations.

particles are controlled through their interfacial tension and viscosity relative to that of the ambient fluid,  $\Lambda$ . The latter is parametrized by  $\Lambda \leq 50$  and controlled as discussed in the last section. Figures 8–12 demonstrate our  $N$ -phase algorithm applied to pressure-driven duct flow of a dense suspension of neutrally buoyant drops. On inspection, our blunted profiles have noticeable departure from parabolic. We assess averaged departure, at normalized cross-duct distances  $\bar{y} = 0.25$  and  $\bar{y} = 0.75$  by defining a blunting  $\beta$ :

$$\beta \equiv \frac{\bar{v}(\bar{y} = 0.25) + \bar{v}(\bar{y} = 0.75)}{2 \times 0.75}, \quad (4.4)$$

in which 0.75 is the height of a normalized parabola. With this definition, a flat velocity profile is characterized by  $\beta = 1.33$  and a parabolic velocity profile by  $\beta = 1.00$ .

A lattice of size  $100 \times 250$  containing drops of initial radii 4 lattice units was used. Data were extracted from steady-state configuration (typically  $1.0 \times 10^5$  simulation time-steps). The upper and lower dot-dashed lines in figures 8 and 9 illustrate the value of  $\beta$  corresponding to a flat and a parabolic velocity profile, respectively. The dashed line represents a second-order interpolation to the data. Details of each simulation are to be found in the appropriate caption.

For rigid suspended particles it is known that the velocity profile is determined solely by the suspension concentration and the relative particle size (Caro *et al.* 1998). By setting  $\Lambda = 50$  (large) and increasing the volume fraction of suspended material we can obtain the expected increase in  $\beta$  (figure 8). We note that no significant

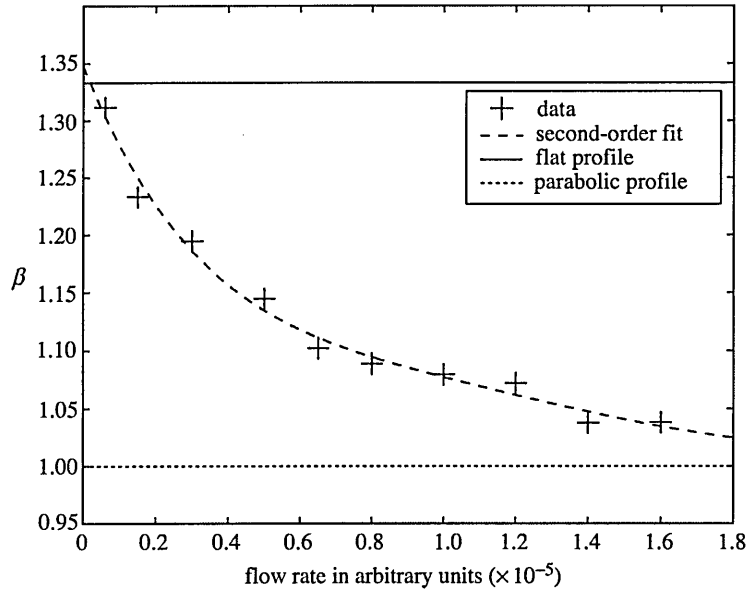


Figure 9. The decrease of blunting with increasing pressure gradient  $\Delta P$  with non-constant deformability. Fixed surface tension (parameter  $\sigma = 0.005$ ) and viscosity ratio  $\Lambda = 1$ .

changes in  $\beta$  were observed for constant volume fraction, on increasing pressure difference, as expected.

For immiscible liquid drops (i.e. flexible particle suspensions,  $\Lambda = 1$ ), on the other hand, we observe the expected dependence of the velocity profile upon the flow rate (applied pressure gradient), with the degree of blunting decreasing as flow rate increases (Caro *et al.* 1998) (figure 9).

In both figures 8 and 9 the expected qualitative features tend to vindicate the method we have used to circumvent lubrication forces (see the last section). The qualitatively correct nature of the variation in the macroscopic suspension flow profiles emerges from the microscopic rules implemented. In particular our device of enforcing an explicit layer of ambient fluid at drop and boundary surfaces seems to be valid, at volume fraction  $\phi = 0.6$  at least.

Recent experimental data confirm the shear-induced positional ordering of dense, intimate suspensions of particles and drops (Frank *et al.* 2003). Figure 10 shows the time-development of the cross-duct location of all the drop centres in an initially randomly placed suspension.

Clearly, starting from a random configuration (figure 11), and after an initial phase of transverse migration, our dense mono-disperse suspension of drops tends to flow in well-defined horizontal layers (figure 12), with occasional ‘hopping’, giving rise to an effective transverse diffusion of suspended drops.

### (c) Lift of deformable particles with linear shear

Liquid drops deform and certainly do not transmit stresses instantaneously. To compare the properties of liquid and solid drops as components in a microscopic model of transport we consider particle lift. Particles of radius  $R$  confined in channels

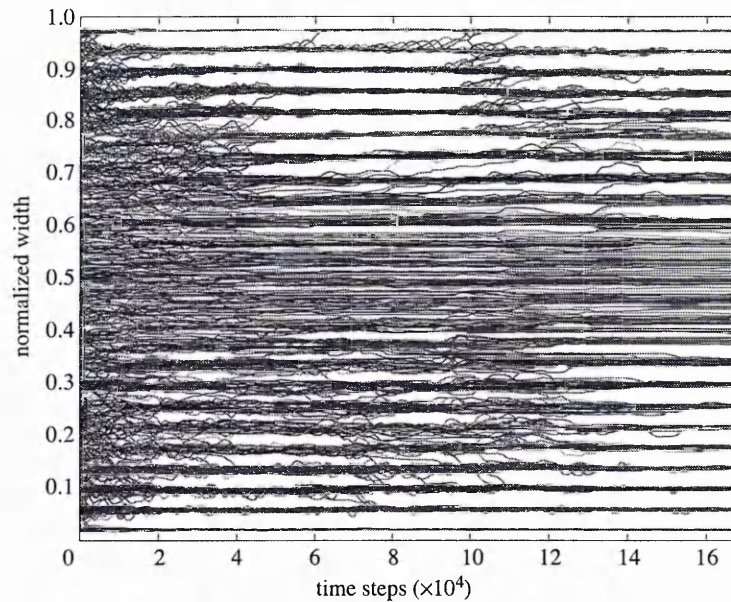


Figure 10. Trajectories of drop centres in time. Drop surface-tension parameter  $\sigma = 0.005$  and viscosity ratio  $\lambda = 1$ . The suspended drop volume fraction was 0.6: the lattice size was  $250 \times 100$  and the drop radius was 4.

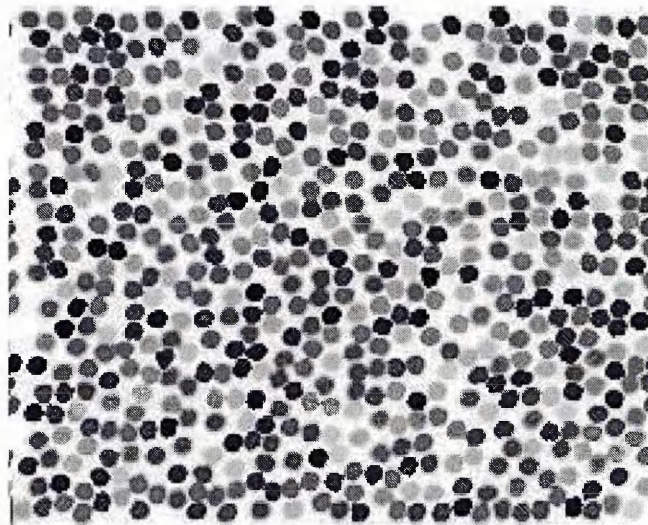


Figure 11. Random initial arrangement of the droplets.

and subject to flow (here a linear shear  $\dot{\gamma}$ ) tend to migrate away from the wall, eventually to advect at some distance from the wall characteristic of the particle Reynolds number:

$$Re_p = \frac{\dot{\gamma} R^2}{\nu}. \quad (4.5)$$

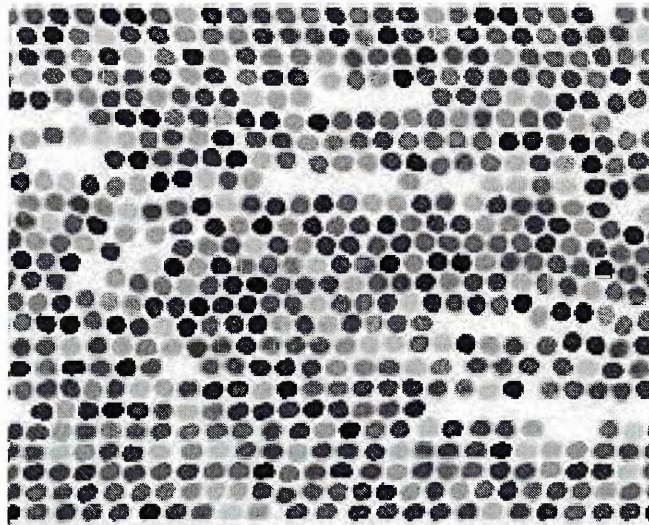


Figure 12. Steady state of the suspension of rigid droplets showing banding and ordering.

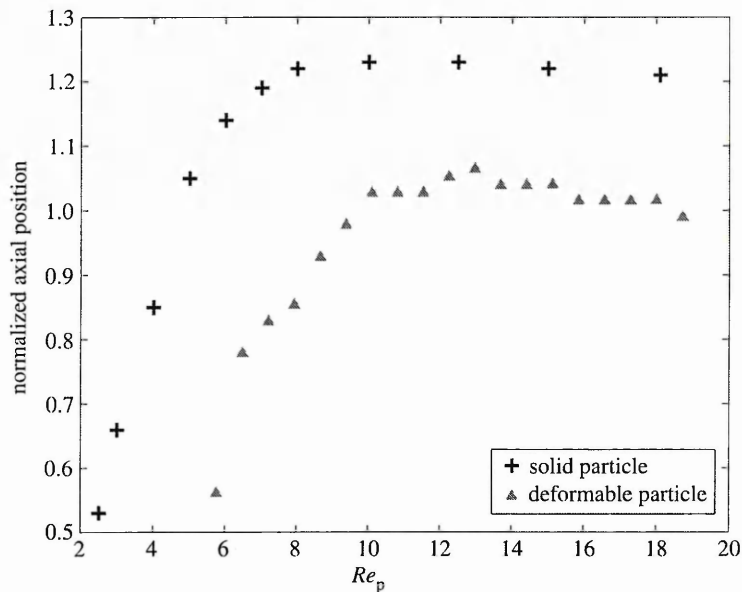


Figure 13. Steady-state elevation of a single droplet in straight channel normalized to its diameter with the particle Reynolds number.

Figure 13 shows the lift (normalized cross-duct displacement) of a neutrally buoyant deformable drop,  $\Lambda = 10$ , for reference, and a solid cylindrical particle of the same size, for a range of  $Re_p$ .

The latter was simulated by the LBM using the algorithm of Ladd (1994). Simulation parametrization for both solid and deformable drops is as specified in the figure caption. The geometry of both simulations was identical. As expected, there

is a some difference between the two objects—a relatively low viscosity drop has an internal flow structure and a different drag. However, within the bounds of simulation error, both solid and deformable drop data show qualitative similarities in the overall shape of the graphs. Note also that the range of accessible  $Re_p$  is appreciable.

## 5. Conclusion

In § 2 of this paper we have derived governing hydrodynamical equations for single-component LBMs and in § 3 we detailed the most recent  $N$ -component extension, predicated on continuum length-scale applications to large numbers of explicitly modelled deformable bodies.

The lattice Boltzmann technique appears to present a numerical scheme for the simulation of complex,  $N$ -component hydrodynamics. In particular it holds out the prospect of realistic simulations, at the continuum length-scale, of high-volume-fraction suspensions of deformable drops, currently modelled as drops of relatively viscous, incompressible fluids.

We present results for pressure-driven flow in internal geometry, demonstrating and validating an efficient single-component implementation (the backward-facing step) and an  $N$ -component extension (chaining, lift). For many engineering computations in the lattice Boltzmann literature, flow is induced by a uniform body forced method for easier algorithmic implementation. Our single-component results suggest that, if only velocity information is required, then this method may be used with confidence and, with appropriate adjustment, can produce a good representation of the pressure field. Our multi-component results, we suggest, point to  $N$ -component lattice Boltzmann simulation as a very useful tool for the explicit modelling of transport in dense suspensions.

For the future, our model should be improved by the inclusion of lubrication forces, which assume increasing importance as the suspended material volume fraction increases. At low volume fraction, suspended particles will, broadly, advect with the flow, embedded in the local fluid. Accordingly, the properties of the interface with low tangential and normal stresses, especially in respect of the micro-current activity assume greater significance. For micro-fluidic applications, to which all the methods reported here apply, this micro-current is, again, of considerable importance. It is our opinion that the most significant challenge to application of the  $N$ -component lattice Boltzmann computation is accurate representation of the interface.

## References

- Abe, T. 1966 *J. Comput. Phys.* **131**, 241–246.  
 Alexander, F. J., Chen, S. & Sterling, J. D. 1993 *Phys. Rev. E* **47**, 2249–2252.  
 Allen, M. P. & Tildesley, D. J. 1997 *Computer simulation of liquids*. Oxford: Clarendon.  
 Anderson, J. D. 1995 *Computation fluid dynamics: the basics with applications*. McGraw-Hill.  
 Armely, B. F., Durst, F., Pereira, J. C. F. & Schönung, B. 1983 *J. Fluid Mech.* **127**, 473–496.  
 Benzi, R., Succi, S. & Vergassola, M. 1992 *Phys. Rep.* **222**, 145–197.  
 Bhatnagar, P. E., Gross, P. E. & Krook, M. 1954 *Phys. Rev. A* **94**, 511–525.  
 Boghosian, B. & Taylor, W. 1997 *Int. J. Mod. Phys. C* **8**, 705–716.  
 Broadwell, J. E. 1964 *Phys. Fluids* **7**, 1243–1247.  
 Cali, A., Luo, L. S., Cancelliere, A., Benzi, R. & Gramignani, M. 1992 *Phys. Rev. A* **45**, 5771–5774.

- Caro, C. G., Pedeley, T. J., Schroter, R. C. & Seed, W. A. 1998 *The mechanics of the circulation*. Oxford Medical Publications.
- Chapman, S. & Cowling, T. G. 1970 *The mathematical theory of non-uniform gases*, 3rd edn. Cambridge University Press.
- Chen, H., Chen, S. & Matthaeus, W. H. 1992 *Phys. Rev. A* **45**(8), 5339–5342.
- Chen, S. & Doolen, G. D. 1998 *A. Rev. Fluid Mech.* **30**, 329–364.
- Chen, S., Chen, H., Martinez, C. & Matthaeus, W. 1991 *Phys. Rev. Lett.* **67**(27), 3776–3779.
- Chen, Y., Ohashi, H. & Akiyama, M. 1997 *JSME Int. J. B* **40**(1), 25–32.
- Chen, Y., Ohashi, H. & Akiyama, M. 1994 *Phys. Rev. E* **50**(4), 2776–2783.
- Conner, J. & Brebbia, C. 1976 *Finite element techniques for fluid flow*. Woburn, MA: Newnes-Butterworth.
- Denham, M. K. & Patrick, M. A. 1974 *Trans. IChE* **52**, 361–367.
- D’Humières, D., Lallemand, P. & Qian, Y. H. 1989 *Review of flow simulations using lattice gases*. Lecture Notes in Mathematics, vol. 1402, pp. 56–58. Springer.
- Do-Quang, M., Aurell, E. & Vergassola, M. 2000 An inventory of lattice Boltzmann models of multiphase flows. Technical Report, ISSN 0348-467X. (Available at [http://www.psci.kth.se/Activities/Reports/Results/R\\_2000\\_03/psci2000\\_03.pdf](http://www.psci.kth.se/Activities/Reports/Results/R_2000_03/psci2000_03.pdf).)
- Dupin, M. M., Halliday, I. & Care, C. M. 2003 Multi-component lattice Boltzmann equation for mesoscale blood flow *J. Phys. A* **36**, 8517–8534.
- Dupin, M. M., Halliday, I. & Care, C. M. 2004 A lattice Boltzmann model of flow blunting. *Phil. Trans. R. Soc. Lond. A* **362**, 1755–1761.
- Español, P. 2002 *SIMU Newsletter*, issue 4, ch. III, pp. 59–77. (Available at <http://simu.ulb.ac.be/newsletters/N4III.pdf>.)
- Ferreol, B. & Rothman, D. H. 1995 *Transport Porous Media* **20**, 3–20.
- Filippova, O. & Hanel, D. 1998 Grid refinement for lattice-BGK models. *J. Comput. Phys.* **147**, 219–228.
- Frank, M., Anderson, D., Weeks, E. R. & Morris, J. F. 2003 *J. Fluid Mech.* **493**, 363–378.
- Frisch, U., Hasslacher, B. & Pomeau, Y. 1986 *Phys. Rev. Lett.* **56**, 1505–1508.
- Goodfellow, J. 1991 *Molecular dynamics*. London: Macmillan.
- Groot, R. D. & Warren, P. B. 1997 *J. Chem. Phys.* **107**, 4423–4435.
- Gunstensen, A. K., Rothmann, D. H., Zaleski, S. & Zanetti, G. 1991 Lattice Boltzmann model of immiscible fluids. *Phys. Rev. A* **43**(8), 4320–4327.
- Halliday, I., Care, C. M. & Thompson, S. P. 1998 Macroscopic surface tension in a lattice Bhatnagar–Gross–Krook model of two immiscible fluids. *Phys. Rev. E* **57**, 514–523.
- Halliday, I., Hammond, L. A., Care, C. M., Good, K. & Stevens, A. 2001 Lattice Boltzmann equation hydrodynamics. *Phys. Rev. E* **64**, 011208.
- Halliday, I., Hammond, L. A. & Care, C. M. 2002 *J. Phys. A* **35**, 157–166.
- Hardy, J., Pomeau, Y. & De Pazzis, O. 1973 *J. Math. Phys.* **14**, 1746–1759.
- Hardy, J., De Pazzis, O. & Pomeau, Y. 1976 *Phys. Rev. A* **13**, 1949–1961.
- He, X. & Doolen, G. D. 1997a *Phys. Rev. E* **56**, 434–440.
- He, X. & Doolen, G. D. 1997b *J. Comput. Phys.* **134**(2), 306–315.
- He, X. & Luo, L. S. 1997a *Phys. Rev. E* **55**(6), 6333–6336.
- He, X. & Luo, L. S. 1997b *Phys. Rev. E* **56**(6), 6811–6817.
- He, X., Zou, Q., Luo, L. S. & Dembo, M. 1997a *J. Stat. Phys.* **87**, 115–136.
- He, X., Luo, L. S. & Dembo, M. 1997b *Physica A* **239**, 276–285.
- Higuera, F. & Luo, L. S. 1989 *Europhys. Lett.* **8**, 517–521.
- Hoogerbrugge, P. J. & Koelman, J. M. V. A. 1992 *Europhys. Lett.* **19**, 155–160.
- Hou, S. 1995 PhD thesis, Kansas State University, Manhattan, KS, USA.
- Hou, S., Zou, Q., Chen, S. & Doolen, G. D. A. C. 1995 *J. Comput. Phys.* **118**, 329–347.

- Hou, S., Sterling, S. & Doolen, G. D. 1996 *Fields Inst. Commun.* **6**, 151–166.
- Kadanoff, L. P., McNamara, G. R. & Zanetti, G. 1989 *Phys. Rev. A* **40**(8), 4527–4541.
- Kueny, L. J. & Binder, G. 1984 Viscous flow over backward facing steps: an experimental investigation, analysis of laminar flow over a backward facing step. *Not. Fluid Mech.* **9**, 32–42.
- Ladd, A. J. C. 1994 *J. Fluid Mech.* **271**, 311–339.
- Landau, L. D. & Lifshitz, E. M. 1995 *Fluid mechanics*. Course in Theoretical Physics, 2nd edn, vol. 6. Oxford: Butterworth-Heinemann.
- Liboff, R. C., Herman, J. & Liboff, R. L. 2003 *Kineic theory*, 2nd edn. Springer.
- Lin, Z., Fang, H. & Tao, R. 1996 *Phys. Rev. E* **54**(6), 6323–6330.
- Lishchuk, S. V., Care, C. M. & Halliday, I. 2003 *Phys. Rev. E* **67**, 036701.
- Luo, L. S. 1998 *Phys. Rev. Lett.* **81**(8), 1618–1621.
- Luo, L. S., Wang, J. & Qian, Y. H. 1997 *Int. J. Mod. Phys. C* **8**(4), 999–1008.
- Luo, L. S. 2000 *Phys. Rev. E* **64**(4), 4982–4996.
- McNamara, G. R. & Zanetti, G. 1988 *Phys. Rev. Lett.* **61**(20), 2332–2335.
- Maier, R. S., Bernard, R. S. & Grunau, D. W. 1996 *Phys. Fluids* **8**(7), 1788–1801.
- Martinez, D. O., Chen, S. & Matthaeus, W. H. 1994 *Phys. Plasmas* **1**, 1850–1867.
- Mei, R., Shyy, S., Yu, D. & Luo, L. S. 2000 *J. Comput. Phys.* **161**, 680–699.
- Noble, D. R., Georgiadis, J. G. & Buckius, R. O. 1995 *J. Stat. Phys.* **81**, 17–33.
- Qian, Y. H. & Zhou, Y. 1998 *Europhys. Lett.* **42**(4), 359–364.
- Qian, Y. H., D’Humières, D. & Lallemand, P. 1992 *Europhys. Lett.* **17**(6), 479–484.
- Qian, Y. H., Luo, L. S., Massaioli, F. & Orszag, S. A. 1996 *Fields Inst. Commun.* **6**, 207–215.
- Reider, M. B. & Sterling, J. D. 1995 *Comput. Fluids* **24**, 459–467.
- Rothmann, D. H. & Zaleski, S. 1994 *Rev. Mod. Phys.* **66**(4), 1417–1479.
- Shan, X. W. & Chen, H. D. 1994 *Phys. Rev. E* **49**(4), 2941–2948.
- Skordos, P. A. 1993 *Phys. Rev. E* **48**(6), 4823–4842.
- Spencer, T. J., Dupin, M. M., Halliday, I. & Care, C. M. 2004 An incompressible Lattice BGK scheme with enhanced stability. (In preparation.)
- Succi, S. 2001 *The lattice Boltzmann equation*. Oxford: Clarendon.
- Succi, S. 2002 *Phil. Trans. R. Soc. Lond. A* **360**, 429–436.
- Succi, S., Foti, E. & Higuera, F. 1989 *Europhys. Lett.* **10**, 433–438.
- Succi, S., Benzi, R. & Higuera, F. 1991 *Physica D* **47**, 219–230.
- Swift, M. R., Osborn, W. R. & Yoemans, J. M. 1995 *Phys. Rev. Lett.* **75**(5), 830–833.
- Thompson, S. P., Halliday, I. & Care, C. M. 1999 Mesoscopic hydrodynamics of diphasic lattice Bhatnagar–Gross–Krook fluid interfaces. *Phys. Chem. Chem. Phys.* **1**, 2183–2190.
- Tölke, J., Krafczyk, M., Schultz, M., Rank, E. & Berrios, R. 1998 *Int. J. Mod. Phys. C* **9**, 1143–1157.
- von Neumann, J. 1966 *Theory of self-reproducing automata*. University of Illinois Press.
- Wagner, L. 1994 *Phys. Fluids* **6**, 3516–3518.
- Wolfram, S. 1986 *Rev. Mod. Phys.* **55**, 601–644.
- Yang, Z. L., Dinh, T. N., Nourgaliev, R. R. & Sehgal, B. R. 2001 *Int. J. Heat Mass Transfer* **44**, 195–206.
- Zou, Q., Hou, S., Chen, S. & Doolen, G. D. 1995 Analytical solutions of the lattice Boltzmann BGK model. *J. Stat. Phys.* **81**, 319–334.

# Bibliography

- [1] M. K. Denham and M. A. Patrick. Laminar flow over a downstream-facing step in a two-dimensional flow channel. *Trans. IChE*, 52:361–367, 1974.
- [2] A. J. Davidson and N. J. Mottram. Flexoelectric switching in a bistable nematic device. *Phys. Rev. E*, 65(05):051710(10), May 2002.
- [3] G. Vertogen and W. H. deJeu. *Thermotropic Liquid Crystals, Fundamentals*. Springer-Verlag Berlin Heidelberg, 1988.
- [4] D. A. Dunmur, A. Fukuda, and G. R. Luckhurst. *Physical Properties of Liquid Crystals: Nematics (EMIS Datareviews)*. Institution of Electrical Engineers, 2001.
- [5] P. J. Collings and M. Hird. *Introduction to liquid crystals*. Taylor and Francis, 1997.
- [6] R. E. Webster. Computer simulation of confined liquid crystal dynamics. *PhD Thesis, Sheffield Hallam University*, November 2001.
- [7] P. R. Kishore, N. V. S. Rao, P. B. K. Sarma, T. F. S. Raj, M. N. Avadhanlu, and C. R. K. Murty. Field and frequency effects in nematic mixtures of negative and positive dielectric anisotropy. *Mol. Cryst. Liq. Cryst.*, 45(3/4):231–241, 1978.
- [8] R. B. Meyer. Piezoelectric effects in liquid crystals. *Phys. Rev. Lett.*, 22(18):918–921, May 1969.
- [9] J. Prost and J. P. Marcerou. On the microscopic interpretation of flexoelectricity. *Le Journal de Physique*, 38:315–324, 1977.
- [10] P. Jemmer, M. Wilson, P. A. Madden, and P. W. Fowler. Dipole and quadrupole polarization in ionic systems: Ab initio studies. *J. Chem. Phys*, 111(5):2038–2049, August 1999.
- [11] <http://www.kentdisplays.com/advantages/advantages.html>. 2004.
- [12] <http://eink.com/>. 2004.
- [13] G. W. Gray, editor. *Critical reports on applied chemistry: Thermotropic liquid crystals*, volume 22. Wiley on behalf of the Society of Chemical Institute, 1987.
- [14] Tutorials lectures. *20<sup>th</sup> ILCC, Slovenia*, 2004.

- [15] M. Schadt and W. Helfrich. Voltage-dependant optical activity of a twisted nematic liquid crystal. *Appl. Phys. Lett.*, 18:127, 1971.
- [16] P. J. Collings. *Liquid crystals: Natures delicate phase of matter*. Adam Hilger, Bristol, 1990.
- [17] T. J. Scheffer and J. Nerring. A new highly multiplexable liquid crystal display. *Appl. Phys. Lett.*, 45:1021, 1984.
- [18] M. F. Schiekol and K. Fahrenschon. Deformation of nematic liquid crystal with vertical orientation in electric fields. *Appl. Phys. Lett.*, 19:391, 1971.
- [19] D. K. Yang, J. L. West, L. C. Chien, and J. W. Doane. Control of reflectivity and bistability in displays using cholesteric liquid crystals. *J. Appl. Phys.*, 76(2):1331–1333, July 1994.
- [20] D. W. Berreman and W. R. Heffner. New bistable cholesteric liquid-crystal display. *Appl. Phys. Lett.*, 37(1):109–111, July 1980.
- [21] G. D. Boyd, J. Cheng, and P. D. T. Ngo. Liquid-crystal orientational bistability and nematic storage effects. *Appl. Phys. Lett.*, 36, 1980.
- [22] X. J. Yu and H. S. Kwok. Bistable bend-splay liquid crystal display. *Appl. Phys. Lett.*, 85(17):3711–3713, October 2004.
- [23] S. Kitson and A. Geisow. Controllable alignment of nematic liquid crystals around microscopic posts: Stabilization of multiple states. *Appl. Phys. Lett.*, 80(19):3635–3637, May 2002.
- [24] J. H. Kim, M. Yoneya, J. Yamamoto, and H. Yokoyama. Surface alignment bistability of nematic liquid crystals by orientationally frustrated surface patterns. *Appl. Phys. Lett.*, 78(20):3055–3057, May 2001.
- [25] Y. L. Cheng, D. N. Batchelder, S. D. Evans, J. R. Henderson, J. E. Lydon, and S. D. Ogier. Imaging of micropatterned self-assembled monolayers with absorbed liquid crystals. *Liquid Crystals*, 27(10):1267–1275, 2000.
- [26] T. Scharf and A. Shlayan. Liquid crystal alignment on replicated nanostructured surfaces. *Mol. Cryst. Liq. Cryst.*, 411:1745–1755, 2004.
- [27] N. A. Clark and S. T. Lagerwall. Submicrosecond bistable electro-optic switching in liquid crystals. *Appl. Phys. Lett.*, 36:899–901, 1980.
- [28] D. W. Berreman and W. R. Heffner. New bistable liquid crystal twist cell. *J. Appl. Phys.*, 52(4):3032–3039, April 1981.
- [29] I. Dozov and G. Durand. Surface controlled nematic bistability. *Liquid Crystals Today*, 8:1–7, 1998.
- [30] G. P. Bryan-Brown, M. J. Towler, M. S. Bancroft, and D. G. McDonnell. Bistable nematic alignment using bigratings. *SID*, pages 209–212, October 1994.

- [31] J. C. Jones, S. Beldon, P. Brett, M. Francis, and M. Goulding. 26.3: Low voltage zenithal bistable devices with wide operating windows. *SID Symposium Digest of Technical Papers*, 34(1):954–957, May 2003.
- [32] F. C. Frank. On the theory of liquid crystals. *Discuss. Faraday Soc.*, 25:19–28, 1958.
- [33] J. L. Ericksen. Anisotropic fluids. *Arch. Ratl. Mech. Anal.*, 4:231–237, 1960.
- [34] F. M. Leslie. Some constitutive equations for anisotropic fluids. *Quart. J. Mech. Appl. Math.*, 19(3):357–370, 1966.
- [35] P. G. deGennes. Short range order effects in the isotropic phase of nematics and cholesterics. *Mol. Cryst. Liq. Cryst.*, 12:193–214, 1971.
- [36] L. D. Landau and E. M. Lifshitz. *Statistical Physics*. Pergamon, Oxford, 2<sup>nd</sup> edition, 1969.
- [37] P. G. deGennes. Phenomenology of short-range-order effects in the isotropic phase of nematic materials. *Phys. Lett. A*, 30a(8):454–455, December 1969.
- [38] E. F. Gramsbergen, L. Longa, and W. H. de Jeu. Landau theory of the nematic-isotropic phase transition. *Physics Reports*, 125(4):195–257, 1986.
- [39] G. Barbero and L. R. Evangelista. *An elementary course on the continuum theory for nematic liquid crystals*. World Scientific, 2001.
- [40] T. Qian and P. Sheng. Generalized hydrodynamic equations for nematic liquid crystals. *Phys. Rev. E*, 58(6):7475–7485, December 1998.
- [41] T. C. Lubensky. Molecular description of nematic liquid crystals. *Phys. Rev. A*, 2(6):2497–2514, December 1970.
- [42] A. N. Beris and B. J. Edwards. *Thermodynamics of flowing systems*. Oxford University Press, Oxford, 1994.
- [43] J. Nehring and A. Saupe. On the elastic theory of uniaxial liquid crystals. *J. Chem. Phys.*, 54(1):337–343, January 1971.
- [44] W. Helfrich. The strength of piezoelectricity in liquid crystals. *Z. Naturforsch.*, 26A(5):833–835, May 1971.
- [45] A. L. Alexe-Ionescu. Flexoelectric polarization and second order elasticity for nematic liquid crystals. *Phys. Lett. A*, 180(6):456–460, September 1993.
- [46] P. G. De Gennes and J. Prost. *The Physics of liquid crystals*. Clarendon Press, 2<sup>nd</sup> edition, 1995.
- [47] B. I. Bleaney and B. Bleaney. *Electricity and Magnetism*. Clarendon Press, Oxford, 1957.
- [48] M. Nobili and G. Durand. Disorientation-induced disordering at a nematic-liquid-crystal-solid interface. *Phys. Rev. A*, 46(10):R6174–R6177, November 1992.

- [49] A. Rapini and M. Papoular. Distortion d'une lamelle nématique sous champ magnétique, conditions d'ancrage aux parois. *J. de Physique*, 30(C4-54):C4-56, 1969.
- [50] H. Stark. Physics of colloidal dispersions in nematic liquid crystals. *Physics Reports*, 351:387-474, 2001.
- [51] O. Parodi. Stress tensor for a nematic liquid crystal. *J. de Phys. (Paris)*, 31(7):581-584, July 1970.
- [52] S. R. De Groot and P. Mazur. *Non-equilibrium Thermodynamics*. Dover Publications, 1984.
- [53] A. M. Sonnet and E. G. Virga. Dynamics of dissipative ordered fluids. *Phys. Rev. E*, 64(3):031705(1-10), 2001.
- [54] D. Forster, T. C. Lubensky, P. C. Martin, J. Swift, and P. S. Perhan. Hydrodynamics of liquid crystals. *Phys. Rev. Lett.*, 26(17):1016-1019, April 1971.
- [55] R. C. Jones. A new calculus for the treatment of optical systems. *J. Opt. Soc. Am.*, 31:488-503, 1941.
- [56] D. W. Berreman. Optics in stratified and anisotropic media: 4×4-matrix formulation. *J. Opt. Soc. Am.*, 62:502-510, 1976.
- [57] E. E. Kriezis, C. J. P. Newton, T. P. Spiller, and S. J. Elston. Three-dimensional simulations of light propagation in periodic liquid-crystal microstructures. *Applied Optics*, 41(25):5346-5356, September 2002.
- [58] C. Z. van Doorn. Dynamic behavior of twisted nematic liquid-crystal layers in switched fields. *J. Appl. Phys.*, 45(9):3738-3745, September 1975.
- [59] D. W. Berreman. Liquid-crystal twist cell dynamics with backflow. *J. Appl. Phys.*, 46(9):3746-3751, September 1975.
- [60] A. Kilian and S. Hess. Derivation and application of an algorithm for the numerical calculation of the local orientation of nematic liquid crystals. *Naturforsch A*, 44A(8):693-703, August 1989.
- [61] H. Mori, E. C. Gartland, J. R. Kelly, and P. J. Bos. Multidimensional director modeling using the q tensor representation in a liquid crystal cell and its application to the pi cell with patterned electrodes. *Jpn. J. Appl. Phys.*, 38(1A):135-146, January 1999.
- [62] M. Reichenstein, H. Stark, J. Stelzer, and H. R. Trebin. Motion, creation, and annihilation of disclinations in multidomain structured nematic liquid crystal cells. *Phys. Rev. E*, 65(1):011709/1-9, January 2002.
- [63] J. L. Ericksen. Liquid crystals with variable degree of orientation. *Arch. Rat. Mech. Anal.*, 113(2):97-120, 1991.
- [64] D. Svensek and S. Zumer. Hydrodynamics of pair-annihilating disclination lines in nematic liquid crystals. *Phys. Rev. E*, 66(2):021712/1-6, August 2002.

- [65] H. Imura and K. Okano. Temperature dependence of the viscosity of liquid crystals. *Jap. J. Appl. Phys.*, 11(10):1440–1446, October 1972.
- [66] S. Hess. Irreversible thermodynamics of nonequilibrium alignment phenomena in molecular liquids and in liquid crystals. i. derivation of nonlinear constitutive laws, relaxation of the alignment, phase transition. *Z. Naturforsch.*, 30A(6/7):728–738, June 1975.
- [67] P. D. Olmsted. Theory of the non-equilibrium phase transition for nematic liquid crystal under shear flow. *Phys. Rev. A*, 41(8):R4578–R4581, 1990.
- [68] S. Hess and I. Parowitz. On the unified theory for non-equilibrium phenomena in the isotropic and nematic phases of a liquid crystal, spatially inhomogeneous alignment. *Naturforsch A*, 36A(6):554–558, June 1981.
- [69] S. Hess. Transport phenomena in anisotropic fluids and liquid crystals. *J. Non-Equil. Thermo.*, 11(3-4):175–193, 1986.
- [70] C. Pereira Borgmeyer and S. Hess. Unified description of the flow alignment and viscosity in the isotropic and nematic phases of liquid crystals. *J. Non-Equil. Thermo.*, 20(4):359–384, 1995.
- [71] S. Hess. Fokker-planck-equation approach to flow alignment in liquid crystals. *Naturforsch A*, 31A(9):1034–1037, September 1976.
- [72] M. Doi. Molecular dynamics and rheological properties of concentrated solutions of rodlike polymers in isotropic and liquid crystalline phases. *J. Polym. Sci. Polym. Phys. Ed.*, 19(2):229–243, February 1981.
- [73] M. Grosso, F. Dupret, and P. L. Maffettone. A closure approximation for nematic liquid crystals based on the canonical distribution subspace theory. *Rheologica Acta*, 39(3):301–310, August 2000.
- [74] T. Tsuji and A. D. Rey. Effect of long range order on sheared liquid crystalline materials. 1. compatibility between tumbling behavior and fixed anchoring. *J Non-Newton. Fluid Mech.*, 73(1-2):127–152, November 1997.
- [75] H. Pleiner, M. Liu, and H. R. Brand. Convective nonlinearities for the orientational tensor parameter in polymeric systems. *Rheol. Acta.*, 41:375–382, May 2002.
- [76] M. Doi and S. F. Edwards. *The theory of polymer dynamics*. Clarendon Press, 1988.
- [77] G. Kloos. On the representation of stresses at the surface of a solid or liquid exposed to an electric or magnetic field. *J. Phys. Condens. Matter*, 11(17):3425–3430, May 1999.
- [78] P. C. Hohenberg and B. I. Halperin. Theory of dynamic critical phenomena. *Rev. Mod. Phys.*, 49(3):435–479, July 1977.
- [79] A. I. Derzhanski and A. G. Petrov. Flexoelectricity in nematic liquid crystals. *Acta Physica Polonica A*, A55(5):747–767, May 1979.

- [80] J. G. McIntosh and F. M. Leslie. Flow induced surface switching in a bistable nematic device. *J. Engin. Math.*, 37(1-3):129–142, February 2000.
- [81] G. E. Durand and E. G. Virga. Hydrodynamic model for surface nematic viscosity. *Phys. Rev. E*, 59(4):4137–4142, April 1999.
- [82] A. Mertelj and M. Copic. Surface-dominated orientational dynamics and surface viscosity in confined liquid crystals. *Phys. Rev. Lett.*, 81(26):5844–5847, December 1998.
- [83] G. McNamara and G. Zanetti. Use of the boltzmann equation to simulate lattice-gas automata. *Phys. Rev. Lett.*, 61(20):2332–2335, November 1988.
- [84] J. F. Higuera and J. Limenez. Boltzmann approach to lattice gas simulations. *Europhysics Letters*, 9(7):663–668, August 1989.
- [85] H. D. Chen, S. Y. Chen, and W. H. Matthaeus. Recovery of the navier-stokes equations using a lattice-gas boltzmann method. *Phys. Rev. A*, 45(8):R5339–R5342, April 1992.
- [86] Y. H. Qian, D. D’Humieres, and P. Lallemand. Lattice bgk models for navier-stokes equation. *Europhysics Letters*, 17(6):479–484, February 1992.
- [87] S. Succi. *The lattice Boltzmann equation for fluid dynamics and beyond*. Oxford : Clarendon Press, 2001.
- [88] S. Chen and G. D. Doolen. Lattice boltzmann method for fluid flows. *Ann. Rev. Fluid Mech.*, 30:329–364, 1998.
- [89] J. Hardy, O. dePazzis, and Y. Pomeau. Molecular dynamics of a classical lattice gas: transport properties and time correlation functions. *Phys. Rev. A*, 13:1949–1961, 1976.
- [90] L. D. Landau and E. M. Lifshitz. *Fluid mechanics*. Oxford : Pergamon Press, 2<sup>nd</sup> edition, 1987.
- [91] A. J. Raudkivi and R. A. Callander. *Advanced fluid mechanics : an introduction*. Edward Arnold, 1975.
- [92] U. Frisch, B. Hasslacher, and Y. Pomeau. Lattice-gas automata for the navier-stokes equation. *Phys. Rev. Lett.*, 56(14):1505–1508, April 1986.
- [93] P. L. Bhatnagar, E. P. Gross, and M. Krook. A model for collision processes in gases, i. small amplitude processes in charged and neutral one-component system. *Phys. Rev.*, 94:511–525, 1954.
- [94] X. He and L. S. Luo. Theory of the lattice boltzmann method: from the boltzmann equation to the lattice boltzmann equation. *Phys. Rev. E*, 56(6):6811–6817, December 1997.
- [95] J. E. Broadwell. Study of rarefied shear flow by the discrete velocity method. *J. Fluid Mech.*, 19:401–404, 1964.

- [96] J. E. Broadwell. Shock structure in a simple discrete velocity gas. *Phys. Fluids*, 7:1243–1247, 1964.
- [97] T. Inamuro and B. Sturtevant. Numerical study of discrete velocity gases. *Phys. Fluids A*, 2:2196–2203, 1990.
- [98] L. Mieussens. Discrete velocity model and implicit scheme for the bgk equation of rarefied gas dynamics. *Math Models Appl Sci*, 10:1121–1149, 2000.
- [99] L. Mieussens. Discrete velocity models and numerical schemes for the boltzmann-bgk equation in plane and axisymmetric geometries. *J. Comput. Phys.*, 162:429–466, 2000.
- [100] S. Chapman and T. G. Cowling. *The Mathematical theory of non-uniform gases : an account of the kinetic theory of viscosity, thermal conduction and diffusion in gases*. Cambridge University Press, 1970.
- [101] A. H. Nayfeh. *Introduction to perturbation techniques*. Wiley, 1981.
- [102] T. E. Faber. *Fluid dynamics for physics*. Cambridge University Press, 1995.
- [103] D. Yu, R. Mei, L. S. Luo, and W. Shyy. Viscous flow computations with the method of lattice boltzmann equation. *Progress in Aerospace Sciences*, 39:329–367, 2003.
- [104] G. Strumolo and B. Viswanathan. New directions in computational aerodynamics. *Phys. World*, 10:45–49, 1997.
- [105] X. He, R. Zhang, S. Chen, and G. Doolen. On three dimensional rayleigh-taylor instability. *Phys. Fluids*, 11:1143–1152, 1999.
- [106] N. S. Martys and H. Chen. Simulation of multicomponent fluids in complex three-dimensional geometries by the lattice boltzmann method. *Phys. Rev. E*, 53:743–750, 1996.
- [107] A. J. C. Ladd and R. Verberg. Lattice boltzmann simulations of particle fluid suspensions. *J. Stat. Phys.*, 104:1191–1251, 2001.
- [108] D. Qi and L.-S. Luo. Rotational and orientational behaviour of a three-dimensional spheroidal particles in couette flow. *J. Fluid Mech.*, 447:201–213, February 2003.
- [109] S. Chen, S. P. Dawson, G. D. Doolen, D. R. Janecky, and A. Lawniczak. Lattice methods and thier applications to reacting systems. *Comput. Chem. Eng.*, 19:617–646, February 1995.
- [110] H. Yu, L. S. Luo, and S. S. Girimaji. Scalar mixing and chemical reaction simulations using lattice boltzmann method. *J. Computat. Eng. Sci.*, 3:73–87, 2002.
- [111] S. Chen, H. Chen, D. Martinez, and W. H. Matthaeus. Lattice boltzmann model for simulation of magnetohydrodynamics. *Phys. Rev. Lett.*, 67:3776–3779, 1991.

- [112] W. Miller and S. Succi. A lattice boltzmann model for anisotropic crystal growth from melt. *J. Stat. Phys.*, 107:173–186, 2002.
- [113] D. P. Ziegler. Boundary conditions for lattice boltzmann simulations. *J. Stat. Phys.*, 71:1171–1177, 1993.
- [114] I. Ginzburg and P. M. Alder. Boundary flow condition analysis for the three-dimensional lattice boltzmann model. *J. Phys. II France*, 4:191–214, 1994.
- [115] A. J. C. Ladd. Numerical simulation of particular suspensions via a discretized boltzmann equation. part i. theoretical foundation. *J. Fluid Mech.*, 271:285–309, 1994.
- [116] M. Bouzidi, M. Firdaous, and M. Lallemand. Momentum transfer of a lattice boltzmann fluid with boundaries. *Phys. Fluids*, 13:3452–3459, 2001.
- [117] X. He, Q. Zou, L. S. Luo, and M. Dembo. Some progress in the lattice boltzmann method. part i, non-uniform mesh grids. *J. Comput. Phys.*, 129:357–363, 1996.
- [118] R. Mei and W. Shyy. On the finite difference-based lattice boltzmann method in curvilinear coordinates. *J. Comput. Phys.*, 143:426–448, 1998.
- [119] J. Tölke, M. Krafczyk, M. Schulz, and E. Rank. Implicit discretization and nonuniform mesh refinement approaches for fd discretisation of lbgk models. *Int. J. Mod. Phys C*, 9(8):1143–1157, 1998.
- [120] M. Bouzidi, D. D’Humières, P. Lallemand, and L. S. Luo. Lattice boltzmann equation on a two-dimensional rectangular grid. *J. Comput. Phys.*, 172:704–717, 2001.
- [121] G. Peng, H. Xi, G. Duncan, and S. H. Chou. A finite volume scheme for the lattice boltzmann method on unstructured meshes. *Phys. Rev. E*, 59:4675–4682, 1999.
- [122] O. Filippova and D. Hänel. Grid refinement for lattice-bgk models. *J. Comput. Phys.*, 147:219–228, 1998.
- [123] D. Yu, R. Mei, and W. Shyy. A multi-block lattice boltzmann method for viscous fluid flows. *Int. J. Numer. Methods Fluids*, 39(2):99–120, May 2002.
- [124] P. Lallemand and L. S. Luo. Theory of the lattice boltzmann method: dispersion, dissipation, isotropy, galilean invariance, and stability. *Phys. Rev. E*, 61:6546–6562, June 2000.
- [125] D. Shizgal and D. P. Weaver, editors. *Rarefied gas dynamics: Theory and Simulations (Progress in Astronautics & Aeronautics Series)*, volume 159, pages 440–458. American Institute of Aeronautics and Astronautics, 1992.
- [126] R. Mei, D. Yu, and W. Shyy. Assessment of the multi-relaxation-time and single-relaxation-time models in the lattice boltzmann equation method. *New York: AIAA paper*, pages 2001–2666, 2001.

- [127] J. von Neumann. *Theory of self-reproducing automata*. Univ. of Illinois Press, 1966.
- [128] R. Benzi, S. Succi, and M. Vergassola. The lattice boltzmann equation theory and applications. *Phys. Reports*, 222:145–197, 1992.
- [129] P. J. Dellar. Incompressible limits of lattice boltzmann equations using multiple relaxation times. *J. Comput. Phys.*, 190(2):351–370, September 2003.
- [130] B. F. Armely, F. Durst, J. C. F. Pereira, and B. Schonung. Experimental and theoretical investigation of backward-facing step flow. *J. Fluid Mech.*, 127:473–496, 1983.
- [131] J. L. Kueny and G. Binder. Viscous flow over backward facing steps: an experimental investigation, analysis of flow over a backward facing step. *Not. Fluid Mech.*, 9:32–42, 1984.
- [132] I. E. Barton. A numerical study of flow over a confined backward-facing step. *Int. J. Numer. Methods Fluids*, 21(8):653–665, October 1995.
- [133] Y. H. Qian, L. S. Luo, F. Massaioli, and S. A. Orszag. A benchmark for lattice bgk model: Flow over a backward-facing step. *Fields Inst. Commun.*, 6:207–215, 1996.
- [134] Y. Chen, H. Ohashi, and M. Akitama. Simulation of laminar flow over a backward-facing step using the lattice boltzmann method. *JSME Int. J. B*, 40(1):25–32, 1997.
- [135] C. M. Care, I. Halliday, and K. Good. Lattice boltzmann nemato-dynamics. *J. Phys. Condens. Matter*, 12:665–671, 2000.
- [136] C. M. Care, I. Halliday, K. Good, and S. V. Lishchuk. Genralised lattice boltzmann algorithm for the flow of a nematic liquid crystal with variable order parameter. *Phys. Rev. E*, 67(6):061703(10), June 2003.
- [137] C. Denniston, E. Orlandini, and J. M. Yoemans. Lattice boltzmann simulations of liquid crystals. *Phys. Rev. E*, 63(5):056702(10), April 2001.
- [138] C. Denniston, D. Marenduzzo, E. Orlandini, and J. M. Yoemans. Lattice boltzmann algorithm for three-dimensional liquid-crystal hydrodynamics. *Philos. T. Roy. Soc. A*, 362(1821):1745–1754, April 2004.
- [139] C. Denniston, G. Toth, and J. M. Yoemans. Domain motion in confined liquid crystals. *J. Stat. Phys.*, 107(1/2):187–202, April 2002.
- [140] C. Denniston, E. Orlandini, and J. M. Yoemans. Simulations of liquid crystal hydrodynamics in the isotropic and nematic phases. *Europhysics Letters*, 52(4):481–487, Nov 2000.
- [141] J. Jung, C. Denniston, E. Orlandini, and J. M. Yoemans. Anisotropy of domain growth in nematic liquid crystals. *Liquid Crystals*, 30(12):1455–1462, December 2003.

- [142] G. Toth, C. Denniston, and J. M. Yeomans. Modeling nematohydrodynamics in liquid crystal devices. *Comp. Phys. Comm.*, 147(1-2):7–12, August 2002.
- [143] C. Denniston, E. Orlandini, and J. M. Yeomans. Simulations of liquid crystals in poiseuille flow. *Comput. Teor. Polym.*, 11(5):389–395, 2001.
- [144] D. Marenduzzo, E. Orlandini, and J. M. Yeomans. Rheology of distorted nematic liquid crystals. *Europhysics Letters*, 64:406–412, 2003.
- [145] G. Toth, C. Denniston, and J. M. Yeomans. Hydrodynamics of topological defects in nematic liquid crystals. *Phys. Rev. Lett.*, 88(10):105504, March 2002.
- [146] C. Denniston and J. M. Yeomans. Flexoelectric surface switching of bistable nematic devices. *Phys. Rev. Lett.*, 87(27):275505, December 2001.
- [147] G. Toth, C. Denniston, and J. M. Yeomans. Hydrodynamics of domain growth in nematic liquid crystals. *Phys. Rev. E*, 67(5):051705, May 2003.
- [148] D. Marenduzzo, E. Orlandini, and J. M. Yeomans. Permeative flows in cholesteric liquid crystals. *Phys. Rev. Lett.*, 92(18):188301, May 2004.
- [149] S. V. Lishchuk, C. M. Care, and I. Halliday. A lattice boltzmann scheme for a nematic-isotropic interface. *J. Phys. Condens. Matter*, 16(19):1931–1944, May 2004.
- [150] A. K. Gunstensen, D. H. Rothman, S. Zaleski, and G. Zanetti. Lattice boltzmann model of immiscible fluids. *Phys. Rev. A*, 43(8):4320–4327, 1991.
- [151] S. V. Lishchuk, C. M. Care, and I. Halliday. Lattice boltzmann algorithm for surface tension with greatly reduced microcurrents. *Phys. Rev. E*, 67(03):036701, March 2003.
- [152] M. M. Dupin, T. J. Spencer, I. H. Halliday, and C. M. Care. A many component lattice boltzmann equation simulation for deformable particles. *Phil. Trans. R. Soc. Lond. A*, 362:1885–1914, 2004.
- [153] D. J. Holdych, D. R. Noble, J. G. Georgiadis, and R. O. Buckius. Truncation error analysis of lattice boltzmann methods. *J. Comput. Phys.*, 193(2):595–619, January 2004.
- [154] M. G. Clark and F. M. Leslie. A calculation of orientational relaxation in nematic liquid crystals. *Proc. R. Soc. Lond. A*, 361:463–485, 1978.
- [155] P. J. Kedney and F. M. Leslie. Switching in a simple bistable nematic cell. *Liquid Crystals*, 24(4):613–618, April 1998.
- [156] L. M. Blinov, M. I. Barnik, H. Ohoka, M. Ozaki, N. M. Shtykov, and K. Yoshino. Surface and flexoelectric polarization in a nematic liquid crystal 5cb. *Eur. Phys. J. E*, 4:183–192, 2001.
- [157] L. A. Parry-Jones, E. G. Edwards, S. J. Elston, and C. V. Brown. Zenithal bistability in a nematic liquid-crystal device with a monostable surface condition. *Appl. Phys. Lett.*, 82(9):1476–1478, March 2003.

- [158] G. P. Bryan-Brown, C. V. Brown, J. C. Jones, E. L. Wood, I. C Sage, P. Brett, and J. Rudin. Grating aligned bistable nematic device. *SID Digest*, 28:37–40, 1997.
- [159] J. C. Jones, G. P. Bryan-Brown, E. Wood, A. Graham, P. Brett, and J. Hughes. Novel bistable liquid crystal displays based on grating alignment. *Proceedings of SPIE*, 3955:84–93, 2000.
- [160] C. V. Brown, M. J. Towler, V. C. Hui, and G. P. Bryan-Brown. Numerical analysis of nematic liquid crystal alignment on asymmetric surface grating structures. *Liquid Crystals*, 27(2):233–242, February 2000.
- [161] K. G. Good. Mesoscopic lattice boltzmann nemato-dynamics. *PhD Thesis, Sheffield Hallam University*, February 2001.
- [162] C. J. P. Newton and T. P. Spiller. A novel approach to modelling nematic liquid crystal cells. *Mol. Cryst. Liq. Cryst.*, 372:167–178, 2001.
- [163] N. Mottram and C. Newton. Introduction to q-tensor theory. *University of Strathclyde Research Reports*, September 2004.
- [164] L. A. Parry-Jones and S. J. Elston. Flexoelectric switching in a zenithally bistable nematic device. *J. Appl. Phys.*, 97(9):93515–7, May 2005.
- [165] J. C. Jones, S. M. Beldon, and E. L. Wood. Greyscales in zenithal bistable lcd: The route to ultra-low power colour displays. *SID*, 11(2):269–275, 2003.
- [166] Q. Zou, S. Hou, S. Chen, and G. D. Doolen. An improved incompressible lattice boltzmann model for time-independant flows. *J. Stat. Phys.*, 81(1-2):35–48, February 1995.
- [167] Z. Lin, H. Fang, and R. Tau. Improved lattice boltzmann model for incompressible two-dimensional steady flows. *Phys. Rev. E*, 54(6):6323–6330, December 1996.
- [168] E. G. Edwards. Novel characterisation techniques for nematic liquid crystal cells containing surface relief structures. *PhD Thesis, Wolfson College, Oxford University*, 2004.